

# Sheffield Hallam University

*Analytical studies of corrosion and wear resistant CrN/NbN superlattice PVD coatings.*

CREASEY, Stuart.

Available from the Sheffield Hallam University Research Archive (SHURA) at:

<http://shura.shu.ac.uk/19511/>

## A Sheffield Hallam University thesis

This thesis is protected by copyright which belongs to the author.

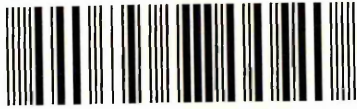
The content must not be changed in any way or sold commercially in any format or medium without the formal permission of the author.

When referring to this work, full bibliographic details including the author, title, awarding institution and date of the thesis must be given.

Please visit <http://shura.shu.ac.uk/19511/> and <http://shura.shu.ac.uk/information.html> for further details about copyright and re-use permissions.

Asset Centre  
Sheffield S1 1WB

101 835 376 3



Return to Learning Centre of issue  
Fines are charged at 50p per hour

12 JUN 2008 *Sp-*

18 JUN 2008 *Spm*

**REFERENCE**

ProQuest Number: 10694392

All rights reserved

INFORMATION TO ALL USERS

The quality of this reproduction is dependent upon the quality of the copy submitted.

In the unlikely event that the author did not send a complete manuscript and there are missing pages, these will be noted. Also, if material had to be removed, a note will indicate the deletion.



ProQuest 10694392

Published by ProQuest LLC (2017). Copyright of the Dissertation is held by the Author.

All rights reserved.

This work is protected against unauthorized copying under Title 17, United States Code  
Microform Edition © ProQuest LLC.

ProQuest LLC.  
789 East Eisenhower Parkway  
P.O. Box 1346  
Ann Arbor, MI 48106 – 1346

**Analytical Studies of Corrosion and Wear  
Resistant CrN/NbN Superlattice PVD  
Coatings**

**Stuart Creasey**

**A thesis submitted in partial fulfilment of the requirements of  
Sheffield Hallam University  
for the degree of Master of Philosophy**

**March 2006**

## Abstract

CrN/NbN nano-scale multilayered coatings have found use in a number of commercial applications where both wear and corrosion resistance are important factors that are required. CrN/NbN nano-scale multilayered coatings have been successfully deposited at temperatures as low as 250°C on 304 stainless steel substrates. This has been achieved by the combined cathodic arc/unbalanced magnetron PVD technique (Arc Bond Sputter) with a coating thickness of 3.0  $\mu\text{m}$  at bias voltages  $U_B$  of -75 and -95 Volts. The coatings exhibited a preferred  $\{111\}$  texture, good adhesion properties and plastic hardness of 38 to 69 GPa. The microstructural and surface morphology properties of these coatings in the as deposited and corroded conditions have been investigated. The corrosion resistance of the coatings was determined using potentiodynamic polarisation measurement in a 3%NaCl solution open to air at room temperature. The low temperature CrN/NbN coatings deposited onto stainless steel exhibited superior corrosion resistance properties than that for stainless steel. Both crevice and pitting corrosion had occurred at selective growth defect sites, beneath which, an under-dense (porous) coating microstructure was present. These under-dense coating regions provide solution pathways through the coating to the substrate. Wherever feasible comparisons were made with CrN/NbN superlattice coatings deposited at higher temperatures (400°C).

## **Acknowledgements**

I would like to express my sincerest thanks to my Director of Studies, Professor Papken Hovsepian who provided me with lots of useful discussions and motivational chats.

I would also like to express my dearest gratitude to Professor Dieter Münz who originally was my Director of Studies and provided me with the opportunity not only to carry out research, but also to be part of his surface engineering team.

My dearest thanks goes to Dr Brian Lewis, a colleague, friend and mentor who has always been there for me. His knowledge and assistance has been invaluable.

I would like to also thank Leon Bowen, Ian Cook, Darrell Horsfield and Andrew Williams for their encouragement and support.

Finally I would like to dedicate this work to my girlfriend Lyndsay Gray for all of her encouragement, inspiration and support. She has been my rock.

# Content

<b>Chapter 1. Introduction.....</b>	<b>8</b>
<b>Chapter 2 Literature review .....</b>	<b>9</b>
2.1 Superlattices.....	9
2.1.1 Superlattice hard PVD coatings.....	9
2.1.2 CrN/NbN superlattice coatings.....	12
2.2 PVD coating process.....	13
2.2.1 Steered cathodic arc evaporation.....	13
2.2.2 Magnetron sputtering.....	15
2.2.3 Arc-Bond-Sputter (ABS™) technology.....	20
2.3 Film growth, interfaces, texture, growth defects and residual stresses of thin films.....	21
2.3.1 Film growth.....	21
2.3.2 The structure of interfaces.....	23
2.3.3 Structure zone models.....	25
2.3.4 Textures in PVD coatings.....	29
2.3.5 Growth defects.....	30
2.3.5.1 Microscopic defects.....	30
2.3.5.2 Macroscopic defects.....	31
2.3.6 Residual stresses in thin films.....	37
2.4 Corrosion.....	40
2.4.1 Corrosion in general.....	40
2.4.2 Potentiodynamic polarisation curves.....	43
2.4.3 Corrosion of CrN/NbN superlattice coatings.....	45
<b>Chapter 3. Experimental.....</b>	<b>49</b>
3.1 Coating system .....	49
3.2 Deposition procedure.....	51
3.2.1 Substrates and substrate preparation.....	51
3.2.2 Deposition parameters of the low temperature process .....	52

3.3 Evaluation techniques.....	55
3.3.1 Structure analysis by X-ray diffraction.....	55
3.3.1.1 Texture.....	55
3.3.1.1.1 Inverse Pole Figures.....	55
3.3.1.1.2 Pole Figures.....	57
3.3.1.2 Residual stress.....	58
3.3.1.3 Superlattice period.....	62
3.3.2 Scanning electron microscopy (SEM).....	64
3.3.2.1 Quantitative analysis (ZAF).....	64
3.3.2.2 Environmental scanning electron microscopy (ESEM).....	65
3.3.3 Mechanical and tribological properties.....	66
3.3.3.1 Layer thickness.....	66
3.3.3.2 Microhardness.....	67
3.3.3.3 Adhesion.....	67
3.3.3.4 Surface roughness.....	68
3.3.3.5 Friction and sliding wear.....	69
3.3.3.6 Corrosion.....	70
<b>Chapter 4. Results and Discussion.....</b>	<b>72</b>
4.1 Texture.....	72
4.2 Residual stress.....	81
4.3 Superlattice period.....	85
4.4 Layer thickness.....	87
4.5 Microhardness.....	88
4.6 Adhesion.....	89
4.7 Friction and sliding wear of CrN/NbN coatings deposited at 250°C.....	90
4.8 Surface quality of CrN/NbN coatings deposited at 250°C.....	92
4.9 Corrosion.....	98
4.9.1 Corrosion behaviour of CrN/NbN coatings of trial_1.....	98
4.9.2 Corrosion behaviour of CrN/NbN coatings of trial_2.....	102
4.9.3 Comparison of the corrosion behaviour of CrN/NbN coatings deposited at 400°C.....	107

<b>Chapter 5. Summary and Conclusions.....</b>	<b>110</b>
<b>A Appendix.....</b>	<b>113</b>
A1 Deposition parameters.....	113
A2 Pin on disc measurement and wear track of trial_1.....	115
A3 Pin on disc measurement and wear track of trial_2.....	117
A4 Surface roughness of CrN/NbN superlattice coatings of trial_1.....	119
A5 Surface roughness of CrN/NbN superlattice coatings of trial_2.....	120
A6 EDX analysis of CrN/NbN superlattice coatings of trial_1.....	121
A7 EDX analysis of CrN/NbN superlattice coatings of trial_2.....	121
A8 EDX analysis of CrN/NbN superlattice coatings deposited at 400°C.....	123
<b>Bibliography.....</b>	<b>124</b>
<b>Publications.....</b>	<b>129</b>

## Abbreviations

PVD	physical vapour deposition
SS	stainless steel
ABS	arc bond sputtering
HTC	Hauzer Techno Coating
UBM	unbalanced magnetron
SZM	structure zone model
CFUBMS	closed-field unbalanced magnetron sputtering
SEM	scanning electron microscope
XRD	X-ray diffraction
GA-XRD	Glancing angle X-ray diffraction
LA-XRD	Low angle X-ray diffraction
EDX	energy-dispersive X-ray
fcc	face centred cubic
WE	working electrode
CE	counter electrode
AE	auxiliary electrode
SCE	saturated Calomel electrode
RE	reference electrode
HSS	high speed steel
dc	direct current
ESEM	environmental scanning electron microscope
SE	secondary electron
HIPIMS	high powered pulsed magnetron sputtering

# 1 Introduction

Nano-scaled multilayered coatings (superlattices) are thin films having an alternating layered structure of two materials with nanometer dimensions. A number of superlattice hard coatings have been produced using the physical vapour deposition (PVD) technique. These coatings usually exhibit high hardness values together with excellent wear and corrosion resistance properties, which therefore mean they become increasingly important in applications where these properties are required.

This report deals with the CrN/NbN superlattice coating system. Hard CrN/NbN superlattice coatings (35GPa) have been developed as a potential alternative to electroplated hard chromium for special industrial applications [1]. This is because PVD processes are considered to be more environmentally friendly. These coatings had normally been produced at 400°C by combined cathodic arc/unbalanced magnetron technique. The deposition of CrN/NbN superlattices on plain carbon and low alloyed steels which are temperature sensitive materials make it necessary to carry out the deposition process at low temperatures in the range of 220°C and 280°C. Investigations revealed that the CrN/NbN superlattice coating can be successfully deposited at these low temperatures. Previous research about this coating system deposited at low temperatures and different bias voltages revealed that the CrN/NbN superlattice coating deposited at a bias voltage of -95V shows outstanding properties. It was also shown that this coating deposited at -95V bias voltage exhibits a strong {111} fibre texture.

In the present work the influence of the texture on the wear and corrosion properties of the of CrN/NbN superlattices is investigated in more detail. Therefore CrN/NbN superlattice coatings deposited at -75V and -95V bias voltage were compared.

The corrosion part of this work also includes additional results of the investigated corrosion behaviour of CrN/NbN superlattice coatings which were deposited at higher temperatures (400°C).

## 2 Literature review

### 2.1 Superlattices

Superlattices are defined as thin films consisting of alternating layers of two different materials (see fig 2.1). They are characterised by the distance between each successive pair of layers which is called a bi-layer repeat period or superlattice period  $\lambda$ . This superlattice period has nanometer dimensions.

Due to many physical effects in superlattices they are scientifically and technologically interesting materials. For example, superlattices combining magnetic and non-magnetic layers exhibiting unique magnetic properties are interesting in the magnetic-recording industry [2]. Another part of superlattice coatings are especially characterised by the substantial increase in hardness and strength which are presented as follows.

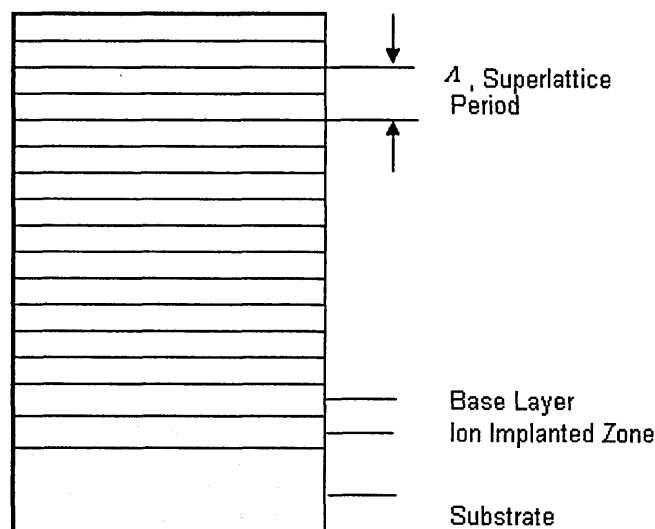


Figure 2.1. Schematic Diagram showing superlattice period in a nano-scaled multilayered coating.

#### 2.1.1 Superlattice hard PVD coatings

An increase in hardness and strength was observed in *metallic superlattices* e.g. aluminium/copper, copper/nickel and iron/platinum and in *ceramic superlattices*, such as titanium nitride combined with either niobium, vanadium or aluminium nitride. The increase in hardness was greater than expected from the "rule of mixtures" of the constituent materials [2]. The reason for this behaviour can be

explained considering the superlattice period. More than thirty years ago, Koehler suggested that the fabrication of a layered structure of two materials with the same crystal structure (i.e. bcc) results in a high strength material. He explained that the interfaces between the layers of materials with different shear moduli would act as barriers to the motion of "dislocations". The atoms in the region around a dislocation in material B are displaced from their normal lattice positions having a strain energy being proportional to the material's shear modulus  $G_B$ . If the dislocation moves into a layer with a higher shear modulus  $G_A$ , the strain energy increases. Hence, there is a repulsive force that increases as dislocations in a layer with a small shear modulus  $G_B$  approach the interface to the layer with a larger shear modulus  $G_A$ . The critical stress which is necessary to move a dislocation across an abrupt interface is proportional to  $Q$ :

$$Q = \frac{(G_A - G_B)}{(G_A + G_B)} \quad (1)$$

A large difference in the shear moduli results in a large critical stress and hence in a large hardness enhancement [2].

Chu and Barnett developed a more detailed model about the dislocation movement in superlattices. This model assumes that the interfaces are not usually abrupt and that interfaces wider than 1nm tend to reduce the effect of having alternate layers with different shear moduli [2]. Their work revealed that for TiN/NbN superlattices the hardness value has a maximum with an intermediate value of  $\lambda$ . This maximum hardness effect is shown in figure 2.2 for the TiN/VN superlattice coating.

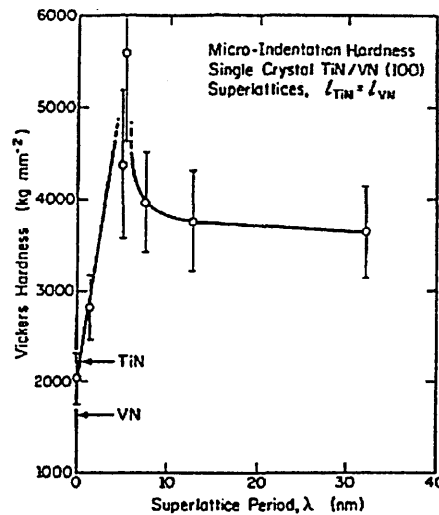


Figure 2.2. Superlattice hardness [3].

If  $\lambda$  is very small, the layers become nearly interdiffused so that the same shear modulus exists in each layer, or if the interfaces are too close together the stress needed to move a dislocation is lowered due to the fact that interfaces can exert opposing forces on a dislocation at an interface. Exceeding an intermediate value for  $\lambda$  the hardness decreases with increasing  $\lambda$  due to the dislocations moving within individual layers.

Beside the high hardness values of superlattice hard coatings another benefit is with the mechanical failure mechanism when compared with monolithically grown multicomponent coatings, as shown schematically in figure 2.3.

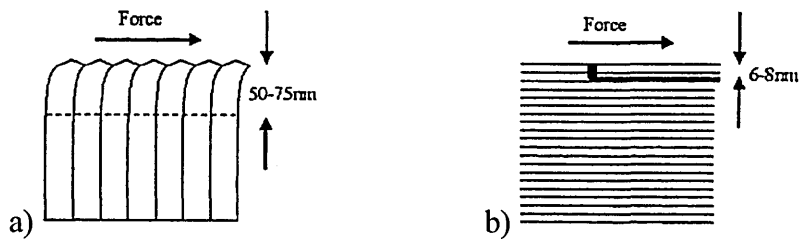


Figure 2.3. Mechanical failure in: (a) monolithically and (b) superlattice coatings [3].

TEM investigations of the wear mechanism of both types of coatings revealed that the individual grains of columnar and monolithically grown coatings suffer severe plastic deformation when exposed to shear forces [3]. This deformation is the source of mechanical failure. The depth of these failures is in the range 50 to 75nm. Due to a chipping or micro-delamination mechanism within the superlattice coatings the failure depth, called chipping depth, is only 6-8nm. Superlattice coatings also exhibit a columnar growth structure but the growth is interrupted, hence, the penetration depth of the cracks is reduced. In addition to this, it is assumed that the wear debris of a superlattice coating generated for example in a pin on disk test are much finer grained than that of a monolithically grown layer leading to a minimised penetration depth.

### 2.1.2 CrN/NbN superlattice coatings

CrN/NbN superlattice coatings, belonging to the group of superhard PVD coatings, were developed to replace electroplated hard chromium. The deposition of CrN/NbN superlattices on temperature sensitive materials at low temperature is necessary to compete with electroplated hard chromium. Investigations revealed that the CrN/NbN superlattice coating could be successfully deposited at low temperatures.

The intention to replace electroplated hard chromium by a superhard PVD coating demands a good corrosion resistance of the coating. Therefore the combination of CrN and NbN as a superlattice was chosen to attain high hardness values together with excellent corrosion resistance [4]. The addition of highly electrochemically stable Nb to the superlattice provides the excellent corrosion resistance properties.

The effective nanoscale modulating of a reasonably dense CrN/NbN superlattice coating provides a significant increase in the pitting potential and reduction in passive current densities compared with a commercial CrN coating deposited on a 304 stainless steel (SS) substrate. The layered structure decreases the coating porosity and therefore the diffusion of solution species to the coating-substrate interface is reduced [1]. In contrast to this, electroplated chromium has a relative open and microcracked structure. Regarding the potentiodynamic polarisation curve of hard chromium, no clear pitting potential and a high current in the passive region is visible, which indicates that the coating/substrate interface suffers crevice and pitting corrosion. CrN/NbN superlattice coatings exhibited current densities in the passive region being one tenth of that of hard chromium electroplating [1].

The wear rate of CrN/NbN coatings can also compete with hard chromium coatings. Comparison of pin on disc test results (load 5N, Al<sub>2</sub>O<sub>3</sub> ball, 50000 revolutions) of a 18µm thick electroplated hard chromium coating with that for a 5µm thick CrN/NbN superlattice coating, showed that the wear rate of the CrN/NbN coating is also one tenth that of the wear rate of the electroplated hard chromium coating [4].

## 2.2 PVD coating process

The CrN/NbN superlattice was produced by a combined cathodic arc/unbalanced magnetron ABS<sup>TM</sup> PVD coating process. The different techniques associated with the PVD coating processes are presented as follows.

### 2.2.1 Steered cathodic arc evaporation

Evaporation is a process of thermal vaporizing of the target in which the heating is carried out at a low pressure [5]. In this case the cathodic arc discharge is used to heat up the material and to produce metallic vapour. The arc strikes on the target which acts as a cathode. The initiation of the arc is by the application of a high voltage pulse to an electrode placed in the vicinity of the target which is to be evaporated. The produced cathode-spot, 10 to 100 $\mu\text{m}$  in size [6], is a high current (30-400 A), low voltage (15-50V) [7] electrical discharge. The current densities on the cathode surface are high ( $10^8$  to  $10^{11}$  A m<sup>-2</sup>) resulting in high localised temperatures on the target [5]. Due to this, small molten pools are formed on the target surface and an explosion-like evaporation takes place emitting atomic particles and small droplets [8]. The atomic particles pass through the arc resulting in the ionisation of the metal atoms which are accelerated away from the cathode due to a non-uniform potential distribution and plasma expansion [50]. This flux of dense plasma consists of electrons, ions, neutral vapour atoms and microdroplets called macroparticles with the size of 0.1 to 100 $\mu\text{m}$  [5], [6], [7]. The emissions from the cathode spots based on the stationary model are shown in figure 2.4.

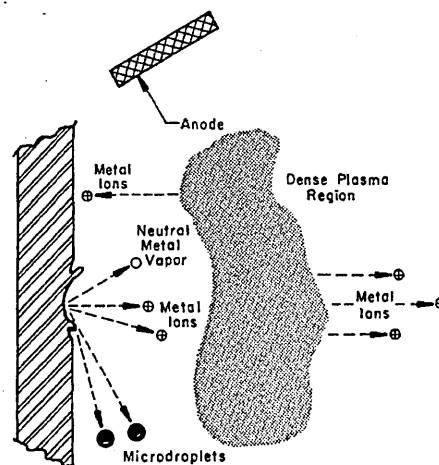
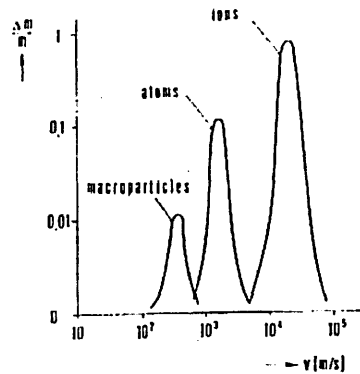


Figure 2.4. Cathode spot region of a vacuum arc [9].

The spatial distribution, energy and quantity of the individual particles are very different. Macroparticles are emitted mainly in the cathode plane while ions move mainly perpendicular to the cathode surface. The spatial distribution of particles emitted from a cathode of high melting material is close to a cosine distribution [6]. The velocity distribution of the emitted ions, atoms and macroparticles is shown in figure 2.5.



**Figure 2.5.** Velocity distribution of macroparticles, atoms and ions of a high melting point metal [6].

There is a high density of particles in the cathode region (electron density up to  $10^{20}\text{m}^{-3}$ ) due to the intensive evaporation of the cathode material in cathode spots. Creating the conducting medium itself the arc is self-sustaining [5]. A high percentage (30-100%) of the evaporated material is ionized [7]. The kinetic energies of the ions are typically in the range of 50 to 150eV [10].

The cathode spot moves randomly on the cathode surface with velocities between 1 and 100 m/s in the absence of a magnetic field [5]. Applying a strong external magnetic field the travelling direction of the arc is steered by the external magnetic field and the arc travel velocity increases [11]. Due to the increased cathode spot velocity the macroparticles emission is lower [6], [7]. If a transverse magnetic field is imposed behind the target the spot moves with velocities up to  $150\text{ms}^{-1}$  in the  $-\mathbf{J}\times\mathbf{B}$  direction, which is known as retrograde motion [10]. The arc spot sits preferentially at the point where the vertical component of the magnetic field is zero [12].

## 2.2.2 Magnetron sputtering

If an ion approaches the surface of a solid, which is called the target, several interactions, shown in figure 2.6, can occur on the target surface and in the target itself.

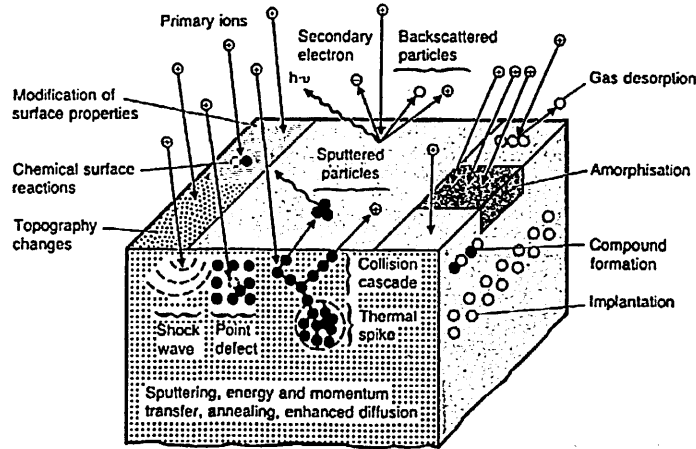


Figure 2.6. Interactions of ions with the surfaces [13].

The interactions in the target itself include generation of collisional cascades, creation of point defects e.g. vacancies and interstitials, local heating, amorphisation, implantation and compound formation.

Possible interactions on the target surface are backscattering, X-ray emission, photon generation, secondary electron emission, desorption of gas atoms from the target surface and liberation of atoms. The ejection of surface atoms by momentum transfer from energetic bombarding species of atomic/molecular size is called sputtering which is a nonthermal vaporisation process [13].

The energy transfer must be greater than the bonding energy to eject an atom of the surface. If the linear momentum and the energy is conserved the fractional energy transferred from the ion with the mass  $m_i$  to a target atom with the mass  $m_t$  is given by the equation (2):

$$\frac{E_t}{E_i} = \frac{4m_i m_t}{(m_i + m_t)^2} \cdot \cos^2 \theta \quad (2)$$

Where  $\theta$  is the angle at which the ion collides with the target atom.

Due to the reason that different interactions between the impacting ion and the surface can take place (see figure 2.5) the sputtering yield  $S$  was introduced defining the number of ejected atoms from the target surface per incident ion. The sputtering yield  $S$  can be expressed by the equation (3)

$$S = \alpha \frac{4m_i m_t}{(m_i + m_t)^2} \cdot \frac{E}{U_0} \quad (3)$$

Where  $U_0$  is the surface binding energy of the material,  $E$  is the energy of the incident ion and  $\alpha$  is a coefficient depending on the mass ratio of the colliding particles [14]. This expression for  $S$  predicting that the yield increases linearly with  $E$  is valid up to above 1 keV.  $S$  becomes relatively constant above 1keV and decreases at very high energies because the ion energy is dissipated well below the surface, which is shown in figure 2.7 for copper as target material.

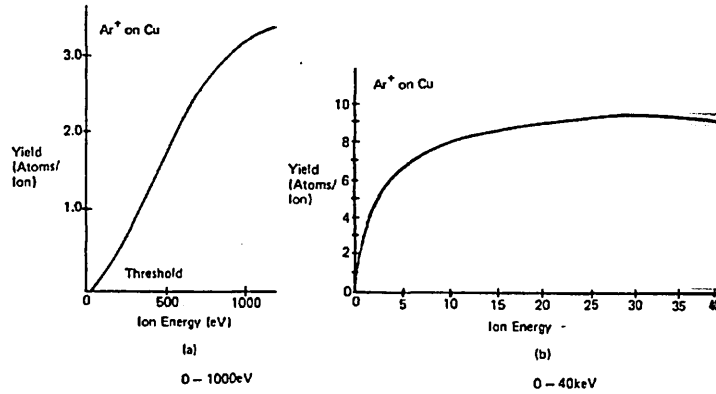


**Figure 2.7.** The variation of sputtering yield for Ar<sup>+</sup> on Cu as a function of the ion bombardment energy [16].

The ejected atom is moved through the space until it strikes and condenses on the surface of the substrate, which is coated by repeating the process over and over. The ions are provided by the working gas e.g. argon. The argon atoms have to be ionised by electrons which come from glow discharge between an anode and a cathode. There are free electrons in the coating chamber which are accelerated towards the anode. Having an Ar atmosphere in the pressure range between 1 to  $50 \times 10^{-3}$  mbar some of the accelerated free electrons collide with the Ar atoms, which results in the production of further electrons ( $e^-$ ) and Ar ions ( $Ar^+$ ).



Plasma, consisting of positive ions and negative electrons in a sea of neutral atoms is formed. The plasma can be divided into several distinct regions with varying voltage potentials.

Electrons and ions can be lost to the electrodes and to all other surfaces within in the chamber. It is necessary to create new ions and electrons to maintain a steady state discharge. This is reached by the emission of secondary electrons due to the impact of  $\text{Ar}^+$  on the target surface, which can then form further ions.

Using a magnetic field in sputtering the efficiency of the electrons can be increased and therefore the ionisation is enhanced [15]. The magnets either permanent or electro-magnets are situated behind the target. A moving particle with the charge  $q$  and the velocity  $v$  in a magnetic field  $B$  is subjected to a force  $F_m$  (Lorentz force) which is perpendicular to the magnetic field and the velocity (5):

$$\vec{F}_m = q\vec{v} \times \vec{B} \quad (5)$$

If the charged particle moves perpendicular to the magnetic field the force  $F_m$  will cause the particle with the mass  $m$  to move in an orbital path with the radius  $r$ :

$$r = mv_{\perp} / qB \quad (6)$$

Equation (6) can be written as (7)

$$r = \frac{\sqrt{2m \cdot E_{kin}}}{q \cdot B} \quad (7)$$

Where  $E_{kin}$  is the kinetic energy of the particle.

The resulting path is helical because the component of the velocity which is parallel to the magnetic field is unaffected. There are Ar ions and electrons in the plasma which are subjected to the force  $F_m$ , but having a great mass the Ar ions have a larger orbit than the coating chamber so that this influence is ignored [17].

A combined electric and magnetic field in the coating chamber which are perpendicular to each other is used in this investigation. The net trajectory of the particles is cyclical. If the charged particle moves in the direction of  $E$  it picks up speed and is less deflected by the magnetic field. Going against the electrical field the particle loses speed and is more deflected by the magnetic field.

The result of this cyclical motion is an effective drift in the direction of  $E \times B$ , as shown in figure 2.8.

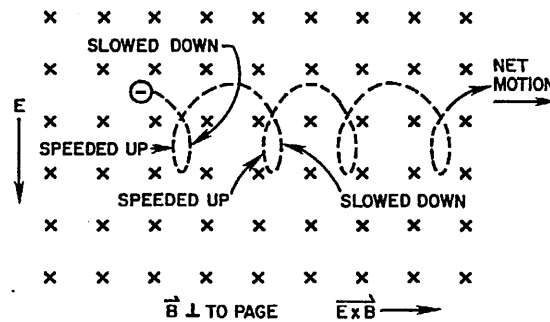


Figure 2.8. The motion of an electron in combined electric and magnetic fields [17].

The magnets are arranged in such a way that one pole is positioned at the central axis of the target and the second pole is formed by a ring of magnets around the outer edge of the target, see figure 2.9a [18].

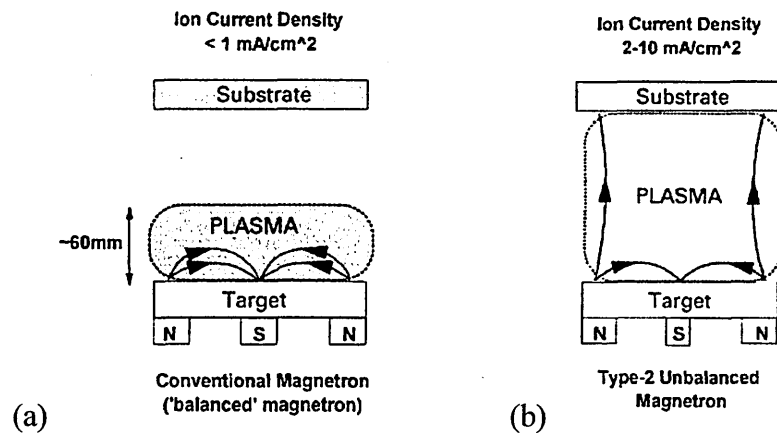
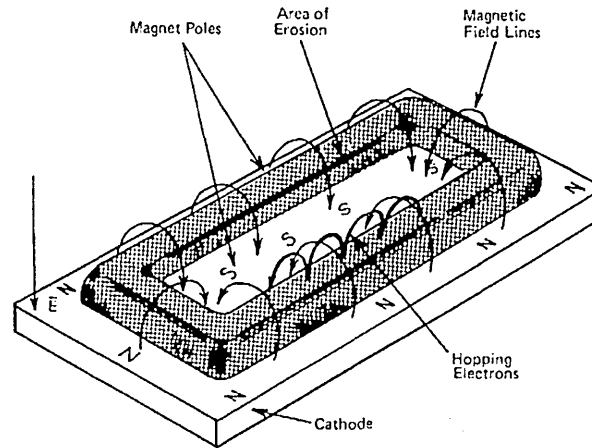


Figure 2.9. Schematic representation of the plasma confinement in (a) balanced magnetrons and (b) unbalanced magnetrons with stronger outer poles [18].

The electrons can be trapped in this way which increases the probability of an ionising electron-atom collision. This results in dense plasma in the target region, which leads to increased ion bombardment of the target and hence a higher sputter rate achieving higher deposition rates at the substrate. Having a greater ionisation efficiency the discharge can be maintained at lower operation pressures ( $10^{-3}$  mbar instead of  $10^{-2}$  mbar) and lower sputtering voltages (-500V instead of -2 to -3kV) compared to the sputtering mode without magnetrons [18].

Applying a negative potential to the substrate ions can be extracted from the discharge surrounding the substrate. The current density incident on the film-substrate surface is quite low, 0.05 to 0.10 ions per deposited atom in conventional dc magnetrons. This ratio should be increased without increasing the energy of the bombarding ions. This can be reached by the use of unbalanced magnetrons [13]. In contrast to the balanced magnetron the field lines of the unbalanced magnetron are not all closed between the central and the outer poles because one magnetic pole, in this case the outer pole, has been made significantly stronger, as shown in figure 2.9b. Hence, the electrons from the cathode region are less tightly trapped and can flow towards the substrate. The electrons tend to pull ions along so that the plasma expands and reaches the sample region [13]. The ion-to-deposited-atom ratio is about 2:1 at low substrate bias potentials [13]. The planar magnetron sputtering configuration for the cathode is shown in figure 2.10.



**Figure 2.10:** Planar magnetron sputtering configuration [16].

A multiple magnetron system is used to deposit CrN/NbN superlattices. Having an even number of cathodes the adjacent magnetrons have opposite magnetic polarities resulting in a closed field configuration where the field lines are linked between the magnetrons, see figure 2.11.

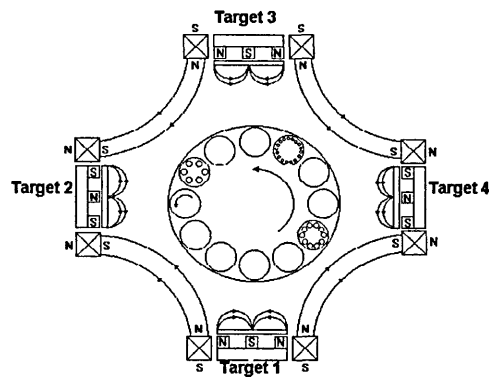


Figure 2.11. Schematic diagram of four target coating system [19].

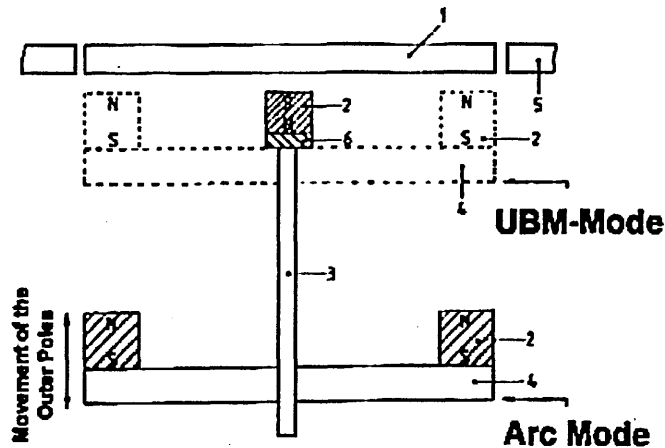
The ion current density at the substrate increases almost linearly with the discharge current [19].

### 2.2.3 Arc-Bond-Sputter (ABS™) technology

The arc bond sputtering (ABS) technology combines the methods of steered arc and unbalanced magnetron technology. The combining of these coating processes lead to the development of the Hauzer Techno Coating (HTC) 1000-4 ABS™ system. The idea of the ABS™ method is to combine the advantages of the arc technology with that of unbalanced magnetron technique [19]. Using this technology the substrates are etched by ions generated by a cathodic-arc discharge prior to deposition of the coating by unbalanced magnetron sputtering. The use of the steered-arc results in the bombardment of highly ionised metal atoms i.e.  $\text{Cr}^+$ , which provide an intensive sputter cleaning of the substrate surface and tailored interface formation with a minimised droplet amount [1]. The metal-ion etching guarantees a superior adhesion of the coating to the substrate [20].

Using the unbalanced magnetron during the deposition step it is possible to deposit coatings at large working distances between the substrate and the target [31]. In addition denser and droplet-free coatings can be deposited by the unbalanced magnetron technique [19], [21].

Cathodes and power supplies must be suitable for the arc mode and magnetron operation. One cathode has to operate in the arc and unbalanced-magnetron (UBM) mode. During the arc operation the outer poles of the typical magnetron arrangement are withdrawn from the back of the target. The central pole of the magnetic field remains close to the target to run the steered arc mode [22]. The arrangement of the magnets is shown in figure 2.12.



1 = target                      3 = fixturing of center poles                      5 = recipient  
 2 = permanent magnets      4 = magnetic yoke                                      6 = magnetic neutral spacer

Figure 2.12. Schematic diagram of the combined Steered Arc™ and unbalanced-magnetron source [22].

## 2.3 Film growth, interfaces, texture, growth defects and residual stresses of thin films

### 2.3.1 Film growth

The condensation of atoms (“adatoms”) on a surface results in atomistic film growth [23]. Oettel describes the stages of layer growth which occur simultaneously as follows [8]:

1. Absorption of the incident particles (in competition with their desorption).
2. Formation of small clusters or nuclei by surface diffusion of the adsorbed particles.
3. Growth of the cluster/nuclei by adding of further particles, cluster migration and coalescence.
4. Ripening and recrystallization processes.

Atoms that impinge the surface in a vacuum environment are either reflected immediately, re-evaporate after a residence time or condense on the surface [23]. The atoms which are not reflected or re-evaporated may not stick to the immediate surface where they impinged. They have a certain degree of surface mobility, which depends on the energy of the atom, the atom-surface interaction (chemical bonding) and the temperature of the surface [23]. The surface diffusion is affected by the different surface free energies of different crystallographic planes e.g. the free energy of the (111)-plane of face-centered cubic metals is less than for the (100)-plane, so the surface mobility of an ad-atom on the (111) surface is higher than on the (100)-surface. As a consequence different crystallographic planes will grow at different rates during ad-atom condensation [23].

The condensing atoms react with the surface to form atom-to-atom chemical bonds hence they lose energy. Depending on the strength of the ad-atom-surface interaction the surface mobility can either be low or high. If the atom-atom interaction is strong, each surface atom can act as a nucleation site due to a low surface mobility. The ad-atom will have a high surface mobility if the ad-atom-surface interaction is weak. In this case the ad-atom will condense at preferential nucleation sites like:

- morphological surface discontinuities (e.g. steps and scratches).
- lattice defects in the surface (e.g. point defects and grain boundaries).
- charge sites in insulator surfaces.
- surface areas having a different chemistry or crystallographic orientation.
- foreign atoms in the surface [23].

Condensed atoms form nuclei. It is a homogeneous nucleation if the surface and the deposited atoms are of the same material. If the surface and the ad-atoms are of different materials then a heterogeneous nucleation takes place. The formation of a closed layer occurs in three stages: At first the island growth takes place with nucleation and growth of nuclei which is parallel to the surface. The nuclei grow by collecting atoms which diffuse over the surface. Reaching a maximum of nuclei density the islands coalesce. Interfacial voids or structural discontinuities at the interface can be a result of growth and coalescence of the nuclei if there is no chemical interaction between the nuclei and the substrate material and growth in a

vertical mode occurs [23]. A tunnel or channel stage occurs if coalescence and secondary nucleation takes place which leads to complete covering.

The following three different types of nucleation mechanisms are known [24]:

- Van der Merwe mechanism (2-dimensional nucleation): monolayer-by-monolayer growth
- Volmer-Weber mechanism: 3-dimensional nucleation and growth
- Stranski-Krastanov mechanism (2-dimensional nucleation): layer growth followed by island formation.

The developed microstructure depends on diffusion (temperature), kinetic energies of the impinging particles, density of the particle flow, angle of the incidence and preferred crystallographic orientation of growth of the layer material.

### **2.3.2 The structure of interfaces**

Interfaces are transition regions between two areas or zones of a material. The deposited film can diffuse and react with the substrate resulting in the formation of an interfacial region. The interface characteristics are important to the adhesion, electrical and electronic properties [23], [24]. Different types of interfacial regions can be distinguished as follows: abrupt, mechanical, diffusion, compound, pseudodiffusion and reactively graded interfaces [23], [24] and are shown schematically in figure 2.13.

If the interfacial region is characterized by an abrupt change in material properties due to the abrupt change from the substrate material to the film material in a distance of the order of the atomic spacing then it is called *abrupt interface*. This interface is formed as a consequence of the absence of bulk diffusion and a weak chemical reaction between the deposited atoms and the substrate. Hence the adhesion of the system is considered to be weak [23], [24].

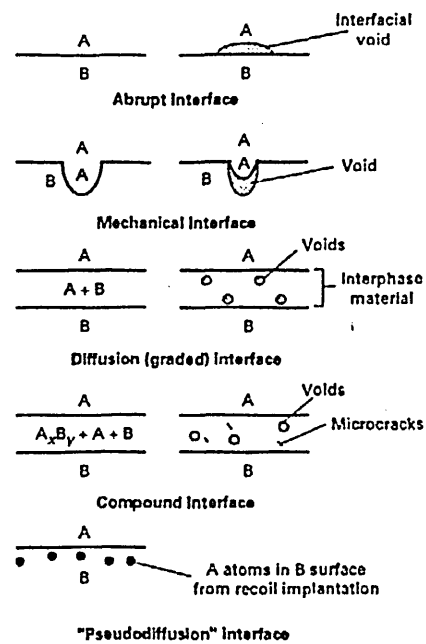


Figure 2.13. Types of interfacial regions [23].

The *mechanical interface* is a special type of the abrupt interface. This kind of interfacial region is formed on a rough surface where the deposited film forms a conforming surface to the roughness, resulting in mechanical interlocking [23], [24].

An interfacial region having a gradual change in composition with no compound formation is known as a *diffusion interface*. It can be formed if there is a mutual solubility between the two materials (A+B) and if there is sufficient temperature and the time to allow diffusion to occur. If the two materials have different diffusion rates then this can create porosity in the interfacial region, known as the Kirkendall effect. This porosity can be a problem because it increases the failure probability with the formation of voids leading to microcracking within the coating [23], [24].

A *compound interface* is formed, if diffusion (A+B) occurs together with a chemical reaction ( $A_xB_y$ ) between the two neighbouring materials. Usually the compounds formed are brittle and introduce high stresses due to volumetric changes in the interfacial region. These stresses can be relieved by microcracking in the interfacial region resulting in a weakened interface. A compound interface, generally being conducive to good adhesion, will lead to poor adhesion if this region is too thick due to porosity and microcracked brittle compounds [23], [24].

A *pseudodiffusion interface* can be achieved by implantation of ions during subsequent or concurrent ion bombardment. It is characterized by a graded interface. In contrast to the diffusion interface it can be formed between insoluble materials. This interface provides an improved adhesion [23], [24].

Controlling the amount of a reactive gas flow during reactive deposition a *reactively graded interface* having a graded compound-matrix material can be formed.

### 2.3.3 Structure zone models

Structure zone models (SZM) describe the film morphology after an appreciable film thickness has been reached where the film establishes a growth mode not being influenced by the substrate [23]. The first SZM, published by MOVCHAN and DEMCHISHIN in 1969 [25], described the formation of the microstructure of vacuum-deposited film in dependence of the homologous temperature  $T/T_m$ , where  $T$  is the deposition temperature (in Kelvin) and  $T_m$  is the melting point (in Kelvin) of the deposited material [25]. The model distinguishes between three zones, as shown in figure 2.14.

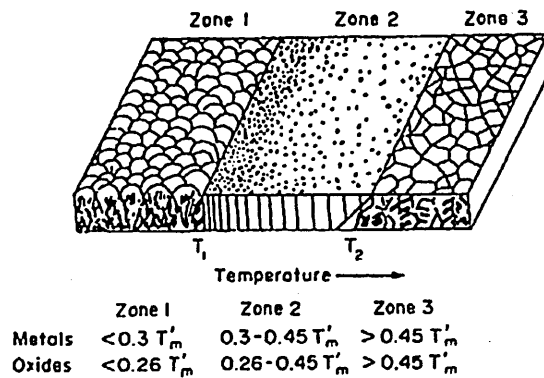


Figure 2.14. SZM by MOVCHAN and DEMCHISHIN, where  $T'_m = T/T_m$  [25].

*Zone 1* is characterised by a restricted or no surface diffusion and no volume diffusion. It shows an open grain structure with very fine fibre-like textured grains having a high defect density and high porosity between the fibres because of shadowing effects of the incident particles. This results in a rough surface, low residual stresses and bad mechanical or tribological properties [25].

*Zone II* allows surface diffusion but volume diffusion is very restricted or does not occur. This zone shows fine and dense columnar grains with texture and smooth surfaces. Due to high defect densities there are significant residual stresses present within the coating. Generally this zone has good mechanical properties [25].

*Zone III* makes all kinds of diffusion possible. The nucleation is homeo-epitactic and grain boundary migration occurs. The morphology is characterised by non-columnar coarse grains with low defect densities. There is a weaker texture. The residual stresses are low and the mechanical properties are reduced [25].

THORNTON extended this model for sputtered films, as shown in figure 2.15 [26].

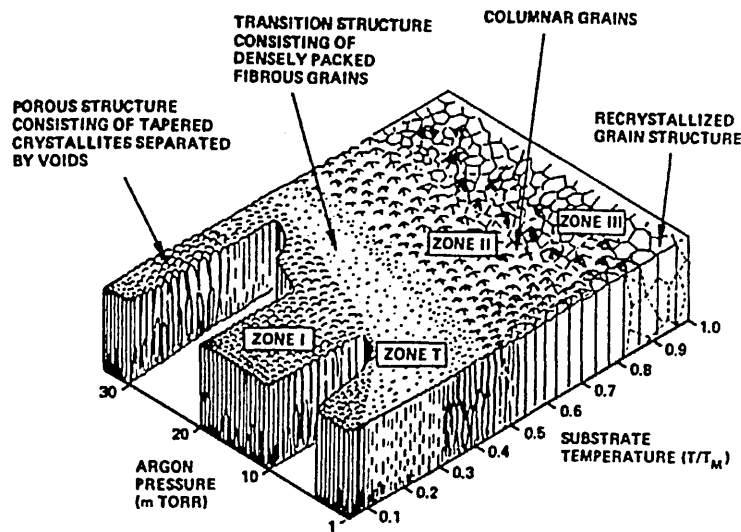


Figure 2.15. SZM by THORNTON [26].

He added a second process parameter: the working gas pressure which is equivalent to the energy of the particles. High gas pressure results in low particle energies due to frequent collisions [26]. The model by THORNTON introduces an additional zone T between zone I ( $T/T_m < 0.3$ ) and zone II ( $0.3 < T/T_m < 0.5$ ) in comparison to the model by MOVCHAN and DEMCHISHIN.

*Zone T* ( $T/T_m < 0.3$ ) is the so called transition zone. It consists of densely packed fibrous grains with optimal mechanical properties and high residual stresses [26]. The formation of this zone is a result of the energetic bombardment from reflected high-energy neutrals from the sputtering target at low gas pressures. Due to this bombardment peaks are eroded and fill in the valleys to some extent [23], [26].

It must be emphasised that these two models have not taken into account important parameters like the particle fluxes and the direction of particle incidence hence they can not describe all features of the microstructure in a generalized manner [26].

In 1984 MESSIER altered the THORTON model by replacing the pressure axis with a substrate bias voltage axis, as shown in figure 2.16 [27]. An increase in the bias voltage results in an increased average energy of the bombarding ions, which enhances the ad-atom mobility. Zone I is suppressed at higher bias voltages in this model [27].

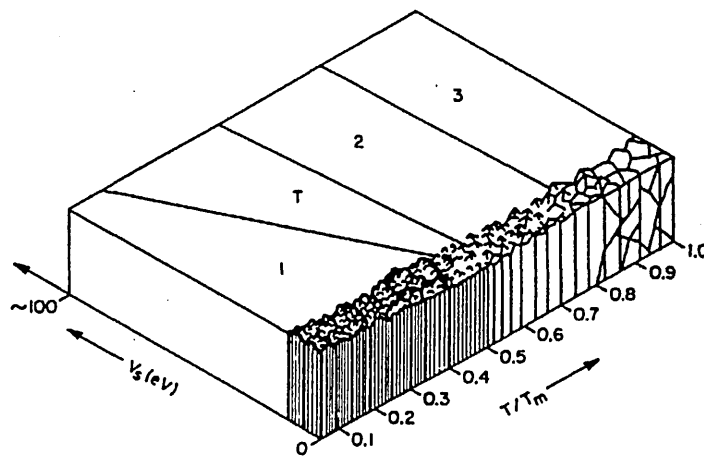


**Figure 2.16.** SZM showing the influence of substrate bias voltage and substrate temperature for thick films after MESSIER [27].

A new SZM for films, which are deposited using closed-field unbalanced magnetron sputtering (CFUBMS) systems has been developed by KELLY and ARNELL in 1998 [28]. This model describes the coating structures in terms of homologous temperature, bias voltage (to represent ion energy) and ion-to-atom ratio. This model is considered to be an advanced model because it allows a separate consideration of the influences of ion flux and ion energy on structure. Aluminium, zirconium and tungsten were deposited and the following parameters were varied in the investigation (Kelly and Arnell) with target current (2-8A), substrate bias voltage (-30 to -70V), coating pressure (0.5 -3mTorr) and substrate-to-target separation. Their investigation revealed that the structures of coatings were either fully dense (zone 3) or dense columnar (zone 2). Structures corresponding to zone 1 were not produced in their investigation, as shown in figure 2.17.

The figure shows that with the CFUBMS “high temperature” structures can be achieved at relatively low homologous temperatures while the formation of the “low temperature” zone 1 and zone T structures is suppressed.

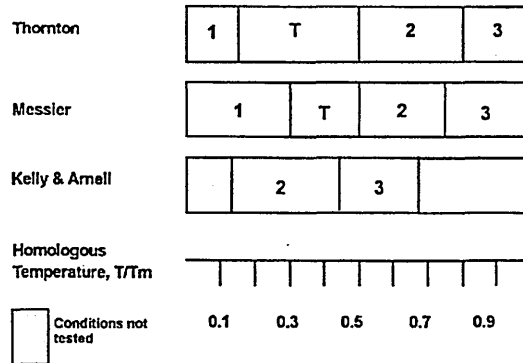


**Figure 2.17.** A comparison, in terms of homologous temperature, of the positions of the zonal boundaries given in published SZMs for other sputtering systems with the boundaries observed for the CFUBMS system [28].

The SZM which accommodates three deposition parameters is shown in figure 2.18a.

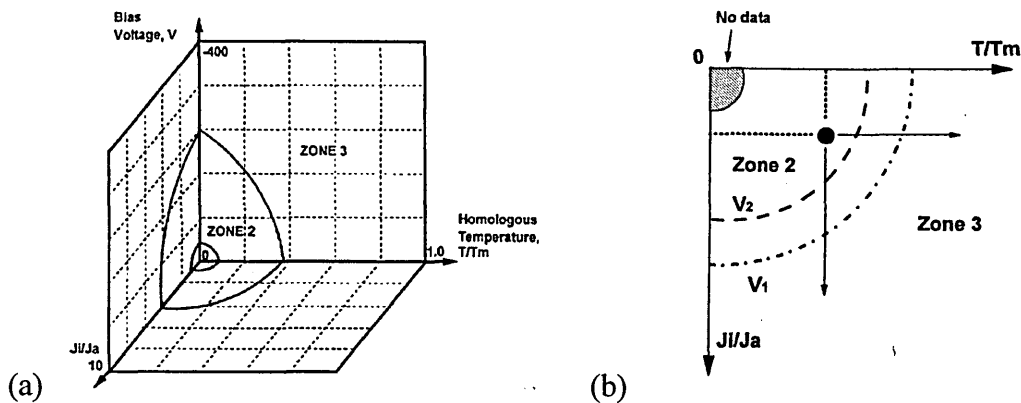


**Figure 2.18.** (a) SZM for films deposited using CFUBMS [19]. (b) Two-dimensional slices through structure zone model at constant voltages  $V_1$  and  $V_2$ , where  $V_2 > V_1$  [28].

A boundary, forming a surface in this three-dimensional model, separates the zone 2 regions, from the zone 3 region. The boundary inside the zone 2 region marks the levels of the used parameters in the investigation by Kelly. A better illustration of the model can be achieved by considering slices through it at constant values of one parameter, as shown in figure 2.18b [28].

### 2.3.4 Textures in PVD coatings

Textures are preferred orientations of the grains in polycrystals. The growth process of the film on the substrate causes the development of textures in films.

Due to the directed incidence of the particles the growth of the crystalline films is nearly uni-directional, which leads usually to a highly textured microstructure. This preferred texture results in anisotropic properties [29]. The texture formation is influenced by a high diversity of factors, which includes: temperature, particle energies, substrate and film materials, composition of gases, gas pressure, substrate and film materials [30].

The grown layers can be divided in three zones considering the texture formation [30]:

**Zone A** is near the substrate interface where epitactic nucleation leads to a texture determined by the substrate's texture. This process takes place at temperatures above the so-called epitactic temperature. It can be supported by small particle fluxes, high surface energy of the nucleus and similar crystallographic structure of the contacting lattice planes resulting in a low energy interface between substrate and nucleus [8].

**Zone C** is the region near the surface of the growing layer. In this region the texture is determined by an energy controlled growth selection. This is influenced by the film material and the process parameters but not by the substrate [30]. The energy controlled orientation selection yields to a minimum energy of the layer system given by equation (8) [8]:

$$E = E_{surface} + E_{grain} + E_{defect} + E_{strain} \Rightarrow \min \quad (8)$$

Where

$E_{surface}$  = total surface energy

$E_{grain}$  = total grain and phase boundary energy

$E_{defect}$  = energy caused by defects

$E_{strain}$  = elastic strain energy.

If the growth selection is *energy-controlled* then the grains with a minimum surface energy of a certain *hkl* plain will grow preferentially.

The growth selection can also be controlled by orientation dependent growth rates known as *growth rate controlled selection* [30]. This includes kinetic-growth velocities where the orientation selection is controlled by the velocity and the orientation-selective sputtering through channelling, which means that the directions with the lowest resputtering effect and the best channelling conditions grow preferentially [31].

**Zone B** is the intermediate area between A and C. The orientation selection conditions are altered inside this zone [30].

The growth direction is influenced by the angle of incidence of the particles. The particles do not impact perpendicularly on the substrate surface using PVD methods. Due to the angular spread of the particles the textures of the thin films are inclined producing fibre textures, which coincide with the columnar axes [30].

### **2.3.5 Growth defects**

The growth of PVD coatings takes place far away from the thermodynamic equilibrium resulting in high defect densities within the coating [8]. Growth defects can be divided in microscopic and macroscopic defects.

#### **2.3.5.1 Microscopic defects**

The microscopic defects appearing in coatings can be further distinguished in point defects (0-dimensional), 1-dimensional, 2-dimensional and 3-dimensional defects:

*0-dimensional defects:*

Due to fast effective quenching of the vapour and due to collision cascades of the incident particles, intrinsic point defects like self interstitials or vacancies appear. As a consequence precipitations are accelerated and intrinsic point defects can form clusters or complexes with extrinsic defects [8]. The incorporation of noble gas atoms or impurities by substitution on regular lattice sites is called extrinsic point defects. These defects arise due to collision cascades or implantation resulting in a

remarkable volume change of the lattice, which leads to residual stresses. Extrinsic point defects are usually generated simultaneously with intrinsic point defects [8].

*1-dimensional defects:*

Dislocations are 1-dimensional defects. It is assumed that in layers with grain sizes larger than 0.1mm the dislocation density is similar to those in highly deformed metals. In contrast to this the existence of dislocations in nanocrystalline materials is discussed controversially. In these materials the annihilation of generated dislocations is favoured because of the high number of grain boundary regions, which makes the material elastically strongly inhomogeneous.

The grain boundaries are *2-dimensional defects*.

*3-dimensional defects:*

Considering the zone I of the microstructure model a remarkable porosity between the grains appears, which results from shadowing effects of the incident particles especially at a low angle of incidence. These defects are called cavities. Clustering of vacancies or coalescence of Ar or N, which are incorporated during the deposition process results in the formation of pores, too.

### **2.3.5.2 Macroscopic defects**

Pinholes, hillocks and droplets are known as macroscopic defects. Pinholes are generated due to particulate contamination of the surface [32]. The formation of pinholes depending on the surface roughness is shown in figure 2.19.

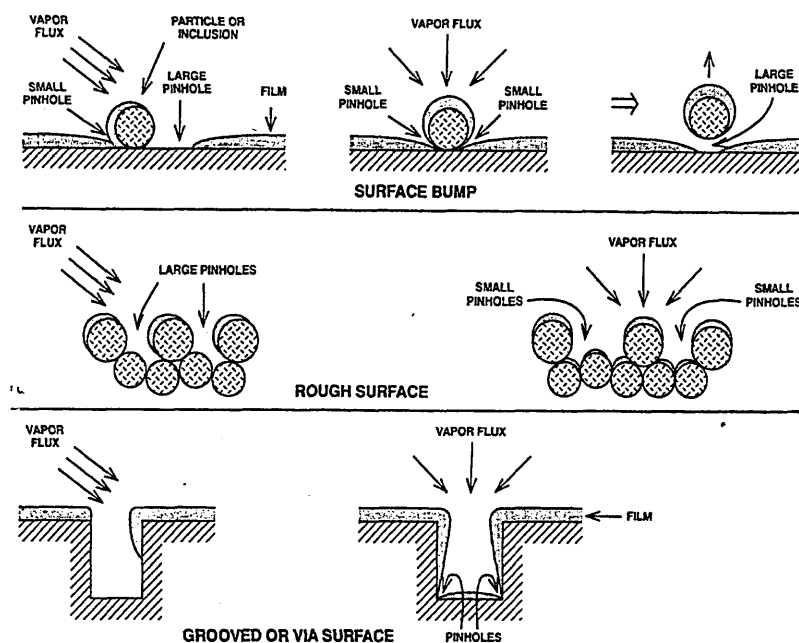


**Figure 2.19.** Effect of surface features and angular distribution of deposition flux on film deposition: top, inclusion or particle contamination; middle, rough surface; bottom, single surface feature [32].

The most-dense PVD coatings can be achieved by a smooth substrate surface because of the lack of macro-columnar morphology, which would result from geometrical shadowing of features on the substrate surface [32].

The existence of droplets has a detrimental influence of the corrosion behaviour of coatings (see section 2.4). Considering the arc bond sputtering (ABS) process (see section 2.2.3) the formation of metallic droplets occurs during metal ion etching by an arc discharge. Growth defects are generated on top of these droplets during the unbalanced magnetron sputtering process [33] due to abnormal coating growth above the droplet. The ejection of melt metal droplets is integral to the vapourisation of neutrals and emission of electrons during the process of arc discharge [34]. During this process an arc travels along spots across the target surface with a short dwell time ( $10^{-7}$ ms). Due to the strong heating of the target surface micro molten pools are developed at the spots. The target metal plasma consisting of vapour ions, vapour neutrals, electrons and liquid metal droplets are ejected by the molten pools. The liquid droplets can solidify during the flight to the substrate and form coating macroparticles there [34]. The number, density and size of droplets depend on parameters like the cathode current or power, target melting point and background gas pressure. The table, given in the appendix, summarises the results obtained from metal ion etching with different materials with the following process parameters:

$U_{\text{Etch}} = -1200\text{V}$ ,  $I_{\text{Arc}} = 100\text{A}$ ,  $P_{\text{Ar}} = 2 \times 10^{-3} \text{ mbar}$ ,  $T_{\text{Etch}} \approx 450^\circ\text{C}$ ,  $t_{\text{Etch}} = 10\text{min}$ ,  $H_{\parallel} = 50\text{G}$  and target to substrate distance  $\approx 30\text{cm}$ . Figures 2.20a and 2.20b show the size distribution of the droplet formation resulting from Cr and Nb metal ion etching [33]. It can be clearly shown that majority of the droplets for both metals are less than 1 micron in diameter.

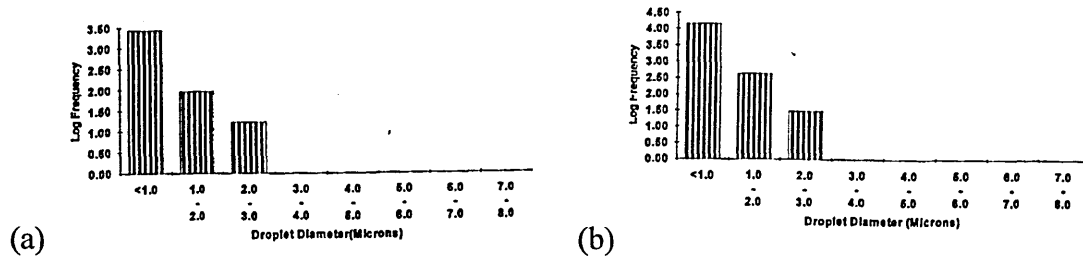


**Figure 2.20.** Frequency of droplet diameter of (a) Nb and (b) Cr etched samples [33].

This investigation revealed that the maximum droplet diameter decreases with increasing melting temperature up to  $2000^\circ\text{C}$ . For materials having a melting temperature greater than  $2000^\circ\text{C}$ , the maximum droplet size and the number of droplets generated seem to be independent of the melting point [35]. It is assumed that full solidification of the droplets from higher melting materials takes place during flight, because these droplets were spherical when they deposit on the substrate surface. In contrast to this, because Al droplets have a much lower melting point, are liquid when they arrive on the substrate surface and solidify on the surface with a typical rapid solidification pattern [35]. Metal ion etching with Cr resulted in a high percentage of smaller droplets than that obtained from similar melting point metals such as Nb and Zr [33]. This was because the Cr exhibits a much higher vapour pressure in comparison with its neighbouring high melting metals. This had an effect that even solidified Cr droplets will shrink due to sublimation either during flight or after arrival at the substrate [33]. A comparison of the number of droplets generated during cathodic arc etching with the number of growth defects detectable on top of a  $3\mu\text{m}$  TiAlN coating surface revealed that there is a correlation between these growth defects and the number of droplets, which does not change after coating. This shows that every droplet causes a defect, which occurs as further material is deposited on top of these microparticles, which often grow during deposition onto the coating surface. This means that practically no new droplets are buried during film growth. However, with regards to Cr etching it was noted that very small Cr droplets were effectively buried by the coating [33]. It was also

observed that the growth defects were larger in size than the droplets from which they had formed. The size of growth defects increases only during the initial growth stage and then remains constant. This means that above a minimum thickness the defect size should be almost independent of the coating thickness [33]. Porous surfaces around the very large size defects were observed for some etched and coated surfaces. It is assumed that these porous surfaces correlate to shadowing effects due to the line of sight nature of the sputter process [35]. A schematical illustration of the formation of a growth defect from a droplet [36] is shown in figure 2.21. Growth defects exhibit a distinct structure from the rest of the coating and as it grows it creates its own boundary. This microstructure is usually composed of dense columnar grains extending in a feathery pattern outwards from the core. Around the base of the defect the coating becomes severely under dense due to shadowing and hence less intense ion bombardment.

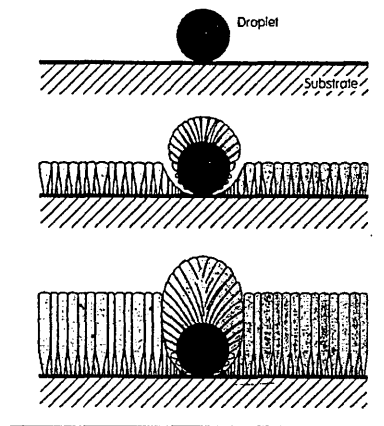
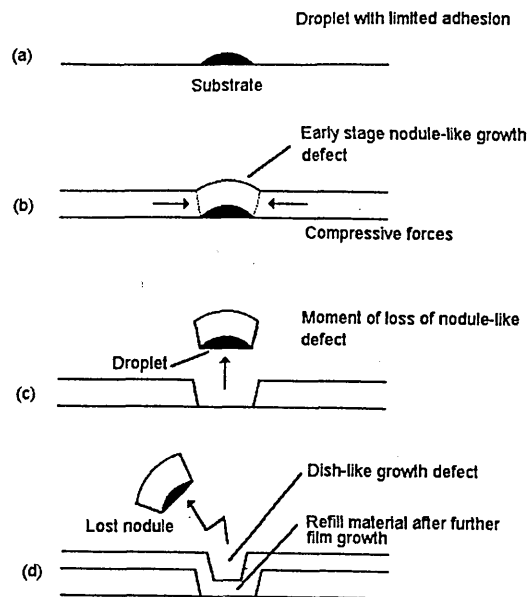


Fig 2.21 Schematic illustration of the formation of a nodular defect overgrowing an arc induced macro particle [36].

The detrimental effects of droplet formation are as follows: local loss of coating adhesion, surface roughening and formation of surface shrinkage porosity due to a droplet self-repulsion mechanism [34]. The self-expulsion mechanism is explained in figure 2.22.



**Figure 2.22.** Schematic explanation of the self-expulsion mechanism of droplets [37].

The bonding strength of the droplets is very often not sufficient to maintain the droplet from being expelled out of the coating due to increasing compressive stress of the growing coating or an undergrowing of the spherical droplets [37]. If the expelling event takes place shortly after the film growth is initiated then the hole will be refilled by the growing film resulting in the formation of a dish-like defect. If droplets leave the substrate and the coating in a late stage of film growth, which is a rare event, then it will result in rather deep holes or craters in the coating [37].

An investigation of the CrN/NbN superlattices, which were treated with a pre-coating steered arc cathodic arc  $\text{Cr}^+$ -etching for 20min at a bias voltage of  $-1.2\text{kV}$  for 20min, then coated with a CrN base layer by magnetron sputtering for 30min and finally coated with CrN/NbN using the unbalanced magnetron-sputtering process for 150min, showed the following morphology [34]: Roughly spherical droplets sized from less than 1 up to  $10\mu\text{m}$  were formed. The density of the large defects was low as shown in figure 2.23a. Occasionally the droplets appeared to form clusters of growth defects, as shown in figure 2.23b.

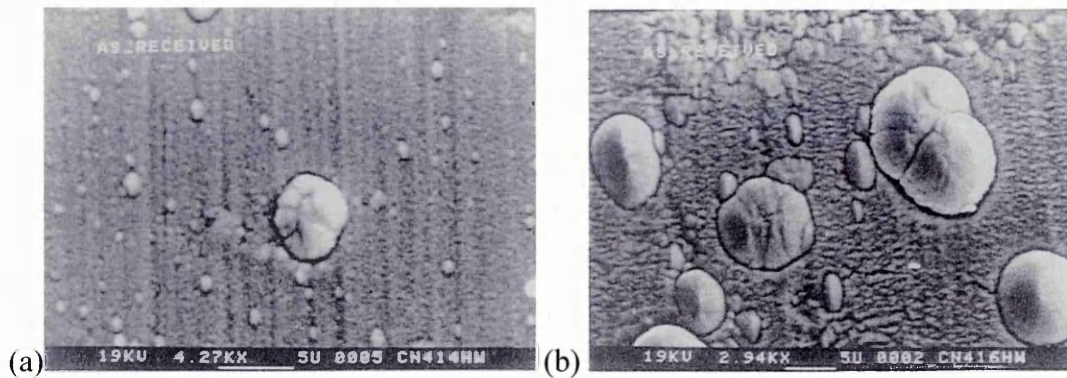


**Figure 2.23.** SEM surface of a 400°C CrN/NbN superlattice coating showing: (a) an isolated; and (b) a cluster of large droplet growth defects [34].

The growth defect surfaces were also shown to be relatively smooth. A shrinkage clearance between the droplets and the surrounding coating was also observed [34]. The defects were either through the thickness of the coating, see figure 2.24a, or embedded within the coatings, see figure 2.24b.

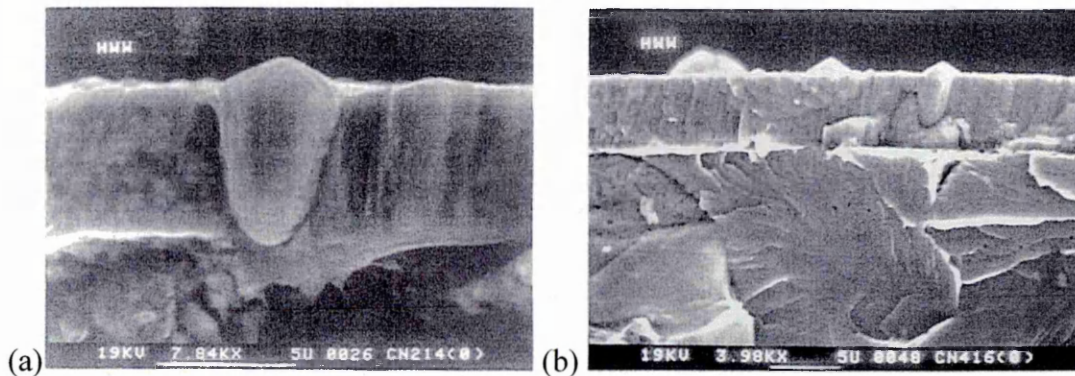


**Figure 2.24.** SEM images cross-section view of CrN/NbN coatings showing a detailed view of (a) thickness-through; and (b) non-thickness-through defects [34].

The through-thickness defects, believed to be initiated from Cr droplets, were formed during the metal ion etching step and the CrN deposition arc process. It is assumed that the embedded defects are produced as a consequence of preferential growth process on small inclusions in the etching of a bond layer [34].

It was observed that the physical bonding of the defect to the coating matrix was obviously poor due to a void zone at the interface between the defect rim or bottom and the neighbouring coatings [34].

### 2.3.6 Residual stresses in thin films

Residual stresses are very often present within hard coatings produced by PVD methods and are mostly compressive in nature [29]. In coatings compressive stresses are more favourable as they increase the resistance to fatigue failure. Very high compressive stresses, however, cause problems with adhesion (base metal/coating separation) and de-cohesion (intracoating spallation). Tensile residual stresses often cause cracking of the coating perpendicular to the direction of the stress. Thus, knowledge of the residual stress present in the coating is important. Typical residual stress values for hard coatings are typically in the range of 1-10GPa.

Residual stresses are internal stresses existing independently of external forces or thermal gradients and affecting the physical and chemical properties of the body. Due to no external forces, the integral over all the stress components in the whole body vanishes [38].

$$\int_V \sigma(x, y, z) dV = 0 \quad (9)$$

Macroscopic residual stresses can be determined using X-ray diffraction (XRD) (see chapter 3.3.1.2). The measured stress state  $\sigma$  is a superposition of several stress components, which are generated during the stages of the PVD process such as nucleation, growth and cooling after deposition [29].

$$\sigma = \sigma_{nucleation} + \sigma_{growth} + \sigma_{cooling} \quad (10)$$

The stress component during the nucleation comes from the structural misfit between the nucleated film and the substrate due to the formation of misfit dislocations:

$$\sigma_{epitactic} \propto r^{-1} \cdot L^{-1} \quad (11)$$

Where  $r$  is the distance to the surface and  $L$  is the distance between misfit dislocations.

The growth induced stresses are generated due to the bombardment of neutrals or ions which leads to the formation of several lattice defects [29]. Hence these stresses depend strongly on the substrate temperature, the total gas pressure and the bias voltage which influences the kinetic energy of the particles [39], [40]. The growth-induced residual stresses depend also on the coating thickness, the coating rate and

the orientation of the specimens [40]. Increasing the bias voltage leads to higher residual stresses. Point defects due to the implantation and displacement cascades result in high intrinsic compressive stresses [29]. The following point defects can occur:

- substitution of regular atoms by metal and / or reactive gas atoms
- incorporation of working gas atoms on regular atom sites
- incorporation of nitrogen on interstitial sites
- incorporation of impurities [29].

The point defects result in a volume change  $\Delta V/V$  in the growing layer and in the formation of intrinsic stresses during the growth stage which are expressed by equation (12):

$$\sigma_{growth} = -\frac{1}{3} \cdot \frac{\Delta V}{V} \cdot \frac{E_L}{1-\nu_L} = -\frac{1}{3} \cdot \frac{E_L}{1-\nu_L} \cdot \sum \Omega_i \cdot c_{Di} \quad (12)$$

Where:

$E_L$  = Young's modulus of the layer

$\nu_L$  = Poisson's ratio of the layer

$\Omega_i$  = specific volume change caused by defect i

$c_{Di}$  = defect concentration of the point defect i.

Consideration of the atomic radii of the ions and atoms participating in the deposition process shows that a positive volume change occurs which leads to compressive stresses [29].

Stresses formed during the cooling step  $\sigma_{cooling}$  result on the one hand from the difference between the thermal expansion coefficients of the coating and the substrate material and on the other hand from solid state reactions, e.g. phase transformation and precipitation processes.

$$\sigma_{cooling} = \sigma_{thermal} + \sigma_{phase\ transformation} \quad (13)$$

Because of low deposition temperatures the contribution of phase transformation and precipitation can be neglected.

The thermal stress component is defined as:

$$\sigma_{thermal} = \frac{E_L}{1 - \nu_L} \cdot (\alpha_L - \alpha_S) \cdot (T_d - T) \quad (14)$$

Where  $T_d$  is the deposition temperature,  $\alpha_L$  and  $\alpha_S$  are thermal expansion coefficients of the layer and the substrate respectively. Equation (14) is valid for a biaxial stress state with equal normal stress components and a fully elastic behaviour of the coating supposing elastic isotropy, an infinite thick and lateral extended substrate.

Exceeding a critical stress value the coating fails. This critical stress can be either flow or creep stress of the coating and the substrate at high temperatures or fracture stress of the coating, as shown in figure 2.25 [29].

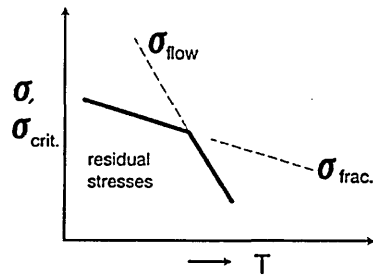


Figure 2.25. Schematic diagram of residual stress limits [29].

High compressive stresses also cause an increase of hardness [40], which may be very beneficial for the coating properties.

It is important to distinguish between *macro residual stresses* and *microstresses*. *Macro residual stresses*, with which XRD coating stress measurements are made, vary continuously through the volume of the body and act over all regions, which are large, compared with atomic dimensions. *Microstresses*, or textural stresses, act over dimensions as small as several unit cells, although their effects may extend throughout most of a grain. Estimates of these residual stresses can be made by a detailed analysis of line broadening of peaks in XRD traces.

## 2.4 Corrosion

### 2.4.1 Corrosion in general

Corrosion can be defined as a degradation of a metal by an electrochemical reaction with its environment [41]. Due to thermodynamic laws there is a tendency of metals to transform from a high energy state into a low energy state, as shown in figure 2.26, which occurs as a recombination with components of the environment leading to corrosion.

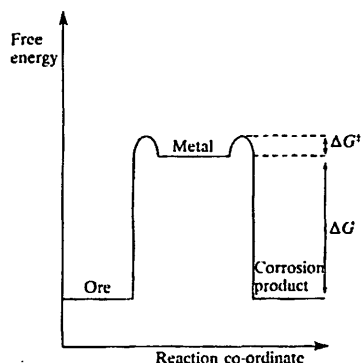


Figure 2.26. Thermodynamic energy profile for metals and their compounds [41].

Because corrosion is an electrochemical process, it is possible to evaluate the overall reaction by the use of an external electrical circuit called a potentiostat. Figure 2.27 shows the different electrical science conventions for a battery and an aqueous corrosion cell, which was used for the corrosion experiments.

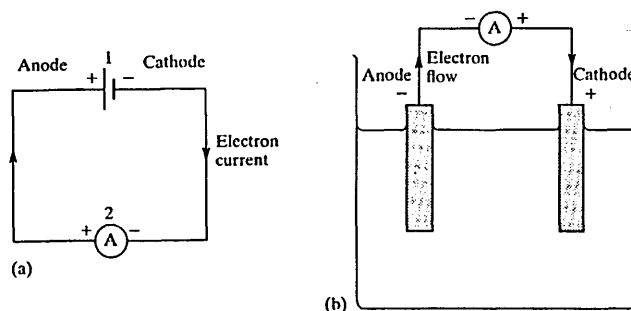


Figure 2.27. Electrical science conventions. (a) positive and negative definitions in a battery (1), (b) positive and negative definitions in a corrosion cell [41].

Electrochemical reactions are chemical reactions in which identifiable loss or gain of electrons takes place. Electrons are produced at the negative electrode in an aqueous corrosion cell. This electrode is called the anode because convention leads us to think of the anode supplying the positive current (positive ions) through the solution [41].

The following two half-reactions occur at the solid/liquid interface in an aqueous corrosion cell:

The *anodic reaction* is an electron-producing process, which is also called oxidation:



The *cathodic reaction* is an electron-consuming reaction which is called reduction, see equation (16) and (17).

The metal/electrolyte interface which behaves as an anode corrodes by loss of electrons from electrically neutral metal atoms in the solid state, forming discrete ions. These ions can either enter the solution or react with other species at the surface forming insoluble solid corrosion products on the metal surface. The formation of solid corrosion products may block further metal dissolution or may retard the corrosion and can result in passivation [41].

The cathode does not corrode. It consumes the electrons generated by the anode.

Reduction reactions which are possible at the cathode are as follows:



The reaction expressed by equation (17) is always possible but varies with the pH value of the solution. The other reduction reaction depends on the level of dissolved oxygen in the solution.

Anodic and cathodic sites are developed on the metal surface when a metal corrodes in an aqueous solution. These sites can be either separated permanently from each other or can shift continually, so that one point of the surface is alternately anodic and cathodic [42].

Crevice corrosion is defined as the attack which occurs because part of a metal surface is in a shielded or restricted environment, compared to the rest of the metal which is exposed to a large volume of electrolyte [41].

Figure 2.28a presents the initial conditions: Corrosion occurs both inside and outside the crevice. There is an electrostatic balance between the creation of positive metal ions and negative hydroxyl ions. Dissolved oxygen is consumed, see equation (16), and more oxygen from the atmosphere diffuses into the solution. The oxygen is less

replaced within the crevice than at other metal surfaces. The lack of oxygen in the crevice results in a diminished generation of negative hydroxyl ions and hence an excess of positive ions occurs. Therefore negative ions from the bulk electrolyte, e.g.  $\text{Cl}^-$ , diffuse into the crevice, as shown in figure 2.28b. The presence of chlorides leads to the creation of complex ions between chloride, metal ions and water molecules resulting in increased acidity (pH). Finally metal dissolution occurs only inside the crevice where the concentration of hydrogen ions is increased resulting in an accelerated metal dissolution process. The reaction becomes self-sustaining [41].

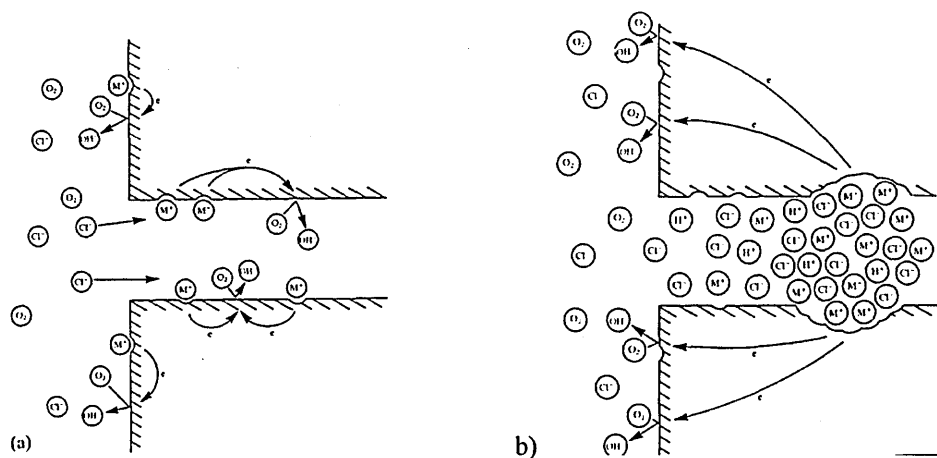


Figure 2.28. The Fontana-Green mechanism of crevice corrosion [41].

If corrosion sites cover only a small proportion of a metal while the remainder of the surface provides a large cathodic area then these sites are very active resulting in considerable penetration. This localised and selective attack is known as pitting corrosion. It is a serious problem especially on metals and alloys that have highly resistant films [42]. It occurs on areas of a metal surface where there is [41]:

- a surface scratch or mechanically included break in an otherwise protective film
- an emerging dislocation or slip step caused by applied or residual tensile stresses
- a compositional heterogeneity like an inclusion, segregate or precipitate.

It is necessary to consider the initiation phase to distinguish between pitting and crevice corrosion. While crevice corrosion is initiated by differential concentration of oxygen or ions in the electrolyte, pitting corrosion is initiated on plane surfaces by metallurgical factors alone [41]. If the pit is once initiated then it will take on very

similar geometrical characteristics to those of a crevice [41]. Pitting is prone to occur particularly in chloride solutions [42]. In general passivity cannot be easily established nor maintained due to the presence of chloride ions. If the concentration of these ions increases then the critical current density is increased, the primary passive potential is raised, the current density under the condition of passivity is enlarged and the passive potential is lowered, as shown in figure 2.29 [42].

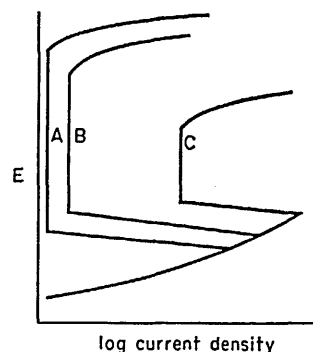


**Figure 2.29.** The effect of chloride ions upon the anodic polarisation curve for a metal that exhibits passivity. (A) No chloride present, (B) A low concentration of chloride ions, (C) A high concentration of chloride ions [42].

Chloride ions interfere with the establishment and maintenance of passive films due to (a) the high charge density on the chloride ion, (b) its capacity to form soluble species and (c) its entry into film lattices where they introduce lattice defects into the film and reduce the resistivity of the oxide. The chloride does not prevent the formation of the film, but makes it less protective. If the film is formed in the presence of a sufficient amount of chloride then the film that is formed will be much more soluble [42].

#### 2.4.2 Potentiodynamic polarisation curves

During the potentiodynamic measurement the sample is polarised from  $-1000\text{mV}$  to  $+1000\text{mV}$ . The measured current density  $I$  is recorded as the dependent variable, which is the sum of all anodic and cathodic currents. For the examination of the corrosion behaviour of materials the potential  $E$  is plotted as ordinate. The values for the current densities is considered to be positive and plotted as  $\lg I$  as abscissa. A graph like in figure 2.30 is obtained.

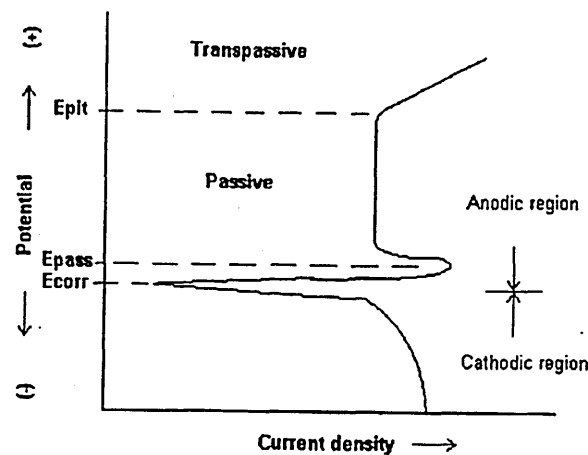
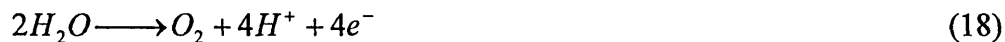


Figure 2.30. Potentiodynamic polarisation curve [12].

The different regions on the graph can be defined as follows [41]:

*Cathodic region:*

Negative currents are measured in the portion of the graph which is called cathodic region. There the working electrode (WE) behaves as a cathode. The counter electrode (CE) is the anode in the cathodic region. This electrode does not corrode in the manner of equation (15). There are other electron-producing reactions, which take place at the CE e.g. the generation of oxygen gas by the oxidation of water:



or the generation of chlorine gas due to the chloride-containing electrolyte [49]:



*Free corrosion potential  $E_{corr}$ :*

The value of potential where the changeover from negative to positive currents takes place is called the free corrosion potential  $E_{corr}$ .

*Anodic region:*

Positive currents are measured in the portion of the graph called anodic region. The WE behaves as an anode. Visible changes to the sample can be observed during this part.

*Passivation potential  $E_{pass}$ :*

The corrosion rate increases above  $E_{corr}$  and reaches a maximum at the passivation potential  $E_{pass}$ .

*Passive zone:*

The formation of a protective film takes place causing a sudden drop in corrosion current density. Then the current density is maintained at a low and steady level until a breakdown of the protective film begins at  $E_{pit}$ .

*Pitting potential  $E_{pit}$ :*

The probability of pitting is greatest at this point.  $E_{pit}$  varies according to metallurgical and environmental conditions and hence it is not an absolute parameter. The current density increases as more and more pits propagate.

*Transpassive region:*

The region of the curve above  $E_{pit}$  is called transpassive zone when the current density rises greatly because of the onset of new anodic processes, rather than because of pitting.

### 2.4.3 Corrosion of CrN/NbN superlattice coatings

Most PVD coatings provide poor barrier properties and generally disappointing corrosion performance due to their columnar microstructure. CrN/NbN superlattice coatings having an effective nanoscale layering offer a significant increase in pitting potential and modest reduction in passive currents in comparison with a commercial CrN coating on a 304 SS substrate. The layered structure reduces effectively the coating porosity, hence the diffusion of solution species to the coating-substrate interface is reduced which leads to the improved corrosion behaviour compared with the commercial CrN coating [1]. The corrosion performance of CrN/NbN superlattices is a function of their chemical composition, residual stress levels and the base layer phase composition. A more noble corrosion potential and lower passive current was observed for the substoichiometric coating compared with a stoichiometric coating. But the pitting potentials of the stoichiometric coatings were raised. This behaviour might be due to the difference in internal stress levels. The stoichiometric coatings have lower internal stresses than the substoichiometric ones. A single-phase CrN base layer results in reduced residual stress levels and hence the corrosion performance is improved [1].

Tomlinson compares the corrosion behaviour of CrN with the CrN/NbN superlattice coatings [43]. The CrN/NbN superlattice coatings, deposited by the combined cathodic arc unbalanced magnetron technique, show an improved corrosion protection compared with the commercial arc-based CrN coating. This improvement is due to the presence of the highly passive element Nb and to an altered microstructure resulting in diffuse porosity and fewer through thickness coating defects [43].

Pitting or crevice corrosion initiates at surface defects like metallic droplets, which are caused by the initial arc-cleaning stage. If there are high internal stresses in the coating then the areas adjacent to defects are more prone to cracking after corrosion has commenced. In this case, corrosion can initiate microcracks or pits which grow as microscopic cracks [1].

The observation of the morphology of the coating after polarisation in a 5% NaCl solution revealed two kinds of corrosion: corrosion of the defects and localised corrosion of the substrate. The defects were often totally dissolved by corrosion leaving an open pore allowing solution to come into contact with the substrate, as shown in figure 2.31 [34].

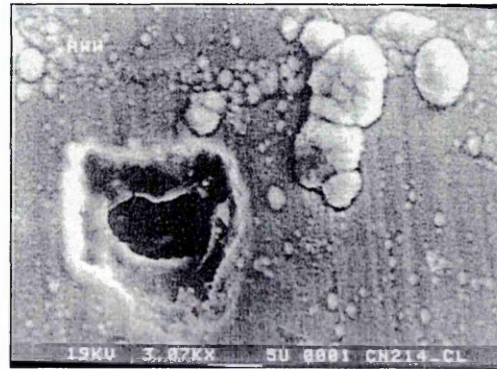


**Figure 2.31.** Morphology of CrN/NbN coating after polarisation in a 5% NaCl solution [34].

The SEM cross section in figure 2.32a [34] shows the corrosion on the substrate through the coating intercolumnar porosity. The corrosion of the substrate through defect-related void paths is shown in figure 2.32b [34].

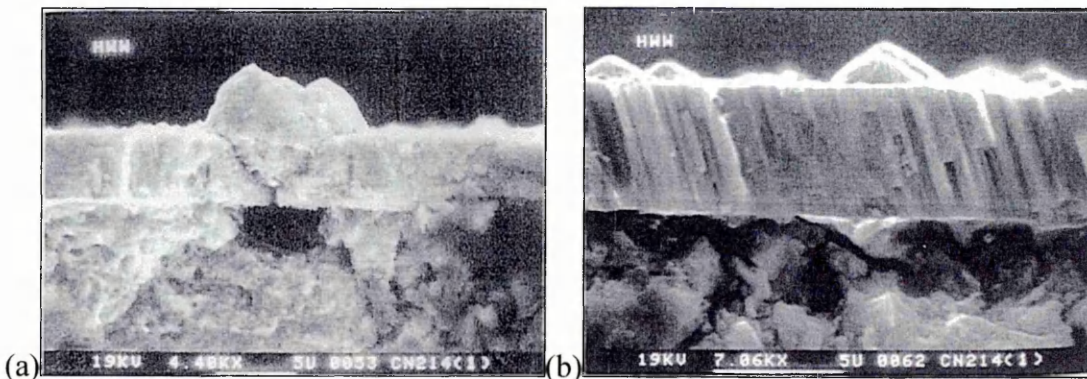


**Figure 2.32.** Morphology of CrN/NbN coatings after polarisation in a 5% NaCl solution [34].

Transition metal nitride coatings are in general relatively inert to chemical attack, but coatings prepared by PVD technique are less inert. The reason for this behaviour is the presence of solution-pathway through defects within the coating. This leads to

galvanic and crevice corrosion between the coating and the substrate via these defects. The porosity of the coating determines the corrosion performance. If the porosity is low, then the substrate will behave totally like the coating. This means that if the coating passivates or pits then the substrate will passivate or pit. A high porosity results in a significant galvanic corrosion with the substrate being the anode and the coating being the cathode, see figure 2.33.

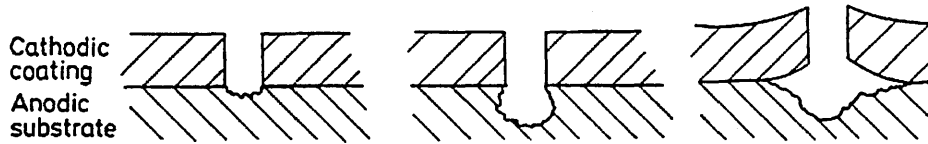
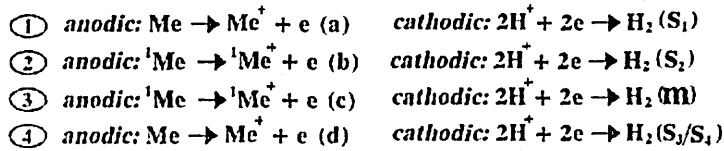
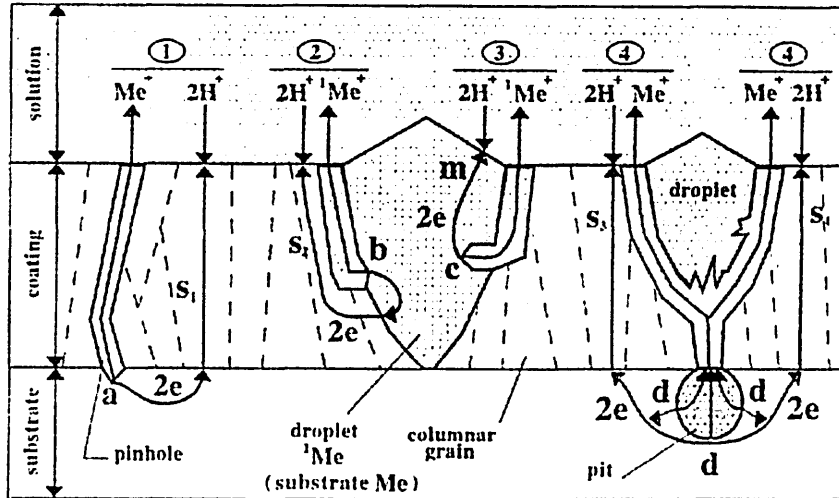


**Figure 2.33.** Schematic representation of galvanic corrosion effects at a pore in a coating on a substrate [44].

In this case the coating behaves like that of the substrate material. Solution penetration through pinholes and void zones around droplets serve as galvanic coupling route between the coating and the substrate. If there were only pinhole defects in the coating, then a form of galvanic corrosion between the coating acting as cathode and the substrate presenting the anode would be created through the solution in the pinholes. The presence of macroparticles leads to complicated situations. Through-thickness macroparticles are compositionally metal-rich or N-deficient. Hence they are anodic and corrode relative to the adjoining coating. But they are cathodic to the substrate which complicates the existing pinhole-induced coating-substrate galvanic-coupling. A growth defect being a cluster of rapidly consolidated large grains might be inhomogeneous considering its phase composition and N-content in the exterior and interior regions. Due to this the growth defect itself can form a local galvanic couple between one part as an anode and another as a cathode. If the base of a macroparticle is N-deficient and hence anodic with respect to the top, then the lower part of the macroparticle will preferentially corrode. In this case, it seems to be an undamaged defect when viewing from the surface.

The corrosion mechanism of macroparticle, growth defects and pinholes are shown schematically in figure 2.34. This figure includes the simplification that the corrosion of the droplets is concurrent with the localised galvanic corrosion of the substrate. The corrosion of the substrate is accelerated as the droplets are corroded and hence a crater becomes available being an additional contact with the solution. It is believed that the droplet corrosion starts from the N-contaminated droplet rims

which are anodic to the neighbouring coating nitrides. The creation of solution pathways is possible, which can lead to the exposure to the relatively N-free droplet interiors which are anodic with respect to the exterior of the droplet. The effect of such droplet corrosion is the trigger of more galvanic dissolution or pitting corrosion of the substrate [34].



a: substrate at interface; b: droplet rim; c: droplet interior;  
 d: pit substrate;  $S_i$ : adjacent coating grains; m: droplet top.

Figure 2.34. Schematic diagram showing the corrosion mechanism [34].

### 3 Experimental

#### 3.1 Coating system

All samples investigated in this report were produced in an industrial sized Hauzer Techno Coating (HTC) 1000-4 Arc Bond Sputtering (ABS) PVD coating system [19].



**Figure 3.1.** HAUZER Techno Coating (HTC) 1000-4 ABS PVD unit.

The vacuum chamber is made out of stainless steel and has a volume of approximately  $1\text{m}^3$ . It is a four-cathode system having an octagonal cross-section as shown in figure 3.2. The four magnetron cathodes are mounted orthogonally which surround a three-fold rotational substrate holder.

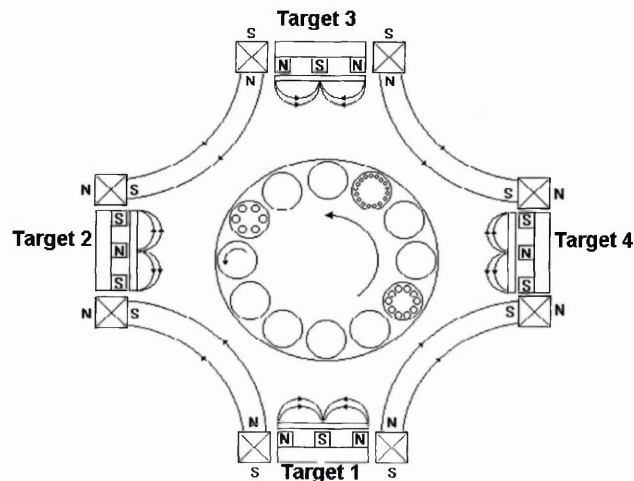


**Figure 3.2.** Cross-section of the ABS coating chamber used for the deposition of CrN/NbN superlattices [1].

The substrate table is located in the centre of the chamber. The samples are attached to satellite assemblies. Depending on the size and geometry of the substrates a one-, two- or three-fold planetary rotation is possible. The vacuum chamber can be

opened from two sides so that targets can be interchanged and samples can be mounted on the substrate holders when the doors are open. The coating chamber is heated by a series of electrical elements, which are situated on each door and under the substrate table. The development of high temperatures on the targets means that they have to be cooled by copper sheets with a water circulation system. The cathodes integrate the functions of a cathodic arc evaporator and the unbalanced magnetron into one single unit. During the magnetron discharge a set of permanent magnets is positioned directly behind the target. Electromagnets disposed concentrically around the cathode and generating a magnetic field of up to 10000 ampere turns/metre [19] make it possible to control the unbalancing effect, as shown in figure 3.3.

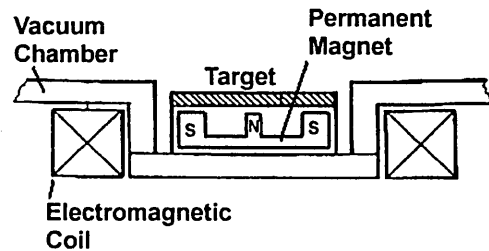


Figure 3.3. UBM cathode with permanent and electromagnets [19].

Adjusting the coil current of the electromagnets the bias current density and hence the temperature development at the substrate can be altered [19]. The closed field configuration is achieved by linking the field lines of adjacent magnetrons. Withdrawing the outer poles far enough back from the target side to become magnetically negligible at the front of the target, the unbalanced magnetron cathode is converted to an arc cathode, as shown in figure 2.12. The central pole, made out of  $\text{Co}_5\text{Sm}$  remains close to the back of the target to perform the etching process in the Steered Arc™ mode. Changing the current in the electromagnetic coils periodically the travelling direction of the arc is steered along a racetrack. The initiation of the arc is reached by the application of a high voltage pulse to tungsten wire, which is placed around the target used for the metal ion etching.

The HTC 1000-4 ABS™ uses two Balzers TPH 2200 turbomolecular pumps in combination with a roots pump with a pumping speed of 500m<sup>3</sup>h<sup>-1</sup> and a rotary vane pump with a speed of 80m<sup>3</sup>h<sup>-1</sup> [19].

## 3.2 Deposition procedure

### 3.2.1 Substrates and substrate preparation

Samples of two different substrate materials, 304 austenitic stainless steel (SS) and M2 high speed steel (HSS), were coated and investigated. The nominal composition of the substrate materials is shown in table 3.1(a) and 3.1(b) respectively.

**Table 3.1a** Nominal elemental composition of 304 SS.

Element	C	Cr	Mn	Fe	Ni	Si	P	S
Mass%	0.08%max	18-20%	2%max	Bal	8-10.5%	1%max	0.045%max	0.03%max

**Table 3.1b** Nominal elemental composition of M2 HSS.

Element	C	Cr	Mn	Mo	V	W	Si	Fe
Mass%	0.82%	4.25%	0.3%	5%	1.8%	6.25%	0.25%	Bal

The samples were sectioned into discs of 30mm diameter and a thickness of 6mm. These samples were subsequently metallurgically prepared to a 1µm diamond polish ( $R_a=0.01\mu\text{m}$ ).

The polished substrates were cleaned and rinsed in an industrial sized computerised controlled cleaning line. This comprised a series of ultrasonically agitated aqueous alkaline baths and de-ionised water rinsing baths. After passing the cleaning line the samples were dried in vacuum assisted hot air to obtain a stain free surface. These samples were immediately placed within the coating chamber.

### 3.2.2 Deposition parameters for the low temperature process

The coating process consists of the following steps (shown schematically in fig 3.4)

1. Pump down and heating
2. Target sputter cleaning
3. Steered cathodic arc etching
4. Cooling
5. Coating deposition
6. Cool down and venting

#### 1. Pump down and heating

Before the deposition the chamber was evacuated and heated until the required pressure and temperature was reached. The chamber was evacuated in two stages. The first stage involved reducing the chamber pressure to  $10^{-2}$  mbar using the roots pump and rotary vane pump. The second stage involved using the fine pumping system with two turbomolecular pumps, which was opened to reduce the pressure to  $7 \times 10^{-5}$  mbar. On reaching a pressure of  $10^{-4}$  mbar the chamber temperature was increased using radiant heating. The controlled temperature was  $120^{\circ}\text{C}$  for the low temperature deposition process.

#### 2. Target sputter cleaning

The targets were sputter cleaned in a glow discharge. During this step surface contamination such as oxides were removed. To protect the substrates prior to pre-coating, shutters were moved in front of the targets.

#### 3. Steered cathodic arc etching

Cr metal ion etching was carried out to the substrates prior to coating deposition. A high negative bias voltage ( $-1100\text{V}$ ) was applied and the substrates were sputtered cleaned by Cr ion bombardment. The ions were provided by steered cathodic arc evaporation, which can be either singly charged or multiply charged metal ions [7], [10]. This metal-ion etching step is carried out in order to obtain a superior adhesion of the coating to the substrate. At this stage the temperature inside the chamber was increased to  $250\text{-}270^{\circ}\text{C}$ .

#### 4. Cooling

Due to high temperatures on the surface of the substrate and the target caused by steered cathodic arc etching the chamber was allowed to cool down to 250°C.

#### 5. Coating deposition

The coating deposition consisted of two stages. The first stage involved the deposition of a base layer of CrN on to the substrate. This was carried out in order to build up a gradient in hardness and also to allow for the further enhancement of the adhesion of the CrN/NbN superlattice coating [1]. This deposition was carried out in the unbalanced magnetron mode with an unbalancing coil current of 6A and a N<sub>2</sub> flow of 240sccm. A bias voltage of -75V was applied to the substrate during the deposition of the base layer.

The CrN/NbN superlattice coating was deposited during the second stage using unbalanced magnetron sputtering. The unbalancing coil current used was 4A and the N<sub>2</sub> flow was reduced to approximately 100sccm. The bias voltage was set to either -75V or -95V and the coating was deposited at a constant temperature of 250° in a common Ar+N<sub>2</sub> atmosphere.

#### 6. Cool down and venting

The chamber was vented and allowed to cool down before opening.

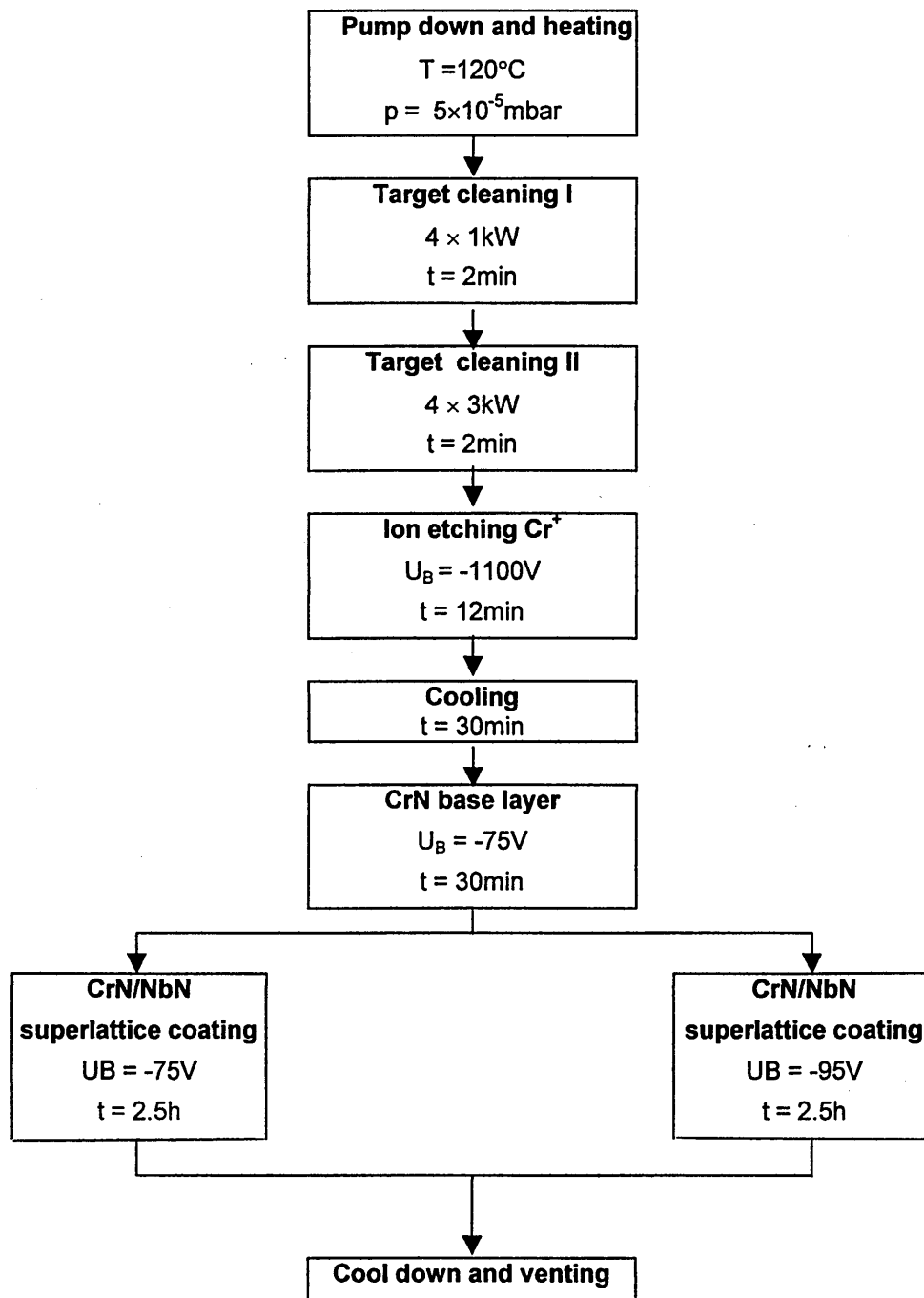


Figure 3.4. Schematic PVD coating process review

### 3.3 Evaluation techniques

#### 3.3.1 Structure analysis by X-ray diffraction

##### 3.3.1.1 Texture

###### 3.3.1.1.1 Inverse Pole Figures

The  $\theta/2\theta$  Bragg-Brentano geometry was used to determine the orientation of the planes which are parallel to the surface. The texture measurement was made using a Philips Analytical X'Pert MPD diffractometer set up with the following conditions:

radiation:	Cu- $K_{\alpha}$ ( $\lambda = 0.154056\text{nm}$ )
monochromator:	single prop graphite
detector:	X'Celerator in scanning mode
start angle $2\theta$ :	$20^{\circ}$
end angle $2\theta$ :	$140^{\circ}$
step size:	$0.04^{\circ}$
time per step:	10s
scan speed:	$0.004^{\circ}/\text{s}$

The proportion of the grains with a certain orientation relative to a randomly orientated powder material was calculated by the Harris inverse pole figure method shown by equation (20):

$$P = \frac{\frac{I_{hkl}}{R_{hkl}}}{\frac{1}{n} \sum_{i=1}^n \frac{I_{hkl}}{R_{hkl}}} \quad (20)$$

$I_{hkl}$  represents the intensities from the  $hkl$  reflections in the sample.  $R_{hkl}$  are the intensities from a random powder (calculated) and  $n$  is the number of reflections considered. The following  $hkl$  reflections were considered in this investigation: (111), (200), (220), (311), (331), (420) and (422), hence  $n=7$ . A  $P$  value of one signifies a random orientation, whilst for  $P$  values greater than one the plane is considered to have a preferred orientation [45]. Therefore the  $P$  value represents the chance out of seven of the plane  $\{hkl\}$  lying parallel to the surface. The peak integral of each reflection provides the  $I_{hkl}$  values. Assuming a random powder the calculation of the  $R_{hkl}$  values derives from equation (21).

$$R_{hkl} = R_{\{hkl\}}^o \cdot I_0 \cdot \frac{S}{\sin \theta} \cdot \int_0^t \exp\left(-\frac{2\mu x}{\sin \theta}\right) dx \quad (21)$$

Leaving out the incident intensity  $I_0$  (assumed to be almost constant throughout the analysis) and the irradiated area  $S \sin^{-1} \theta$ , (which depends on the angle but will be the same for both calculated and experimental uses and therefore can be ignored) and solving the integral, equation (21) becomes:

$$R_{hkl} = R_{\{hkl\}}^o \cdot \left(\frac{1}{2\mu}\right) \cdot \left(1 - e^{-\frac{2\mu t}{\sin \theta}}\right) \quad (22)$$

Where  $t$  is the coating thickness and  $\mu$  is the average linear absorption coefficient of CrN and NbN, which can be obtained from formula (23).

$$\mu = \frac{w_{NbN}}{100} \mu_{NbN} + \frac{w_{CrN}}{100} \mu_{CrN} \quad (23)$$

Where  $w$  are weight percentages of CrN and NbN which were determined by energy-dispersive (EDX) SEM analysis, see section 3.3.2.1.

$R_{hkl}^o$  can be calculated by equation (24):

$$R_{\{hkl\}}^o = \frac{1}{V^2} \cdot X \cdot F^2 \cdot LP \cdot M \cdot e^{-2m} \quad (24)$$

Where:

- $V$  = volume of the unit cell
- $X$  = irradiated volume
- $F$  = structure factor
- $LP$  = Lorentz polarisation factor = angular factor
- $M$  = multiplicity factor
- $e^{-2m}$  = temperature factor.

The volume of the unit cell can be ignored because the lattice parameter is constant as the materials are the same.

CrN/NbN coatings exhibit single-phase NaCl fcc unit-cell structures [46]. The 4 metal atoms (Nb and Cr) and the 4 nitrogen atoms are located as follows:

Nb, Cr	0 0 0	½ ½ 0	½ 0 ½	0 ½ ½
N	½ ½ ½	0 0 ½	0 ½ 0	½ 0 0

Knowing this the structure factor  $F$  can be determined for unmixed indices  $hkl$  by equation (25) if  $(h + k + l)$  is even and by equation (26) if  $(h + k + l)$  is odd.

$$F = 4 \cdot [(f_{Nb} + \Delta f'_{Nb}) \cdot c_{Nb}^{at\%} + (f_{Cr} + \Delta f'_{Cr}) \cdot c_{Cr}^{at\%} + (f_N + \Delta f'_N) \cdot c_N^{at\%}] \quad (25)$$

$$F = 4 \cdot [(f_{Nb} + \Delta f'_{Nb}) \cdot c_{Nb}^{at\%} + (f_{Cr} + \Delta f'_{Cr}) \cdot c_{Cr}^{at\%} - (f_N + \Delta f'_N) \cdot c_N^{at\%}] \quad (26)$$

Where  $f$  is the atomic scattering factor,  $\Delta f$  is the dispersion correction factor and  $c_i^{at\%}$  is the atomic concentration of the respective element  $i$  [47]. This concentration was determined by EDX SEM analysis, see section 3.3.2.1.

The multiplicity factors  $M$  are given in table 3.2:

**Table 3.2** Multiplicity of the planes [47].

planes	{hkl}	{hhl}	{0kl}	{0kk}	{hhh}	{00l}
multiplicity	48	24	24	12	8	6

The Lorentz-polarisation factor was calculated using equation (27) including an additional factor which is necessary in the presence of a monochromator because the beam is further polarised.

$$LP = \frac{1 + \cos^2 2\theta \cdot \cos^2 2\alpha}{\sin^2 \theta \cdot \cos \theta} \quad (27)$$

The angle  $\alpha$  is the Bragg angle of the monochromating crystal which equals 13.15° for copper radiation [45].

The factor  $X$  for the irradiated volume in equation (24) was left out because it is constant.

The temperature factor  $e^{-2m}$  varies very little with angle  $2\theta$  and therefore assumed to be 1 [47].

### 3.3.1.1.2 Pole figures

A Philips Analytical X'Pert MPD diffractometer fitted with the PW 3068/100 Automatic Texture Cradle ATC-3 was used for the determination of the direct pole figures. The incident beam used was set to point focus. The following conditions were used:

radiation:	Cu-K $_{\alpha}$ ( $\lambda = 0.154056\text{nm}$ )
monochromator:	single prop graphite
detector:	X'Cellerator in receiving slit mode
measured reflections:	(111), (200) and (220)

tilting  $\Psi$ :  $0^\circ$  to  $85^\circ$  with a step size of  $5^\circ$   
 rotation  $\Phi$ :  $0^\circ$  to  $360^\circ$  with a step size of  $5^\circ$  and 5s time per step

In addition to this a normal  $\theta/2\theta$  Bragg-Brentano scan on each considered plane was made so that a background correction could be performed on all of the pole figures. An example of the background position taken at  $-3^\circ$   $2\theta$  from the (111) peak maximum at  $36.068^\circ$   $2\theta$  is shown in figure 3.5.

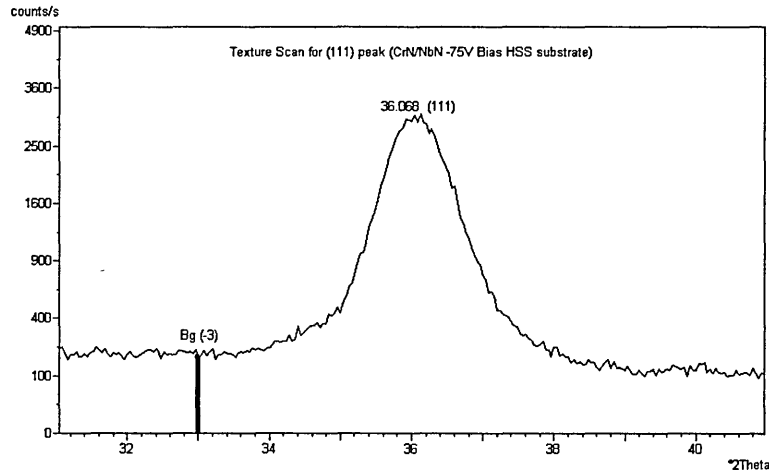


**Figure 3.5.** Diffraction pattern for the determination of the distance between background and the (111) peak of the  $-75\text{V}$  trial\_2 sample

The pole figure data for each sample was imported into a Philips X'pert Texture computer software. Each pole figure was plotted as both 2D and 2.5D colour profile maps with a maximum contour (intensity) definition levels set to 30.

### 3.3.1.2 Residual stress

The macroscopic residual stress of the coatings was determined using Glancing Angle (GA-XRD). In the glancing angle parallel geometry, the angle of incidence  $\gamma$  of the x-ray beam to the specimen is kept constant, see figure 3.6. The counter is driven such that when the Bragg condition is satisfied all of the allowed planes will diffract, so that a series of diffraction peaks corresponding to individual lattice spacings from planes nearly parallel to the surface to those nearly perpendicular to the surface as the Bragg angle increases. The system is not focussing but the beam is parallel as it enters the flat plate monochromator because of a long collimator.

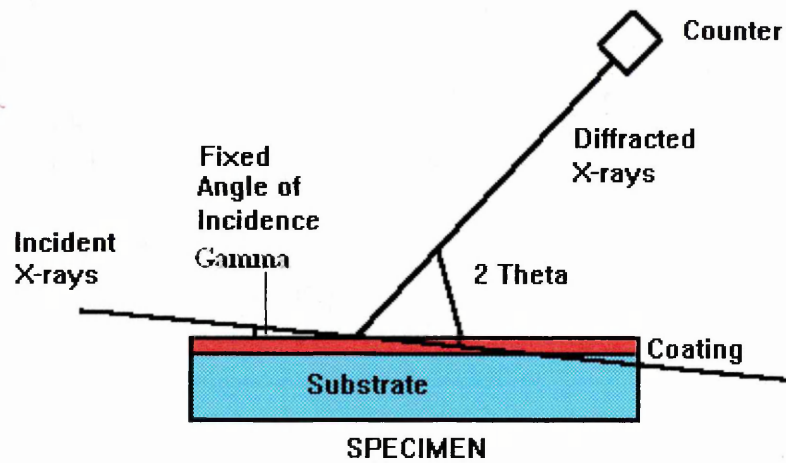


Figure 3.6 Schematic representation of GA-XRD technique

The diffracting planes are at the angle  $\psi$  to the specimen surface, which is given by equation (28).

$$\psi = \theta - \gamma \quad (28)$$

Where  $\theta$  is the Bragg angle and

$\gamma$  is the angle of incidence of the x-ray beam to the specimen surface.

Hence in this technique the diffracting planes are at an angle  $\theta - \psi$  to the specimen surface.

The measured volume  $\Delta V_m$  of the sample is considered to be very small in comparison with that of the whole sample  $V_0$  and very large in comparison to the mean grain size  $V_G$  ( $V_0 \gg \Delta V_m \gg V_G$ ) [38]. A schematic diagram of the incident beam path AB and the diffracted beam path BC is shown in figure 3.7.

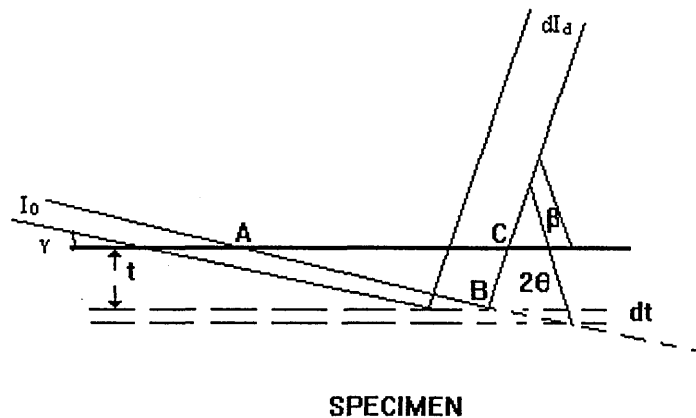


Figure 3.7. Schematic representation of the beam path in glancing angle technique

A small incidence angle of  $\gamma$  of  $2^\circ$  was used in order to obtain a shallow and nearly constant penetration depth of the X-rays [48] so that the residual stress can be measured in the coating without substrate effects (see fig 3.7). The depth of penetration  $X_e$  is often defined as the depth from which the diffracted intensity has a value of  $1/e$  of the incident intensity for a linear absorption coefficient  $\mu$ , which for glancing angle geometry is given as

$$\text{Glancing Angle} \quad X_e = \frac{\sin \gamma \sin(2\theta - \gamma)}{\mu(\sin \gamma + \sin(2\theta - \gamma))} \quad (29)$$

The parameters of the GA-XRD measurements were as follows:

radiation:	Cu-K $_{\alpha}$ ( $\lambda = 0.156406\text{nm}$ )
monochromator:	single graphite flat plate
detector:	proportional counter
start angle $2\theta$ :	$30^\circ$
end angle:	$140^\circ$
step size:	$0.04^\circ$
time per step:	10s
scan speed:	$0.004^\circ/\text{s}$

The calculation of the stress was carried out on the diffraction peaks of (111), (200), (220), (311), (222), (400), (331), (420) and (422) lattice planes. The intensities were recorded versus  $2\theta$  and a Pearson IV software programme was used to accurately fit the peaks. For cubic structures, the corresponding lattice parameters  $a_{hkl}(\psi)$  can be calculated for each diffraction peak and plotted against  $\sin^2 \psi$  i.e.  $a_{hkl}(\psi)$  vs  $\sin^2 \psi$  plot see figure 3.8. For a thin film in a state of equi-biaxial stress the equation describing the  $a_{hkl}(\psi)$  vs  $\sin^2 \psi$  plot (SSP) is given as follows:

$$a_{\psi} = \sigma a_0 \left\{ \left[ \frac{(1+\nu)}{E} \right] \sin^2 \psi - \frac{2\nu}{E} \right\} + a_0 \quad (30)$$

Where:

$a_0$  = unstressed lattice parameter

$E$  = Elastic modulus (GPa)

$\nu$  = Poisson's ratio (assumed to be 0.3 corresponding to that of TiN).

The elastic modulus can usually be determined by nano-indentation. However, it was not possible to measure the lattice parameter  $a_0$  for the unstressed coating directly, because there are always stresses in the coating. One method of determining  $a_0$  is to dissolve the substrate away and perform a  $\theta/2\theta$  scan on the coating, however, this is unfeasible. The unstressed lattice parameter,  $a_0$  can be determined using the equation of the curve  $a_{\psi}$  versus  $\sin^2 \psi$  (31) where  $\sin^2 \psi$  equals 0.6/1.3, see equation (32).

$$a_{\psi} = m \cdot \sin^2 \psi + n \quad (31)$$

Where:

$$\sin^2 \psi = \frac{2\nu}{1+\nu} = \frac{0.6}{1.3} \quad (32)$$

The unstressed lattice parameter is therefore given, as shown in equation (33) and is extrapolated from the graph as shown in figure 3.8.

$$a_0 = m \cdot \frac{0.6}{1.3} + n \quad (33)$$

The stress  $\sigma$ , can be determined from the slope of the least-squares fit of the SSP plot as shown in equation (34) and figure 3.8. Where, E is the Youngs Modulus of the material.

$$\sigma = \frac{\text{Slope } E}{a_0(1 + \nu)} \quad (34)$$

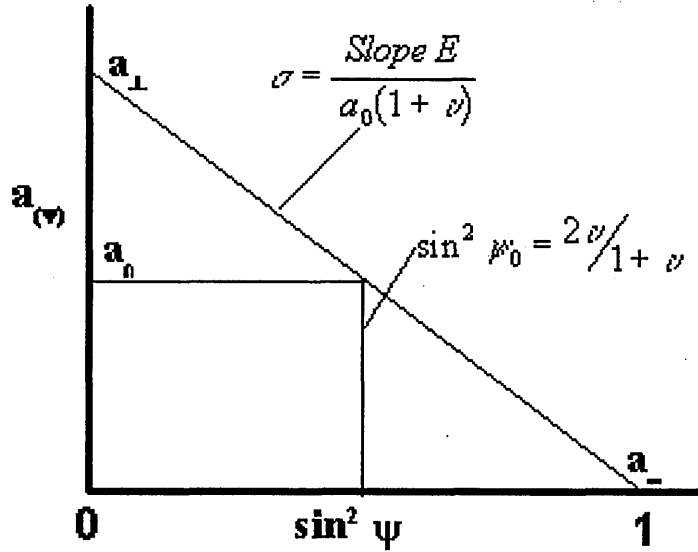


Figure 3.8 Schematic plot of lattice parameter (a) vs  $\sin^2 \psi$

### 3.3.1.3 Superlattice period

The superlattice period,  $\Lambda$  can be defined as the distance between each successive pair of layers, which is also called bi-layer repeat period [2]. In this case the bi-layer consists of alternating CrN and NbN. The  $\theta/2\theta$  Bragg-Brentano geometry in low-angle ( $1-10^\circ 2\theta$ ) configuration was utilised to estimate the superlattice period  $\Lambda$ .

Modification of the Bragg's law (35) is usually used to determine the distance  $d$  between lattice planes.

$$n \cdot \lambda = 2 \cdot d \cdot \sin \theta \quad (35)$$

From knowing the wavelength  $\lambda$  of the X-rays used, the order of diffraction  $n$  and the Bragg angle  $\theta$ ,  $d$  can therefore be calculated.

The bi-layer in the superlattice coating acts as a lattice plane where the incident beam is reflected, see figure 3.9.

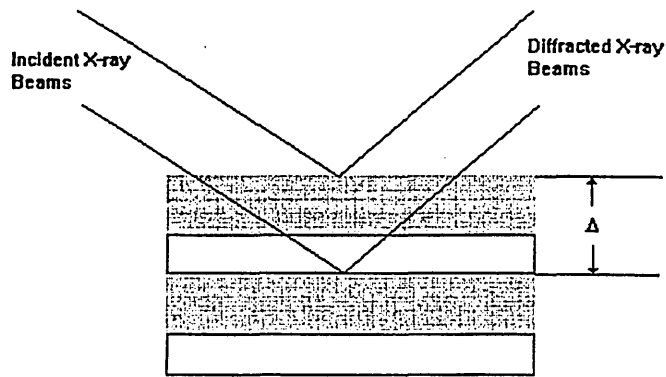


Figure 3.9. Schematic representation of the reflection of X-rays on the bi-layer in superlattice coatings

The superlattice period  $\Lambda$  can be calculated by the modified Bragg equation (36):

$$\Lambda = \frac{n \cdot \lambda}{2 \cdot \sin \theta} \quad (36)$$

Using low angles results in a low penetration depth of the X-rays, which is necessary, therefore no influence of the substrate.

The measurement was made with the Philips Analytical X'Pert MPD diffractometer using the following conditions:

radiation:	Cu-K $\alpha$ ( $\lambda = 0.154056\text{nm}$ )
detector:	Diff. Beam X'Celerator in scanning mode
fixed divergence slits:	1/16 ° and 1/8 ° primary X-rays
start angle 2 $\Theta$ :	1.81°
end angle 2 $\Theta$ :	10°
step size:	0.0334°
scan speed:	0.005305 °/s

A fixed knife edge was used in order to reduce the intensity of the primary beam. The quality of the deposited superlattice coating can be assessed by LA-XRD, because as the peak becomes sharper and more intense this indicates that the interface between the component layers is becoming flatter and better defined.

### 3.3.2 Scanning Electron Microscopy (SEM)

A Philips XL40 scanning electron microscope (SEM) equipped with an Oxford Instruments ISIS300 Energy Dispersive X-ray (EDX) analyser was used to determine the ratio of chromium and niobium in the coatings. These ratios were required for the calculation of the texture parameter and therefore quantitative microanalysis (ZAF corrected) was performed.

#### 3.3.2.1 Quantitative analysis (ZAF)

A Philips XL 40 SEM was used for the determination of the concentrations of chromium and niobium in the CrN/NbN coating with the following measurement conditions:

electron source:	tungsten filament
accelerating voltage:	20kV
detector:	Oxford instrument ATW (Atmospheric Thin Window)
working distance:	10 mm
process time:	4
spotsize:	5.7
chamber pressure:	$8.6 \times 10^{-6}$ mbar
standard:	Co

A Co reference standard was analysed immediately prior to the sample using the same microscope parameters as shown above. It is very important to note that no beam focusing was carried out between analysing the Co standard and the samples, as this would affect the beam conditions. Focusing was performed by manually moving the stage to maintain a working distance of 10mm in all cases. The position of the measured Co  $K_{\alpha}$ -peak from the standard was obtained and saved in order to calculate the gain calibration. The Cr and Nb content of each sample were measured as the average of five independent readings from five different regions on the specimen surface. The results were presented in atomic percent. The portion of Cr, Nb and N was needed in atomic-percent for the calculation of the structure factor  $F$ , see equation (37).

$$F = 4 \cdot [(f_{Nb} + \Delta f'_{Nb}) \cdot c_{Nb}^{at\%} + (f_{Cr} + \Delta f'_{Cr}) \cdot c_{Cr}^{at\%} \pm (f_N + \Delta f'_N) \cdot c_N^{at\%}] \quad (37)$$

Assuming that the nitrogen content is 50at-% and the metal content is 50at-% the atomic percentage of Nb and Cr was calculated.

The CrN and NbN in weight percent was needed for the calculation of the average absorption coefficient  $\mu$ , see equation (23).

$$\mu = \frac{w_{NbN}}{100} \mu_{NbN} + \frac{w_{CrN}}{100} \mu_{CrN} \quad (23)$$

Assuming a NaCl fcc unit cell structure as described in section “3.3.1.1 Texture” where the number of nitrogen atoms and chromium atoms are equal in a CrN unit cell the weight percentage of CrN was calculated using equation (38):

$$wt\%_{CrN} = \frac{at\%_{Cr} (at.weight_{Cr} + at.weight_N) \cdot 100\%}{at\%_N \cdot at.weight_N + at\%_{Nb} \cdot at.weight_{Nb} + at\%_{Cr} \cdot at.weight_{Cr}} \quad (38)$$

The NbN content was determined analogous to CrN.

### 3.3.2.2 Environmental Scanning Electron Microscopy (ESEM)

Electron images from the coating surface before and after corrosion were obtained using a Philips XL30 ESEM-FEG with the following conditions:

electron source:	field emission gun (FEG)
accelerating voltage:	20kV
detector:	large field detector
detection signal:	gaseous secondary electrons
spotsizes:	3.0

The imaging was carried out using a low vacuum H<sub>2</sub>O-mode with a water pressure of 13 mBar in the chamber. The presence of the small amount of H<sub>2</sub>O vapour within the chamber provided gas ionisation, which helps to eliminate charging due to non conductive surfaces. A special ESEM bullet inserted into the base of the column maintained the pressure difference between the electron column and the chamber. The images were obtained using Gaseous Secondary Electron (GSE) mode using a large field detector (LFD).

Before observing the sample surface, the samples were attached to a sample holder with carbon adhesive pad. The electrical contact between the sample and its holder was provided by silver paint.

The surface quality of the deposited coatings was examined in order to assess the number of growth defects present for each sample. The growth defects were manually counted over 20 independent fields using a grid area of 60x80 microns (total area is 96000  $\mu\text{m}^2$ ).

In the case of the corroded samples, the wire and the beeswax/resin coating from the sample base were removed. The beeswax/resin coating however, was not removed from the sample surface but was coated with silver paint to avoid any charging effects. Because the sample was not cleaned with deionised water to avoid the removal of corrosion products salt crystals were observed on the sample surface.

The elemental composition of some corrosion sites was determined by EDX analysis. The measured intensities of selected elements associated with corrosion defects were presented in elemental maps. The presence of oxygen however, could not be accurately identified because the O  $K_{\alpha}$ -peak (0.525KeV) lies in between the Cr  $L_{\alpha}$ -peak (0.573KeV) and the V  $L_{\alpha}$ -peak (0.511KeV); both these elements were present in the HSS substrates.

### **3.3.3 Mechanical and tribological properties**

#### **3.3.3.1 Layer thickness**

The thickness of the coating was calculated from a ball crater test (see fig 3.10). A rotating steel ball with a diameter of 30mm using the KALOPRAEP instrument produced the crater. Using diamond water based suspension, which was applied to the ball; abrasive removal of the coating and the substrate was performed. The ball craters were observed using an Olympus BX 400 optical microscope, which showed two visible concentric circles.

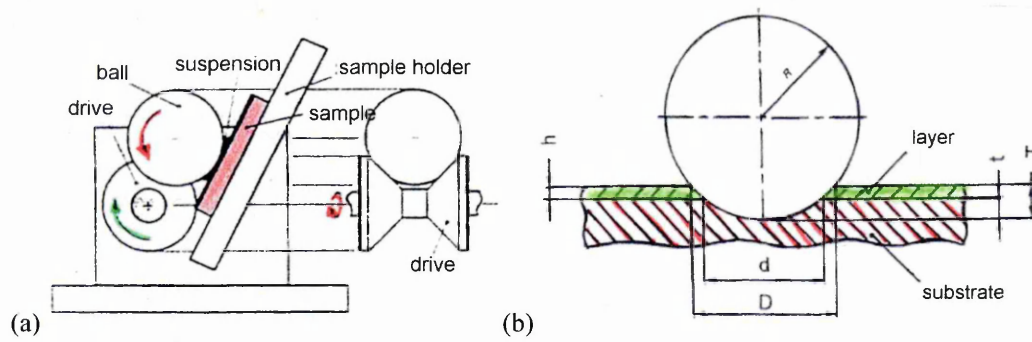


**Figure 3.10.** Schematic principle of the thickness measurement of thin films: (a) device for the creation of a ball crater, (b) diameters of the created circles ( $h=d_c$ ).

The smaller inner circle with a diameter  $d$  belongs to the interface between substrate and coating. The coating surface is marked by the outer circle with the diameter  $D$ . The thickness of the coating  $d_c$  can be calculated using the circles' diameters and the radius of the ball  $R$  in the equation (39).

$$d_c = \sqrt{\frac{R^2 - d^2}{4}} - \sqrt{\frac{R^2 - D^2}{4}} \quad (39)$$

The ball-cratered samples were observed using an image capture optical microscope connected to a computer. Both the inner and outer circles were fitted to new circle profiles in order to calculate their diameters and hence the layer thickness  $d_c$ .

### 3.3.3.2 Microhardness

The Knoop hardness of the coatings was obtained using the Mitutoyo MVK-H2 Hardness Testing Machine. An average of five independent readings were obtained using a diamond Knoop indenter with an indentation load of 25g.

The plastic hardness of the coatings was also determined using the Fisherscope and was calculated using the load/indentation depth curve,  $h_r$ ' and the maximum test load.

### 3.3.3.3 Adhesion

The adhesion of the coatings is expressed as the critical load  $L_c$  for delamination, which was measured by a CSEM REVETEST scratch tester. A scratch was produced by a cone shaped diamond stylus (Rockwell C) exerting a gradually increasing applied load to the coating over a distance,  $d$ . The sample was moved in

one direction while the load was increased progressively by a function  $dF/dx = 10 \text{ N/mm}$ . The load  $L_s$  at the start of the test was 5N and was increased until it reached 50N. The Rockwell C diamond stylus had a radius of  $200\mu\text{m}$ . A schematic view of the abrasive scratch test procedure is shown in figure 3.11.

The scratch was observed using a NIKON optical microscope at a magnification of 200X. The place  $x$  where the first spallation along the scratch edge occurred could be measured and the critical load  $L_c$  for adhesive failure was calculated by (40).

$$L_c = x \cdot 10 \text{ N/mm} + L_s \quad (40)$$

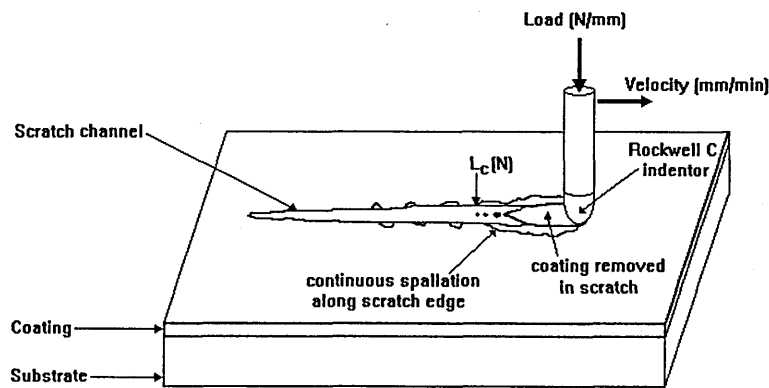


Figure 3.11. Schematic view of the realisation of a scratch test [49].

### 3.3.3.4 Surface roughness

The surface roughness was measured using a TAYLOR-HOBSON talysurf\_120L. This measurement provided a surface roughness resolution of 10nm. A diamond stylus with a radius of  $2 \mu\text{m}$  scanned over the surface in direct contact along the length  $L_0$  of 5.6mm. This length was broken down into six sample lengths  $l$  of 0.8mm and two further lengths of 0.4mm at the beginning and the end of the profile. The six sample lengths  $l$  form the assessment length  $L_s$ , which is the length of profile used for the measurement of the surface roughness. The  $R_a$  value defines the surface roughness of the coating and this value is the arithmetic mean of the departures of the roughness profile from the mean datum line (See Appendix A4). The  $R_a$  value is calculated as follows (41):

$$R_a = \frac{1}{L} \int_0^L |y(x)| dx \quad (41)$$

### 3.3.3.5 Friction and sliding wear

Friction can be defined as the resisting force tangential to the common boundary between two bodies, when one body moves relative to the surface of the other body under the action of an external force. The contact can be expressed in both rolling and sliding modes. Sliding is the dominant movement for the investigations in this report. The coefficient of friction  $\mu$  describes the magnitude of the frictional force. The coefficient of friction, for most common materials sliding in air fall within a value ranging from 0.1 to 1. It is defined as the quotient of the frictional force  $F_f$  tangential to the sliding direction and the normal load  $F_n$  (42).

$$\mu = \frac{F_f}{F_n} \quad (42)$$

Wear is the removal from a solid surface as a result of sliding or rolling contact [45]. The wear coefficient  $k$  can be calculated by equation (43).

$$k = \frac{V}{W \cdot L} \quad (43)$$

Where

V = Volume loss [m<sup>3</sup>]

W = Normal load [N]

L = Sliding distance [m].

The CSEM TRIBOMETER Pin on disc tester was used for the determination of the friction coefficient. Figure 3.12 shows it schematically.

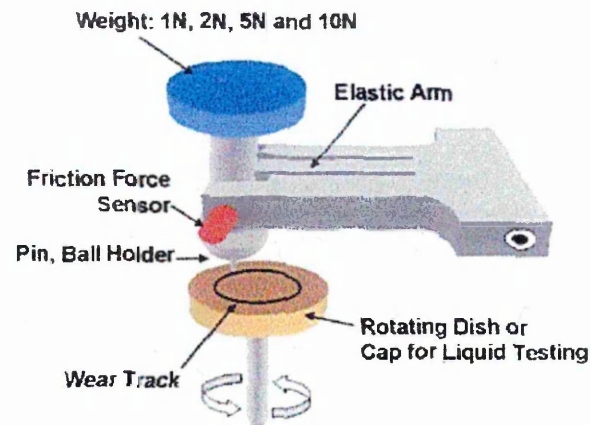


**Figure 3.12.** Schematic view of the pin-on-disc tribometer.

The samples were rotated with a linear speed of  $0.10\text{ms}^{-1}$  whilst an  $\text{Al}_2\text{O}_3$  ball as counterpart under a load of 5N was applied to the sample over a defined distance. The chosen number of laps was 40000. The tests were carried out at room temperature of  $22^\circ\text{C}$  and 20% humidity. The coefficient of friction was measured using a sensor connected to a computer and the results were shown graphically, where the sliding distance was plotted as a function of friction coefficient. The mean coefficient of friction was calculated from the graph using a computer program.

The sliding wear coefficient was measured from the volume loss, which was determined by measuring the average of four profiles of the transverse section of the wear track with the TAYLOR-HOBSON Talysurf\_120L. The area of the wear track was determined from these profiles and the sliding coefficient  $K_c$  was calculated using the “Tribox” software.

### 3.3.3.6 Corrosion

The corrosion resistance of the CrN/NbN superlattice coatings was determined by a potentiodynamic polarisation measurement in a 3% NaCl solution open to air at room temperature. A stainless steel wire was fastened tightly around each sample in order to suspend it within the solution. The whole sample and the surrounding wire was coated with a beeswax/resin mixture (approximately 3:1) except for a circular area on the coated surface, which had a diameter of 1cm (surface area exposed to the solution was  $0.7854\text{cm}^2$ ).

The coated sample was placed in a glass filled with the 3% NaCl solution and polarised as the working electrode (WE). The wire fixed around the sample made the electrical contact. It was therefore necessary to ensure that there was no exposed wire present in the solution, or else the corrosion of the wire would influence the measurement. An electrode made out of titanium and coated with platinum was used as auxiliary (AE) or counter electrode (CE). A saturated Calomel electrode (SCE) was used as the reference electrode (RE) and placed between WE and CE. The RE was also very closely situated to the WE.

A potential was applied to the WE with respect to the RE, which provides a very stable datum. The potential was scanned at a certain rate between the potential limits. The CE is present to carry the current created in the circuit. The current density was recorded as the dependent variable.

At first the solution was aerated with oxygen for 55 minutes. During the aeration process, the sample and the electrodes were already placed in the solution. The samples were cathodically cleaned at a potential of -1.5V for 100sec. this was followed by a 40 min wait in order to allow the stabilisation of the free corrosion potential. Finally the actual potentiodynamic measurement started. During this measurement the sample was polarised from -1V to +1V at a scan rate of 0.5mV/s.

The instrument used for the corrosion test of the samples of trial\_1 and trail\_2 and the samples of CrN/NbN coatings deposited at high temperature was called ACM (Applied Corrosion Monitoring). The sequence of the experiment was controlled by the "Gil AC Serial no 950 -sequencer" computer program. This program recorded the measurement as well.

## 4 Results and Discussion

Four different samples were observed from the low temperature coating deposition process designated as “trial\_1” and “trial\_2” in the following presentation of the results, as shown in table 4.1.

**Table 4.1** Sample overview (see details of substrate composition on page 51).

	trial 1		trial 2	
<b>Bias voltage</b>	-75 V	-95V	-75V	-95V
<b>deposition temperature</b>	250°C	250°C	250°C	250°C
<b>substrate</b>	SS	SS	HSS	HSS

The results obtained from the samples of trial\_1 were more conclusive in their findings than that for trial\_2. This was because unstable arcing occurred during the metal ion etching of the -95V samples of trial\_2, which therefore affected their analytical studies as can be seen further within this work.

### 4.1 Texture (XRD)

The  $\theta/2\theta$  Bragg-Brentano geometry was used to determine the orientation of the grains parallel to the surface of the coating. The X-ray traces exhibited single phase fcc (NaCl) structures. The diffraction peaks which are situated between the individual positions of CrN and NbN data markers, correspond to the weighted mean of the constituent layers. This is shown in figure 4.1 where the known peak positions of CrN and NbN are marked in the diffraction pattern of the -75V sample of trial 1. Any displacement in the peak positions from those of the weighted mean is a result of residual stress. The diffraction patterns of the investigated samples are shown in figure 4.2 and figure 4.3. The planes associated with each peak are shown on each trace together with those for the substrate labelled as (S). The X-ray patterns show that in all cases the  $\{111\}$  reflection was very intense relative to the other reflections, indicating the presence of a  $\{111\}$  texture. Furthermore, the intensity of the  $\{111\}$  reflection relative to the other reflections increased as the bias voltage increased from -75V to -95V, thus indicating an increase in the intensity of the  $\{111\}$  texture with increasing bias voltage.

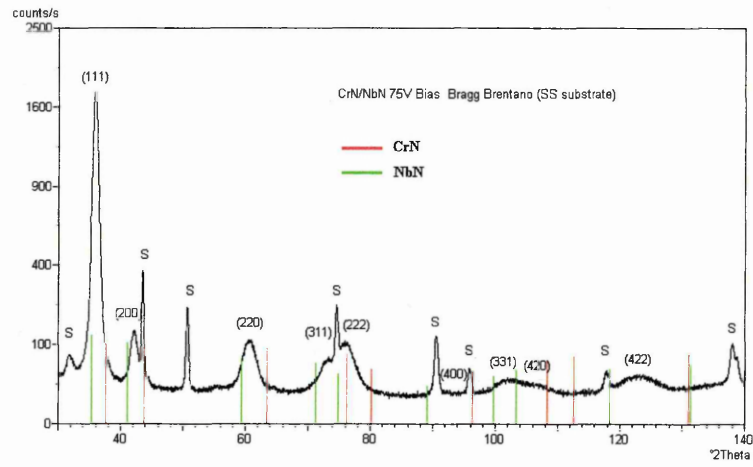
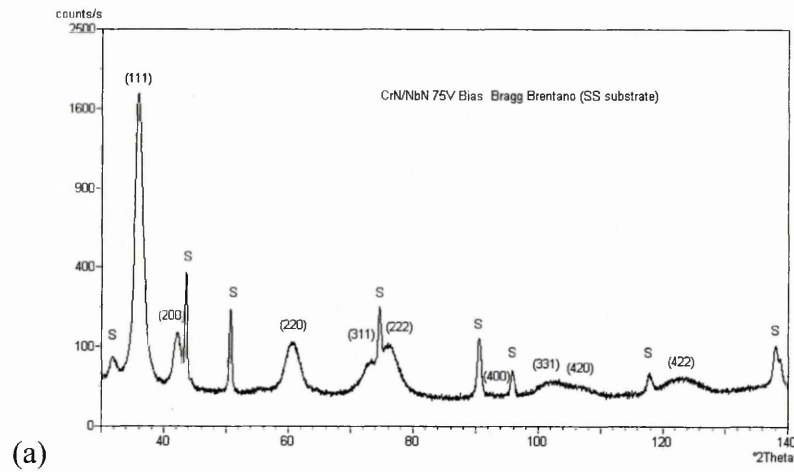
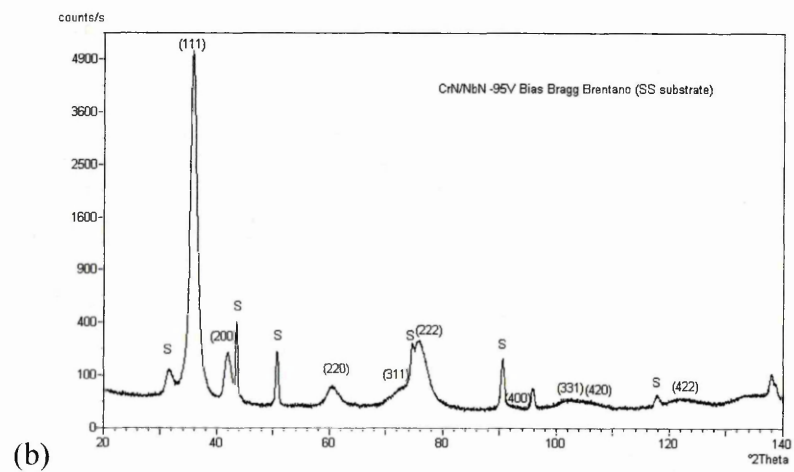


Figure 4.1. Bragg-Brentano diffraction pattern of the -75V sample trial\_1.



(a)



(b)

Figure 4.2. Bragg-Brentano diffraction pattern of the (a) -75V and (b) -95V sample of trial\_1.

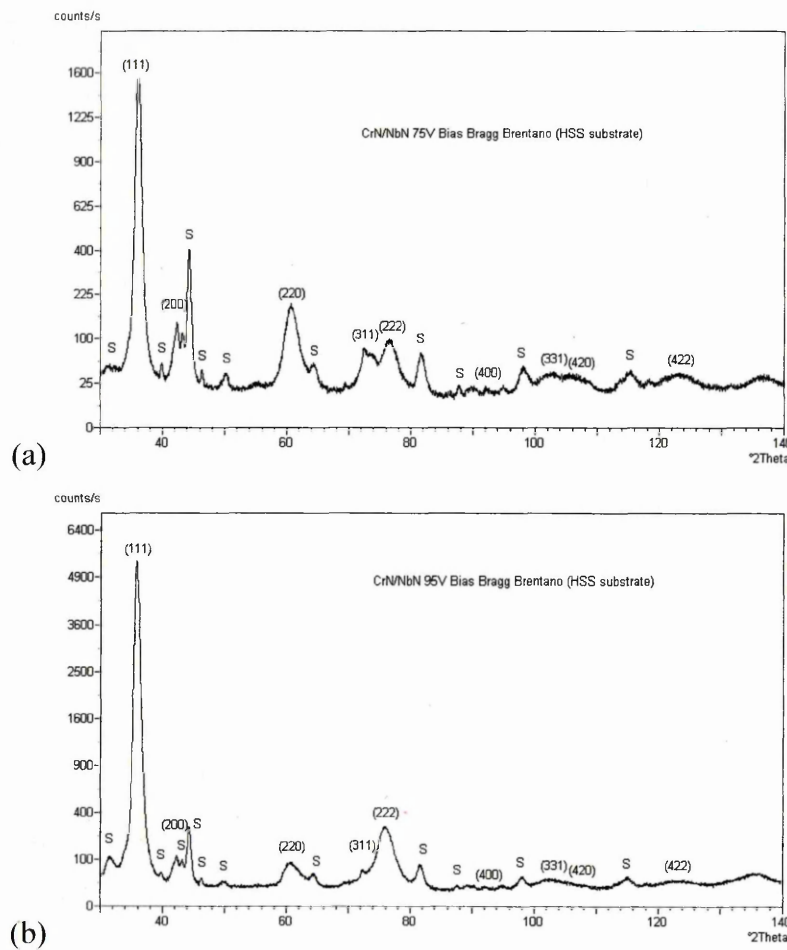


Figure 4.3. Bragg-Brentano diffraction pattern of the (a) -75V (b) -95V sample of trial\_2.

The texture parameter  $P$  was calculated using equation (20). The following seven (hkl) planes were considered in the calculation of  $P$  namely: (111), (200), (220), (311), (331), (420) and (422). Seven planes were considered in all cases. The  $P$ -value for (111), (200) and (220) planes of both trials is shown in figure 4.4 and tabulated in Table 4.2.

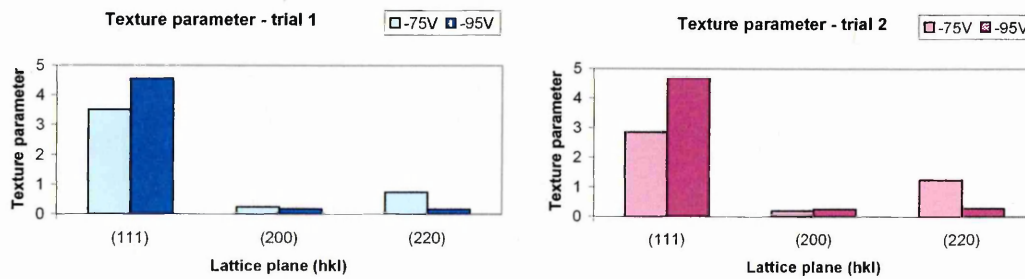


Figure 4.4. Texture parameter  $P$  of the {111}, {200} and {220} planes Trial\_1 and 2.

Table 4.2 Texture Parameter P of the {111}, {200} and {220} planes Trial 1 and 2.

Sample	Texture Parameter, P {111}	Texture Parameter, P {200}	Texture Parameter, P {220}
-75V Bias Trial_1	3.51	0.24	0.73
-95V Bias Trial_1	4.55	0.17	0.16
-75V Bias Trial_2	2.91	0.22	1.24
-95V Bias Trial_2	4.81	0.32	0.32

The texture parameter of the {111} plane for all the samples was calculated to be greater than one, which signifies a preferred {111} texture. With the exception of the (220) plane in the -75V bias trial\_2 sample, which has a P value of 1.2, all the other planes have P values less than 1. In all cases the coatings had a {111} texture, which supports the indicated results from the X-ray patterns. Furthermore, the intensity of the {111} increases systematically with increasing bias voltage from P values of 3.5 and 2.9 respectively at -75V bias to 4.6 and 4.8 respectively at -95V bias.

The 2-dimensional {111} stereographic pole figures also show the strong {111} fibre texture present for all of the coatings deposited at low temperature (250°C), as shown in figure 4.5 and figure 4.7. The 2.5-dimensional pole figures also aids in visualising the {111} texture as shown in figure 4.6 and figure 4.8. It was observed that within the pole figures, regions of high contour density were present normal to the coating surface centre around the {111} pole and uniformly distributed about the  $\psi$  direction. This indicates the presence of a strong {111}, fibre texture.

The textures were also shown to be increasingly sharp as the bias voltage was increased from -75V to -95V, as shown by the density (high intensity) of the contour bands around the {111} pole axis. This can also be seen with the sharper peaks observed in the corresponding 2.5D pole figures.

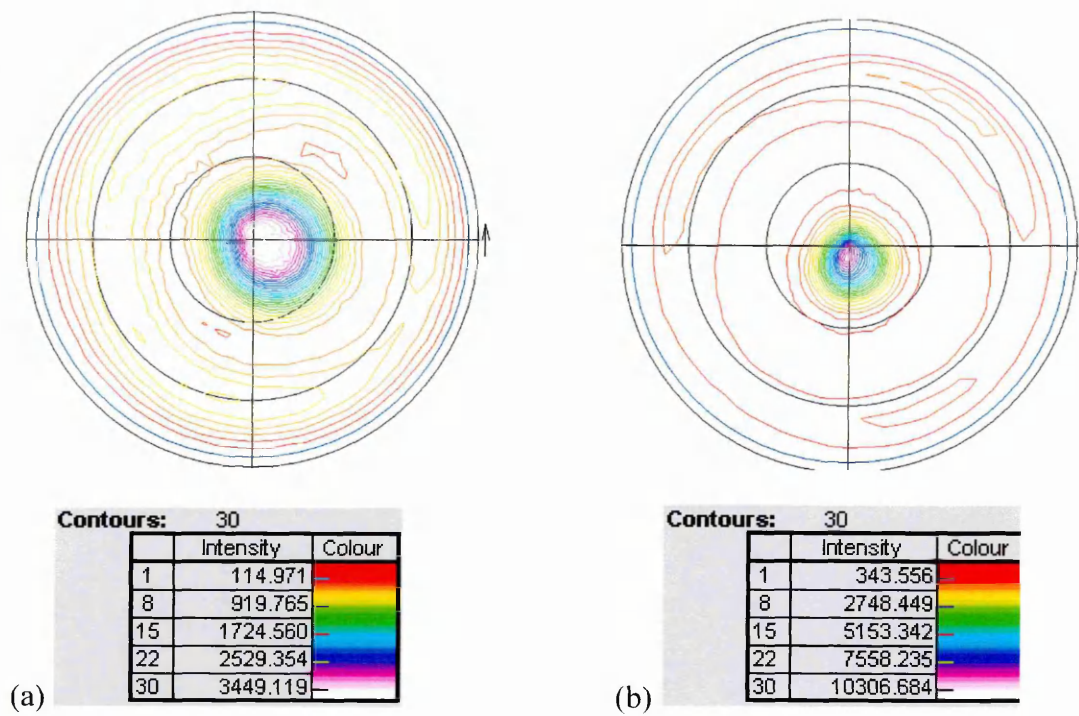


Figure 4.5. 2-dimensional  $\{111\}$  pole figures: (a)  $-75V$  and (b)  $-95V$  of trial\_1.

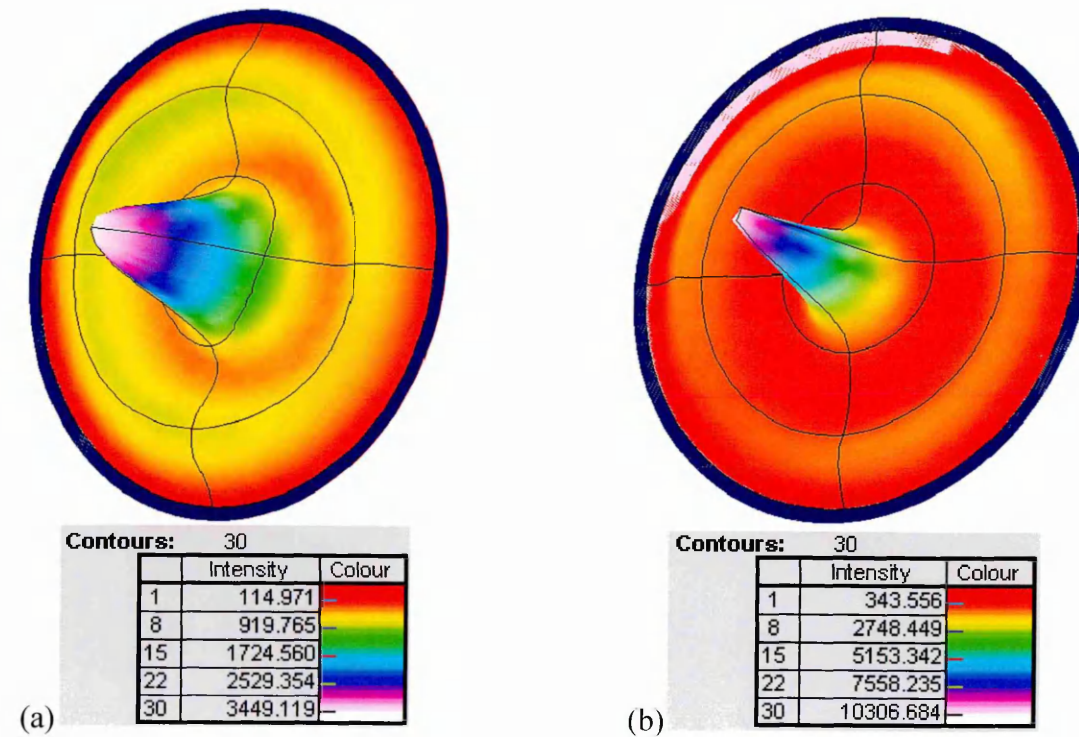


Figure 4.6. 2.5-dimensional  $\{111\}$  pole figures: (a)  $-75V$  and (b)  $-95V$  of trial\_1.

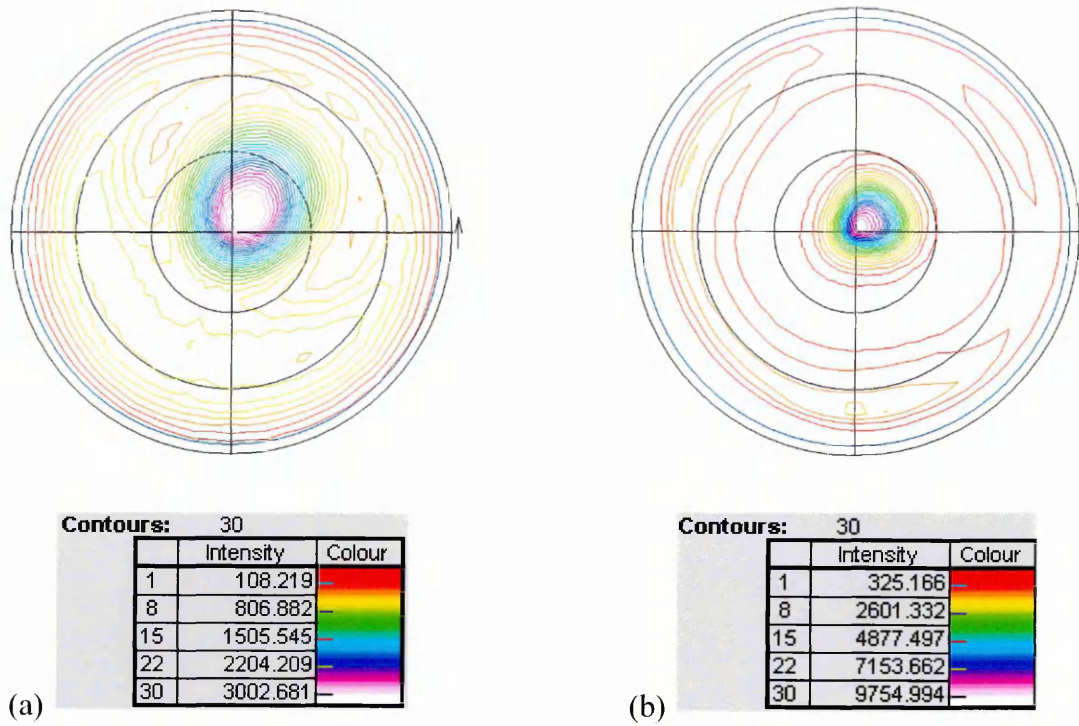


Figure 4.7. 2-dimensional  $\{111\}$  pole figures: (a)  $-75V$  and (b)  $-95V$  of trial\_2.

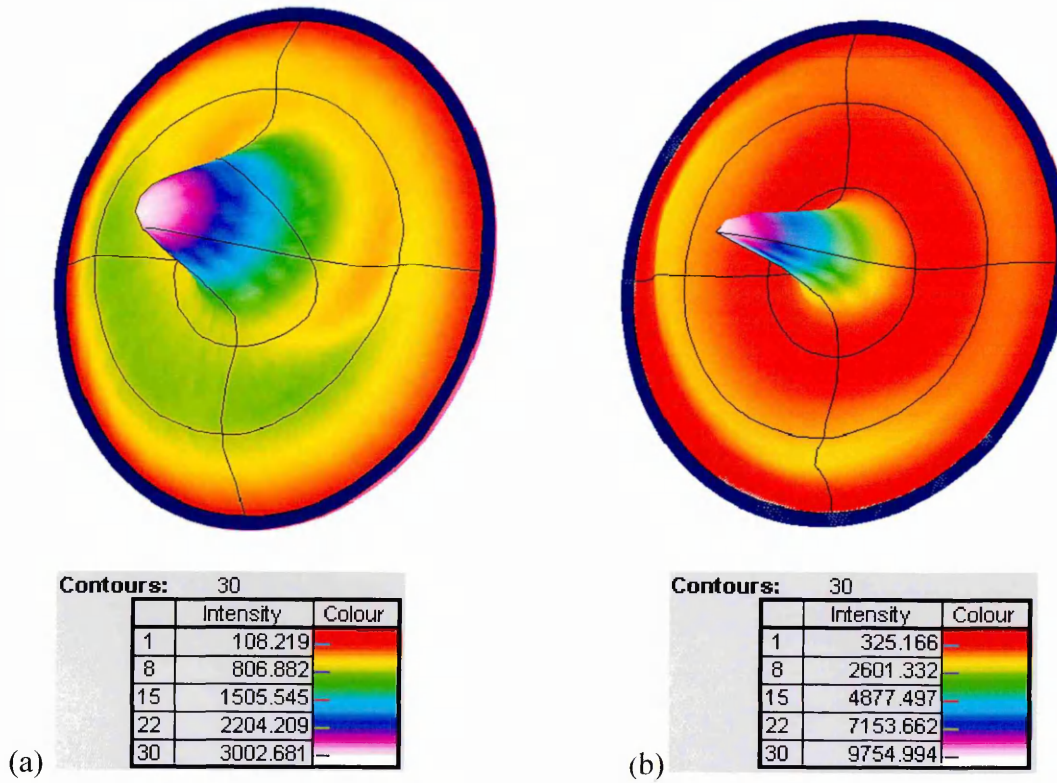
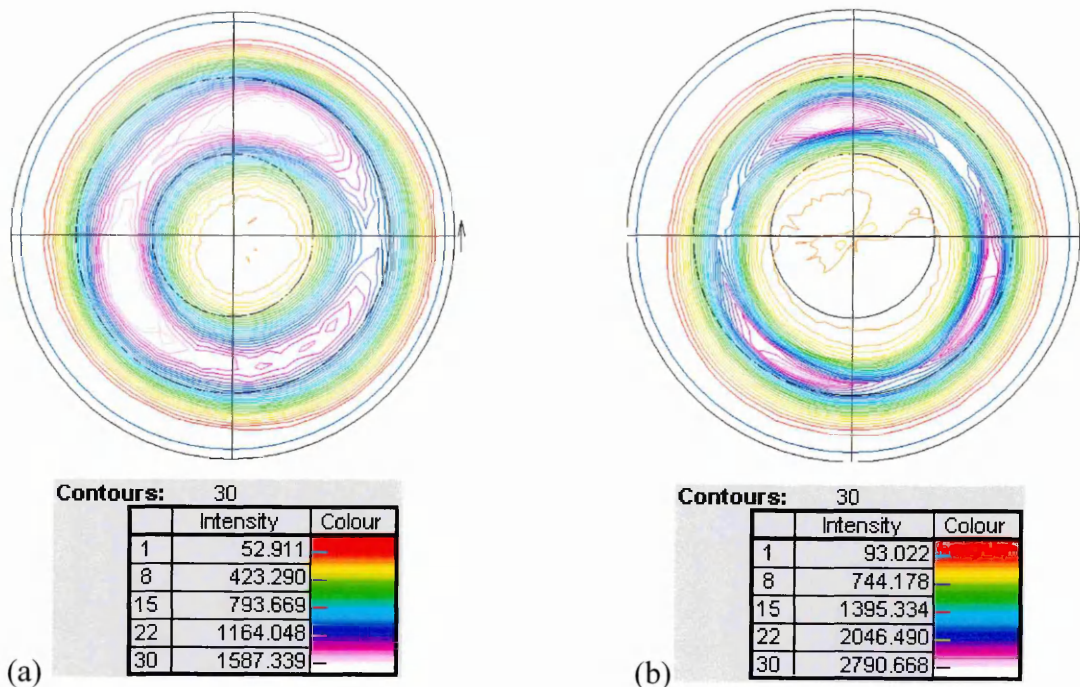


Figure 4.8. 2.5-dimensional  $(111)$  pole figures: (a)  $-75V$  and (b)  $-95V$  of trial\_2.

The 2-dimensional  $\{200\}$  pole figures for the samples of trial\_1 and trial\_2 are shown in figure 4.9 and figure 4.10 respectively. The presence of  $\{111\}$  texture is further emphasised in the  $\{200\}$  pole figures, where regions of high pole density are spread at approximately  $55^\circ$  from the coating normal. The angle relationship between the crystallographic cubic  $\{200\}$  plane and the  $\{111\}$  plane is known to be  $54^\circ44'$  [50].

The  $\{200\}$  pole figures also showed that the  $\{111\}$  exhibits increasing sharp intensity contours with the higher -95V bias sample further indicating a stronger  $\{111\}$  texture. The -95V bias sample in both trials 1 and 2 also exhibited regions of higher pole densities at  $120^\circ$  to each other in  $\{111\}$  plane, which suggest three-fold symmetry. This would therefore indicate, that even though the coating at -95V bias exhibited strong  $\{111\}$  texture, there was also some plane anisotropy present.



**Figure 4.9.** 2-dimensional  $\{200\}$  pole figures: (a) -75V and (b) -95V of trial\_1.

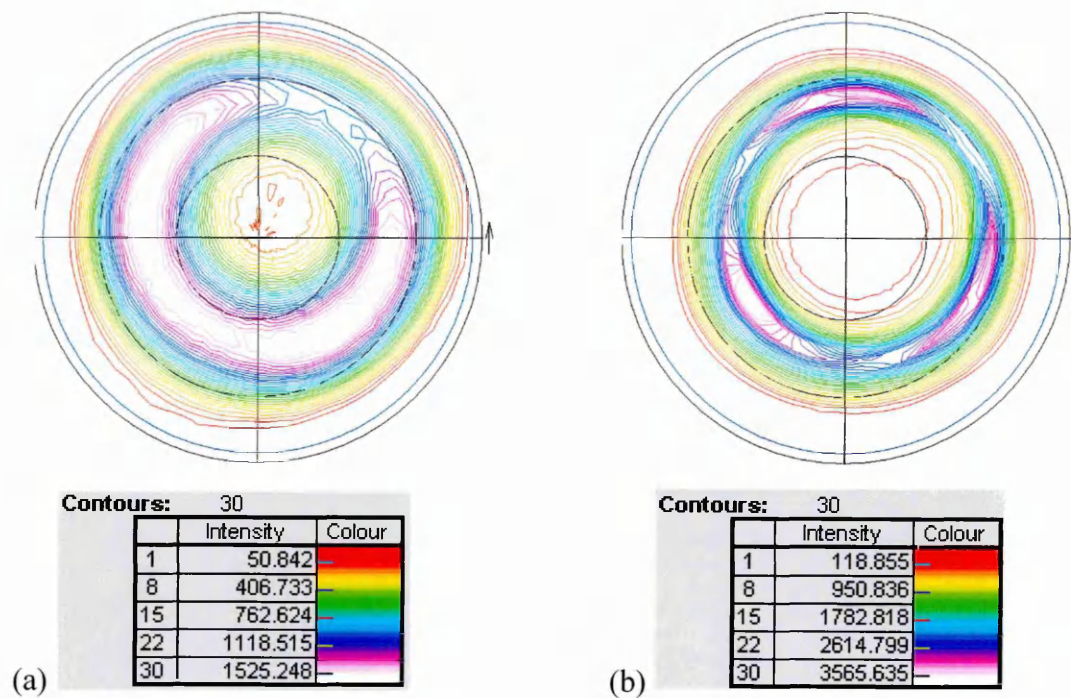


Figure 4.10. 2-dimensional {200} pole figures: (a) -75V and (b) -95V of trial\_2.

The 2-dimensional (220) pole figures for samples of trial\_1 are shown in figure 4.11 and for samples of trial\_2 are shown in figure 4.12. These have been included for reference.

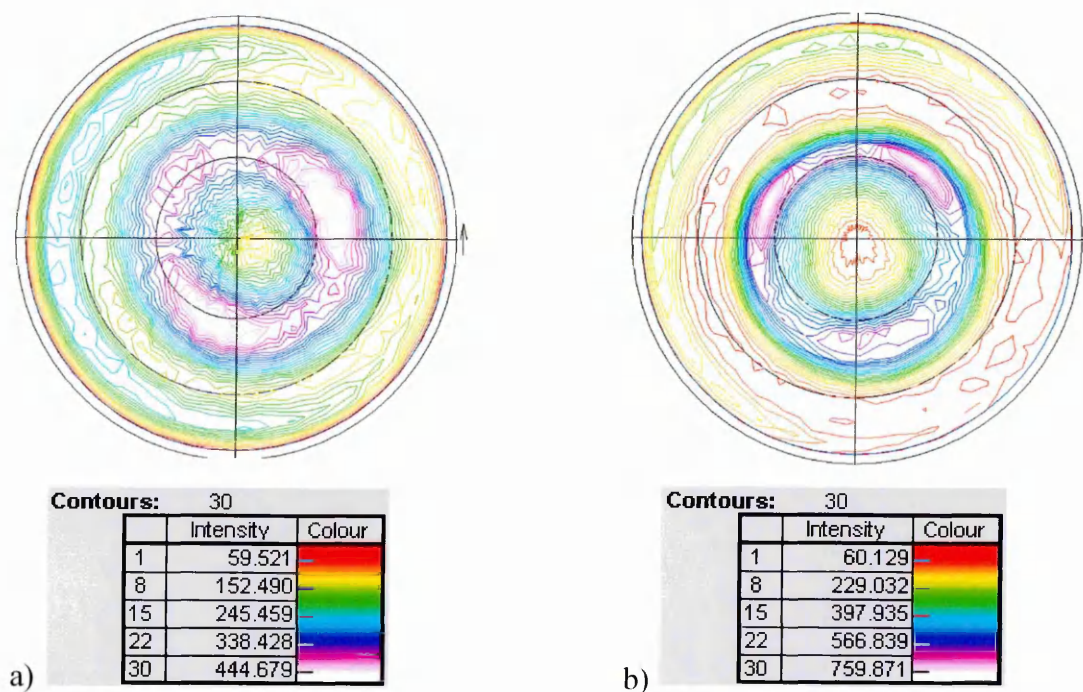
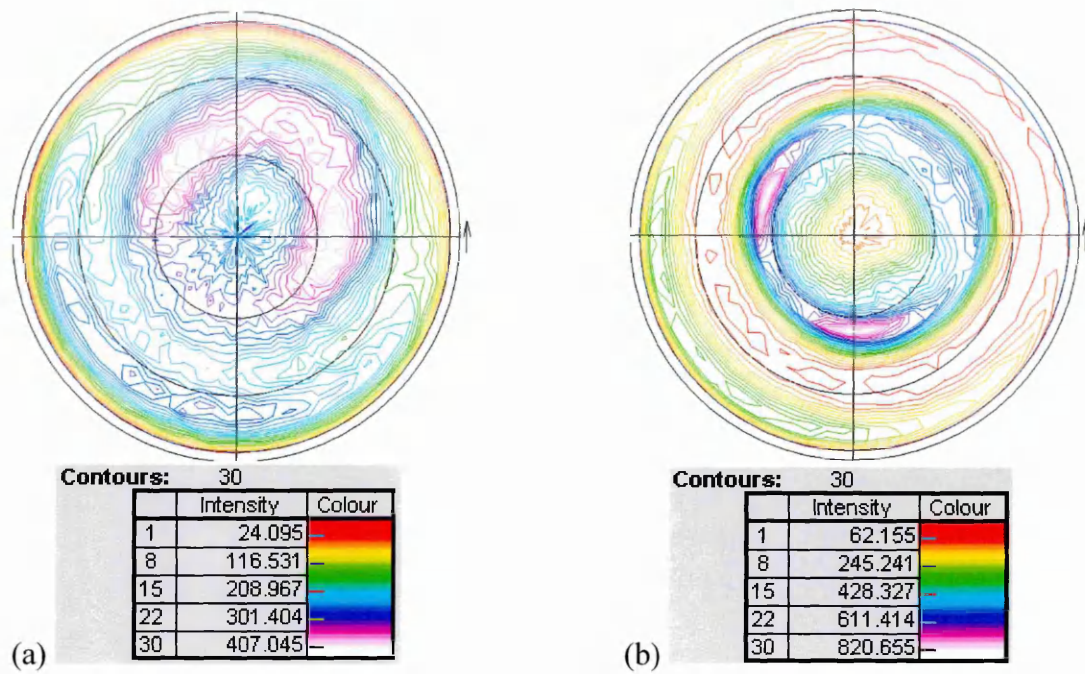


Figure 4.11. 2-dimensional {220} pole figures: (a) -75V and (b) -95V of trial\_1.



**Figure 4.12.** 2-dimensional {220} pole figures: (a) -75V and (b) -95V of trial\_2.

Texture analysis measurements performed on CrN/NbN coatings deposited at higher temperatures (400°C) showed that they developed {100} textures. This can be observed from the P texture values obtained from CrN/NbN superlattice coatings deposited at 400°C shown in Table 4.3.

**Table 4.3** Texture Parameter P of the {111},{200} and {220} planes for 400°C deposited coatings

Sample	Texture Parameter, P {111}	Texture Parameter, P {200}	Texture Parameter, P {220}
-75V Bias 400°C	<b>0.46</b>	<b>2.66</b>	<b>0.76</b>
-95V Bias 400°C	<b>0.32</b>	<b>3.28</b>	<b>0.64</b>

The reasons why the low temperature deposited CrN/NbN coatings exhibited {111} textures, whilst those deposited at higher temperature exhibited {100} textures has been explained with theoretical predictions of the growth mechanism by [51] and furthermore by [52]. They stated that both the surface energy and strain energies must be considered as the driving force for the texture evolution. Thus, for metal (fcc) nitrides, because the {100} plane has the highest atom packing density (4.0 at/a<sup>2</sup> compared with 2.83 at/a<sup>2</sup> {220} and 2.31 at/a<sup>2</sup> {111}) and hence, the lowest surface free energy, then the development of the {100} texture is favoured if the surface free energy is the dominant parameter. Conversely, when the strain energy is the dominant parameter, the texture development is towards the {111} plane, which has the lowest strain energy. It can be therefore assumed that at lower temperature

coating depositions the strain energy is a dominant factor, leading to the formation of competitive columnar growth favouring the development of a {111} texture. Recent work using a gradual exposure technique has shown that the 165 nm thick base layer has a {100} texture [53]. In the thinner low temperature CrN/NbN coatings (300 nm thick) deposited at -75 V the {100} component is dominant. This would indicate at the lower bias initially the surface energy is dominant with possibly some templating on the {100} oriented CrN base layers. With increasing coating thickness the {111} component increases and becomes the major texture in thicker coatings. In contrast the coating deposited at -95 V developed a {111} texture even in the thinnest 300 nm coatings. The intensity of this component continued to increase with increasing coating thickness. This is clearly consistent with the development of {111} textures, which develop by a competitive growth mechanism. Clearly the development of a {111} texture at -95V even in the thinnest coatings resulted in a stronger {111} texture at -95 V bias. The presence of a {111} texture indicated that in all cases the strain energy became dominant in thicker coatings leading to the development of a {111} texture by competitive growth. This is in contrast to coatings deposited at temperatures of 400°C where the surface energy was dominant which developed {100} textures [4], [20], [45].

## 4.2 Residual stress (XRD)

Residual stresses of the CrN/NbN coatings were measured using Glancing Angle X-ray diffraction (GA-XRD) where an incident angle of 2° was used. A GA-XRD trace for the -75V bias trial\_1 sample is shown in figure 4.13. The major advantage of glancing angle is the substrate (S) peaks are effectively eliminated leaving only the peaks from the coating.

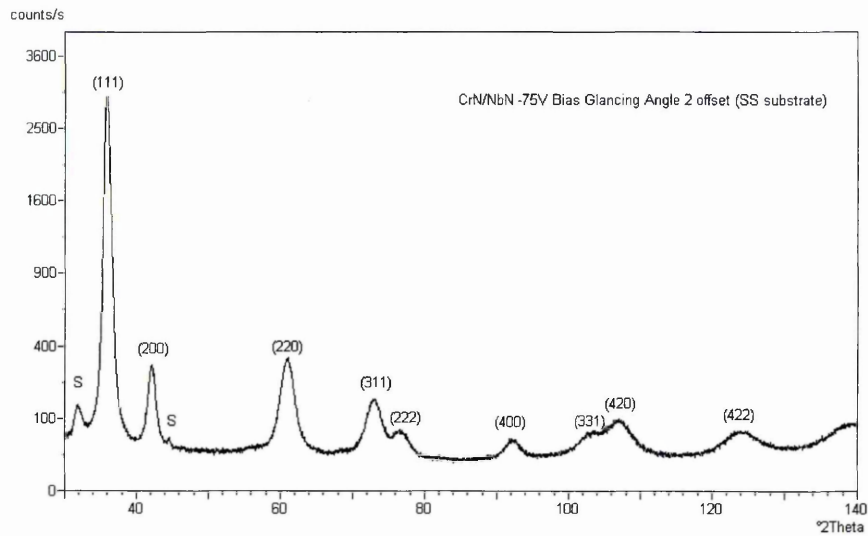
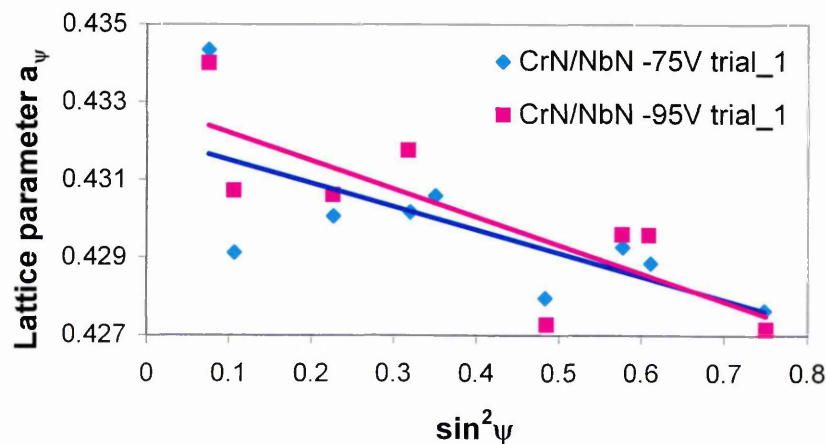
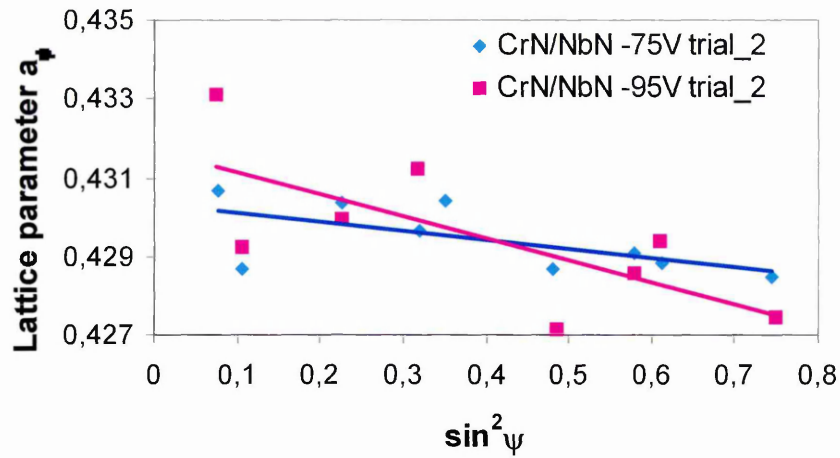


Figure 4.13 GA-XRD trace for -75V Bias sample trial\_1

Equation (30) was used to plot the lattice parameter  $a_\psi$  v's  $\sin^2\psi$  values for the range of peaks. The plots for the CrN/NbN coatings of trial\_1 are shown in figure 4.14a and in figure 4.14b for the CrN/NbN coatings of trial\_2. The slope of the linear regression curve was used to calculate the stress value using equation (34). The unstressed lattice parameter  $a_0$  was obtained using equation (33) and extrapolating from the  $\sin^2\psi$  up to the line and across as shown in figure 3.7. The negative slope indicates the presence of compressive stresses in all of the coatings.



(a)



(b)

**Figure 4.14.** Plotting of the lattice parameter  $a_\psi$  versus  $\sin^2\psi$  of CrN/NbN superlattice coatings of (a) trial\_1 and (b) trial\_2.

The  $R^2$ -value of the linear regression line was calculated, the intersection,  $n$  and the slope,  $m$  for each graph was obtained as shown in Table 4.4. The value obtained for the slope was used in the calculation of residual stress values.

**Table 4.4** Values of the slope  $m$ , the intersection  $n$  with the  $y$ -axis and the  $R^2$ -value obtained from the regression line.

	$\gamma = 2^\circ$		
	$m$	$n$	$R^2$
-75V trial_1	-0.006	0.432	0.498
-95V trial_1	-0.007	0.433	0.636
-75V trial_2	-0.002	0.432	0.380
-95V trial_2	-0.006	0.432	0.500

**Table 4.5.** Residual stresses in the CrN/NbN superlattice coatings of trial\_1 and trial\_2.

Sample	Residual Stress (GPa)
-75V Bias Trial_1	$-4.4 \pm 0.6$
-95V Bias Trial_1	$-5.2 \pm 0.8$
-75V Bias Trial_2	$-1.7 \pm 0.2$
-95V Bias Trial_2	$-4.1 \pm 0.7$

The calculated residual stresses are presented in Table 4.5. The Fischerscope was used to determine the Young's modulus ( $E$ ) of these coatings, however, due to a large scatter and unrealistic high values they were ignored. Therefore the value for the Young's modulus used in the calculation of the residual stress was taken from

former investigations of CrN/NbN superlattice coatings. An E-value of 406GPa was used for the calculation of the residual stress for all four samples.

All of the low temperature deposited coatings exhibited compressive stresses, which are expected for PVD coatings. The CrN/NbN coatings deposited at -95V exhibited a higher compressive stress (-5.2GPa) than the -75V bias sample (-4.4GPa). The stresses calculated for trial\_2 also showed the same trend (-1.7GPa for -75V bias and -4.1GPa for -95V bias). The increase in compressive residual stress with increasing bias voltage is a result of higher defect densities mainly caused by higher-energetic ion bombardment at high bias voltages. Both Ar and N<sub>2</sub> can be forced into tetrahedral interstitial sites hence providing the lattice strain for residual stresses to increase. The fact that increasing the bias voltage results in denser PVD coatings also can support the increase in compressive residual stresses shown.

The coatings deposited on the SS substrates exhibited higher compressive stresses than the coatings deposited on HSS substrate. A possible reason for this might be that different stresses are induced by the nucleation due to a larger structural misfit between the SS substrate and the CrN/NbN coating than between the HSS substrate and the CrN/NbN coating. Another explanation might be due to differences between the thermal expansion coefficients of the two substrates (SS or HSS) and the coating (see equation 14). The thermal expansion coefficients for SS and HSS over the temperature range are 17.0  $\mu\text{m m}^{-1} \text{ }^\circ\text{C}^{-1}$  and 11.5  $\mu\text{m m}^{-1} \text{ }^\circ\text{C}^{-1}$  respectively.

Higher temperature (400°) deposited CrN/NbN coatings onto stainless steel, exhibited much lower compressive residual stresses using the same bias voltages (shown in table 4.6) compared with those coatings deposited at lower temperatures of 250° C.

**Table 4.6** Residual stresses in CrN/NbN superlattice coatings deposited at 400°C (ss)

Sample	Residual Stress (GPa)
-75V Bias (400°C)	-1.8 ± 0.5
-95V Bias (400°C)	-3.7 ± 0.7

One reason for this is the effect of the temperature component on the residual stress (see equation 14). The lower temperature deposited coatings exhibit lower differences in the expansion coefficient between the metal substrate and coating than that for the higher temperature deposited coatings. It is well known that the level of residual stress in hard coatings depends on deposition temperature, with higher deposition temperatures favouring the development of lower residual stresses [39]. It is also thought that deposition of coatings at higher temperatures provide a mechanism for stress relaxation to occur through some form of plastic deformation or recovery (annealing) of interstitial defects that formed during deposition. In the fcc (NaCl) coatings structures, point defects can form by the incorporation of Ar and N<sub>2</sub> in tetrahedral holes of the lattice during deposition. These point defects produce higher compressive stresses than just due to Ar alone. At higher deposition temperatures thermally activated relaxation takes place, which decreases the number of point defects by a diffusion process. At first the N<sub>2</sub> diffuses however, the Ar content is stable upto 600°C, which suggest that stress relaxation at low temperatures, is by the annealing of N<sub>2</sub> interstitial sites. Therefore coatings deposited at lower temperatures exhibited higher compressive stresses.

### 4.3 Superlattice period

The superlattice period  $\lambda$  was measured using the  $\theta/2\theta$  Bragg-Brentano geometry in low angle (LA) configuration. The low angle X-ray diffraction (LA-XRD) pattern of the -75V and -95V sample of trial\_1 and trial\_2 are given in figure 4.15a and figure 4.15b respectively. The calculated superlattice period  $\lambda$  results are presented in Table 4.7.

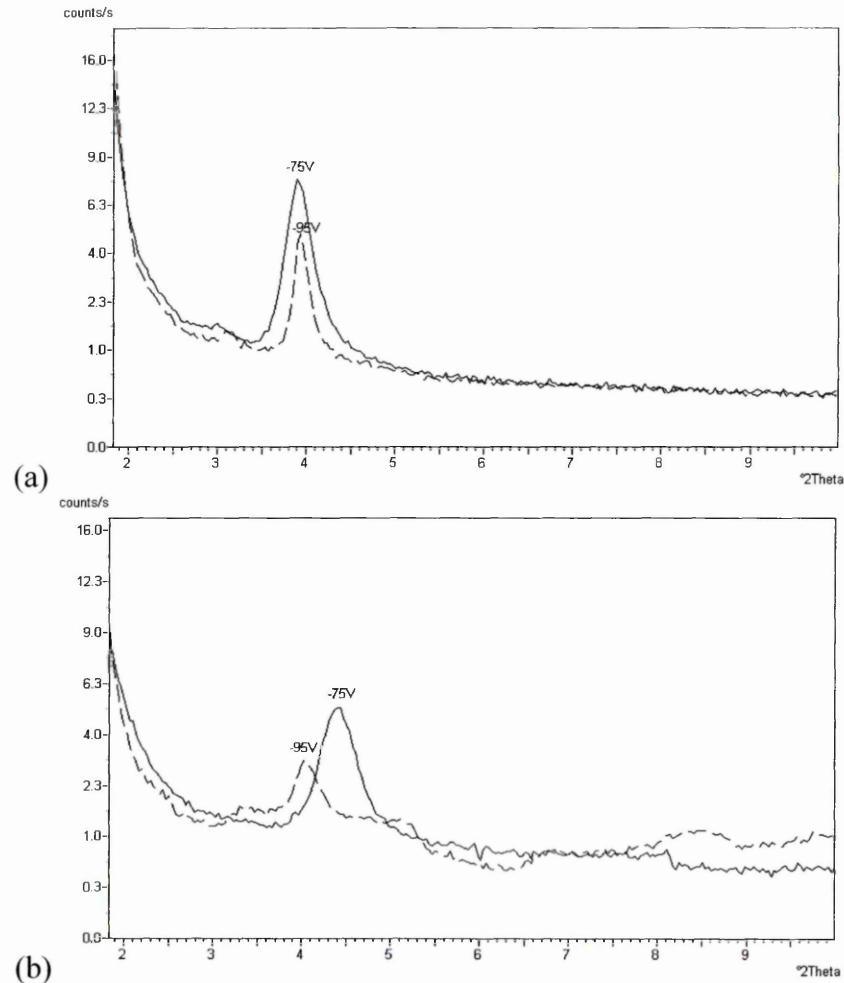


Figure 4. 15. LA-XRD traces of the  $-75\text{V}$  and  $-95\text{V}$  sample of (a) trial\_1 and (b) trial\_2.

Table 4.7 Superlattice period of the deposited CrN/NbN coatings ( $250^\circ\text{C}$ )

Sample	Superlattice Parameter, $\lambda$ (nm)
-75V Bias Trial_1	$2.3 \pm 0.1$
-95V Bias Trial_1	$2.2 \pm 0.1$
-75V Bias Trial_2	$2.0 \pm 0.1$
-95V Bias Trial_2	$2.2 \pm 0.1$

The superlattice period of the  $-75\text{V}$  bias and  $-95\text{V}$  bias samples for trial\_1 were found to be similar at  $2.3\text{nm}$  and  $2.2\text{nm}$  respectively. In the case of the trial\_2 samples clearly shows that the superlattice periods of the  $-95\text{V}$  bias sample ( $2.2\text{nm}$ ) was clearly larger than that for the  $-75\text{V}$  bias sample ( $2.0\text{nm}$ ), which was not the expected trend. However, it was known that there was a problem associated with the plasma arc for the  $-95\text{V}$  bias coating for trial\_2 and therefore this may account for the results obtained. The LA-XRD trace for the  $-95\text{V}$  bias trail\_2 sample was also shown to be very peculiar (see figure 4.15b). It was thought that because the sample exhibited a

relatively weak peak intensity it indicated that a poorly defined superlattice interface was present in the coating.

#### 4.4 Layer thickness

Figure 4.16 shows the ball craters on the surface of the substrate which were used for the calculation of the coating thickness  $d_L$ .

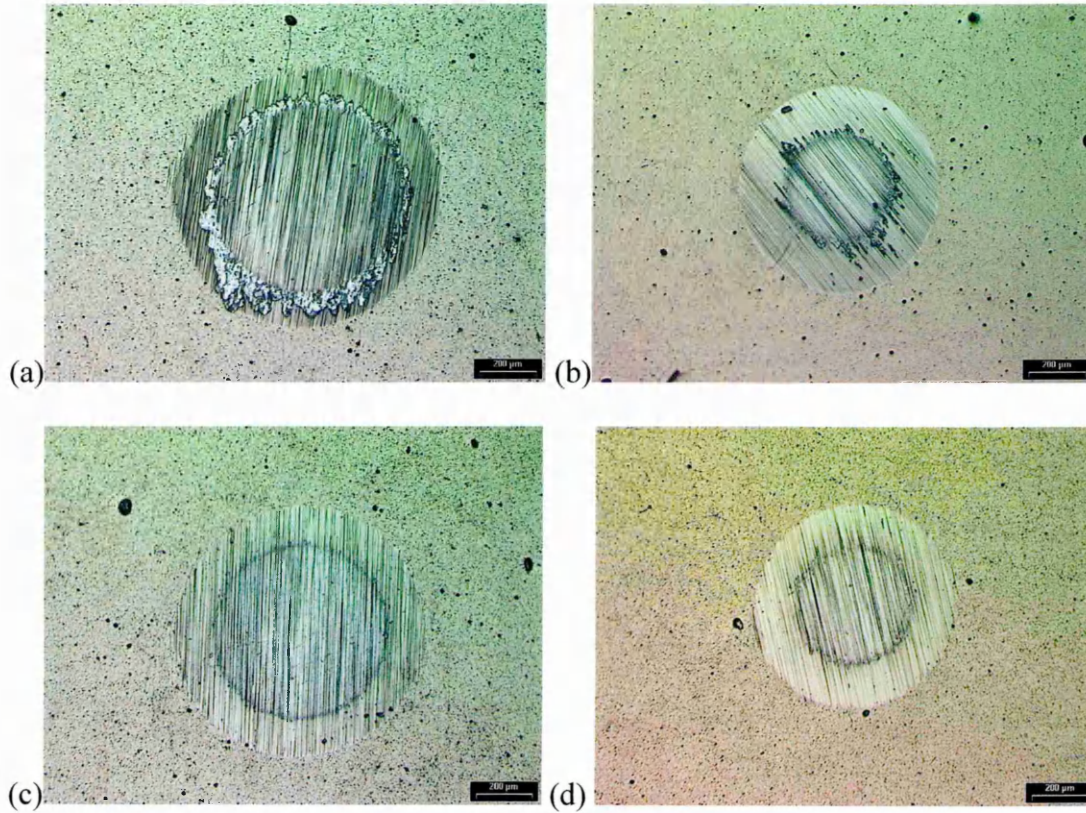


**Figure 4.16.** Ball craters on (a) –75V trial\_1, (b) –95V trial\_1, (c) –75V trial\_2, (d) –95V trial\_2 samples.

It is expected that with increasing bias voltage, whilst maintaining the same deposition time, the layer thickness  $d_L$  of the superlattice coating should decrease due to the formation of thinner monolayers resulting from a greater resputtering rate. This behaviour was shown by the layer thickness measurements obtained with the ball cratering method, shown in Table 4.8. However, it has to be mentioned that this measuring method provides less accuracy when compared to cross-sectional measurement of the layer thickness using an SEM.

**Table 4.8** . Layer thickness of CrN/NbN coatings deposited at 250°C.

Sample	Layer Thickness $d_L$ ( $\mu\text{m}$ )	
	-75V Bias	-95VBias
Trial_1	$3.5 \pm 0.2$	$3.3 \pm 0.2$
Trial_2	$3.5 \pm 0.2$	$3.0 \pm 0.1$

#### 4.5 Microhardness

The hardness, shown in Table 4.9, was measured using a 25g static load Knoop diamond indentation. As expected for trial\_1 the Knoop hardness significantly increased with a higher bias voltage (compare  $2542H_k$  for -75V bias and  $2823H_k$  for -95V bias), which also relates favourably to the calculated compressive stress exhibited by the samples. However in the case of the trial\_2 samples the hardness decreased as the bias voltage increased. The reason for this was thought to be due to problems during the deposition of the -95V bias sample and the formation of a poorly defined superlattice.

**Table 4.9**, Knoop Hardness of trial\_1 and trial\_2 samples

Sample	-75V Bias	-95V Bias	-75V Bias	-95V Bias
	Trial_1	Trial_1	Trial_2	Trial_2
Knoop Hardness, $H_k$	$2542 \pm 60$	$2823 \pm 70$	$2710 \pm 60$	$2488 \pm 40$

The plastic hardness, shown in Table 4.10, was measured with the Fischerscope, which also showed that the trend for trial\_1 that, with increasing bias voltage, the hardness also increases (as expected). The opposite however, was found to be the case for trial\_2.

**Table 4. 10.** Plastic hardness of trial\_1 and trial\_2

Sample	-75V Bias	-95V Bias	-75V Bias	-95V Bias
	Trial_1	Trial_1	Trial_2	Trial_2
Plastic Hardness, (GPa)	$51 \pm 2$	$70 \pm 3$	$49 \pm 2$	$38 \pm 2$

## 4.6 Adhesion

Previous investigations revealed that the phase composition of the base layer influences strongly the adhesion of CrN/NbN superlattice coatings. It was shown that the adhesion, measured by the scratch test, can be improved by a factor of two for coatings deposited on a single-phase CrN base layer ( $L_c=46\text{N}$ ), when compared with coatings having a two-phase base layer ( $L_c=24\text{N}$ ) containing a mixture of the brittle hexagonal  $\beta\text{-Cr}_2\text{N}$  phase and a fcc (NaCl) CrN phase [1], [46]. All of the trial samples in this study had a single-phase CrN base layer due to the chosen deposition parameters. The critical loads  $L_c$  obtained for the samples measured in the scratch test are shown in Table 4.11.

**Table 4.11.** Adhesion of CrN/NbN superlattices coatings deposited at  $250^\circ\text{C}$ .

Sample	Critical Load $L_c$ (N)
-75V Bias Trial_1	$38 \pm 1$
-95V Bias Trial_1	$43 \pm 2$
-75V Bias Trial_2	$46 \pm 2$
-95V Bias Trial_2	$38 \pm 1$

The  $-95\text{V}$  bias deposited coating (trial\_1) exhibited better adhesion properties ( $L_c=43\text{N}$ ) than the  $-75\text{V}$  bias deposited coating ( $L_c=38\text{N}$ ). A comparison between typical abrasive scratches for trial\_1 for coatings deposited at  $-75\text{V}$  and  $-95\text{V}$  bias are presented in figure 4.17. These showed less coating spallation for the  $-95\text{V}$  bias sample.

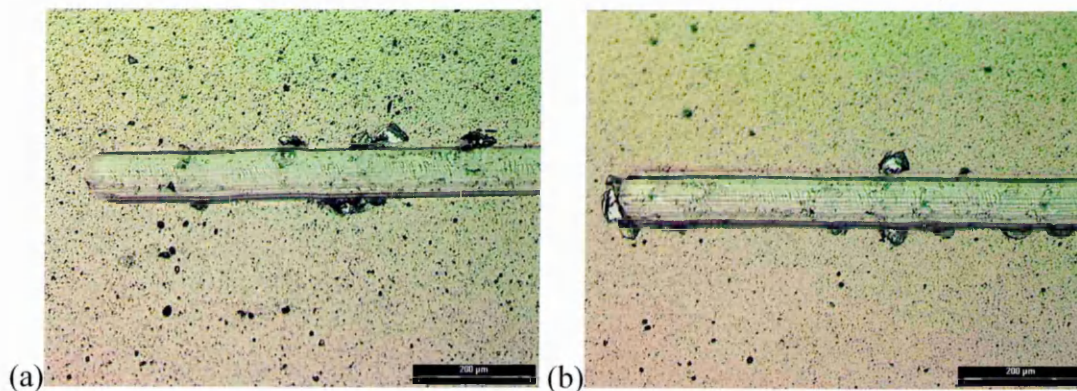


**Figure 4.17.** Scratches produced on the CrN/NbN superlattice coating: (a)  $-75\text{V}$  bias trial\_1, (b)  $-95\text{V}$  bias trial\_1.

The -75V bias deposited coating (trial\_2) exhibited the best adhesion properties of all the samples tested with a critical load value of  $L_c=46\text{N}$ . The -95V bias deposited coating (trial\_2) exhibited a lower critical load  $L_c=38\text{N}$ . The typical abrasion scratches for the trial\_2 samples are presented in figure 4.18, which showed greater amounts of spalling for the -95V bias sample.

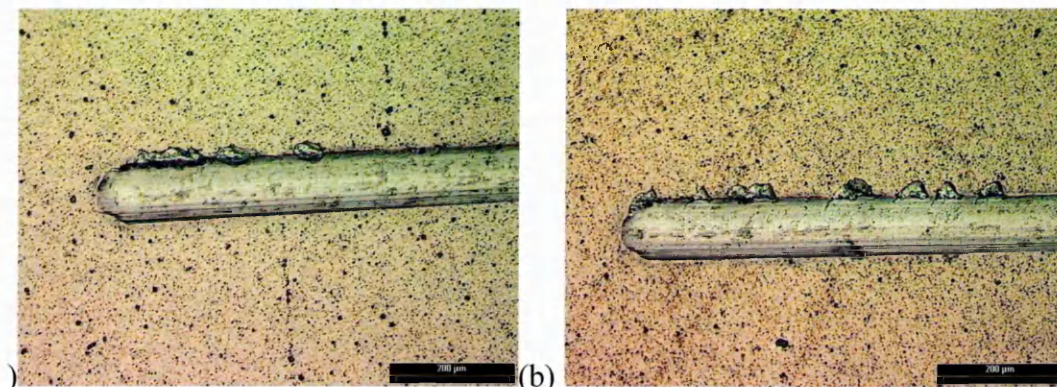


**Figure 4.18.** Scratches produced on the CrN/NbN superlattice coating (a) -75V sample trial\_2, (b) -95V bias trial\_2.

#### 4.7. Friction and sliding wear of CrN/NbN superlattices deposited at 250°C

The friction coefficient  $\mu$  was determined using a pin-on-disc measurement, which generated abrasive wear debris during the tests. This debris was not removed from the wear track and therefore acted as a third body abrasive medium. It was noted that green wear debris was observed on both the sample surface and in the wear track after the measurements. The composition of the wear debris was investigated by EDX analysis, X-ray photoelectron spectroscopy and Raman spectroscopy in previous studies [20]. It revealed that the wear product released during dry sliding comprised of a mixture of  $\text{Cr}_2\text{O}_3$ ,  $\text{CrNbO}_4$  and  $\text{Nb}_2\text{O}_5$  [20]. The formation of these oxides during the wear test is explained as a result of the high flash temperatures in the asperities, which can be magnified by high contact pressures and low thermal conductivity of the ceramic coatings.

A wear track produced on the -95V sample trial\_1 is shown in figure 4.19. An example of the measured transverse section of the wear track is given in the Appendix (see A2). The measured friction coefficients  $\mu$  and coefficients of sliding  $K_c$  of the samples of trial\_1 are shown in table 4.13.

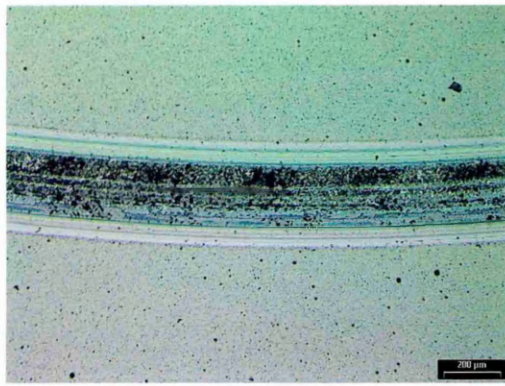


Figure 4.19. Wear track of the -95V sample trial\_1.

Table 4.12 Area of the transverse section.

Sample	Transverse section [ $\mu\text{m}^2$ ]	
	Taly surf	Laser profilometer
-75V	777	844
-95V	772	846

Table 4.13. Coefficient of friction and coefficient of sliding of the samples of trial\_1.

Sample	Coefficient of friction, $\mu$ (including debris)	Coefficient of sliding, $K_c * 10^{-15} [\text{m}^{-2} \text{N}^{-1}]$
-75V bias trial_1	0.57	3.89
-95V bias trial_1	0.58	3.86
-75V bias trial_2	1.0	4.82*
-95V bias trial_2	0.68	2.72*

The friction coefficient results presented in Table 4.13 were determined after 40000 laps. With regards to the trial\_1 samples, the measured friction coefficient was slightly higher for the -95V sample ( $\mu=0.58$ ) when compared with the -75V sample ( $\mu=0.57$ ). The increase in friction coefficient for coatings deposited at higher bias voltages has been reported previously [20], which was thought to be attributed to the higher residual stresses in these coatings that promotes a brittle failure mechanism. However, other factors also play a major part in determining the wear behaviour of these coatings, namely its microstructure (grain structure, density and texture, porosity, and interface structures), it is therefore difficult to directly relate the influence of residual stresses on the wear rate [5].

The measured friction coefficient for the -75V bias trial\_2 sample was shown to be very large ( $\mu=1.0$ ) in comparison with the rest of the results, whilst the -95V bias trial\_2 sample also gave a high friction coefficient of  $\mu=0.68$ . The unexpected large friction coefficient value obtained for the -75V bias trial\_2 was thought to be associated with unreliable data and it was therefore thought necessary to repeat the pin on disc test for these samples. In fact on the basis of grain structure, density,

porosity and texture, one would expect that the coating deposited at the higher bias voltage would exhibit a lower coefficient of friction because of the smoother surface, which is reflected in the surfaced roughness values, where the multilayers are more parallel with the surface [4]. There is also some evidence to suggest that more strongly texture multilayered coatings and in this case, coatings deposited at a bias voltage of  $-95$  V exhibit lower friction coefficients [54].

The measured area of the wear track obtained with the Talysurf was used for the calculation of the sliding wear coefficient. It has been revealed in former investigations that the sliding coefficient is proportional to the friction coefficient measured against the  $\text{Al}_2\text{O}_3$  counterpart [4]. Due to a lower measured value for the area of the transverse section of the wear track for the  $-95\text{V}$  bias coating resulting in a slightly smaller  $K_c$ -value, the area was also measured with the laser profilometer, see table 4.12. The sliding wear values obtained for the  $-75\text{V}$  bias and  $-95\text{V}$  bias (trial\_1) are very similar (see table 4.13) and hence, reflect the proportionality between  $\mu$  and  $K_c$ .

#### 4.8. Surface quality of CrN/NbN coatings deposited at $250^\circ\text{C}$

The average surface roughness measurements obtained for the samples are shown in Table 4.14. Examples of the full measured profile for each sample are also provided in the Appendix (A4). As expected the surface roughness of the coatings decreased with increasing bias voltage.

**Table 4.14** Surface roughness  $R_a$  of the CrN/NbN deposited at  $250^\circ\text{C}$ .

Sample	Surface Roughness $R_a$ ( $\mu\text{m}$ )
-75V Bias Trial_1	$0.079 \pm 0.008$
-95V Bias Trial_1	$0.051 \pm 0.007$
-75V Bias Trial_1	$0.051 \pm 0.007$
-95V Bias Trial_2	$0.039 \pm 0.007$

A smoother coating surface was observed in the images taken using an optical microscope for the samples deposited at  $-95\text{V}$  bias, see figures 4.20 (trial\_1) and figure 4.21 (trial\_2). The black marks indicate the presence of surface irregularities

such as growth defects. Qualitatively the number of growth defects appear to be less in the -95V bias samples.

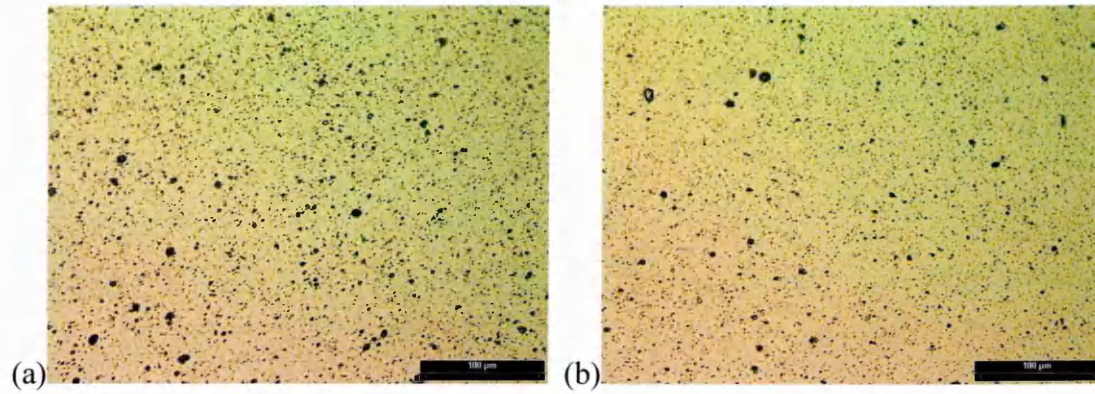


**Figure 4.20.** Images of the CrN/NbN coating surface (on HSS substrate) taken with an optical microscope: (a) -75V trial\_1, (b) -95V trial\_1.

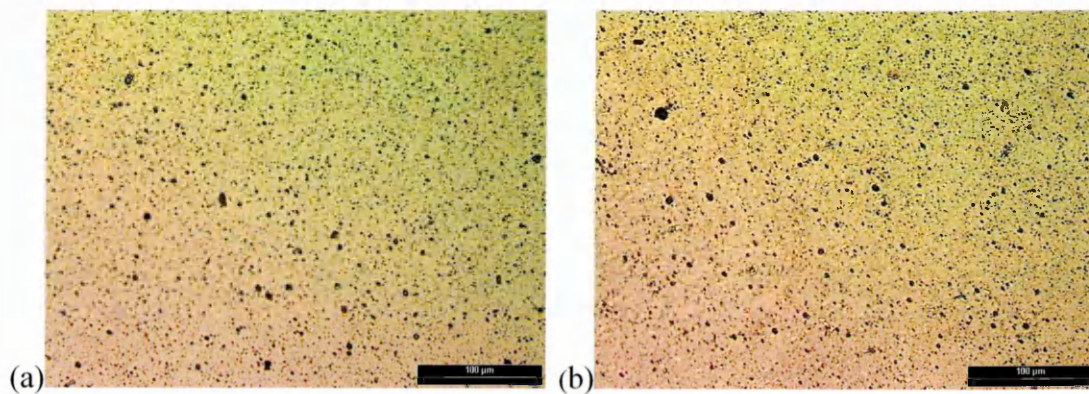


**Figure 4.21.** Images of the CrN/NbN coating surface (on HSS substrate) taken with an optical microscope: (a) -75V trial\_2, (b) -95V trial\_2.

The surface quality of the coatings can also be assessed using the ESEM, where typical images, taken at the same magnification, of the trial\_1 sample surfaces are shown in figure 4.22. As expected fewer growth defects in the coating deposited at higher bias voltage are seen. The majority of the growth defects were rather small ( $1\mu\text{m}$  or less) and spherical in shape, however larger growth defects were also apparent.

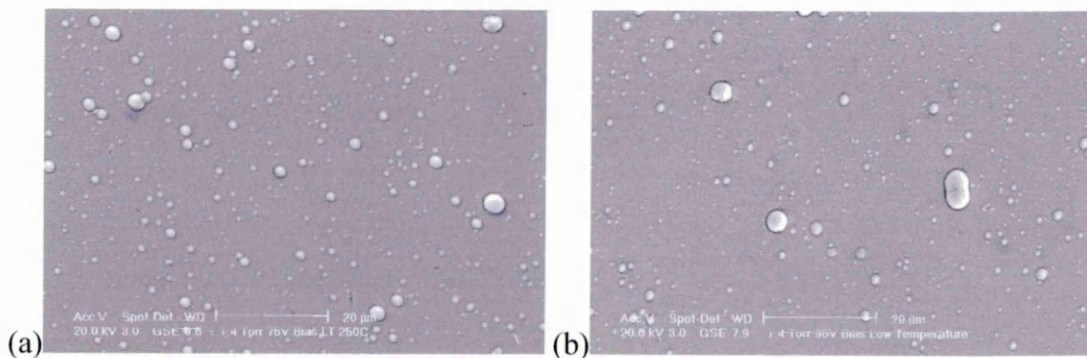


**Figure 4.22.** ESEM images of the samples' surfaces (a) -75V trial\_1, (b) -95V trial\_1.

The qualitative assessment of the number of growth defects present in the surface of each sample is presented in table 4.15. This confirmed that the higher bias samples contained fewer growth defects from the examination over a total area of  $96000\mu\text{m}^2$ .

**Table 4.15** Assessment of the number of growth defects over total area  $96000\mu\text{m}^2$

Sample	Number of Growth Defects
-75V Bias Trial_1	2448
-95V Bias Trial_1	1826
-75V Bias Trial_2	2328
-95V Bias Trial_2	1716

The presence of fewer growth defects deposited at higher bias voltages is due to a combination of higher residual stress and ad-atom mobility. Due to higher residual stresses growth defects may even be annihilated if the bias voltage used was high enough. As a result of this, the higher stressed coatings have fewer surface perturbations.

Increasing the bias voltage also produced a finer, more-dense coating, as shown by the columnar grain structures in figure 4.23 (for trial\_1) and figure 4.24 (for trial\_2). This is also supported by the surface roughness measurements which produced lower  $R_a$  values for the -95V bias samples. The decrease in coating roughness can, therefore, be attributed to both the smoothing of surface coating with increasing bias voltage and the presence of fewer growth defects both of which result from increased ion bombardment.

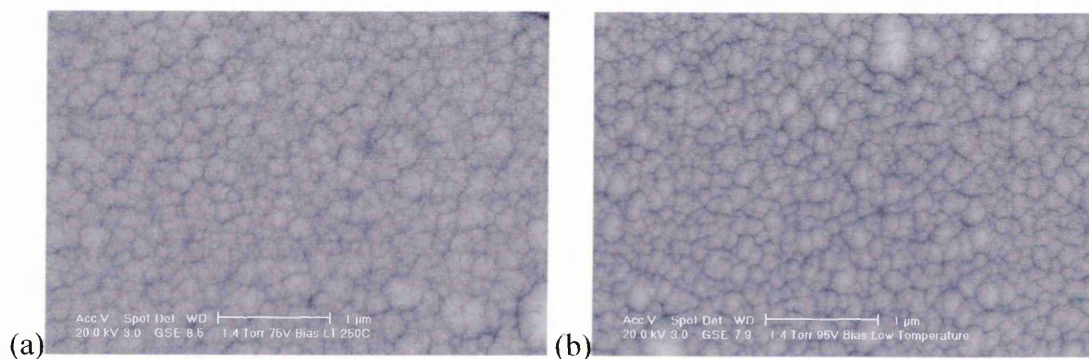


**Figure 4.23.** ESEM image of the samples' surfaces (a) -75V trial\_1, (b) -95V trial\_1.

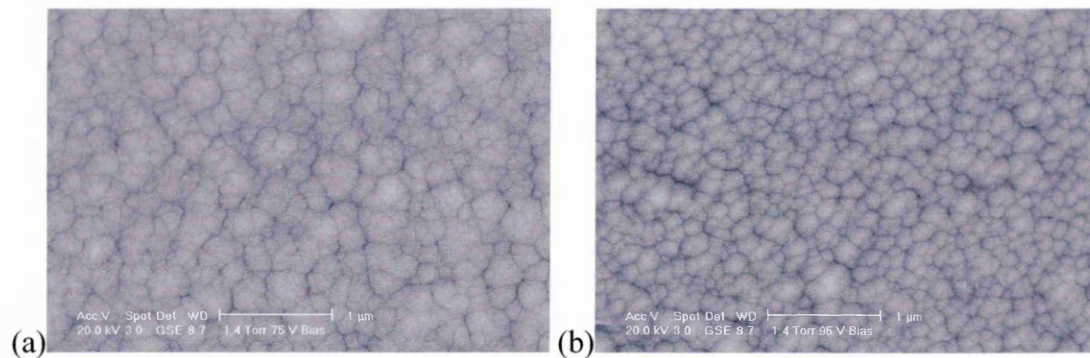


**Figure 4.24.** ESEM image of the samples' surfaces (a)  $-75\text{V}$  trial\_2, (b)  $-95\text{V}$  trial\_2.

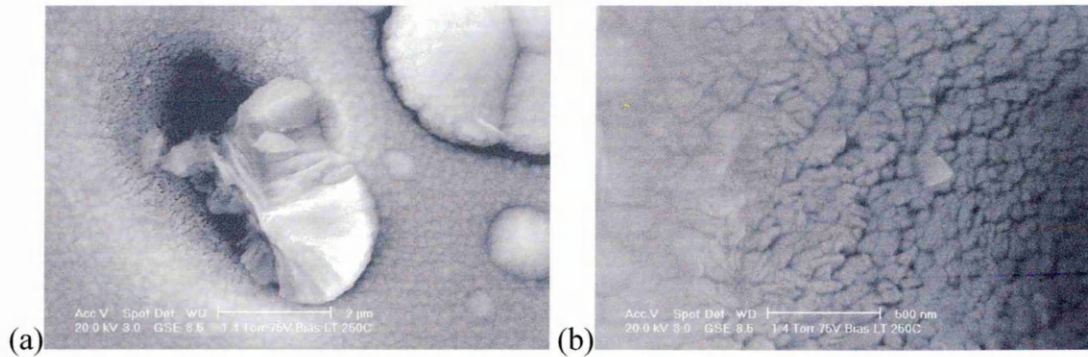
The growth defects are a result of droplets, which were formed during the metal-ion etching step to pre-treat the samples. During the subsequent deposition of the coating growth defects are generated on top of the droplets. These growth defects usually grow during further deposition process until they protrude from the top of the coating. Some growth defects, however, can be buried under the coating due to high compressive stresses. This has been shown to be the case with Cr etched samples, where there are very small droplets, which are known to be buried [33]. The ESEM image, shown in figure 4.25, shows a typical growth defect (approximately  $3\mu\text{m}$  in size) protruding from the coating surface, which is oval in shape. An interfacial boundary can be clearly observed between the growth defect and the coating, which creates a spherical crevice.



**Figure 4.25.** Growth defect in the CrN/NbN coating of the  $-75\text{V}$  trial\_1 sample.

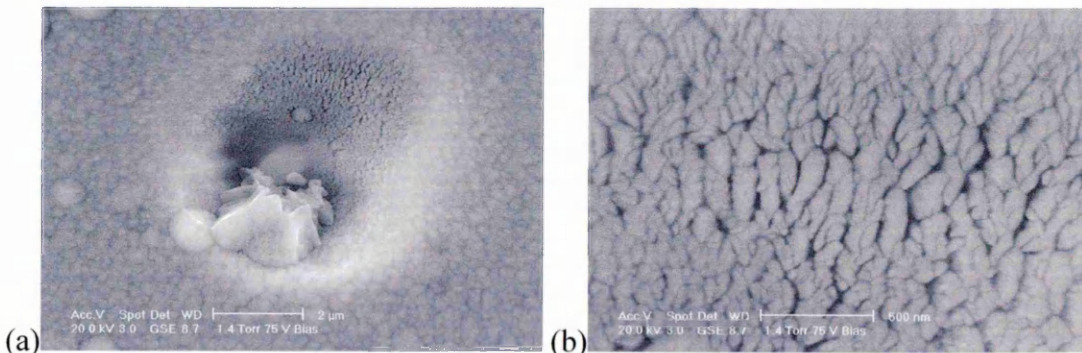
Some growth defects were found to be fractured, which was thought to be due to the effect of residual stresses, as shown in figure 4.26a. These fractured defects exhibited dense columnar grains extending in a 'feather-like' pattern growing from a central core. It also revealed that at the base of the defect under-dense regions of the coating were apparent. The under-dense region is characterised by an open grain structure, see figure 4.26b, which is now the exposed as the coating surface underneath the defect. The formation of the underdense region is attributed to "shadowing" effects during ion bombardment, where coatings are deposited under

different intensities of ion bombardment [36]. The top of the defect grows in a regime of intense ion bombardment, whilst the lower defect region is in a less intense ion bombardment due to shadowing from the droplet. These growth defects can, therefore, act as possible initiation sites for corrosion. This is because the underdense, porous coating provides solution pathways for corrosion media to react with the substrate material.



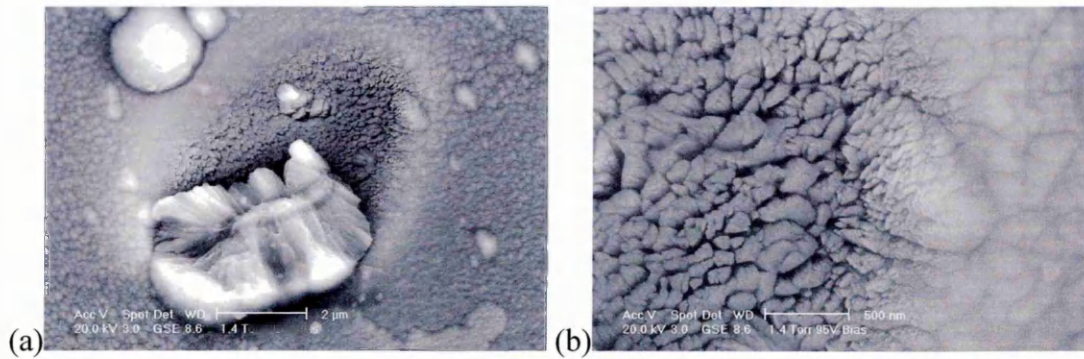
**Figure 4.26.** ESEM image of (a) a broken growth defect and (b) the interface coating /growth defect.

Further examples of typical fractured growth defects found for both samples are shown in figures 4.27 to 4.29. Figure 4.27a shows a fractured growth defect with the majority of defect being actually expelled from the surface leaving behind a dimple in the coating. The underlying coating was shown (Fig 4.27b) to be underdense with an open (porous) grain microstructure.



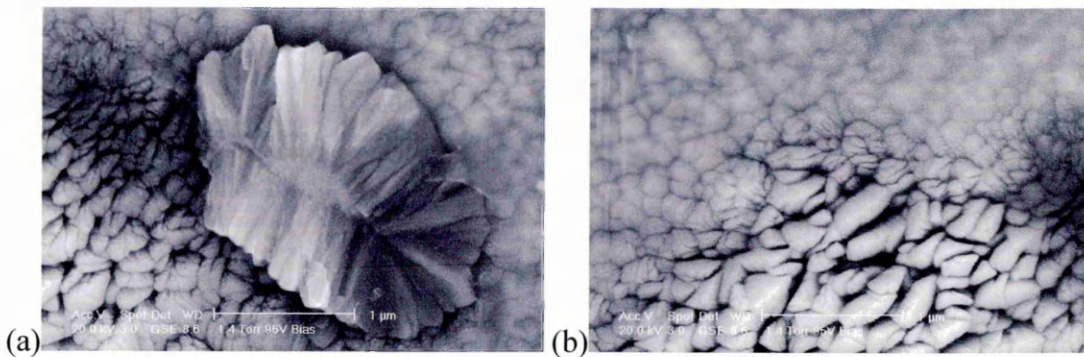
**Figure 4.27.** ESEM image of the -75V trial\_2 sample of (a) a broken growth defect and (b) open grain structure in the hole.

Figure 4.28a shows a fractured growth defect exhibiting dense feathery columnar grains extending from its centre. The discrete interface boundary between the growth defects and the coating can be seen. The underlying porous coating microstructure can also be clearly observed, whereby another smaller growth defect is associated with it, see figure 4.28b.



**Figure 4.28.** ESEM image of the  $-95\text{V}$  trial\_2 sample of (a) a fractured growth defect and (b) open grain structure underlying region containing another growth defect.

The columnar grains structure for another fractured growth defect is shown in figure 4.29a and the change in the grain density at the underlying coating region is shown in figure 4.29b.



**Figure 4.29.** ESEM image of the  $-95\text{V}$  trial\_2 sample of (a) a fractured growth defect showing the columnar grains and (b) underlying open grained structure in the coating.

## 4.9 Corrosion

### 4.9.1 Corrosion behaviour of CrN/NbN coatings of trial\_1

The potentiodynamic polarisation curves for the -75V bias and -95V bias CrN/NbN superlattice coatings deposited at 250°C together with that for a polished uncoated SS substrate are shown in figure 4.30.

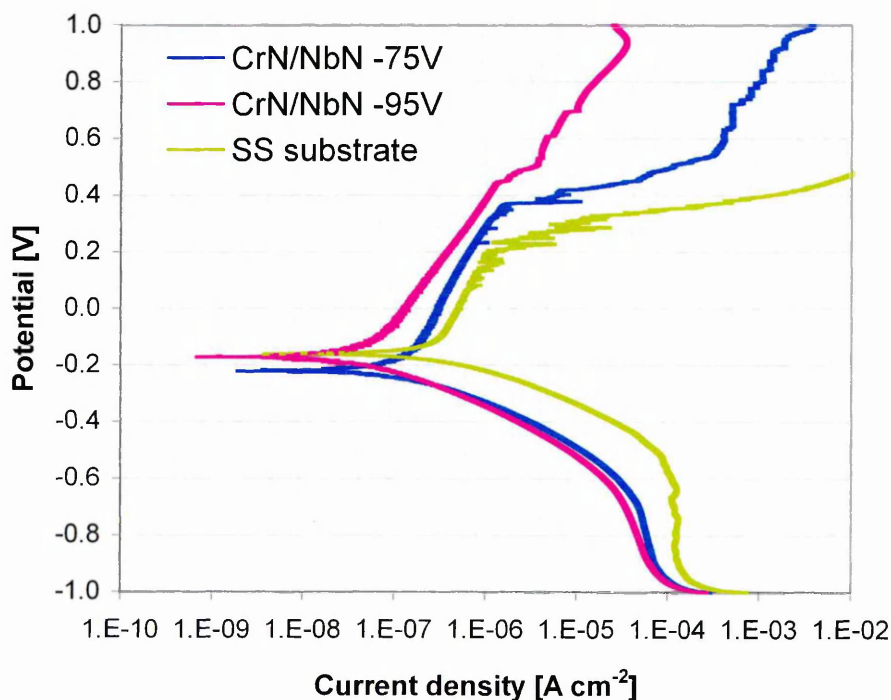


**Figure 4.30** Potentiodynamic polarisation curves of CrN/NbN coatings and a polished SS substrate.

The CrN/NbN superlattice coatings exhibited both lower corrosion current densities and higher pitting potentials than the uncoated 304 SS sample. This indicates that enhanced corrosion resistance in 3%NaCl solution has been achieved by the low temperature deposition of CrN/NbN superlattice coatings onto SS substrates. Furthermore, the -95V bias deposited coating exhibited lower corrosion current density and higher pitting potential than the coating deposited at -75V bias. The increase in bias voltage was also shown to improve the corrosion resistance of the deposited coating onto the SS substrate. The increase in bias voltage results in denser coatings with fewer voids and pores. Denser coatings are conducive to better corrosion resistance, because there are fewer pathways for corrosive media to penetrate the coating and reach the substrate surface. It is also known that increasing the bias voltage will decrease the number of growth defects protruding from the coating surface [20]. These defects are known to act as potential sites for localised

Chapter 4 Results and Discussion

crevice and pitting corrosion [1], [34] and therefore a reduction in their number will decrease the potential for corrosion to occur at these sites. The combination of denser microstructures and fewer growth defects in higher bias deposited superlattice coatings therefore indicates that better corrosion resistance is provided.

It has been shown in previous studies [20] that similar CrN/NbN coatings deposited at higher temperatures exhibited better corrosion resistance than the coatings deposited at lower temperatures. A typical corrosion current density of  $3$  to  $5 \times 10^{-7}$  A  $\text{cm}^{-1}$  with a pitting potential of  $370$  mV has been obtained for  $-75$ V bias CrN/NbN coatings deposited at higher temperatures. It is known that higher deposition temperatures also result in denser coatings with fewer voids and pores because of increased ad-atom mobility, which therefore enhances corrosion resistance.

In both low and high temperature CrN/NbN coating deposition at higher bias voltages the presence of fewer voids and pores result in better corrosion resistance despite having higher residual stresses within the coatings. Previous studies [46] have indicated that, in coatings with high residual stresses, areas adjacent to the growth defects are subject to microcracking or pits, which can grow as microscopic cracks in the coating. These cracks can be restricted in their propagation by the layer interfaces in the superlattice providing a crack deflection mechanism, which together with the single-phase CrN base layer contributes towards enhanced corrosion resistance. It would appear however, that the beneficial effects of increases in bias voltage more than offsets the deleterious effects of increased residual stresses resulting from increases in bias voltage. It is also thought that texture effects may also play a part in the corrosion resistant performance of the superlattice coatings.

The ESEM was used to examine the coating surfaces after the potentiodynamic polarisation measurements for evidence of corrosion. In the ESEM images particles of cubic morphology on the corroded samples are sodium chloride crystals from the 3% salt solution, which was not washed off.

ESEM examination of the corroded -75V bias Trial\_1 sample surface, showed that a series of pits had been formed as a result of selective corrosion at growth defects sites (see fig 4.31a and b). These pits are associated with the exposure of the under dense regions beneath the expelled growth defects to the corrosive species (see fig 4.32). Selective corrosion can commence at these under dense regions, as they provide pathways for the corrosive media to penetrate the coating and react with the substrate.

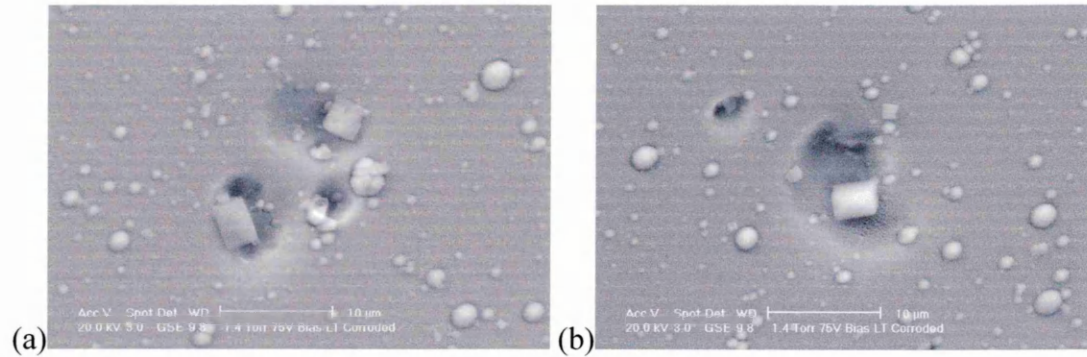


**Figure 4.31.** Growth defects pits initiation sites on the -75V trial\_1 sample's surface.

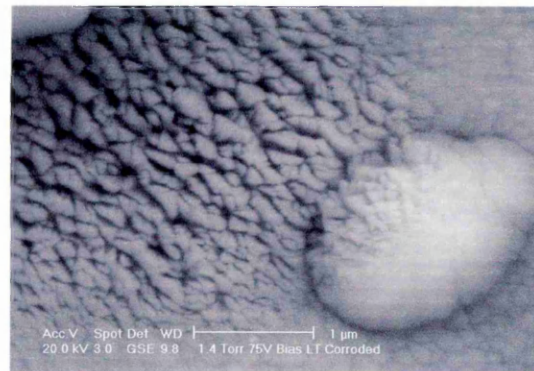


**Figure 4.32.** Under dense grain structure within pit

An ESEM image of a corrosion pit that had reached the substrate of the -75V bias trial\_1 sample is shown in figure 4.33. The resultant crater (dark) exhibited associated corrosive (iron based) products, which originated from the substrate. This is supported by EDX elemental distribution mapping of the pit (see figures 4.34a and b), which clearly shows that iron (Fe) from the substrate is associated with the pit. The evidence of microcracking suggests that the coating is starting to spall as corrosive media is interacting with the substrate. The lower intensity of the Fe K $\alpha$  x-rays shown in figure 4.34 (b) results from the shadowing of the X-rays produce within the pit.

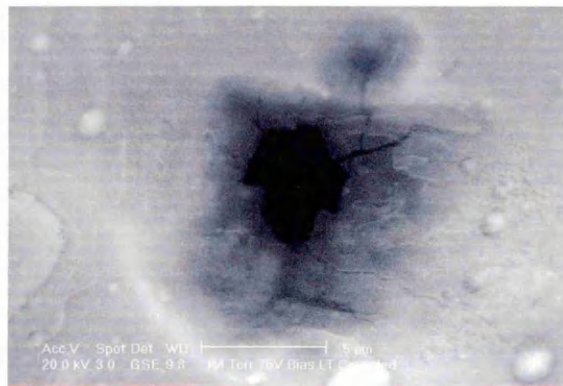


**Figure 4.33.** ESEM image of a corrosion pit of the -75V sample trial\_1.

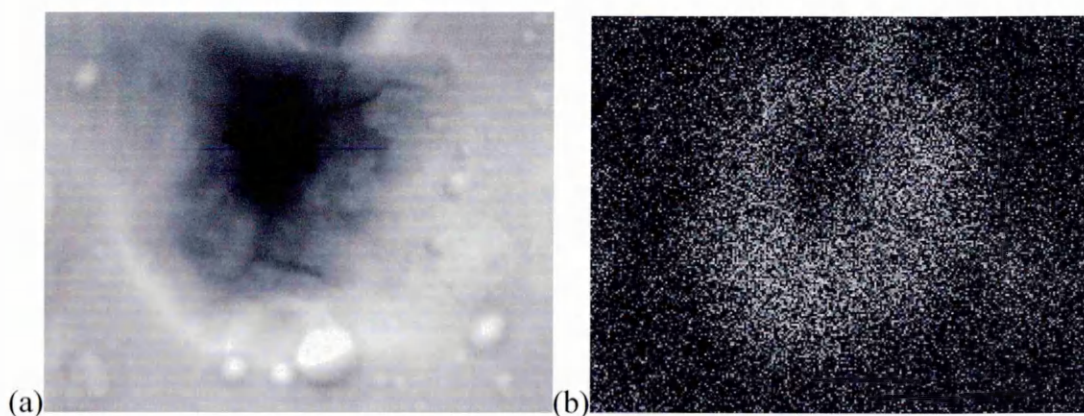


**Figure 4.34.** EDX elemental map of a corrosion site of the -75V sample trial\_1: (a) Secondary Electron (SE) image, (b) Fe distribution map.

The complete EDX distribution map for the selected elements of this corrosion site is provided in Appendix A6.

ESEM examination of the corroded -95V bias (trial\_1) surface also revealed similar corrosion pit initiation sites present at under dense regions associated with expelled growth defects (see figure 4.35).

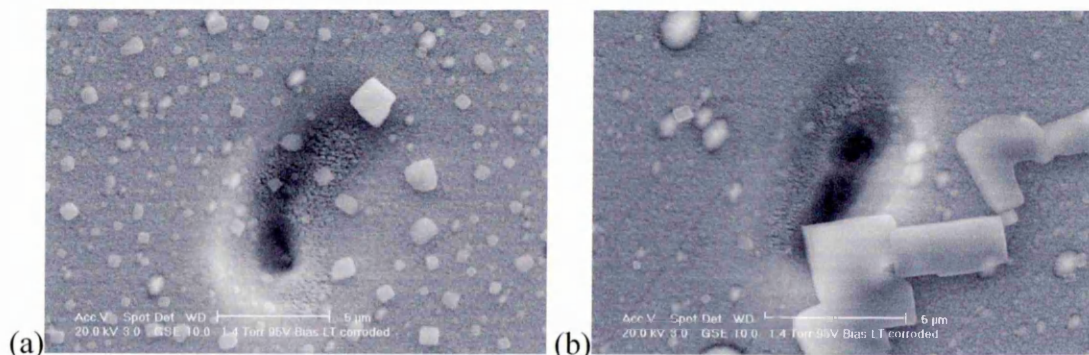


**Figure 4.35.** Pit initiation sites present at under dense regions in the at -95V bias trial\_1 sample

The under dense region and associated pitting is shown in figure 4.36. It was noted that it was more difficult to find any significant corrosion craters on the surface of the -95V bias (trial\_1) sample than that for the -75V bias (trial\_1) sample.



Fig 4.36. Under dense region and pit in -95V bias trial\_1 sample

#### 4.9.2 Corrosion behaviour of CrN/NbN coatings of trial\_2

The potentiodynamic polarisation curves of the trial\_2 coatings are shown in figure 4.37.

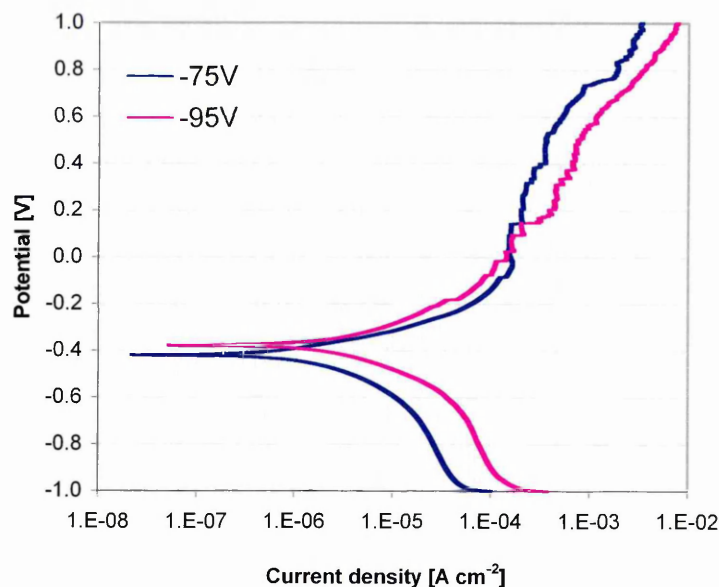


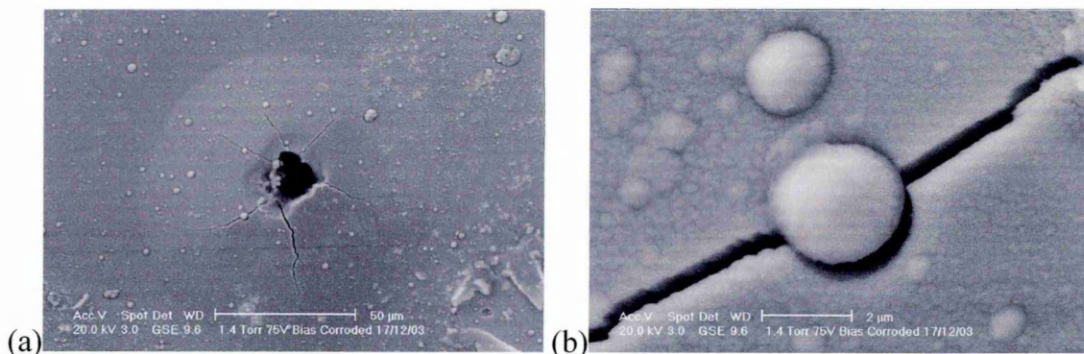
Figure 4.37. Potentiodynamic polarisation curves of CrN/NbN coatings trial\_2.

It's interesting to note that at the start of the anodic region (about -400mV) the -95V bias deposited coating exhibited a lower current density compared with the -75V bias sample. However, at a potential greater than 0.0mV the current density of the -95V sample remains almost constant and then becomes higher than for the -75V sample. This levelling out was thought to be due to the formation of a passive film

for the -95V sample, which is attributed to a denser coating. The denser coating is formed due to an increased ion bombardment at higher bias voltage.

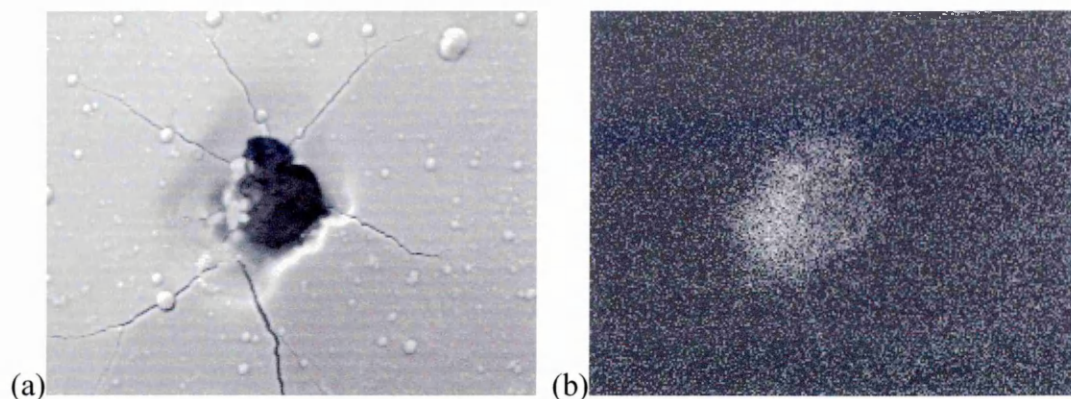
ESEM examination of these samples had found a number of regions of selective corrosion at growth defect sites, a few of which are discussed as follows:

Figure 4.38a shows an ESEM image of a corrosion pit on the -75V sample. The coating around this pit appears to be delaminating away from the substrate, which indicates adhesion problems as a result of corrosion attack along the coating/substrate interface. The delaminated coating also showed radial cracking originating from the pit, which will cause the coating to spall and break up. One of the cracks, shown in figure 4.38b had propagated around a growth defect and closer examination showed that the crack had propagated through the coating by an intergranular mode.



**Figure 4.38.** CrN/NbN coating surface of the -75V sample trial\_2: (a) corrosion pit with delaminated coating, (b) crack propagating around a growth defect.

An EDX elemental distribution map of this region, clearly showed the presence of Fe associated with the corrosion pit (see fig 4.39), which originated from the substrate. The complete elemental distribution map obtained for this pit is presented in the Appendix A7 (figure A7.1).



**Figure 4.39:** EDX analysis of a corrosion site of the  $-75\text{V}$  sample trial\_2 (a) SE image, (b) Fe distribution map.

Another type of corrosion pit found on the  $-75\text{V}$  bias trial\_2 sample is shown in figure 4.40. EDX elemental distribution maps for Fe, sodium (Na), Cr and Nb are shown in figure 4.41(a-d) respectively. These maps clearly show that Fe is associated with the pit and that both Cr and Nb intensities are reduced, which indicates that the corrosion of the substrate had occurred. The white particle in the corrosion pit was shown to be a salt crystal, as Na was present at this region. The complete EDX distribution map for this corrosion pit is shown in Appendix A7 (figure A7.2).

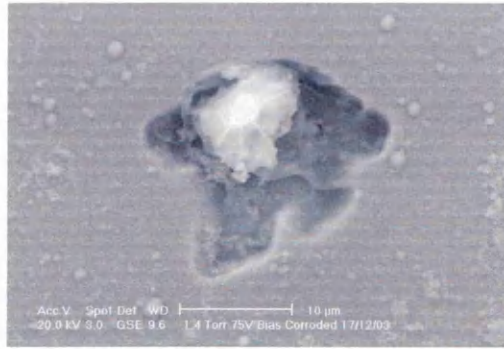


**Figure 4.40.** Corrosion pit in the CrN/NbN coating of the -75V sample trial\_2.

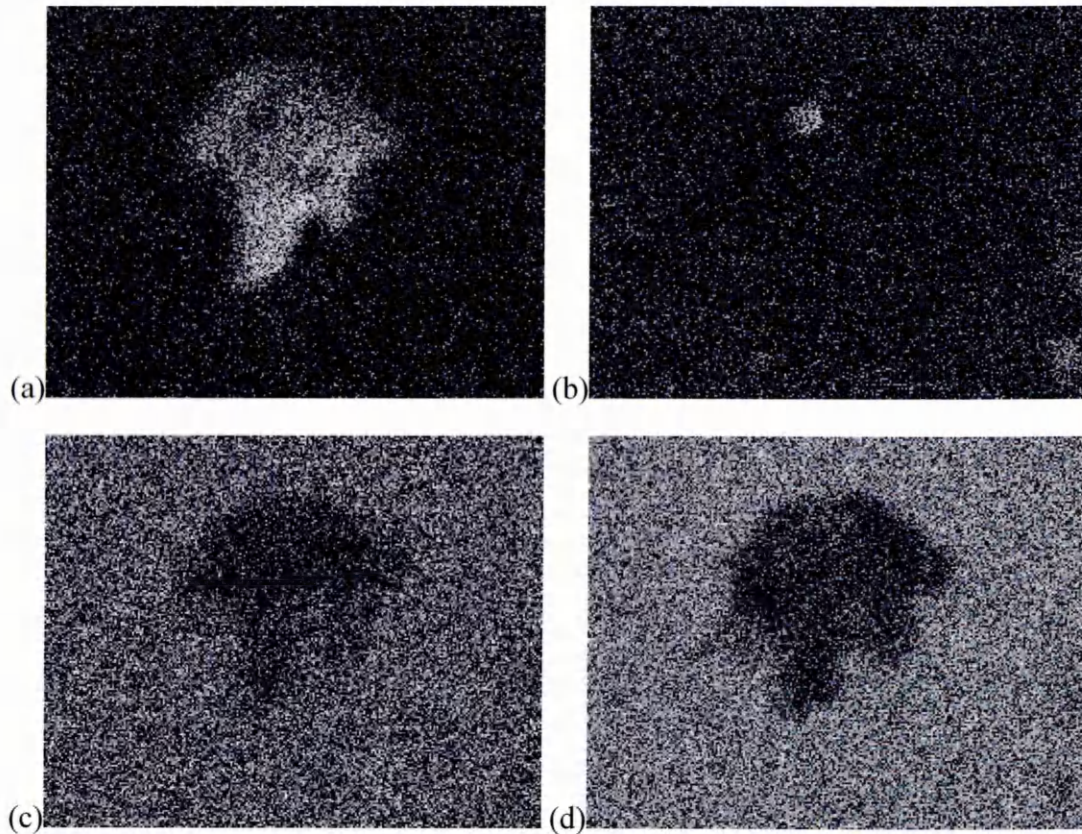


**Figure 4.41.** EDX analysis of the pit given in figure 4.57: (a) Fe distribution map (b) Na distribution map (c) Cr distribution map (d) Nb distribution map.

Yet again it was noted that it was more difficult to find any significant corrosion craters on the surface of the -95V bias (trial\_2) sample than that for the -75V bias (trial\_2) sample. However with the -95V bias several regions of severe corrosion effects were observed an example of which is as follows:

The corrosion site shown in figure 4.42 was in the order of 30 microns in size and clearly indicates that corrosion had occurred at an underdense region associated with growth defects. EDX elemental distribution mapping of this pit (see fig 4.43) confirmed that Fe was present resulting from corrosive media reaching the substrate. The complete EDX distribution map of this corrosion site is shown Appendix A7 (figure A7.3).

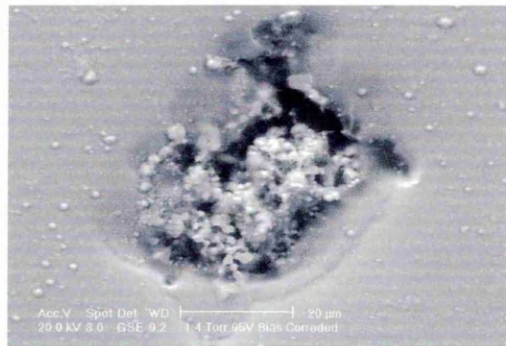


**Figure 4.42.** ESEM image of a corrosion pit in the -95V sample trial\_2

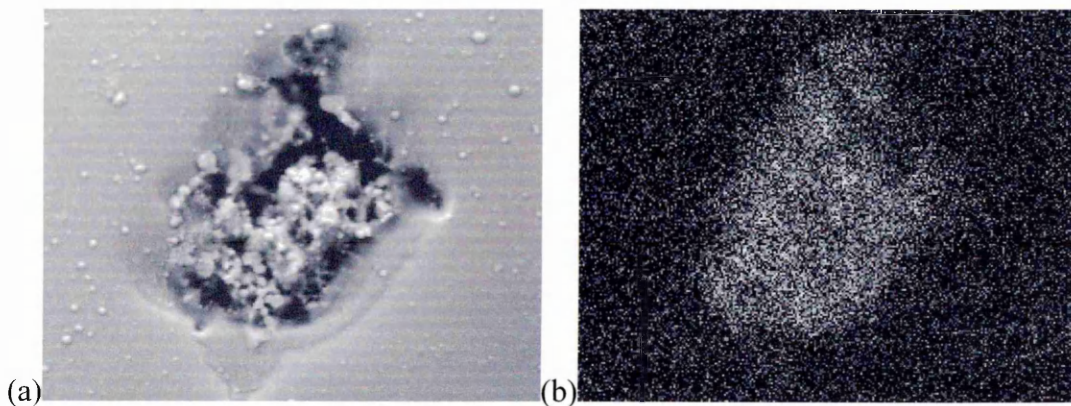


**Figure 4.43.** (a) ESEM image of corrosion pit. (b) Fe distribution map.

Very large corrosion sites (approximately 500 $\mu$ m in size) were found in the -95V bias trial\_2, which are shown in figures 4.44 and 4.45. The CrN/NbN superlattice coating was shown to be delaminating and breaking up into smaller splinters due to corrosive attack of the substrate. These images may provide an insight into how the corrosion progresses once an initial pit is created. The progressive corrosion of the underlying substrate will cause further delamination of the coating, which will break apart due to the residual stresses. Higher magnification images (fig 4.45) clearly shows the breakdown of the CrN/NbN superlattice coating into splinters and the underlying corrosion product. The volume changes (expansion) due to the formation of the corrosion product will contribute significantly to the loss of adhesion and spalling of the coating.

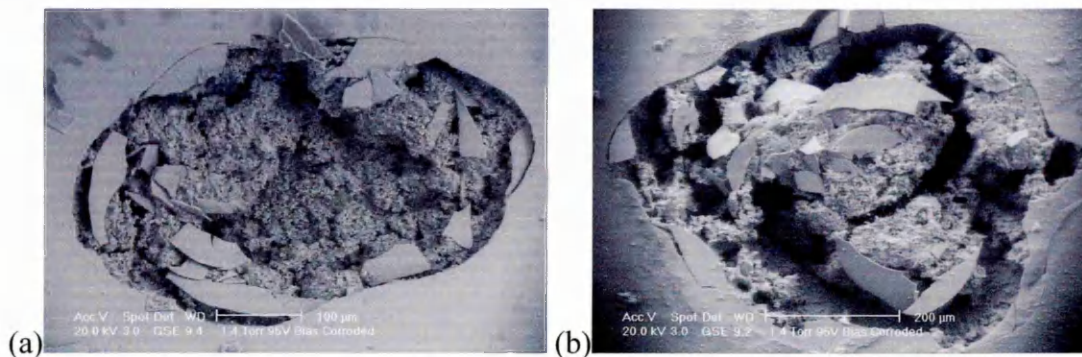


**Figure 4.44.** ESEM image of corrosion sites found on the CrN/NbN surface of the -95V sample trial\_2.

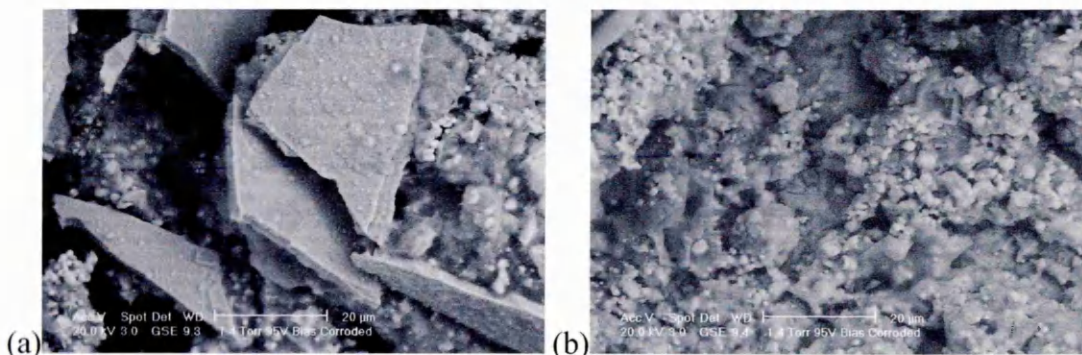


**Figure 4.45.** ESEM image of the -95V sample trial\_2: (a) splinters of the CrN/NbN coating, (b) corrosion product.

### 4.9.3 Comparison of the corrosion behaviour of CrN/NbN coatings deposited at 400°C

ESEM examination of CrN/NbN superlattice coatings deposited at 400°C found fewer corrosion sites than those for the low temperature deposited coatings. A corrosion site found on the -75V bias coating deposited at 400°C is shown in figure 4.46. Extensive corrosive media can be seen originating from a pit (Fig 4.47a), which at higher magnification (Fig 4.47b) was shown to be associated with an expelled growth defect site.

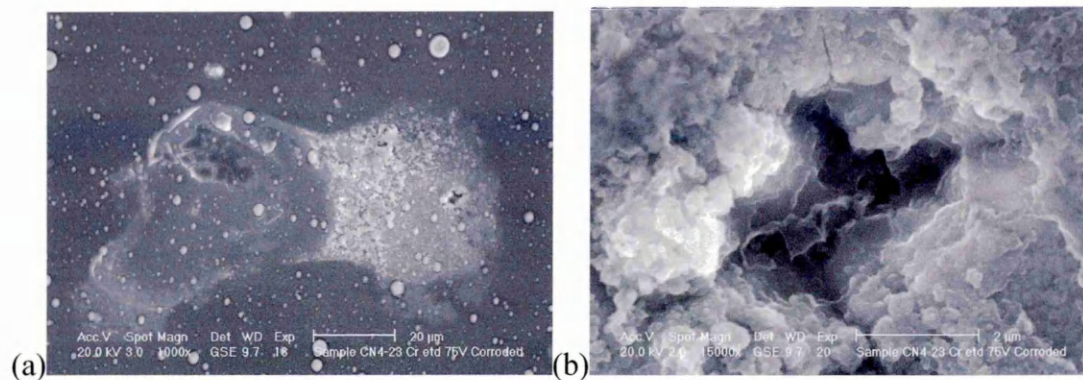


**Figure 4.46.** ESEM image of a corrosion site found on the CrN/NbN surface of the  $-75\text{V}$  bias coating deposited at  $400^\circ\text{C}$ .

ESEM examination of the  $-95\text{V}$  bias coating deposited at  $400^\circ\text{C}$  also showed a corrosion pit associated with an expelled growth defect (see figure 4.47a). At higher magnification (Figure 4.47b) the under dense coating associated with the base of the growth defect can be observed. Selective corrosion was observed at this site, which is confirmed in the EDX elemental distribution map shown in figure 4.48, whereby Fe from the substrate was present within the pit. The complete elemental distribution map is shown in Appendix A8.

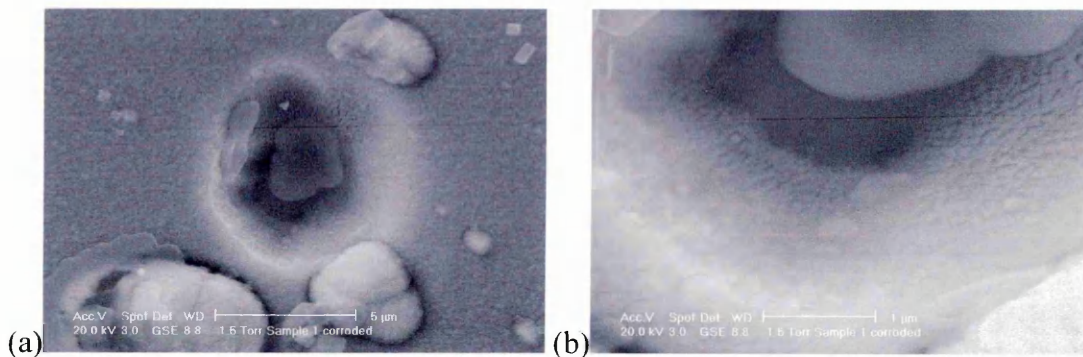


**Figure 4.47.** ESEM image of a corrosion pit in the  $-95\text{V}$  bias CrN/NbN coating deposited at  $400^\circ\text{C}$ : (a) corrosion pit associated with expelled growth defect (b) edge of pit with under dense grain structure.

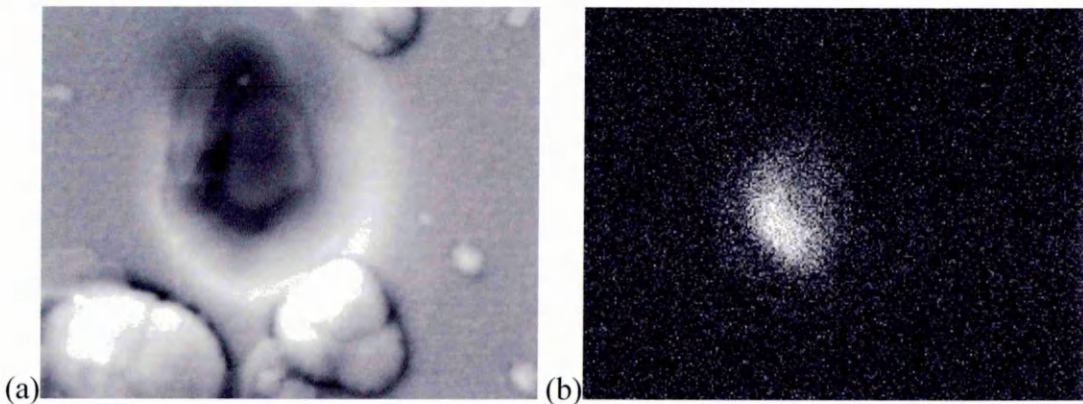


**Figure 4.48.** EDX distribution map of the corrosion pit: (a) SE image, (b) Fe intensity distribution map

There is therefore clear evidence from examination of the CrN/NbN superlattice deposited coatings at different bias voltages and deposition temperatures that the growth defects act as potential sites for both crevice and pitting corrosion. If the growth defect is expelled then the under dense porous coating becomes exposed and provides solution pathways for corrosive media to react with the substrate. It is well established that growth defects are created from droplets [33] [37], which are metal rich and nitrogen deficient and therefore anodic with respect to both the surrounding coating and substrate. This also contributes towards the corrosion behaviour, as the droplet will also corrode at the substrate/coating interface leaving a crater, resulting in direct contact with the metal surface. This creates a localised galvanic corrosion cell at the substrate surface (see figure 2.34). The corrosion mechanisms are therefore very complicated with regards to the deposition of PVD coatings that exhibit growth defects, where adjacent regions are less dense.

## 5 Summary and Conclusions

CrN/NbN superlattice coatings were successfully deposited at -75V bias and -95V bias onto 304 SS (and not as reliably onto HSS) substrates at a temperature of 250°C.

The CrN/NbN superlattice coatings deposited at low temperatures exhibited a preferred {111} texture (strain energy dominant). The higher bias (-95V) deposited coating had a stronger {111} texture with three fold symmetry. This compared with similar coatings deposited at 400°C, which exhibited a {100} texture (surface free energy dominant).

The low temperature deposited coatings exhibited compressive residual stresses, which as expected increased with increasing deposition bias voltage. These residual stresses were higher than those present in similar bias voltage coatings deposited at 400°C. The lower stresses obtained in the high temperature deposited coating is attributed to the temperature dependence on interstitial diffusion for stress relief.

Superlattice periods of 2.3nm were obtained for the low temperature coating deposition on SS. The presence of reasonably sharp and intense XRD peaks obtained suggests that distinct bi-layer boundaries exist within the superlattice coating. The formation of a distinct super lattice period resulted in Knoop Hardness values of 2542H<sub>k</sub> and 2823 H<sub>k</sub> together with plastic hardness values of 51GPa and 70GPa for the -75V bias and -95V bias deposited coatings respectively. The higher hardness values obtained for the higher bias voltage related to the increased compressive residual stress present due to intensified ion bombardment. The total layer thickness of the coatings was determined to be in the range of 3.0 to 3.5 μm as measured by the ball crater test

The low temperature deposited coatings exhibited good adhesion properties with critical load values ranging from 38N to 46N. The presence of a single phase CrN base layer for these may have helped provide the good adhesion properties.

The coefficients of friction (with debris) and sliding wear for both of the coatings deposited at different bias voltages onto SS were  $\sim 0.57$  and  $\sim 3.8 \times 10^{-15} \text{ m}^2 \text{ N}^{-1}$  respectively. These values were thought to be typical for this type of coating and are similar results to those obtained previously [1].

The surface quality of the coatings deposited at low temperature was assessed in which the surface roughness ( $R_a$ ) was shown to decrease with increasing deposition bias voltage. The smoother coating surfaces obtained for the higher bias voltages was due to the formation of a denser columnar grain structure and the presence of fewer growth defects.

The presence of growth defects originating from droplets deposited during the etching stage are cause for great concern. These growth defects are known to be highly stressed and during coating deposit will grow with their own discrete interfacial boundary with the rest of the coating. If the growth defect reaches the surface it will protrude from the coating and hence create a localised crevice effect. Microscopic examination had shown that severely under-dense porous regions exist within the coating in the lower region of the growth defects. The growth defect microstructure however, is composed of dense columnar grains extending in a “feather-like” pattern growing from a central core. It had been shown that crevice and pitting corrosion had taken place at selective growth defect sites. The under-dense porous coating in the lower region of the growth defect is a solution pathway to the substrate surface. This can create a complex mechanism for potential pitting corrosion to occur. Also the droplet at the base of the growth defect is anodic with respect to the coating resulting in localised galvanic corrosion at the coating substrate interface.

All of the CrN/NbN superlattice coatings deposited at  $250^\circ\text{C}$  had superior corrosion resistance than that of the 304 SS substrate. These coatings exhibited lower corrosion current densities and higher pitting potentials than did the 304 SS substrate. The corrosion resistance of the coatings was also shown to be superior at higher bias voltages, as both denser and fewer growth defects are present.

The corrosion resistance of similar coatings deposited at higher temperatures was in all cases superior to those deposited at lower temperatures.

It is clear from this study that the corrosion resistance of the CrN/NbN superlattice coatings is improved by having denser coatings with fewer growth defects. One obvious method of doing this is by deposition at even higher bias voltages, which is known to form denser coatings with fewer growth defects. However, consideration must also be taken with respect to the increase residual stresses to the coatings at these higher bias voltages, which may also influence the corrosion resistance.

It is also known that using an Nb etch instead of Cr etch will not only provide good adhesion properties, but will also increase the corrosion resistance at the substrate/coating interface [1].

Recent developments have been carried out in order to obtain droplet free CrN films using (HIPIMS) High Powered Pulsed Magnetron Sputtering PVD technique [55], [56]. The HIPIMS process allows high plasma density and ionised metal particle to be produced at low pressures and without macro particle generation. Hence the formation of growth defects from these particles is eliminated. Recent Studies had shown that deposited CrN films exhibited excellent adhesion, with high critical load values of 85N. The high-density plasma environment of the HIPIMS discharge resulted in a highly dense columnar microstructure, with no droplet or other macroscopic growth defects evident. It would therefore seem feasible that HIPIMS can be used in the deposition of dense, macroscopic growth defect free superlattice coatings.

## A Appendix

### A1 Deposition parameters

Table A1.1 Deposition parameters of trial\_1.

<b>1. Pump down and heating</b> $p = 5 \times 10^{-5}$ mbar $T = 120^\circ\text{C}$ 15% rotation	
<b>2. Target cleaning I</b> cathode power $4 \times 1$ kW $p = 2.1 \times 10^{-3}$ mbar Ar gas flow = 200 sccm 55% rotation $t = 2$ min	
<b>3. Target cleaning II</b> cathode power $4 \times 3$ kW $p = 2.1 \times 10^{-3}$ mbar Ar gas flow = 200 sccm 55% rotation $t = 2$ min	
<b>4. Cr<sup>+</sup> metal ion etching (cathode 3)</b> $U_B = -1100$ V $p = 1 \times 10^{-3}$ mbar Ar gas flow = 65 sccm power cathode 3 = 1.2 kW $T_{\text{max}} = 340^\circ\text{C}$ 55% rotation $t = 12$ min	
unbalancing coil current = 1.8A	unbalancing coil current = 1.6A
<b>5. Cooling</b> $T_{\text{final}} = 250^\circ\text{C}$ 55% rotation	
<b>6. CrN base layer deposition</b> $U_B = -75$ V $p = 3.9 \times 10^{-3}$ mbar gas flow $\text{N}_2 = 240$ sccm, gas flow Ar = 200 sccm cathode power Nb (1&4) = 0.5 kW cathode power Cr (2&3) = 5 kW unbalancing coil current (1-4) $I = 6$ A $T = 250^\circ\text{C}$ 55% rotation $t = 30$ min	
<b>7. CrN/NbN coating deposition</b>	
$U_B = -75$ V	$U_B = -95$ V
gas flow $\text{N}_2 = 100$ sccm, gas flow Ar = 200 sccm $p = 3.3 \times 10^{-3}$ mbar cathode power Nb (1&4) = 6 kW cathode power Cr (2&3) = 3 kW unbalancing coil current (1-4) $I = 4$ A 55% rotation $t = 150$ min	

Table A1.2 Deposition parameters of trial\_2.

<p><b>1. Pump down and heating</b>  <math>p = 5 \times 10^{-5}</math> mbar  <math>T = 120^\circ\text{C}</math>                      15% rotation</p>	
<p><b>2. Target cleaning I</b>                      cathode power 4x1kW  <math>p = 2.1 \times 10^{-3}</math> mbar                      Ar gas flow = 200sccm                      55% rotation  <math>t = 2</math> min</p>	
<p><b>3. Target cleaning II</b>                      cathode power 4x3kW  <math>p = 2.1 \times 10^{-3}</math> mbar                      Ar gas flow = 200sccm                      55% rotation  <math>t = 2</math> min</p>	
<p><b>4. Cr<sup>+</sup> metal ion etching (cathode 3)</b>  <math>U_B = -1100</math> V  <math>p = 1 \times 10^{-3}</math> mbar                      Ar gas flow = 65sccm                      power cathode 3 = 1.2kW (current controlled mode I = 100A)                      unbalancing coil current = 0.8A  <math>T_{\text{max}} = 340^\circ\text{C}</math>                      55% rotation  <math>t = 12</math> min</p>	
<p><b>5. Cooling</b>  <math>T_{\text{final}} = 250^\circ\text{C}</math>                      55% rotation</p>	
<p><b>6. CrN base layer deposition</b>  <math>U_B = -75</math> V                      cathode power Nb (1 &amp; 4) = 0.5kW                      cathode power Cr (2 &amp; 3) = 5kW                      unbalancing coil current (1-4) I = 6A                      55% rotation  <math>t = 30</math> min</p>	
<p><math>p = 3.9 \times 10^{-3}</math> mbar                      gas flow N<sub>2</sub> = 240sccm,                      gas flow Ar = 200sccm</p>	<p><math>p = 3.9 \times 10^{-3}</math> mbar                      gas flow N<sub>2</sub> = 230sccm,                      gas flow Ar = 200sccm</p>
<p><b>7. CrN/NbN coating deposition</b></p>	
<p><math>U_B = -75</math> V                      gas flow N<sub>2</sub> = 108sccm                      gas flow Ar = 200sccm</p>	<p><math>U_B = -95</math> V                      gas flow N<sub>2</sub> = 104sccm                      gas flow Ar = 200sccm</p>
<p><math>p = 3.9 \times 10^{-3}</math> mbar                      cathode power Nb (1 &amp; 4) = 6kW                      cathode power Cr (2 &amp; 3) = 3kW                      unbalancing coil current (1-4) I = 4A                      55% rotation  <math>t = 150</math> min</p>	

## A2 Pin on disc measurement and wear track of trial\_1

### Tribo parameters

Acquisition	Sample	Static Partner	Environment
Radius : 8.00 [mm]	-Coating : CrNNbN LT -75V	Coating : Al <sub>2</sub> O <sub>3</sub>	Temperature : 29.00 [°C]
Lin. Speed : 10.00 [cm/s]	-Substrate : HSS	-Cleaning : no	Atmosphere : air
Normal load : 5.00 [N]	-Cleaning : as deposited	-Dimension : 6.00 [mm]	Humidity : 21.00 [%]
Stop condition : 40000 [laps]		-Geometry : Ball	
Acquisition rate : 1 [Hz]			

Sample	Static Partner	Calculations
Worn Track Section : 777.0 um <sup>2</sup>	Worn Cap Diameter : 0.0 um	Sample Wear Rate : 0.000 mm <sup>3</sup> /N/m
Young's Modulus : 0.0 GPa	Young's Modulus : 0.0 GPa	Static Part. Wear Rate : 0.000 mm <sup>3</sup> /N/m
Poisson Coef. : 0.000	Poisson Coef. : 0.000	Max Herzian Stress : 0.000 GPa

### Curve

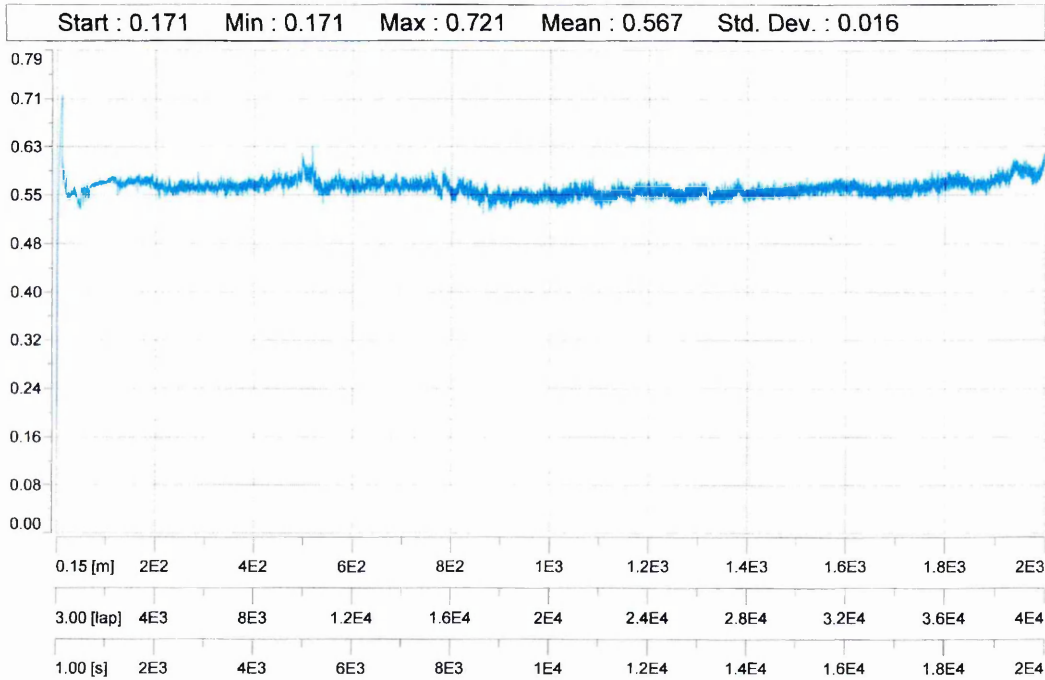


Figure A2.1. Pin on disc measurement of the -75V sample trial\_1.

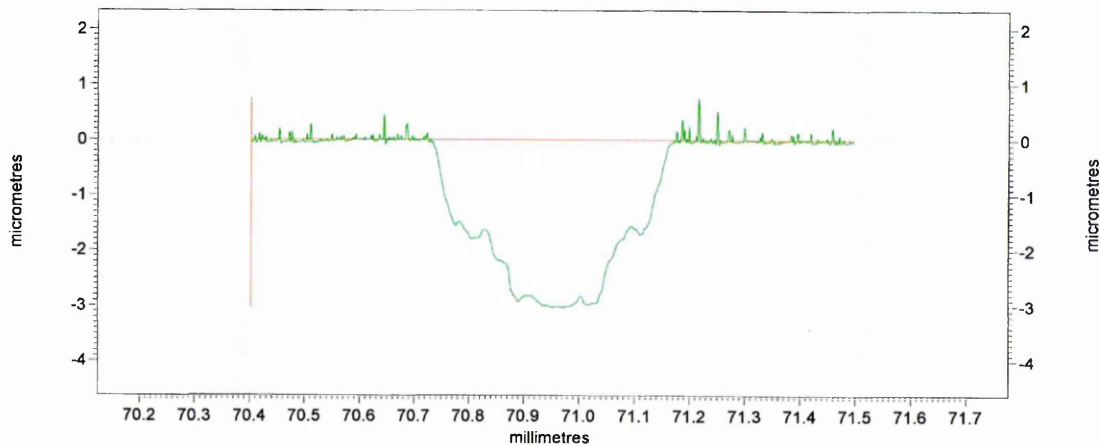


Figure A2.2. Profile of the produced wear track on the -75V sample trial\_1.

**Tribo parameters**

Acquisition	Sample	Static Partner	Environment
Radius : 10.00 [mm]	-Coating : CrNNbN LT -95V	Coating : Al2O3	Temperature : 28.00 [°C]
Lin. Speed : 10.00 [cm/s]	-Substrate : HSS	-Cleaning : no	Atmosphere : air
Normal load : 5.00 [N]	-Cleaning : as deposited	-Dimension : 6.00 [mm]	Humidity : 21.00 [%]
Stop condition : 40000 [laps]		-Geometry : Ball	
Acquisition rate : 1 [Hz]			

Sample	Static Partner	Calculations
Worn Track Section : 772.0 um2	Worn Cap Diameter : 0.0 um	Sample Wear Rate : 0.000 mm3/N/m
Young's Modulus : 0.0 GPa	Young's Modulus : 0.0 GPa	Static Part. Wear Rate : 0.000 mm3/N/m
Poisson Coef. : 0.000	Poisson Coef. : 0.000	Max Herzian Stress : 0.000 GPa

**Curve**

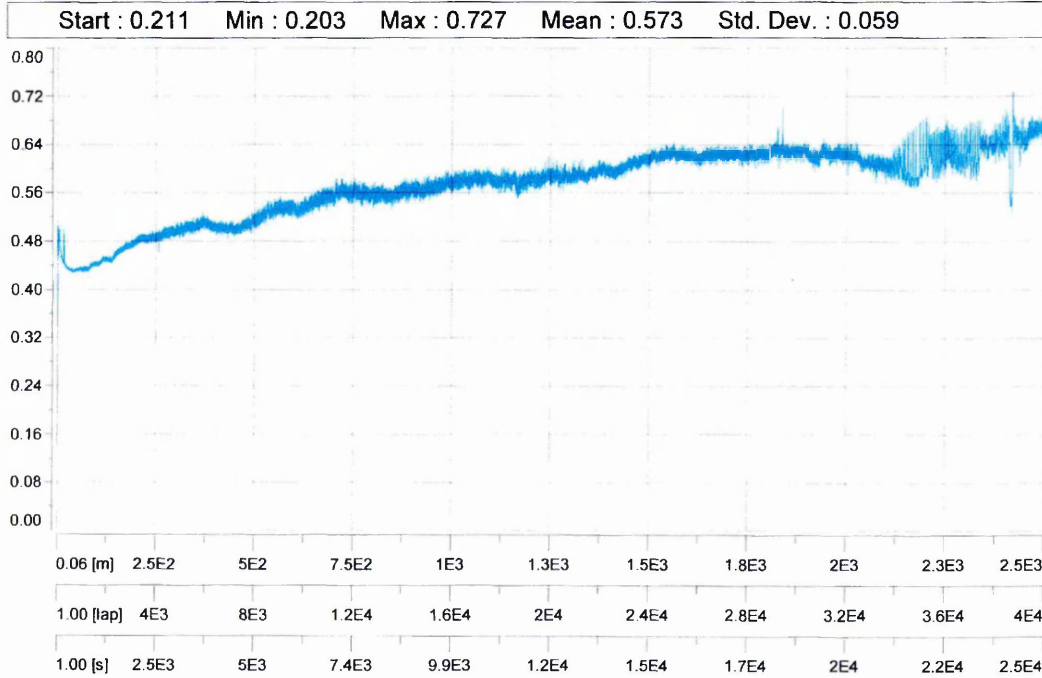


**Figure A2.3.** Pin on disc measurement of the -95V sample trial\_1.

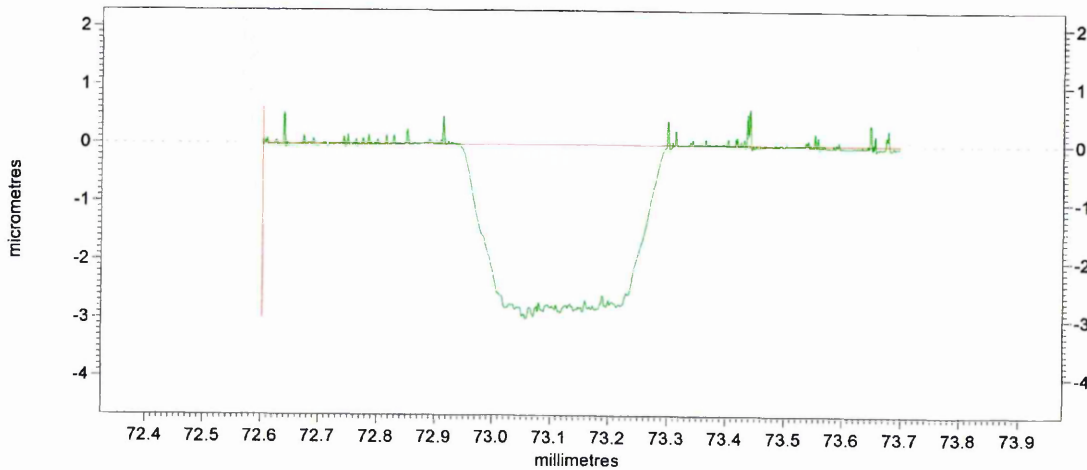


**Figure A2.4.** Profile of the produced wear track on the -95V sample trial\_1.

### A3 Pin on disc measurement and wear track of trial\_2

#### Tribo parameters

Acquisition	Sample	Static Partner	Environement
Radius : 8.00 [mm] Lin. Speed : 10.00 [cm/s] Normal load : 5.00 [N] Stop condition : 20000 [laps] Acquisition rate : 1 [Hz]	-Coating : CrN/NbN -Substrate : HSS	-Coating : Al2O3 -Cleaning : no -Dimension : 6.00 [mm] -Geometry : Ball	Temperature : 23.00 [°C] Atmosphere : air Humidity : 21.00 [%]

Sample	Static Partner	Calculations
Worn Track Section : 482.0 um2 Young's Modulus : 0.0 GPa Poisson Coef. : 0.000	Worn Cap Diameter : 0.0 um Young's Modulus : 0.0 GPa Poisson Coef. : 0.000	Sample Wear Rate : 0.000 mm3/N/m Static Part. Wear Rate : 0.000 mm3/N/m Max Herzian Stress : 0.000 GPa

#### Curve

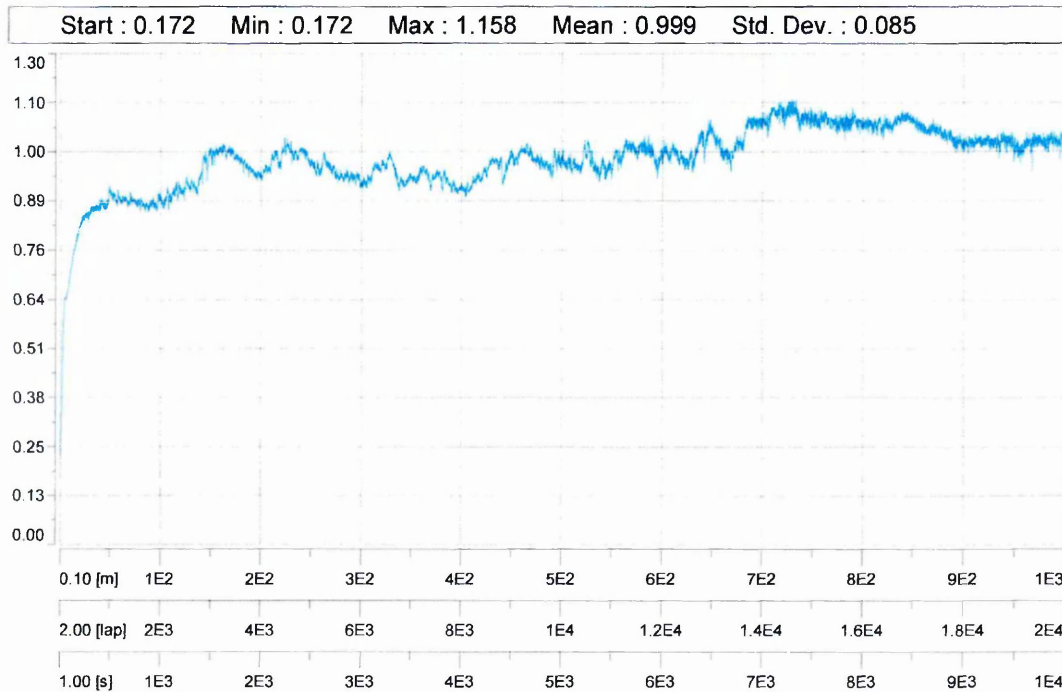


Figure A3.1. Pin on disc measurement of the -75V sample trial\_2.

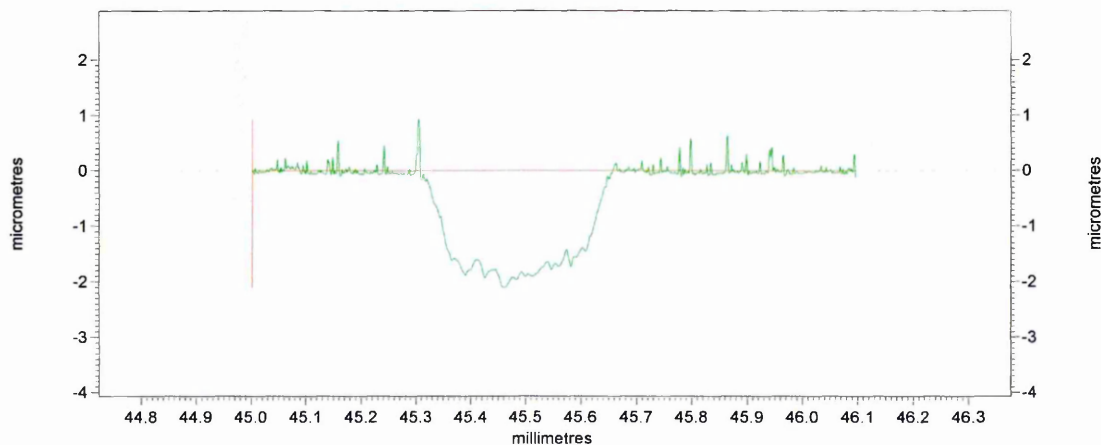
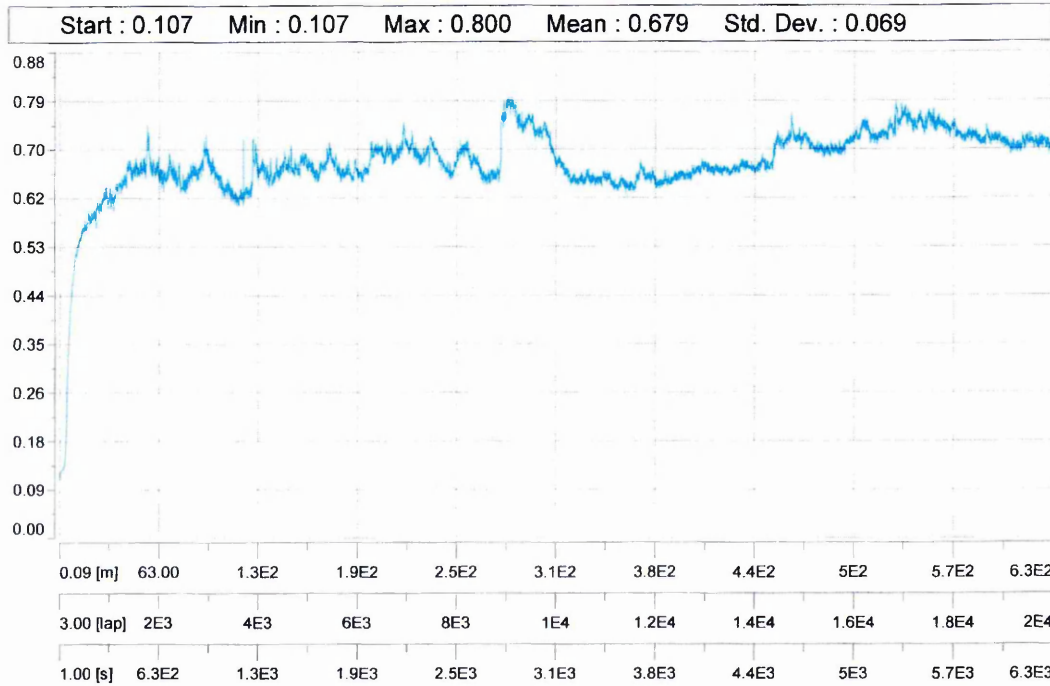


Figure A3.2. Profile of the produced wear track on the -75V sample trial\_2.

**Tribo parameters**

<b>Acquisition</b> Radius : 5.00 [mm] Lin. Speed : 10.00 [cm/s] Normal load : 5.00 [N] Stop condition : 20000 [laps] Acquisition rate : 1 [Hz]	<b>Sample</b> -Coating : CrN/NbN -Substrate : HSS	<b>Static Partner</b> -Coating : Al2O3 -Cleaning : no -Dimension : 6.00 [mm] -Geometry : Ball	<b>Environnement</b> Temperature : 22.00 [°C] Atmosphere : air Humidity : 16.00 [%]
<b>Sample</b> Worn Track Section : 272.0 um2 Young's Modulus : 0.0 GPa Poisson Coef. : 0.000	<b>Static Partner</b> Worn Cap Diameter : 0.0 um Young's Modulus : 0.0 GPa Poisson Coef. : 0.000	<b>Calculations</b> Sample Wear Rate : 0.000 mm3/N/m Static Part. Wear Rate : 0.000 mm3/N/m Max Herzian Stress : 0.000 GPa	

**Curve**



**Figure A3.4.** Pin on disc measurement of the -95V sample trial\_2.

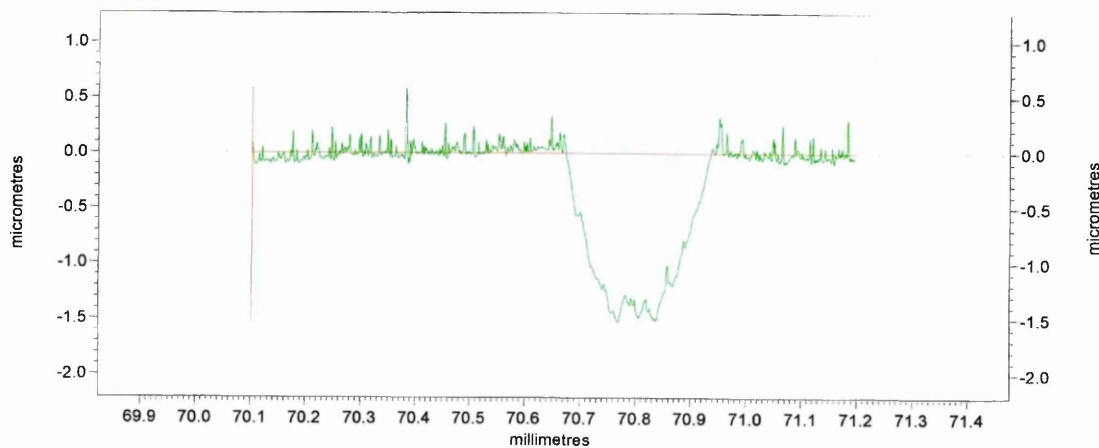


**Figure A3.5.** Profile of the produced wear track on the -95V sample trial\_2.

# A4 Surface roughness of CrN/NbN superlattice coatings of trial\_1

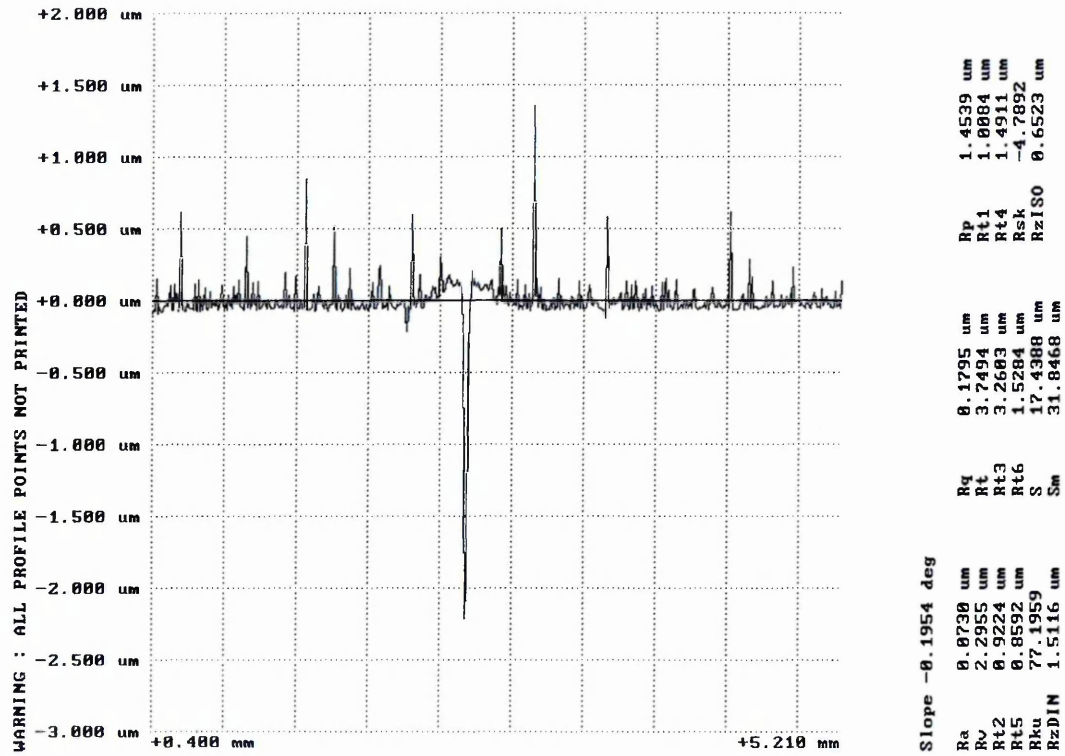


Figure A4.1. Profile of the measured surface roughness of the -75V sample trial\_1.

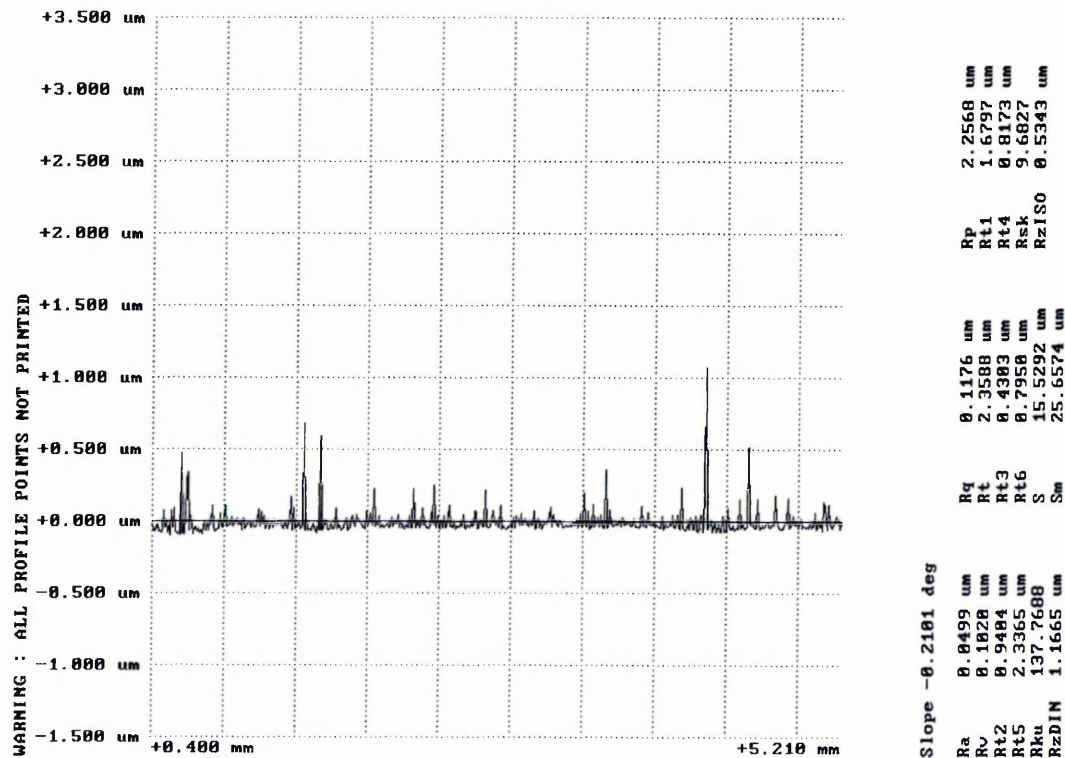


Figure A4.2 Profile of the measured surface roughness of the -95V sample trial\_1.

# A5 Surface roughness of CrN/NbN superlattice coatings of trial\_2

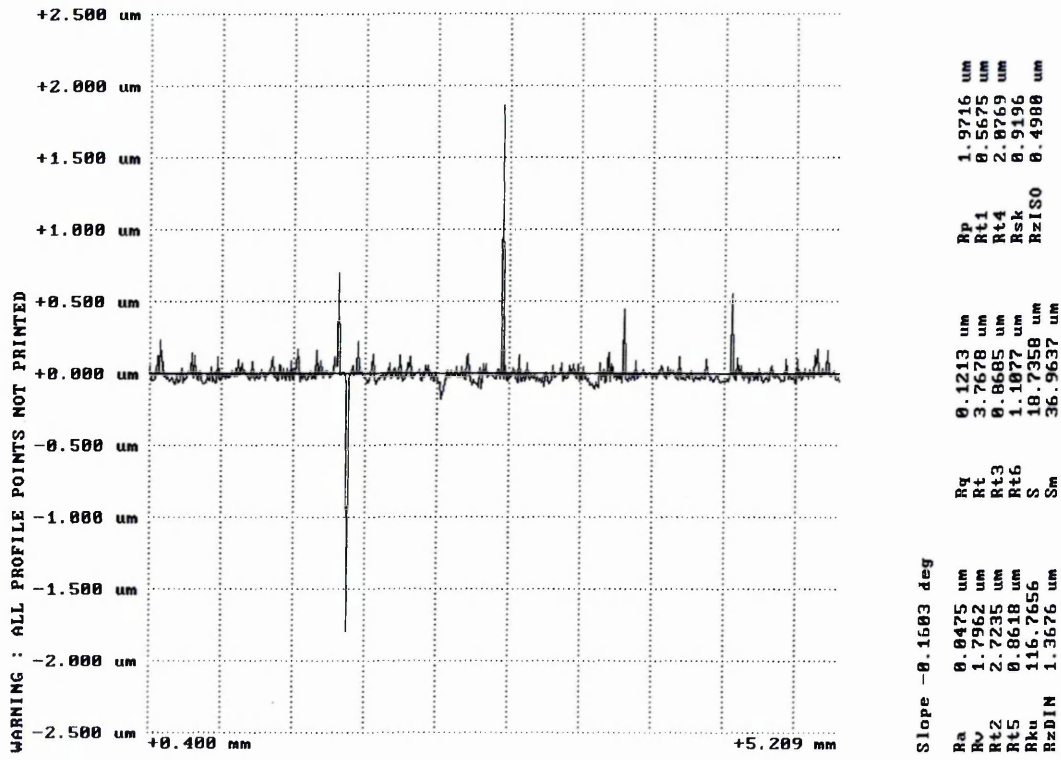


Figure A5.1. Profile of the measured surface roughness of the -75V sample trial\_2.

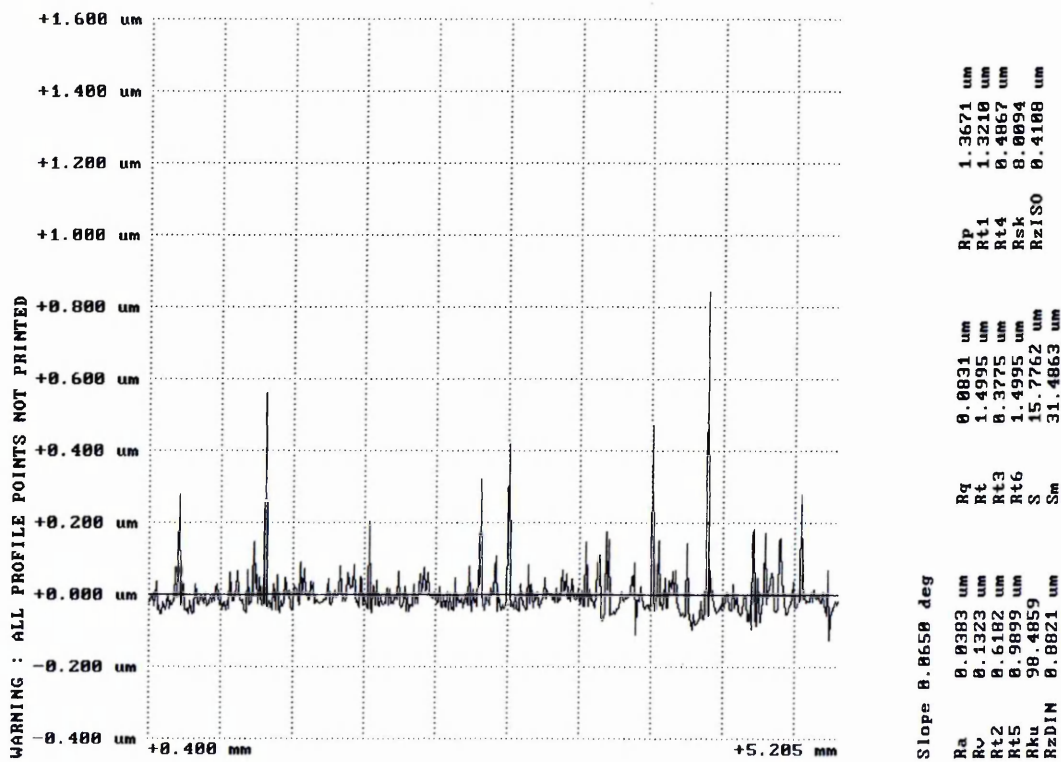


Figure A5.2. Profile of the measured surface roughness of the -95V sample trial\_2.

## A6 EDX analysis of CrN/NbN superlattice coatings of trial\_1

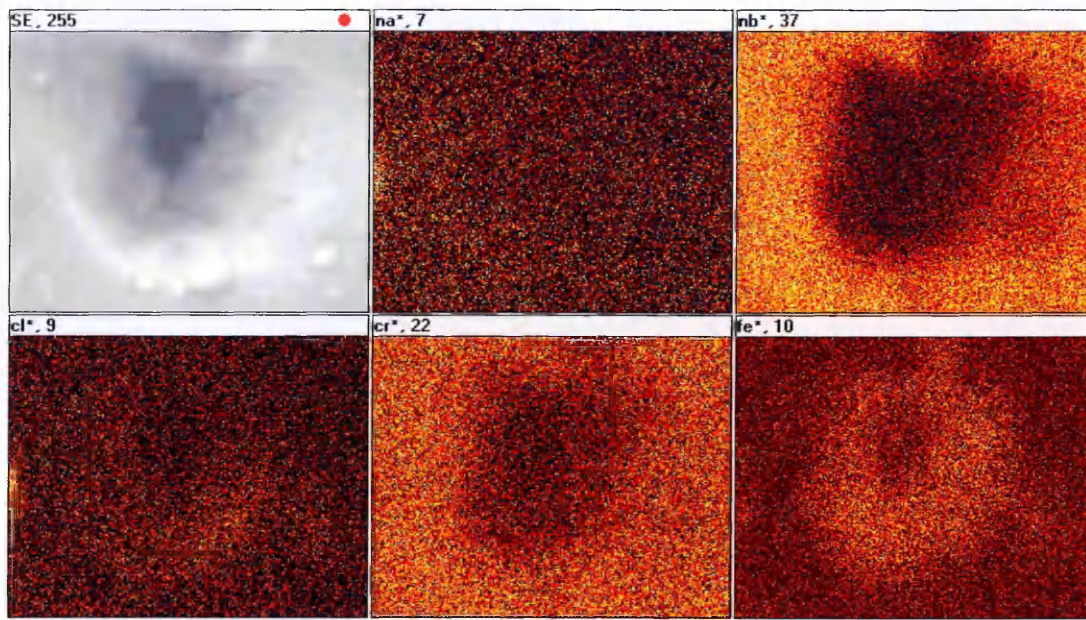


Figure A6.1 EDX distribution map of corrosion site (-75V bias trial\_1 see figure 4.34).

## A7 EDX analysis of CrN/NbN superlattice coatings of trial\_2

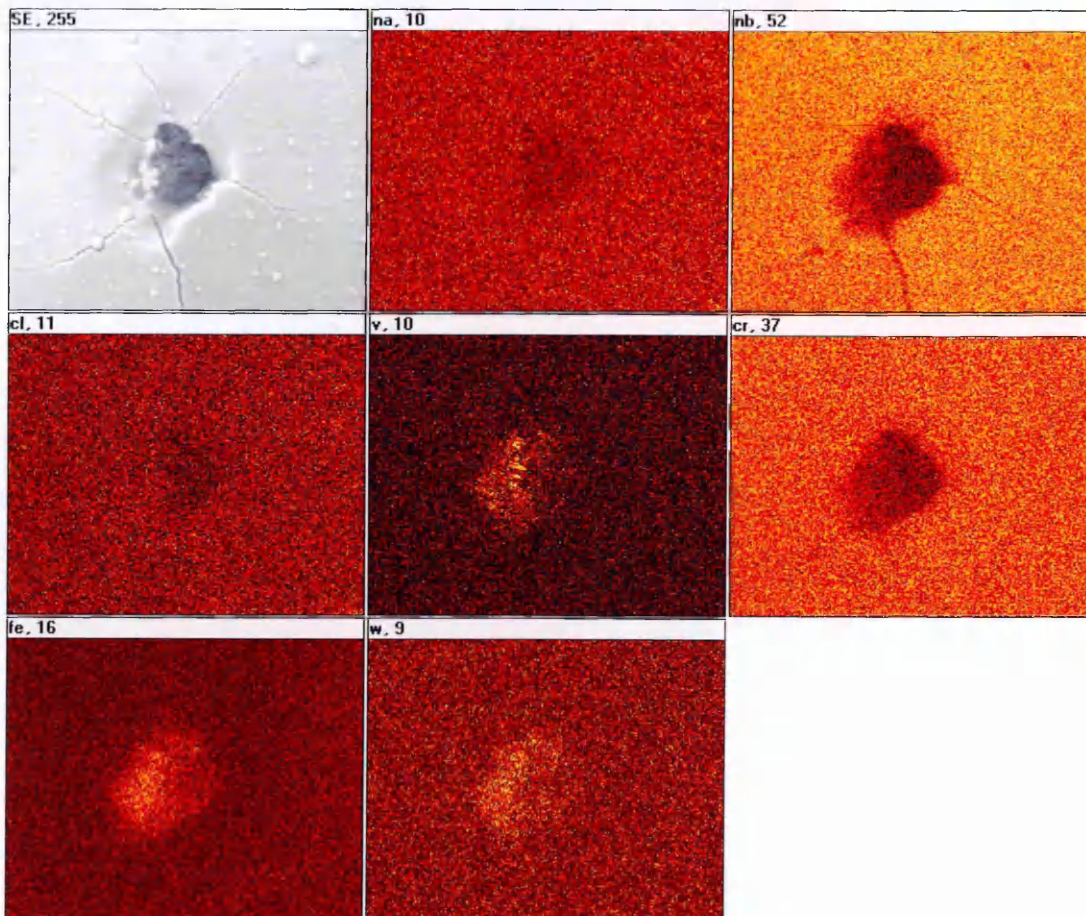


Figure A7.1. EDX distribution map of corrosion site (-75V bias trial\_2 see figure 4.40).

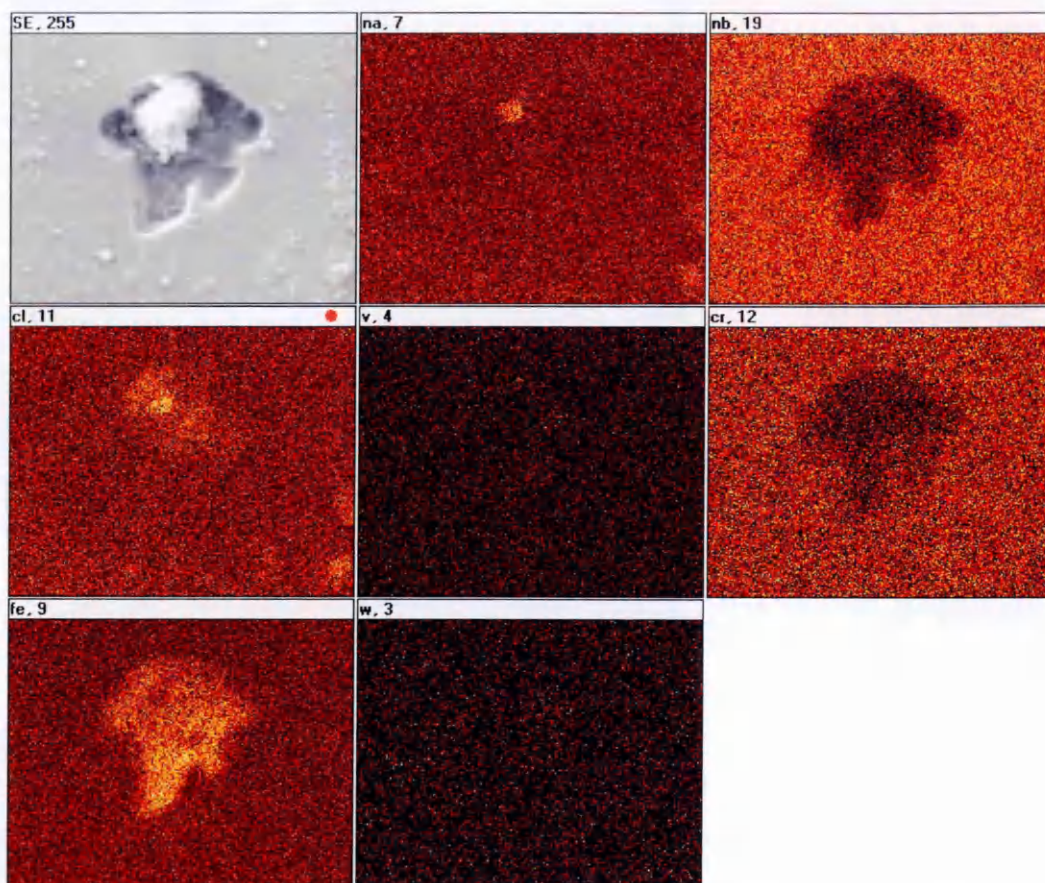


Figure A7.2. EDX distribution map of corrosion site (-75V bias trial\_2 see figure 4.41).

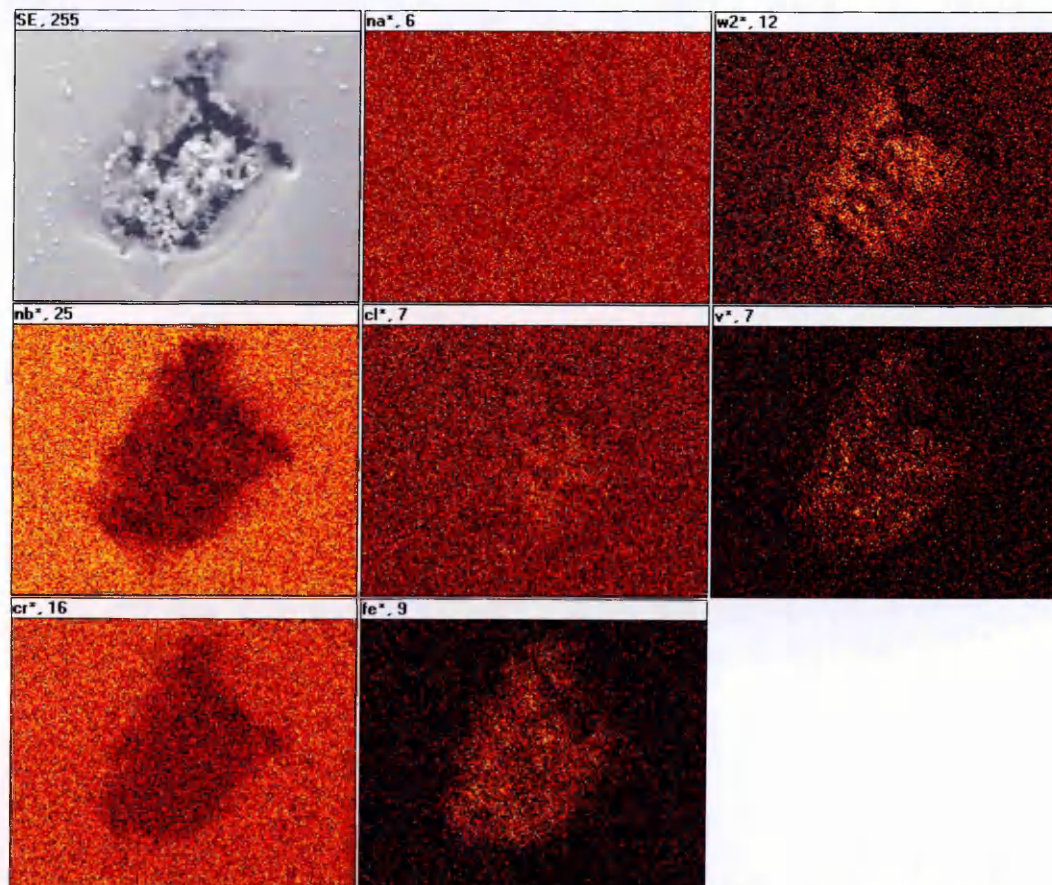
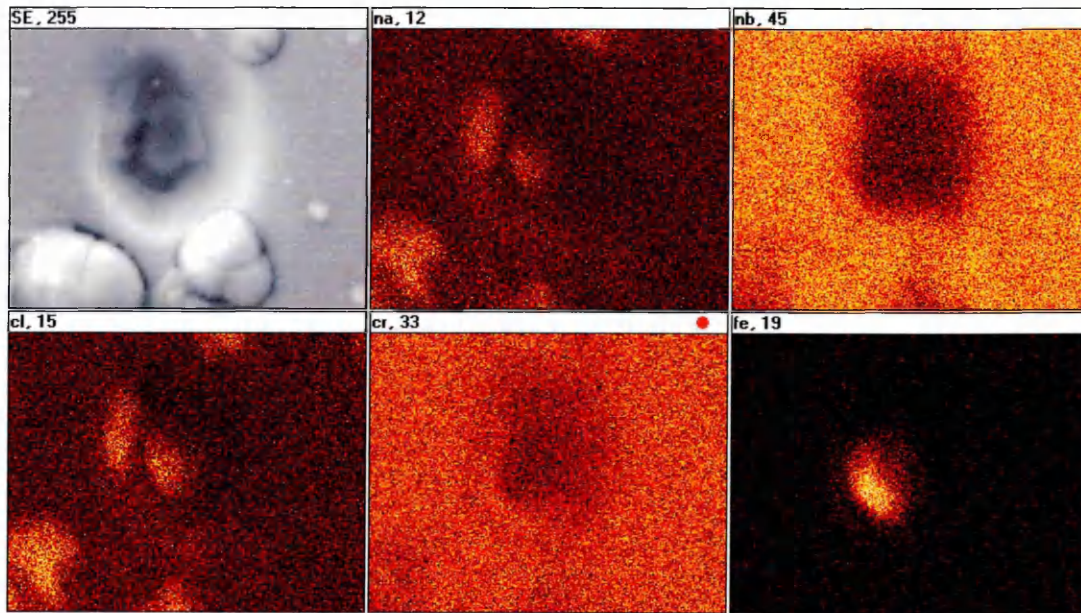


Figure A7.3. EDX distribution map of corrosion site (-95V bias trial\_2 see figure 4.43).

**A.8 EDX analysis of CrN/NbN superlattice coatings deposited at 400°C.**



**Figure A8.1 .** EDX distribution map of corrosion site (-95V bias CrN/NbN deposited at 400° C (figure 4.48).

## Bibliography

- [1] Alberts, L.; Leutenecker, R.; Wolf, G.K.:  
Texture of IBAD TiN films as a function of ion-beam intensity and angular incidence.  
Surface and Coatings Technology 84 (1996) 443-447.
- [2] Barrett S. C.  
Structure of Metals  
McGraw-Hill Book Group, 1952.
- [3] Barnett, S.; Madan, A.:  
Superhard superlattices.  
Physics World, January 1998, 45-48.
- [4] Boxman, R.L.; Goldsmith, S.:  
Cathode-Spot Arc Coatings: Physics, Deposition and Heating Rates, and some Examples.  
Surface and Coatings Technology, 33 (1987) 153-167.
- [5] Boxman, R.L.; Sanders, D.M.; Martin, P.J.:  
Handbook of Vacuum Arc Science and Technology – Fundamentals and Applications.  
Noyes Publication, Park Ridge, New Jersey, U.S.A., 1995, 498.
- [6] Carter, V.E.:  
Metallic Coatings for Corrosion Control.  
Butterworth & Co Ltd, London, 1977.
- [7] Chapman, B.:  
Glow Discharge Processes.  
John Wiley & Sons, 1980.
- [8] Creasey, S.; Lewis, D.B.; Smith, I.J.; Münz, W.-D.:  
SEM image analysis of droplet formation during metal ion etching by a steered arc discharge.  
Surface and Coatings Technology 97 (1997) 163-175.
- [9] Cullity, B.D., Stock, S.R.:  
Elements of X-Ray Diffraction.  
3<sup>rd</sup> edition, Prentice-Hall, Inc., New Jersey USA, 2001.
- [10] Ehasarian, A., P., Münz, W.-D., Hultman, L., Helmersson, U., Petrov, I.  
High power pulsed magnetron sputtered CrN<sub>x</sub> films.  
Surface and Coatings Technology 163-164 (2003) 267-272.

- [11] Ehiasarian, A., P., Hovsepien, P., Eh., Hultman, L., Helmersson, U.  
Comparison of microstructure and mechanical properties of chromium nitride-based coatings deposited by high power impulse magnetron sputtering and by the combined steered cathodic arc/unbalanced magnetron technique.  
Thin Solid Films 457 (2004) 270-277
- [12] Hovsepien, P.E.; Lewis, D.B.; Münz, W.-D.; Lyon, S.B.; Tomlinson, M.:  
Combined cathodic-arc / unbalanced magnetron grown CrN/NbN superlattice coatings for corrosion resistant applications.  
Surface and Coatings Technology 120-121 (1999) 535-541.
- [13] Hovsepien, P.E.; Lewis, D.B.; Münz, W.-D.; Rouzad, A.; Juliet, P.:  
Chromium nitride / niobium nitride superlattice coatings deposited by combined cathodic-arc / unbalanced magnetron technique.  
Surface and Coatings Technology 116-119 (1999) 727-734.
- [14] Hovsepien, P.E.; Lewis, D.B.; Münz, W.-D.:  
Recent progress in large scale manufacturing of multilayer/ superlattice hard coatings.  
Surface and Coatings Technology 133-134 (2000)166-175.
- [15] Hovsepien, P.Eh.; Münz, W.-D.:  
Thin films deposition and surface modification by sputtering and ion implantation.  
IEE Science Education and Technology - Training School on Plasma Technology. 26-29 June 2000, Buxton.
- [16] Hovsepien, P.E.; Lewis, D.B.; Luo, Q., Farinotti, A.  
Corrosion resistance of CrN/NbN superlattice coatings grown by various physical vapour techniques.  
Thin Solid Films 488 (2005) 1-8
- [17] Ives, M.; Cawley, J.; Brooks, J.S.:  
Fundamental studies of the ABS-enhanced magnetron sputter technique.  
Surface and Coatings Technology, 61 (1993) 127-132.
- [18] Johnson, P.C.:  
The Cathodic Arc Plasma Deposition of Thin Films. in Physics of Thin Films – Contemporary Preparative Techniques, edited by Francombe, M.H.; Vossen, J.L., vol. 14, 1989, 130-195.
- [19] Kelly, P.J.; Arnell, R.D.:  
Development of a novel structure zone model relating to the closed-field unbalanced magnetron sputtering system.  
Journal of Vacuum Science Technology A 16(5) (1998) 2858-2869.
- [20] Knotek, O.; Elsing, R.; Kraemer, G.; Jungblut, F.:  
On the origin of compressive stresses in PVD coatings – an explicative model.  
Surface and Coatings Technology, 46 (1991) 265-274.

- [21] Knuyt, C., Quaeys, C., D'Haen, J., and Stals, L.M.  
A quantitative model for the evolution from random orientation to an unique texture in PVD thin film growth.  
Thin Solid Films, Volume 258, Issues 1-2, (March 1995) 159-169.
- [22] Lewis, D.B.; Hovsepian, P.Eh.; Münz, W.-D.  
Interrelationship between Atomic Species, Bias Voltage, Texture and Microstructure of Nano-Scale Multilayers.
- [23] Lewis, D.B.; Reitz, D., Wüstefeld, C., Ohser-Wiedemann, R., Oettel, H., Ehasarian, A. P., Hovsepian, P.Eh.  
Chromium nitride/niobium nitride nano-scale multilayer coatings deposited at low temperature by the combined cathodic arc/unbalanced magnetron technique  
Thin Solid Films (2005) In Press
- [24] Luo, Q., Rainforth, W.M., Münz, W.-D.  
TEM observations of wear mechanisms of TiAlCrN and TiAlN/CrN coatings grown by combined steered arc/unbalanced magnetron deposition  
Wear 225-229 (1999) 74-82
- [25] Luo, Q.  
Tribology of PVD Coatings.  
IGDS Lecture notes, SHU, 2002.
- [26] Mattox, D.M.:  
Growth and Growth-Related Properties of Films Formed by Physical Vapor Deposition. In: ASM Handbook Vol.5 Surface Engineering. ASM International, p.538-555.
- [27] Mattox, D.M.:  
Surface effects on the growth, adhesion and properties of reactively deposited hard coatings.  
Surface and Coatings Technology 81 (1996) 8-16.
- [28] [www.matweb.com](http://www.matweb.com)
- [29] Münz, W.-D.; Hauzer, F.J.M.; Schulze, D.; Buil, B.:  
A new concept for physical vapor deposition coating combining the methods of arc evaporation and unbalanced-magnetron sputtering.  
Surface and Coatings Technology 49 (1991) 161-167.
- [30] Münz, W.-D.; Schulze, D.; Hauzer, F.J.M.:  
A new method for hard coatings: ABS<sup>TM</sup> (arc bond sputtering):  
Surface and Coatings Technology 50 (1992). 169-178.
- [31] Münz, W.-D.; Lewis, D.B.; Creasey, S.:  
Defects in TiN and TiAlN coatings grown by combined cathodic arc/unbalanced magnetron technology.  
Vacuum 46 (1995) 4. 323-330.

- [32] Münz, W.-D.; Smith, I.J.; Lewis, D.B., Creasey, S.:  
Droplet formation on steel substrates during cathodic steered arc metal ion etching.  
Vacuum 48 (1997) 473-481.
- [33] Münz, W.-D.; Lewis, D.B.; Hovsepian, P.Eh.; Schönjahn, C.; Ehiasarian, A.; Smith, I.J.:  
Industrial Scale Manufactured Superlattice Hard PVD Coatings.  
Surface Engineering, Vol.17 No.1 (2001) 15-27.
- [34] Musil, J.; Vyskocil, J.; Kadlec, S.:  
Hard Coatings Prepared by Sputtering and Arc Evaporation.  
Physics of Thin Films, 1993 Vol.17, 79-144.
- [35] Oettel, H.; Wiedemann, R.; Preißler, S.:  
Residual stresses in nitride hard coatings prepared by magnetron sputtering and arc evaporation.  
Surface and Coatings Technology 74-75 (1995) 273-278.
- [36] Oettel, H.:  
Determination of Residual Stresses in Coated Materials.  
Mechanical Behaviour of PVD Coated Materials – Proceedings of the International Workshop, October 13-17, 1997 in Holzau.
- [37] Oettel, H.:  
PVD Methods and Microstructure of Coatings.  
Mechanical Behaviour of PVD Coated Materials – Proceedings of the International Workshop, October 13-17, 1997 in Holzau.
- [38] Oettel, H.; Klimanek, P.:  
Textures of Thin Films.  
Materials Science Forum 273-275 (1998) 55-65.
- [39] Paritong, H.  
Development of Corrosion Resistant Niobium-Based PVD Coatings.  
Thesis, Sheffield Hallam University, 2000.
- [40] Pelleg, J., Zevin, Z. L., Lungo, S. and Croitoru, N.  
Reactive-sputter-deposited TiN films on glass substrates.  
Thin Solid Films, Volume 197 (1991) 117-
- [41] Perry, A.J.; Valvoda, V.; Rafaja, D.; Williamson, D.L.; Sartwell, B.D.:  
On the residual stress and picostructure of titanium nitride films I: Implantation with argon or krypton.  
Surface & Coating Technology, Vol.54-55 (1992) 180-185.
- [42] Petrov, I., Losbichler, P., Bergstrom, D., Greene, J.E., Münz, W.-D., Hurkmans, T., Trinh, T.  
Ion-assisted growth of  $Ti_{1-x}Al_xN/Ti_{1-y}Nb_yN$  multilayers by combined cathodic-arc/magnetron-sputter deposition.  
Thin Solid Films, Vol 302 (1997) 179-192.

- [43] Randhawa, H.; Johnson, P.C.:  
 Technical Note: A Review of Cathodic Arc Plasma Deposition Processes and their Applications.  
 Surface and Coatings Technology, 31 (1987) 303-318.
- [44] Rickbery, D.S.; Matthews, A.:  
 Advanced surface coatings – a handbook of surface engineering.  
 Blackie & Son Ltd, 1991.
- [45] Rohde, S.L.:  
 Sputter Deposition.  
 ASM Handbook Vol. 5 – Surface Engineering, ASM International, 1994, 573-581.
- [46] Scully, J.C.:  
 The Fundamentals of Corrosion.  
 3<sup>rd</sup> edition. Oxford: Pergamon Press, 1990.
- [47] Smith, I.J.: The Improvement of  $Ti_{1-x}Al_xN$  coatings by incorporation of Y and Cr.  
 PhD Thesis, Sheffield Hallam University, 1998.
- [48] Tomlinson, M.; Lyon, S.B.; Hovsepian, P.; Münz, W.-D.:  
 Corrosion performance of CrN/NbN superlattice coatings deposited by the combined cathodic arc/unbalanced magnetron technique.  
 Vacuum 53 (1999) 117-121.
- [49] Trethewey, Kenneth R.; Chamberlain, John:  
 Corrosion for Science and Engineering.  
 2<sup>nd</sup> edition. Harlow: Addison Wesley Longman Limited, 1995.
- [50] Vyskocil, J.; Musil, J.:  
 Arc Evaporation of hard coatings: Process and Film Properties:  
 Surface and Coatings Technology, 43/44 (1990), p.299-311.
- [51] Wang, H.W.; Stack, M.M.; Lyon, S.B.; Hovsepian, P.; Münz, W.-D.:  
 The corrosion behaviour of macroparticle defects in arc bond-sputtered CrN/NbN superlattice coatings.  
 Surface and Coatings Technology 126 (2000) 279-287.
- [52] Wiedemann, R.; Oettel, H.:  
 Residual Stresses in Coated Materials.  
 Mechanical Behaviour of PVD Coated Materials – Proceedings of the International Workshop, October 13-17, 1997 in Holzau.



# Defects in TiN and TiAlN coatings grown by combined cathodic arc/unbalanced magnetron technology

W-D Münz, D B Lewis and S Creasey, *Materials Research Institute, Sheffield Hallam University, Pond Street, Sheffield S1 1WB, U.K.*

and

T Hurkmans, T Trinh and W v Ijzendorp, *Hauzer Techno Coating Europe bv, PO Box 226, 5900 AE Venlo, The Netherlands*

received 19 February 1994

*During the cathodic arc enhanced metal ion etching process of steel substrates droplets are generated on the cathode which deposit on the substrate surface. The concentration of the droplets obviously depends upon the melting point of the target material. The number of droplets is much greater for TiAl than for Ti. The composition of the TiAl droplets also depends on their size. Large droplets tend to have the same composition as the target material, whereas smaller droplets are enriched in Ti. The adhesion of the droplets to the substrate is very poor, certainly below  $L_c = 20$  N. A subsequent coating of the droplet contaminated surface with the unbalanced magnetron leads to growth defects. Nodule-like defects continue to form on the droplet itself, whereas other droplets are expelled from the coating surface during film growth, generating craters and dish-like growth defects. A simple explanation for the self-expulsion mechanism of droplets is given.*

## 1. Introduction

The new ABS<sup>TM</sup> (Arc Bond Sputtering) PVD technique combines the cathodic arc evaporation and the unbalanced magnetron (UBM) sputter deposition methods<sup>1</sup>. The cathodic arc discharge is used to generate a plasma consisting of multiply ionised metal atoms<sup>2</sup> which bombard the substrate surface. Under the influence of an applied voltage, typically  $-1200$  V, these ions perform two functions: they etch the substrate surface and are also implanted into it<sup>1,3</sup>. The coating procedure itself is carried out by unbalanced magnetron sputtering.

In a recent paper on TiAlN coatings grown by ABS<sup>TM4</sup>, it has been pointed out that films deposited without this metal ion sputter cleaning process, exhibited a smoother surface morphology than those coatings which have undergone this *in vacuo* ion pretreatment prior to UBM coating. In the electron microscope, defects were observed in the form of 'droplets' typical of the cathodic arc deposition. Conversely, it has been clearly demonstrated in this paper<sup>4</sup> that the metal ion sputter cleaning step improves the adhesion of TiAlN coatings, as measured by critical load  $L_c$  and Rockwell indentation criteria, substantially when compared to UBM coatings, where the substrates were etched *in vacuo* only with Ar<sup>+</sup> ions. The increase in surface roughness could be greatly avoided if a sufficiently large shutter was used mid-way between the arc generating cathodes and the substrates, whilst still maintaining extraordinarily high adhesion values. In the case of the cathodic arc free deposition mode (only

UBM) a roughness of  $R_a = 0.04$   $\mu\text{m}$  was observed. With the shutter in operation, the  $R_a = 0.05$   $\mu\text{m}$  were evaluated. In the case of the metal ion cleaned substrates, the surface of the approximately 3  $\mu\text{m}$  thick coating of TiAlN was surprisingly rough with  $R_a = 0.17$   $\mu\text{m}$ .

The purpose of this study was to investigate the origin of this difference in surface roughness, as UBM deposited coatings themselves should not be affected by droplet-like defects. Besides TiAlN coatings, TiN coatings have been prepared for comparison and to investigate eventual differences in the droplet formation mechanism.

## 2. Experimental

All the coating experiments were performed in a commercially available PVD coater HTC 1000 ABS produced by Hauzer Techno Coating Europe B.V. This machine uses four vertically mounted cathodes which can be operated either in the cathodic arc or in the unbalanced magnetron mode. The cathodes are magnetically coupled in a closed field manner, in particular by the appropriate use of strong electromagnets assembled concentrically to the cathodes.

Figure 1 shows the cathode placement and the typical closed magnetic field line distribution<sup>5</sup>. Figure 2 outlines, schematically, the dual purpose cathode for cathodic arc and unbalanced magnetron operation. Further details are given in Ref. (1). The pro-

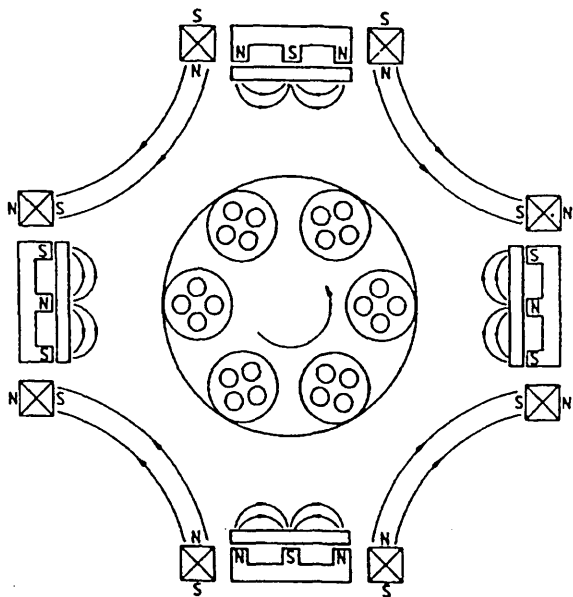


Figure 1. Cathode placement in the PVD coater HTC 1000 ABS™ with multipolar magnetic closed field.

cess sequence is outlined in Figure 3. The most important deposition parameters are summarised in Table 1.

TiAlN films were grown by reactive sputtering using powder, metallurgically prepared, hot, isostatic, pressed targets with a composition of 50 at%Ti, 50 at% Al. TiN films were prepared by reactive sputtering using vacuum cast 99.8% Ti targets. The substrates throughout these experiments were made of polished M2 high speed steel. Samples used for fracture cross-sectioning were coated on a stainless steel substrate.

The morphology of the samples was examined using either a Philips XL40 or a JEOL 840 scanning electron microscope. Droplets were subsequently analysed by energy dispersive X-ray (EDX) microanalysis.

The surface roughness was tested with a Rank Taylor Hobson Talysurf 6 instrument. The colour of the uncoated samples was

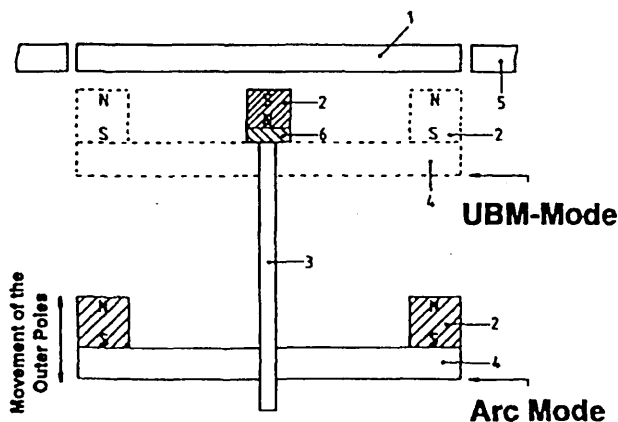


Figure 2. Schematic outline of dual purpose cathodic arc/unbalanced magnetron cathode; (1) target; (2) permanent magnets; (3) fixturing of centre poles; (4) magnetic yoke; (5) recipient; (6) magnetic neutral spacer.

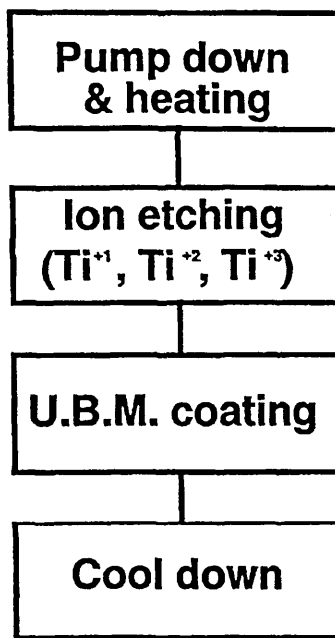


Figure 3. Process step sequence of ABS™ technology.

measured with a Minolta colorimeter in CIELAB units ( $L^*$ ,  $a^*$ ,  $b^*$ ). Adhesion tests were carried out using a CSEM critical load 'Revetest' instrument. The thickness of the films was evaluated by using a CSEM 'Kalotest'.

### 3. Results

In a first set of experiments, HSS samples were exposed to either a 5 min Ti ion etch or, alternatively, to a 5 min TiAl ion etching

Table 1. Important process parameters

Pump down and heat		
Residual gas	mbar	$2.10^{-5}$
Substrate temperature	°C	300
Metal ion etching		
Pressure Ar	mbar	$1.10^{-3}$
Substrate bias	V	-1200
Arc current	A	200
Substrate temperature	°C	350-500
Etching time	min	5
Coating		
Total pressure	mbar	$3, 5, 10^{-3}$
Power density cathode	mW cm <sup>-2</sup>	7-10
Discharge voltage cathodes	V	520
Substrate temperature	°C	450
Substrate bias	V	-75
Bias density	mW cm <sup>-2</sup>	3
Coating time	h	1.5-2
Cooling		
Cooling	h	0.5-1.5

step. Figure 4 represents a secondary electron emission image of a Ti ion etched surface ( $M = 250$ ).

The centre of the image shows the trace of a 20 N scratch test indentation. After closer examination it is clear that there is a reduction in the number of 'bright spots' inside the scratch surface compared to the outside of it. In Figure 5 a chemically cleaned surface of a HSS substrate is compared with those of Ti and the TiAl ion etched surfaces at the higher magnification of  $M = 1000$ . The 20 N scratch test trace covers the left part of the images and is very easily recognised by the grooves originating from the scratch stylus. There is practically no visible difference between the spot density inside and outside the scratch trace if one observes the as-chemically cleaned surface [Figure 5(a)].

However, it appears that the scratched part of the surface seems to be somewhat 'cleaner' suggesting that the stylus may have removed residues not taken away by the cleaning agent. Figure 5(b) represents the higher magnified image of Figure 4. The difference in spot density inside and outside the trace is even more difficult to recognise under these conditions. Only a careful intentional visual comparison allows the conclusion that the 'bright spot' density inside the scratch trace is lower than outside. Similarly, as with the chemically treated sample [Figure 5(a)] the trace area seems to be 'cleaner' again than the outer region. Figure 5(c) appears very different, here one observes the surface after the TiAl ion etch. It is very obvious that the trace inside is less populated by 'bright spots'. In the outside region we find many additional small spots, which cannot be found within the trace region. In general, we find a greater density of 'bright spots' outside the scratch trace when compared to the Ti ion etched samples.

Figure 6 summarises the equivalent results using elemental X-ray distribution mapping for the elements W, Al and Ti. It can be easily concluded that the majority of the 'bright spots' correlate to tungsten-rich carbide present in the HSS. Figure 6(a) is a SEM image and the corresponding X-ray mapping results show a very uniform tungsten distribution on the chemically cleaned substrate. Clearly no difference is found in the density of the 'bright spots' and the correlating tungsten signals inside and outside the scratch trace. In Figure 6(b) and Figure 6(c) the elemental mapping of Ti and Al is added, in order to analyse macroparticles

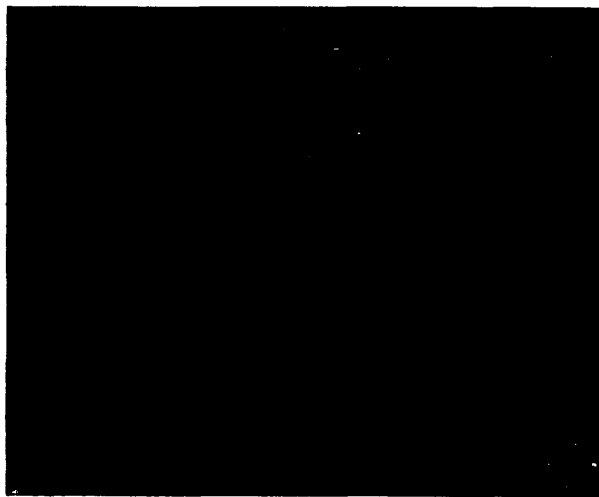


Figure 4. Secondary electron SEM image of Ti-etched sample surface ( $M250$ ).

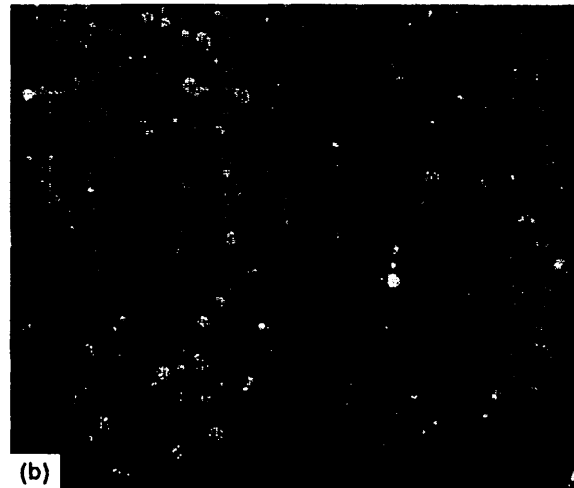
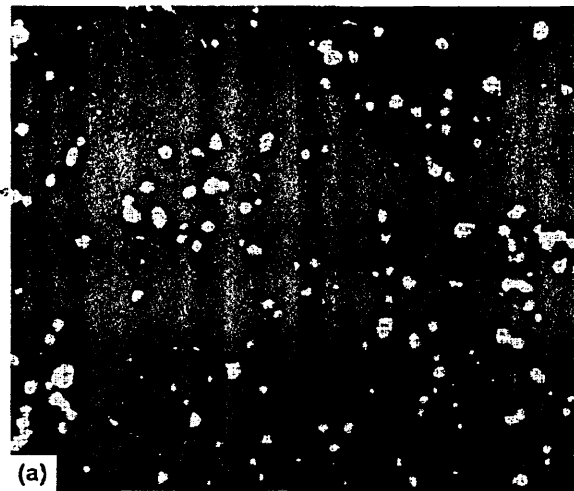


Figure 5. Secondary electron SEM image of differently pretreated sample surfaces ( $M2000$ ). (a) Chemically cleaned only. (b) Chemically cleaned and *in vacuo* Ti ion etched. (c) Chemically cleaned and *in vacuo* TiAl ion etched.

generated during the arc ion etching. Logically, one finds similar results for the tungsten elemental mapping, as compared to the chemically cleaned sample. The Ti and Al elemental mapping

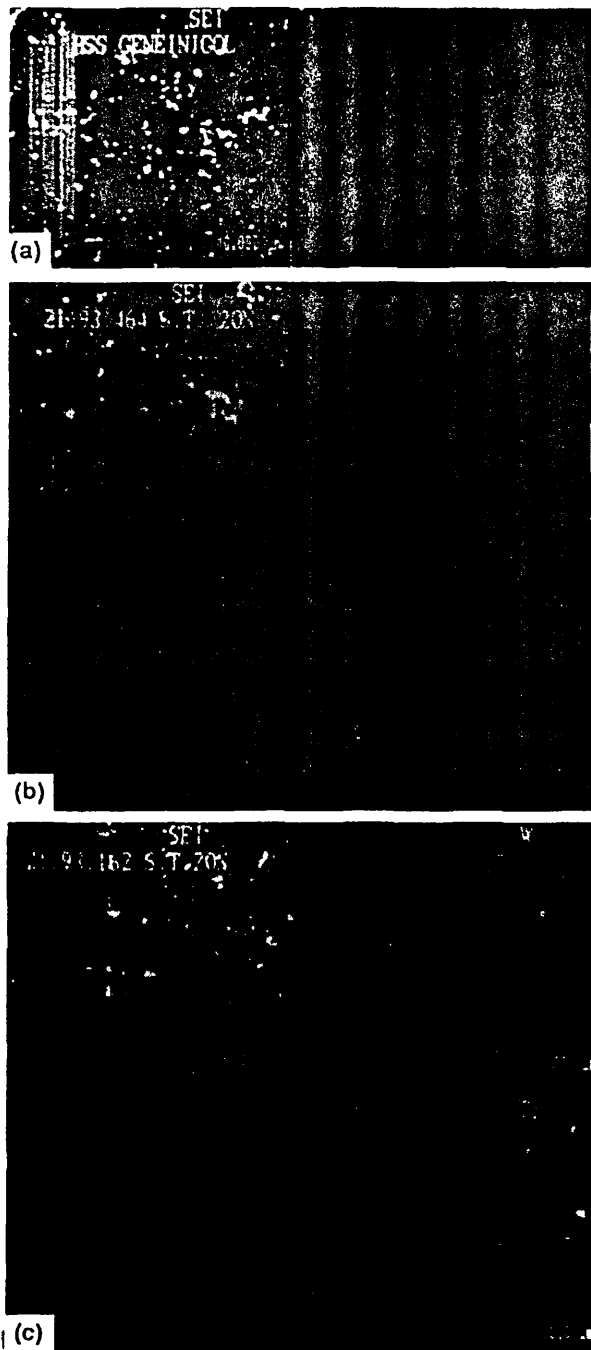


Figure 6. SEM image and EDX elemental mapping of W, Al and Ti on differently pretreated sample surfaces. (a) Chemically cleaned only. (b) Chemically cleaned and *in vacuo* Ti ion etched. (c) Chemically cleaned and *in vacuo* TiAl ion etched.

experiments, however, show (as in the case of the SEM images) quite different results. In the case of TiAl ion etching [Figure 6(c)] one recognises many signal spots in the right half of the Ti and Al mapping image, whereas in the scratch trace region, none, (except one single Ti signal) are present. One recognises also, that most of the Al signals coincide with Ti signals and that there are many more, mainly smaller, Ti signals counted than Al signals. In comparison to the TiAl ion etching case, there are

significantly fewer Ti signals present when the samples are etched with Ti ions. The density of small Ti signals is also significantly less in the specimen etched with Ti ion. Especially, the large amount of small signals is missing. There appears to be only two strong signals outside the scratch etch region, which indicates that there are really only very few droplets generated. Naturally, no Al signals were found, as no Al etching was involved.

Higher magnification images reveal that the macroparticles generated during the metal ion etching step by using the cathodic arc discharge, are strictly spherical in shape [Figure 7(a) and (c)]. This sort of defect is commonly understood as 'droplet'. During the entire investigation, only one macroparticle was found of a meteoritic impact, which is actually expected when a fluid droplet hits on the substrate surface. Figure 7(b) shows this rare object found on a Ti ion etched sample. The size of the spheres may reach up to several microns in certain cases. The average size ranges between  $0.5\ \mu\text{m}$  and  $1.5\ \mu\text{m}$ , this means that the droplets originally generated during the etching process are, in general, much smaller than the typical thickness of a hard coating, namely  $3\ \mu\text{m}$ . There also exist many extremely small spheres on the surface of the TiAl etched samples [Figure 7(c)]. Some of them have a diameter of only  $0.05\ \mu\text{m}$ . Smaller and larger spheres arrange themselves in clusters. Figure 7(c) also shows that, occasionally, one droplet sticks upon the other or that smaller spheres are covered by larger ones.

Interesting results are found by operating the SEM in the backscattering mode. In this mode of operation, elements with high atomic numbers appear bright and those with low atomic numbers appear dark to black. The very bright spots in Figure 8 represent the carbide particles in the substrate surface. The rest of the circular signals represent macroparticles or droplets characterised in varying shades of grey levels. The larger ones indicate a high Al content, since they appear darker than the smaller defects with higher Ti content. The EDX spot analysis confirmed semi-quantitatively, that the larger macroparticles had a much higher Al content than the smaller, brighter ones. In the case of the large spheres, the Al content was approximately 50 at%, practically identical with the target composition, whereas the very small spheres consist of up to 90 at% of Ti. This result satisfactorily explains the observation made in Figure 6(c), that the spot density in the case of Ti is found to be much higher than that of Al, as only Ti is present in the smaller, but more frequent, droplets.

The different pretreatments prior to coating deposition were also investigated with respect to their micro-roughness and their optical appearance. Table 2 reveals that the micro-roughness increases from the chemically cleaned case to the Ti ion etched case and, furthermore, to the TiAl ion etching pretreatment. Accordingly, the decrease of the  $L^*$  value indicates that the polished substrate loses brilliance when the surface is contaminated with droplets. The colour values for red/green  $a^*$  and blue/yellow  $b^*$ , however, are uninfluenced by the various pretreatment steps, although the enhanced  $b^*$  values of around 4 for Ti and 2.5 for TiAl pretreated samples, seem to indicate a first sign of colouration caused by oxides. Because of the higher refractive index of  $\text{TiO}_2$  when compared to  $\text{Al}_2\text{O}_3$ , the minor colour change is consequently more pronounced for the Ti and pretreated sample. These results therefore correspond with the SEM and EDX results.

Figure 9 and Figure 10 show SEM images of samples coated with TiN and TiAlN with a magnification of  $M = 2000$  and  $M = 10,000$ . At the lower magnification one again observes the

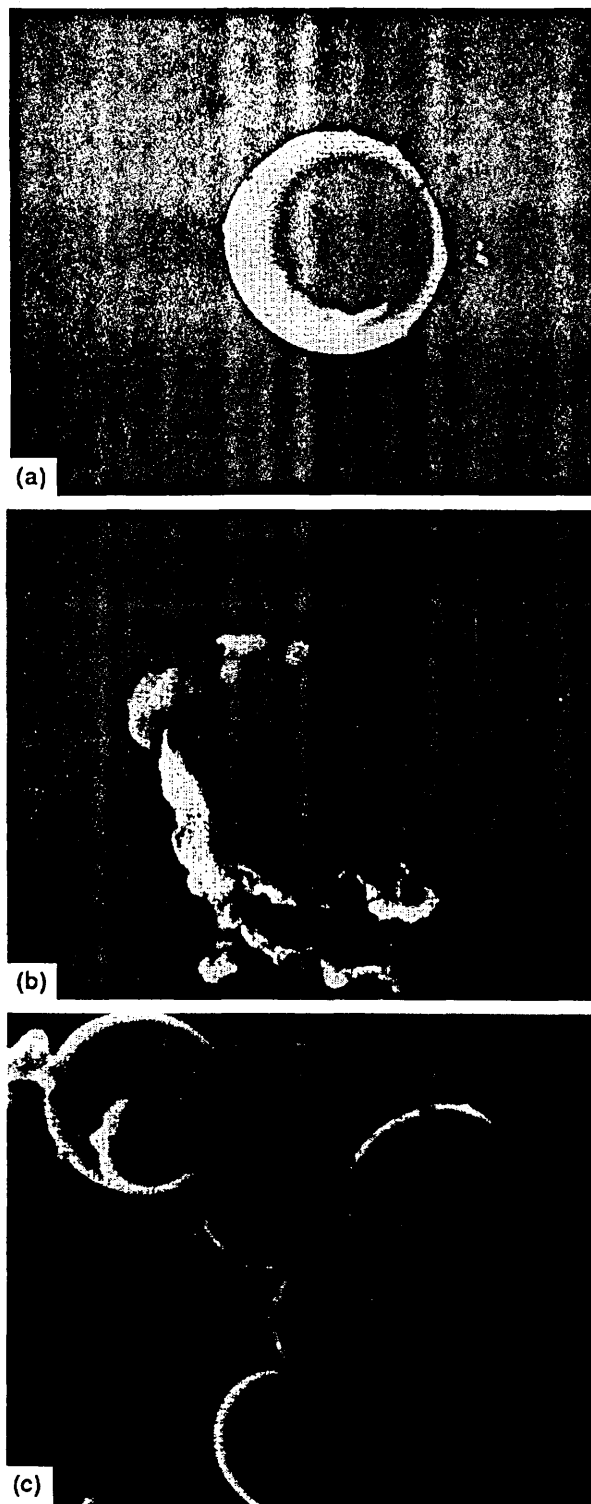


Figure 7. Various types of droplet formation (*M*20000). (a) Spherical Ti droplet. (b) Splash-like Ti droplet. (c) Cluster of TiAl droplet.

great difference in the defect density between the Ti and TiAl etched samples. The Ti ion etched and subsequently TiN coated sample, suffers apparently much less droplet deposition than do

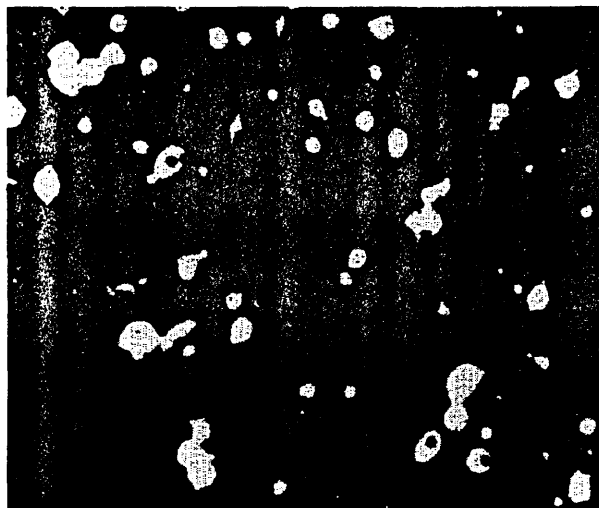


Figure 8. Backscattered electron SEM image of TiAl ion etched surface.

the TiAl ion etched and TiAlN coated samples; but, in both cases, one finds identical defect phenomena.

There are defects in a variety of sizes, from less than 1  $\mu\text{m}$  up to 5  $\mu\text{m}$  diameter, and craters in similar concentrations but of larger sizes. The higher magnification gives the impression that some of the macroparticles 'sit' rather loosely bound in the film. Some of the craters appear like open dishes [Figure 10(b)].

Fracture images show that, on one hand, the craters may extend almost from the substrate up to the top surface of the coating [Figure 11(a), centre]. On the other hand, one finds defects which reach from the bottom of the coating up to the coating surface. Such defects cannot be simply designated as droplets any more.

These defects are termed as pure nodule-like growth defects. They extend with cone-shaped tops from the coating surface [Figure 11(a)]; craters or holes were found to be variable in depth; but nodule-like growth defects always extended throughout the complete film thickness [Figure 11(b)]. In general, it seems that the defects observed after coating are larger than the droplets generated during the etching process.

Finally, we have examined the growth defects and the dish-like craters by EDX (Figure 12). The composition of the growth defects and the inside of the craters was always identical with that of the film composition, which differed only marginally from the composition of the target, namely, 50 at% Ti, 50 at% Al.

#### 4. Discussion

The results presented here clearly show that the origin of the unexpected high surface roughness of TiAlN coated steel samples has to be correlated directly to the metal ion etching procedure, prior to coating deposition. Obviously, depending on the melting

Table 2. Comparison of differently pretreated but uncoated samples

Sample	Ra ( $\mu\text{m}$ )	$L^*$	$a^*$	$b^*$
Chemically cleaned	0.016	82.7	0.21	0.62
Ti ion etched	0.018	79.3	0.17	7.18
TiAl ion etched	0.035	78.6	0.07	2.39

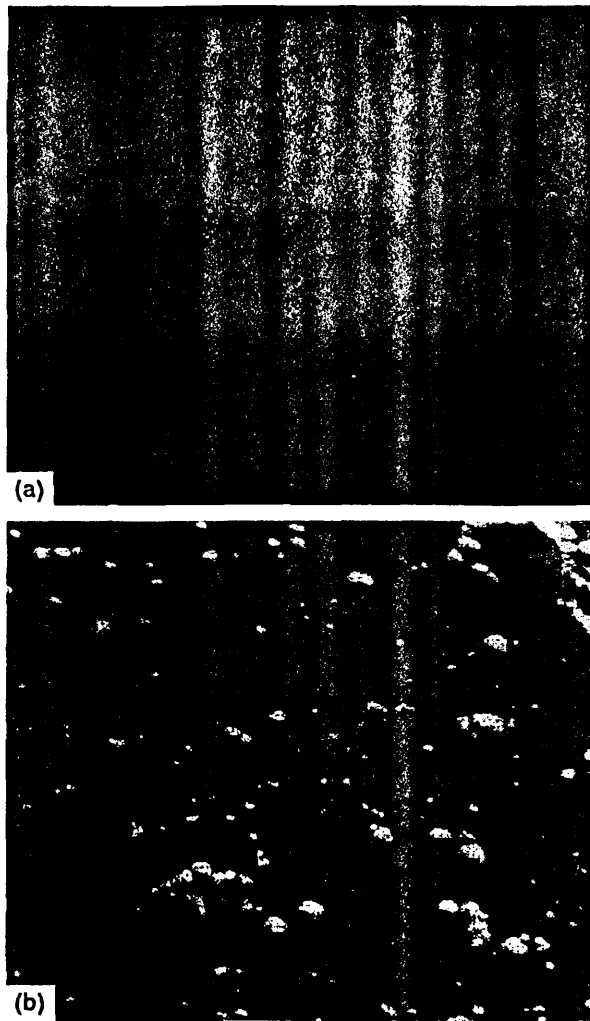


Figure 9. Secondary electron SEM image film surface ( $M2000$ ). (a) TiN. (b) TiAlN coating.

point of the target materials,  $1720^{\circ}\text{C}$  for Ti,  $1450^{\circ}\text{C}$  for the alloy TiAl and  $665^{\circ}\text{C}$  for Al<sup>6</sup>, droplets form under the eruptive influence of the cathodic arc discharge impinging on the target. They leave the target surface and deposit onto the substrate. They leave the target surface and deposit onto the substrate. Most of these droplets have an exact spherical shape, which indicates that they had already solidified before they arrived on the substrate surface (Figures 5 and 7). These findings are in good agreement with results of the excellent cross-sectional TEM study on the nature of droplet formation during the random arc evaporation of TiN<sup>9</sup>. Only very few droplets have a structured surface, like that droplet in the centre of the cluster in Figure 7(c) or the splash-like droplet in Figure 7(b). Here, one might conclude that the solidification process took place right on the substrate surface and that the droplet arrived in liquid phase. It is, under these circumstances, not surprising that the adhesion of the vast majority of the droplets on the uncoated surface must be rather poor. The scratch test, with a load of only 20 N, completely removes the spherical droplets. The critical load of the coating itself, either TiN or TiAlN, reveals typical values on HSS of greater than 50 N. The totally droplet-free scratch traces in Figures 4, 5 and 6 verify this conclusion.

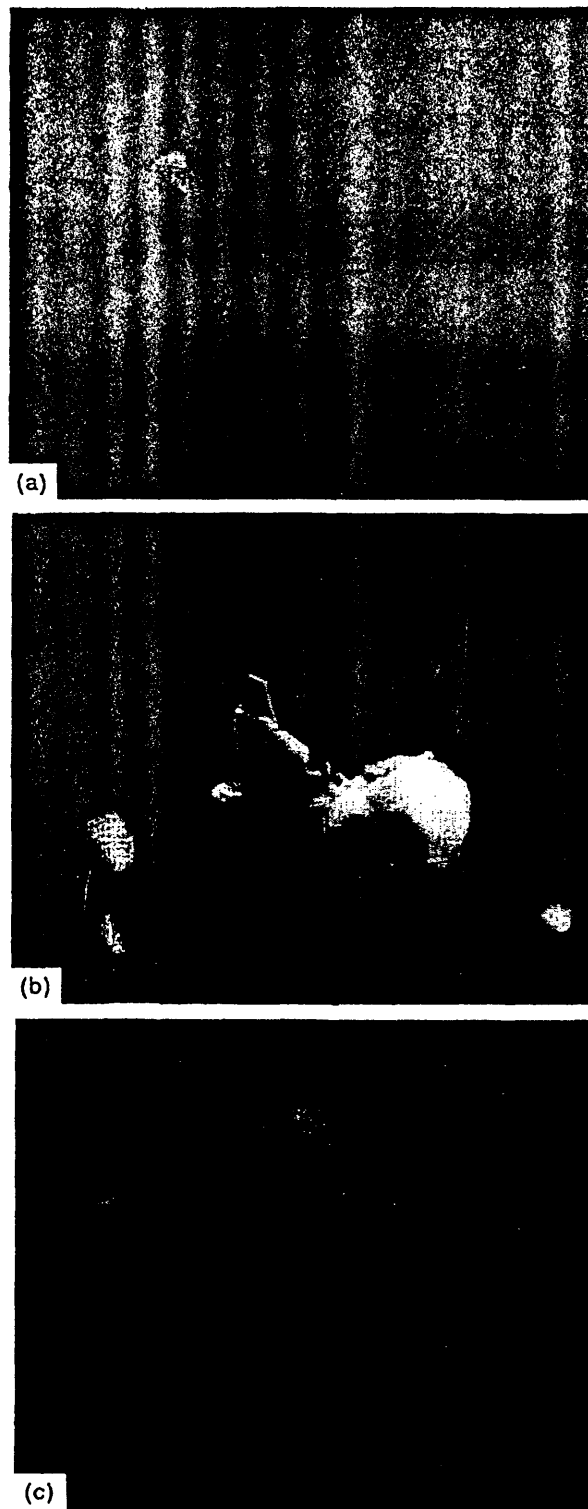


Figure 10. Various shaped growth defects ( $M10000$ ). (a) Nodule-like defects in TiN. (b) Accumulation of dish-like growth defects in TiN. (c) Nodule-like growth defects in TiAlN.

When the cathodic arc impinges on the target surface, the Ti and Al powder is going to melt locally and the liquid phases mix in the composition of the target. The local temperatures reported

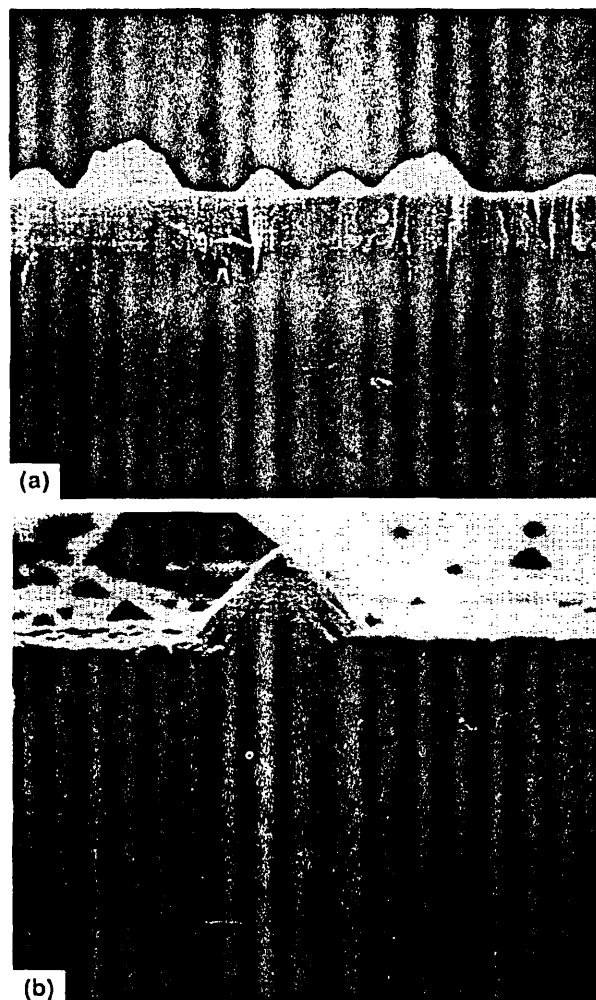


Figure 11. SEM fracture cross-section ( $M10000$ ). (a) TiAlN with cones and craters. (b) TiN with large droplet caused growth defects.

are as high as several thousand degrees<sup>7</sup>. For Mo, e.g., a local temperature of 7000 K is estimated<sup>8</sup>. It may be assumed that some of the Al and Ti is vaporised immediately and that another part of the melt is splashed towards the substrates as larger and smaller droplets. The larger spheres seem to preserve the composition of the melt, as the EDX spot analysis results showed. The smaller spheres, however, lose proportionally more of the low melting Al, presumably due to differential evaporation and their higher surface area to volume ratio. Consequently, the SEM backscattering image (Figure 8) shows the continuous gradient in the grey tone of the spherical droplets, caused by the change in concentration of the low atomic number material, Al.

The higher number of droplets produced during the TiAl ion etching procedure may be explained by the lower melting point of the liquid TiAl alloy. The expected lower viscosity of the probably superheated alloy melt may be one reason for the high amount of small sized Ti-rich droplets [Figure 6(c)] when etching with ionised TiAl vapour takes place.

The SEM images in Figures 9, 10 and 11 show that the droplets deposited during the metal ion etching step remain only partially on the substrates during film growth. However, some of them are firmly embedded within the coating and others seem to stick

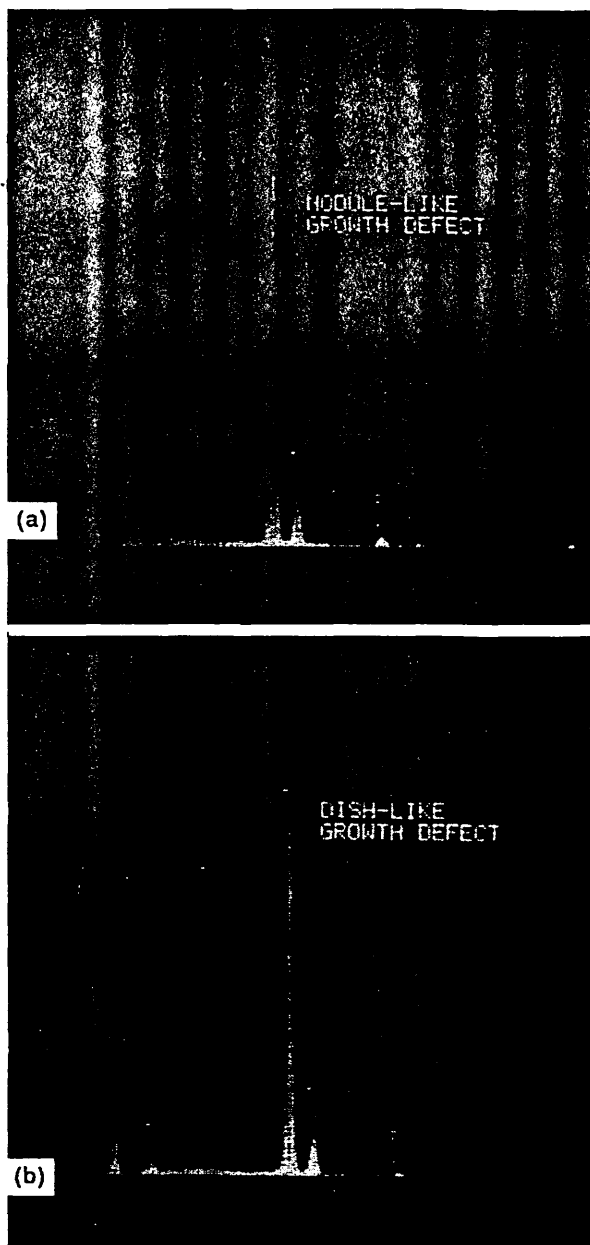


Figure 12. EDX spot analysis of droplet caused growth defects. (a) Nodule shaped defects. (b) Dish shaped defect.

loosely on the substrate. In any case, the objects seen in the SEM after coating seem to be enlarged growth defects. The droplets generated during the etching step may have served as seeds for the growth of nodule-like defects which reach practically from the substrate interface to the top surface of the coating, as Figure 11(a) and (b) confirm. They enhance the surface roughness of the substrate surface after ion etching from  $0.035 \mu\text{m}$  (Table 2) to  $0.17 \mu\text{m}$  after coating as reported<sup>4</sup> for TiAlN. This result is in contrast to very recent findings by cross-section transmission electron microscopy<sup>9</sup>. There, no growth defects were found in their investigations in TiN coatings originating from the substrate coating interface through the film to the coating surface, if pure random arc technology was used for metal ion etching, as well

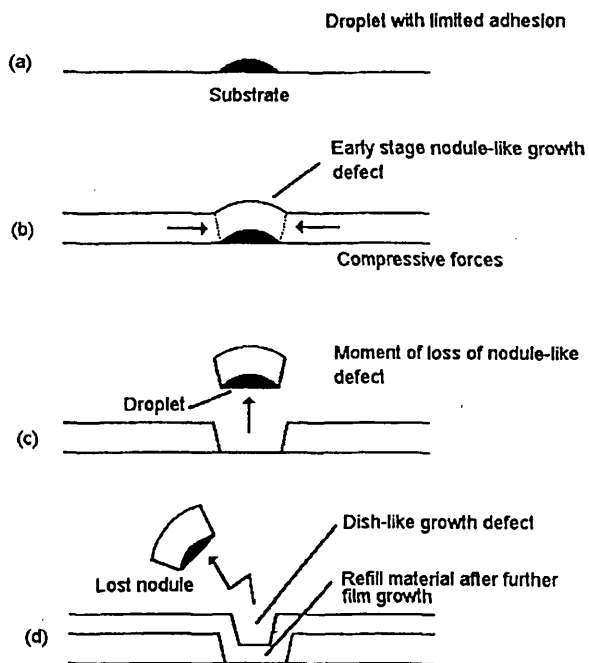


Figure 13. Schematic explanation of the self-expulsion mechanism of droplets.

as for film deposition. Only droplets were found, which were generated during the deposition phase of the film.

The craters are particularly clear, as shown in Figure 10(b). They may be related to solid droplets which have left the substrate surface during deposition. Figure 13 explains schematically a possible self-expulsion mechanism. Whether it is the increasing compressive stress of the growing coating or whether it is simply an undergrowing of the spherical droplets, the bonding strength of the droplets is in many cases not sufficient to maintain the droplet from simply being expelled out of the coating. The depth of the craters varies, obviously. EDX spot analysis showed that in the majority of the cases investigated, only the coating element, e.g. Ti, could be detected in the crater of a 3  $\mu\text{m}$  thick film. The signal of the substrate material Fe was normally very weak (Figure 12); but in other cases, the Fe signal was relatively strong. This indicates that the expelling event takes place, probably shortly after the film growth is initiated. The resulting empty hole is refilled by the growing film, forming dish-like defects, as can be observed experimentally in Figure 10(b) and schematically in Figure 13. Nevertheless, it may happen that the droplets leave the substrate and the coating in a late stage of film growth. Then one has to expect rather deep holes or craters in the coating. The deep hole shown in the centre of the SEM fracture image in Figure 11(a) proves this assumption.

## 5. Conclusions

As mentioned previously, the investigations definitely show that the enhanced roughness of ABS<sup>TM</sup> deposited TiAlN coatings is derived from droplet deposition during the cathodic arc-generated metal ion etching process step. No specific defects could

be located which were solely caused by the unbalanced magnetron coating step. Because the growth defects observed after film deposition clearly originated from cathodic arc droplets, if one works with TiAl targets in the arc mode, the droplet formation may be reduced by magnetically steering the cathodic arc. However, this has already been the case in this study, as in the experiments carried out in the PVD coating system, HTC 1000-4 ABS<sup>TM</sup> 'Steered Arc'<sup>TM</sup>, cathodes are customarily used<sup>1,10,11</sup>. As an electromagnetically guided arc filtering system<sup>12,13</sup> is too complicated for large scale industrial hard coating applications, the use of adjustable shutters in the coating machine seems to be the most practical method to substantially reduce the droplet formation during the etching step. This possibility has been pointed out previously<sup>1,4</sup>.

However, because of the self-expulsion effect of many of the deposited droplets, the damage which may be caused by droplets is less than one may have expected solely by considering the results after the etching step. Most of the craters are 'refilled'. Practical experience has also shown that in many wear, cutting or forming applications, the remaining cone-shaped growth defects which extend beyond the coating surface, are ground off to the level of the coating surface after a relatively short time of operation.

Last but not least, it should be mentioned that without shutters, deposited ABS<sup>TM</sup> coatings still have an overall roughness far lower than solely conventional random cathodic arc deposited TiAlN coatings<sup>4</sup>. The additional droplet deposition during the growth stage of random arc deposited coatings, as reported in Ref. (9), gives an indication in the same direction.

## Acknowledgement

Part of this work has been carried out within the BRITE/EURAM Programme project BE-4118 'COCO'.

## References

- W-D Münz, D Schulze and F J M Hauzer, *Surface Coat Technol.*, **50**, 169 (1992).
- I G Brown and X Godediot, *IEEE Trans Plasma Science*, **19**(5), 713 (1991).
- G Håkansson, L Hultman, J-E Sundgren, J E Greene and W-D Münz, *Surface Coat Technol.*, **18**, 51 (1991).
- W-D Münz, T Hurkmans, G Keiren and T Trinh, *J Vac Sci Technol.*, **A11**(5), 2583 (1993).
- S Kadlec and J Musil, US Patent 5, 234, 560, Priority Date: 14 August 1989.
- M Hansen, *Constitution of Binary Alloys*, p 140, McGraw-Hill Book Comp Inc, New York (1958).
- G Ecker, in *Vacuum Arcs—Theory and Applications* (Edited by J M Lafferty) p 229, Wiley Interscience (1980).
- H O Schrade, M Aweter-Kurtz and H L Kurtz, *IEEE Trans Plasma Science*, Vol PS-11, 103, Sept (1983).
- H Ljungcrantz, L Hultman, J-E Sundgren, G Håkansson and L Karlsson, *Surface Coat Technol.*, **63**, 123 (1994).
- S Ramalingam and C B Qi, US Patent 4, 673, 477, Priority Date: 2 March 1984.
- Ch F Morrison Jr, US Patent 4, 724, 058, Priority Date: 13 August 1984.
- I I Aksenov, V A Belous, V G Padalka and V M Khoroshikh, *Sov J Plasma Phys.*, **4**, 425 (1978).
- P J Martin, R P Netherfield and T J Kinder, *Thin Solid Films*, **193/194**, 77 (1990).



# Droplet formation on steel substrates during cathodic steered arc metal ion etching

W-D Münz, I J Smith, D B Lewis and S Creasey, Materials Research Institute, Sheffield Hallam University  
Pond Street, Sheffield S1 1WB, UK

received 6 June 1996; accepted in revised form 7 August 1996

*Cathodic arc discharges are commonly used as metal ion sources to carry out, in vacuo, the precleaning procedure in cathodic arc evaporation and combined cathodic arc/unbalanced magnetron deposition processes. During this very efficient etching step, droplets are generated, which give rise to growth defects in the subsequently deposited hard coating.*

*The number and size of droplets depend on the melting point of the metals used during ion etching. The present paper investigates the generation of droplets by target materials Al, Cu, TiAl, Ti, Zr, Cr, Nb and Mo with melting points in the range 660–2650°C. Under the process parameters used, the TiAl alloy target showed the highest number of droplets generated ( $100 \times 10^3 \text{ mm}^{-2}$ ) whereas the largest, up to 20  $\mu\text{m}$  diameter and quite often 'splash like', formed during evaporation from Al targets. Both metals with melting points greater than 2000°C show very similar droplet generation, with mean droplet deposition densities of  $5-10 \times 10^3 \text{ mm}^{-2}$  and diameters up to 5  $\mu\text{m}$ .*

*A comparison between the as-etched and as-coated samples indicates that the number of droplets deposited during the etching phase with TiAl and Mo formed an identical number of growth defects. In the case of Cr the number of defects on top of the coated surface were less. In general, following a non droplet producing unbalanced magnetron deposition process, defects were observed to extend from the substrate/coating interface to the coating surface. © 1997 Elsevier Science Ltd. All rights reserved*

## Introduction

Cathodic steered arc metal ion etching is an important process step in the recently developed combined cathodic steered arc/unbalanced magnetron ABS<sup>TM</sup> (Arc Bond Sputter) PVD hard coating technique.<sup>1</sup> By polarising the substrates with a negative bias voltage, typically -1200 V, metal ions generated during vigorous evaporation in the cathodic arc discharge initiate high *in vacuo* etching rates in addition to the formation of a graded substrate interface zone enriched with the elemental target species.<sup>2-4</sup> Both effects produce favourable conditions to enhance critical load values, as measured by a scratch adhesion test, of deposited hard coatings. The coatings may be applied, e.g. as nitrides using either the identical cathode arc source<sup>2</sup> or in the case of the ABS technique an unbalanced magnetron.<sup>1,3,5,6</sup> In parallel to this strong cleaning and favourable pre-conditioning effect, well known arc typical 'droplets' will be deposited on the substrate surface, which may cause substantial growth defects.<sup>5,7-9</sup> This is true for both random and steered arc discharges, although in the case of a magnetically controlled arc discharge, droplet formation should be considerably reduced.<sup>8,10-12</sup> Particularly dense droplet formation has been observed when a TiAl alloy is used as both a metal etching and a coating media.<sup>13-17</sup> Even when the non-droplet generating unbalanced magnetron deposition source was

used after the arc etching procedure, a considerable increase of coating roughness was observed, when TiAl targets were used for metal ion etching in contrast to an inert gas ion etch with Ar<sup>+</sup>.<sup>5</sup> The growth defects contribute considerably to an increase in the coating micro roughness due to the presence of cone shaped defects.<sup>17</sup> These grow during film deposition on top of the smaller droplets<sup>3</sup> and stem either from the arc etching or from an eventual arc deposition phase.<sup>9</sup> In the following, the macroparticles, which are produced by the cathodic arc discharge and which are deposited on the substrate during the etching phase are designated as 'droplets'. On top of these 'droplets' 'growth defects' are formed during the UBM sputtering phase, which protrude through the growing film.

Two practical applications have been used in our field tests. Here, the existence of droplet caused growth defects definitely influenced the performance of coated tools. Under the severe conditions of dry drilling operations, the life of coated HSS drills was markedly reduced. This was obviously due to strong friction effects caused by the roughened surface.<sup>18</sup> The second case was fine blanking. Here it is thought that a build up of metallic materials occurred in the cavities of the coatings. Under the highly pressurised conditions prevailing in fine blanking, cold welded bridges to the substrate material at the bottom of the

holes, caused by droplets, are followed by fatigue failures in the substrate material.<sup>19</sup>

In order to find solutions to avoid these deleterious droplet induced side-effects, an investigation of various metals typically used in PVD hard coatings has been started. Analysis on, in particular, the influence of their melting temperature (MP) on the number and size of droplets generated during the metal ion etching phase has been made. The following materials have been examined: Al (MP = 660°C) TiAl 50:50 (MP = 1450°C), Ti (MP = 1660°C) Zr (MP = 1860°C), Cr (MP = 1870°C), Nb (MP = 2450°C) and Mo (MP = 2650°C). In addition to these materials the industrial alloy Cu Al8 Fe3 has also been tested, which has a melting point ranging between Al and TiAl ( $\approx 1000^\circ\text{C}$ ). Furthermore TiAl, Cr, and Mo etched steel samples have been coated with  $\approx 3 \mu\text{m}$  of TiAlN in order to evaluate the resultant microroughness of the hard coating grown on the differently etched substrates.

**Experimental**

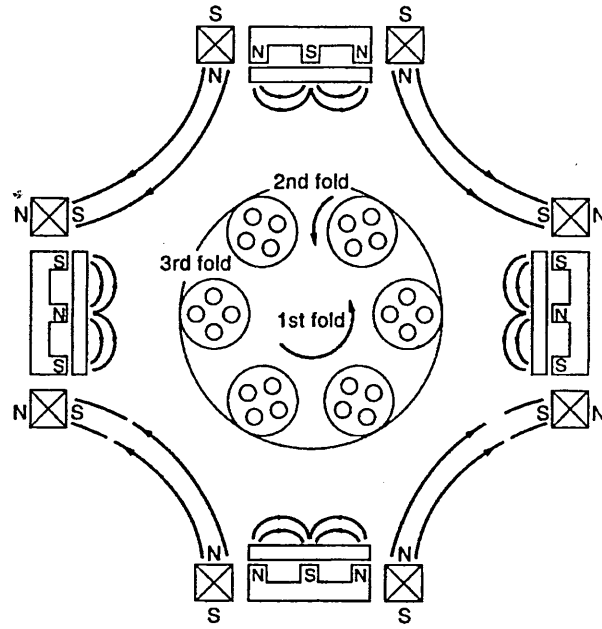
All coating experiments were performed in a commercially available industrially sized PVD coater HTC1000 ABS produced by Hauzer Techno Coating Europe BV, Venlo, The Netherlands.<sup>1</sup> One of four vertically mounted, orthogonally opposing cathodes were used for the metal ion etching experiments, whereas the other three cathodes were equipped with vacuum cast TiAl targets with a composition of 50 at% Ti and 50 at% Al to coat the etched samples in the unbalanced magnetron mode. The magnetic steering field controlling the cathodic arc discharge was generated by an array of permanent SmCo magnets ( $B_{\text{target}} < 25 \text{ Gauss}$ ). Moved closer to the target, the same magnets were used in the coating phase ( $B_{\text{target}} \approx 250 \text{ Gauss}$ ). The magnetic field was made unbalanced by means of electromagnets furnished concentrically to the magnetron cathodes. However, the magnetron discharge itself was controlled almost solely by the permanent SmCo magnets.<sup>1</sup> During coating the magnetrons were used in the 'closed field' mode, allowing high substrate bias current densities of up to  $5 \text{ mA cm}^{-2}$  during film growth. All substrates were subjected to a three fold planetary rotation. Further details on the coating apparatus and its principles are given in Ref. 1. Figure 1 outlines schematically the experimental set up.

The etching and coating process sequence is outlined in Figure 2. After pump down and heating of the vacuum chamber, the targets to be used were sputter cleaned. To avoid contamination of the substrates adjustable shutters were used to cover the cathodes during sputter cleaning. After this procedure either etching or an etching with subsequent coating procedure was performed. The most important process parameters are listed in Table 1.

The substrate materials used were martensitic stainless steel (416) and high speed steel (HSS:M2). All the substrates were 30 mm in diameter, 5 mm thick and polished to a  $1 \mu\text{m}$  diamond finish giving a microroughness of  $R_a < 0.005 \mu\text{m}$ . The morphology of the metal ion etched samples was examined using a Philips XL40 scanning electron microscope. In selected cases the surface was subsequently analysed by energy dispersive X-ray (EDX) microanalysis. The surface roughness was measured with a Rank Taylor Hobson Talysurf 120L instrument utilising a  $2 \mu\text{m}$  radius diamond stylus. This was used to determine  $R_a$  and  $R_z$  roughness values with a resolution of  $0.005 \mu\text{m}$ .

**Results**

The SEM images collected in Figure 3 express clearly a general decrease of surface contamination by droplets with increasing



Schematic of the Hauzer HTC 1000-4 ABS™ PVD coater

Figure 1. Schematic diagram of the experimental set up.

melting point of the materials used during cathodic steered arc ion etching. The number and the maximum diameter of the droplets have been evaluated from these micrographs (M 1000) quantitatively by visual means. The estimated spatial resolution for small droplets is  $0.1 \mu\text{m}$ . Table 2 summarises the results. For metals with low melting temperatures, in particular for Al, the maximum droplet diameter is much larger than that of higher melting temperature materials. Al defects are present with diameters as large as  $20 \mu\text{m}$ . A more detailed examination of the Al

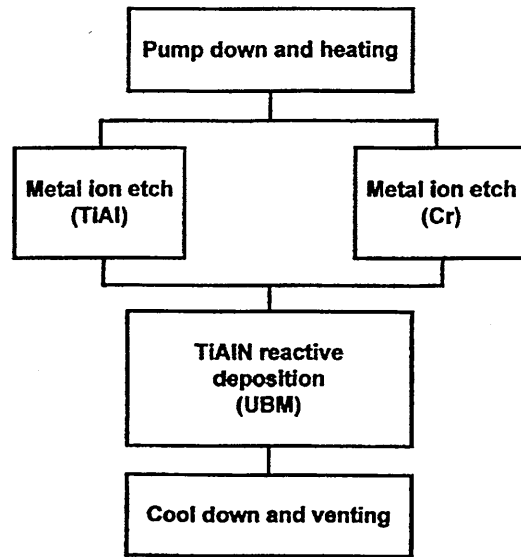


Figure 2. The etching and coating process sequence.

Table 1. Process Parameters

PUMP DOWN	
$t = 90 \text{ min}$ , $\Phi_{\text{Ar}} = 300 \text{ sccm}$ Heat to $400^\circ\text{C}$	
TARGET CLEANING	
$t = 10 \text{ min}$ , $\Phi_{\text{Ar}} = 160 \text{ sccm}$ Target power = $4 \times 5 \text{ kW}$	
METAL ION ETCH:	
$t = 30 \text{ min}$ (10 cycles of 2 min ON: 1 min OFF)	
$\Phi_{\text{Ar}} = 160 \text{ sccm}$ , $V_s = -1200 \text{ V}$ (Substrate Bias)	
Arc current = $100 \text{ A}$ (1 target: Al, Cu, TiAl, Ti, Zr, Cr, Nb, Mo.)	
$400 < T < 450^\circ\text{C}$ , $I_s = 4 \text{ A}$ (Bias current)	
COATING	
$t = 240 \text{ min}$	
$\Phi_{\text{Ar}} = 200 \text{ sccm}$ , $V_s = -75 \text{ V}$	
Target power: $3 \times \text{TiAl}$ : $8 \text{ kW}$	
$P_{\text{total}} = 3.4 \times 10^{-3} \text{ mbar}$ ,	
$\Phi_{\text{N}_2} = 170 \text{ sccm}$	
$400 < T < 440^\circ\text{C}$	
COOLING	
$t = 40 \text{ min}$ , $T < 250^\circ\text{C}$	
$\Phi_{\text{Ar}} 500 \text{ sccm}$	

etched sample (Figure 5(a)) shows circular and splash like defects, the latter of which is very similar to particular shapes experienced from rapid solidification. The larger particles, especially, surrounded concentrically by a halo, which is distinctly brighter than the background of the rest of the micrograph. In contrast to the other etching materials almost no small particles are observed after etching with aluminium. Quantitative analysis indicates the highest number of droplets for TiAl (Figure 3(c)), whereas the number of droplets stemming from the Cu-alloy (Figure 3(b)) ranges between those of the Al and the TiAl etched samples. The maximum droplet diameter seems to decrease rapidly with increasing melting temperature as can be observed for Al, Cu, TiAl and Ti (Figure 3(d)) cathode materials. However, for materials with higher melting temperatures, i.e. greater than  $2000^\circ\text{C}$ , both the maximum droplet size and the number of droplets generated seem to be independent of the melting temperature, at least within the accuracy of the observation method used here. The maximum droplet sizes remain  $< 5 \mu\text{m}$  and the number of droplets is  $< 10 \times 10^{-3} \text{ mm}^{-2}$ . However, the majority of the large Cr droplets (Figure 3(f)) were approximately  $1 \mu\text{m}$  in diameter,

therefore smaller than those observed from the higher melting point materials Nb and Mo (Figures 3(g) and (h)). However, a few of the larger Cr droplets were also of a similar size to those encountered from Nb and Mo.

The surface profiles illustrated in Figures 4(a)–(h) complement the SEM micrographs. Corresponding to the SEM results for lower melting point materials, the surface appears full of spikes and therefore much rougher. Quantitative analysis (Table 2) with  $R_a$  up to  $0.1 \mu\text{m}$  and  $R_z$  up to  $1.2 \mu\text{m}$  confirms this impression. For Cr, Nb and Mo as etching media, the evaluated roughness values appear to be much lower, with  $R_a < 0.01 \mu\text{m}$  and  $R_z < 0.15 \mu\text{m}$  more or less independent of the melting point of the cathode material. This quantitative result corresponds also to the qualitative results of the surface profiles shown by Figures 4(f)–(h), where only a few spikes are observed for the relevant materials and this is in full agreement with SEM examination.

Roughness measurements have also been carried out on coated samples. The following results were found: TiAl etched samples had the highest roughness value with typical,  $R_a$  of  $0.15 \mu\text{m}$ . Cr and Mo etched samples, however, showed a much lower roughness value,  $R_a$  typically  $0.05 \mu\text{m}$ . That means that the surface roughness of UBM deposited TiAlN coatings may be controlled by the choice of the etching material.

## Discussion

The importance of the melting temperature of cathodic arc cathode/target materials with respect to the generation of droplets has been emphasised by Daalder, when comparing the fraction of mass erosion in the form of droplet formation during the operation of cadmium and copper cathodes.<sup>20</sup> There, the lower melting Cd developed approximately five times as many droplets as the comparably higher melting Cu. Similar results, up to a factor of 20 in difference, have been found by Anders *et al.*<sup>8</sup> investigating Pb in comparison to W.

The results presented from this investigation (Table 2) generally confirm the above findings. The maximum droplet diameter decreases almost monotonically from  $10\text{--}20 \mu\text{m}$  for Al to  $3\text{--}5 \mu\text{m}$  for Nb and Mo. With the exception of aluminium the number of droplets decreases with increasing melting point of the target material. There, the majority of droplets found were large, only a few small ones were observed. It seems, that rather large liquid droplets of Al arrive and splash on the substrate surface. Firstly, they reacted as a hot melt with the solid substrate surface ( $400^\circ\text{C}$ )

Table 2

Material	Melting point (MP) ( $^\circ\text{C}$ )	Vapour pressure at $200^\circ\text{C}$ mbar	Thermal conductivity $\text{Wm}^{-1}\text{K}^{-1}$	Resistivity $\rho$ $\mu\Omega$ (cm)	Maximum droplet size ( $\mu\text{m}$ )	Number of droplets/area ( $10^3 \text{ mm}^{-2}$ )	$R_a$ ( $\mu\text{m}$ )	$R_z$ ( $\mu\text{m}$ )
Al	660	92	238	2.67	10–20	25	0.099	1.07
Cu (Al Fe)	1000	53**	394**	1.7	6	18	0.055	1.22
Ti Al	1450	***	***	***	5	100	0.071	1.08
Ti	1660	$2.6 \times 10^{-1}$	16	54	4	24	0.017	0.78
Zr	1850	$20 \times 10^{-3}$	22.6	44	4	6	0.011	0.30
Cr	1870	13	91.3	13.2	1	10	0.009	0.14
Nb	2450	$2.6 \times 10^{-6}$	56.5	14.6	3	4	0.005	0.10
Mo	2650	$5.3 \times 10^{-5}$	142	5.7	4	5	0.009	0.14

\* Measured at  $20^\circ\text{C}$  <sup>23</sup>

\*\* Value for pure Cu

\*\*\* Not available

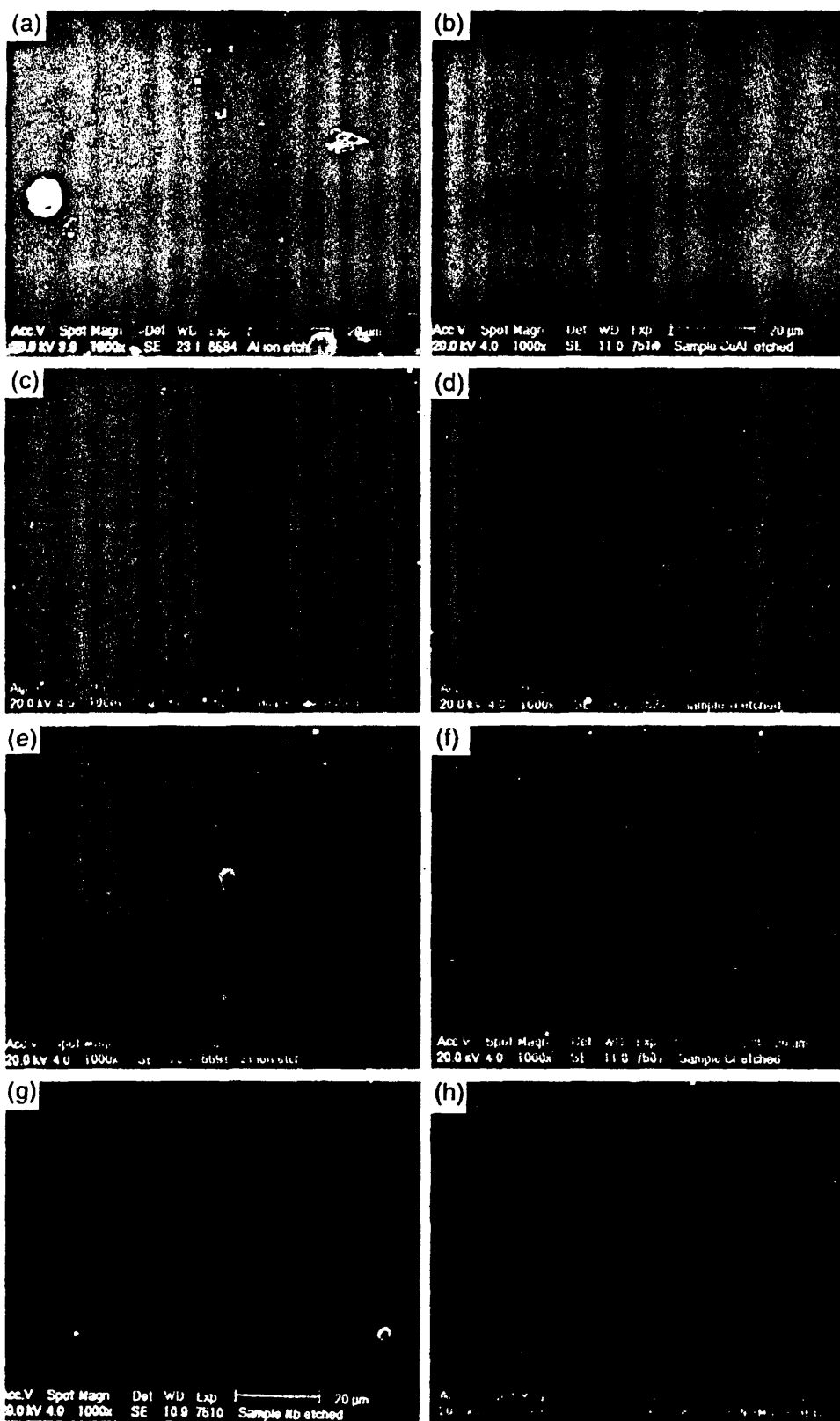


Figure 3. Scanning Electron Micrographs showing the surface topography of the metal ion etched surfaces (a) aluminium, (b) copper alloy, (c) titanium-aluminium, (d) titanium, (e) zirconium, (f) chromium, (g) niobium and (h) molybdenum.

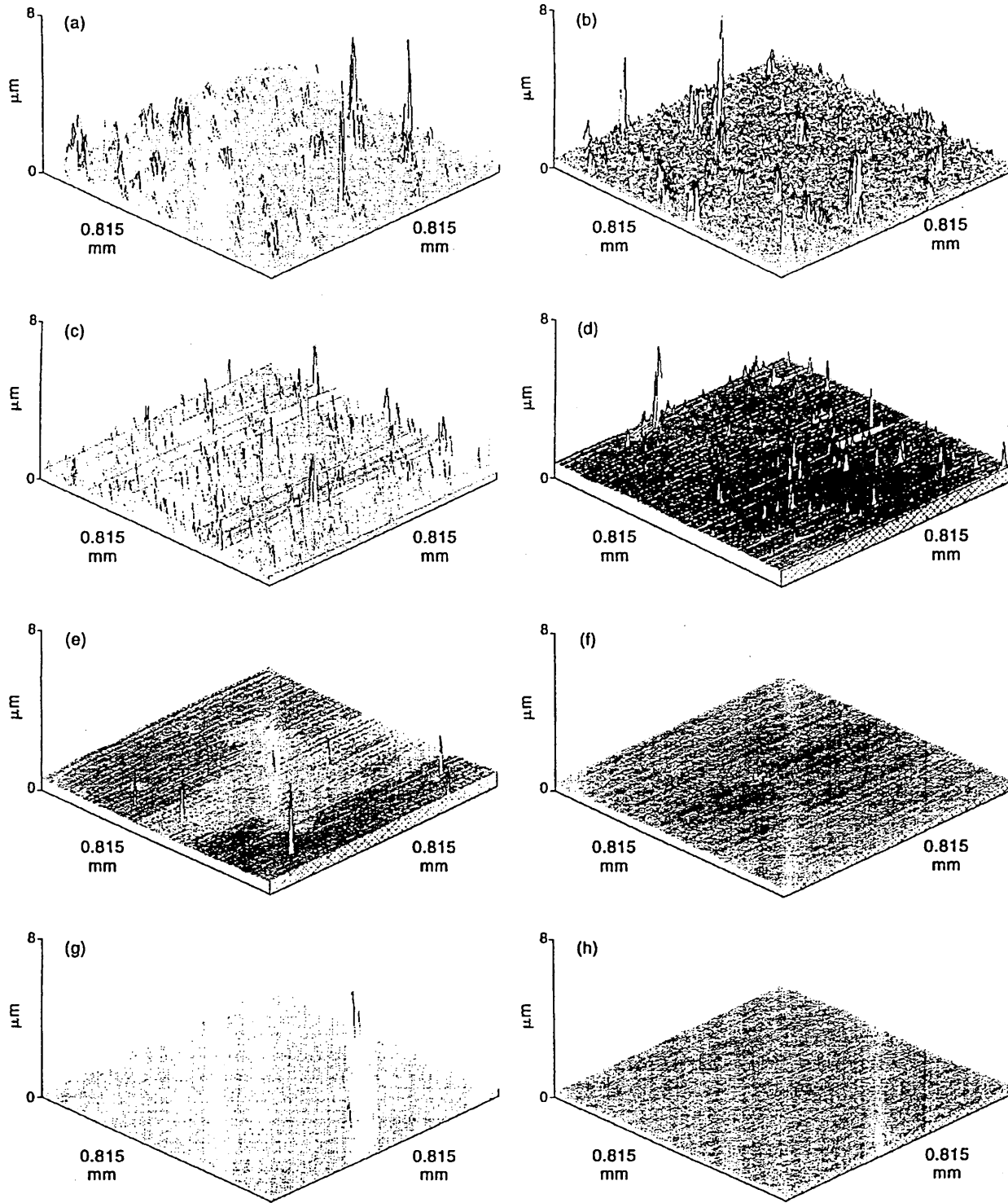


Figure 4. Surface Profiles of the metal ion etched surfaces (a) aluminium, (b) copper alloy, (c) titanium-aluminium, (d) titanium, (e) zirconium, (f) chromium, (g) niobium and (h) molybdenum.

and then, during the cooling down phase, the liquid droplets seemed to further vapourise and shrink. Finally, the droplets solidified with a typical rapid solidification pattern. Figure 5(a) shows a further magnified pair of droplets in the centre of two surrounding and overlapping halos. The EDX mapping measurements indicate an accumulation of Al in the edge zone of the splashed droplet (Figure 5(b)). Together with the enhanced Fe signal in the centre of the droplet, (Figure 5(c)), one may conclude, therefore, that a reduced thickness of Al exists in the centre of the droplet. This droplet morphology is in agreement with results found by Anders *et al.*<sup>8</sup> for W with a substrate to target distance as low as 6 cm. Figure 5(b) shows that EDX mapping is not sensitive enough to detect the presence of Al in the halo region, indicating that the reaction depth is very thin. Only the more sensitive EDX spot analysis, carried out within and just outside the observed halo, confirms the presence and therefore the reaction of molten Al with the steel substrate (Figures 6(a) and (b)). It is also interesting to note that in various cases the droplet has vapourised completely thus leaving back droplet-free halos. The lack of small droplets may be explained by vapourisation effects on the way from the target to the substrates.

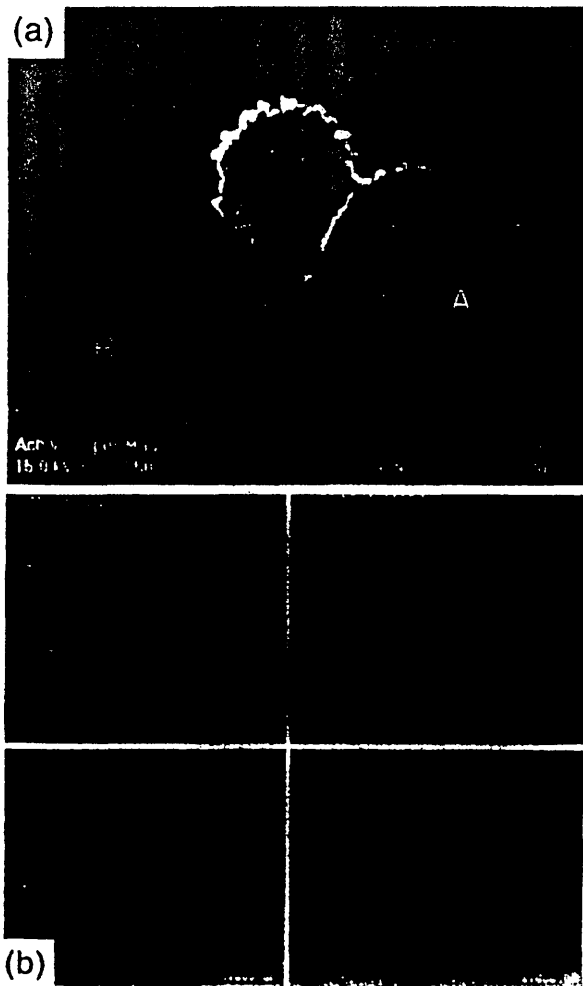


Figure 5. Scanning Electron Micrograph of the aluminium ion etch surface at a higher magnification (a) and X-ray distribution maps from the same surface for Al K  $\alpha$ , (b) and (c) Fe K  $\alpha$ .

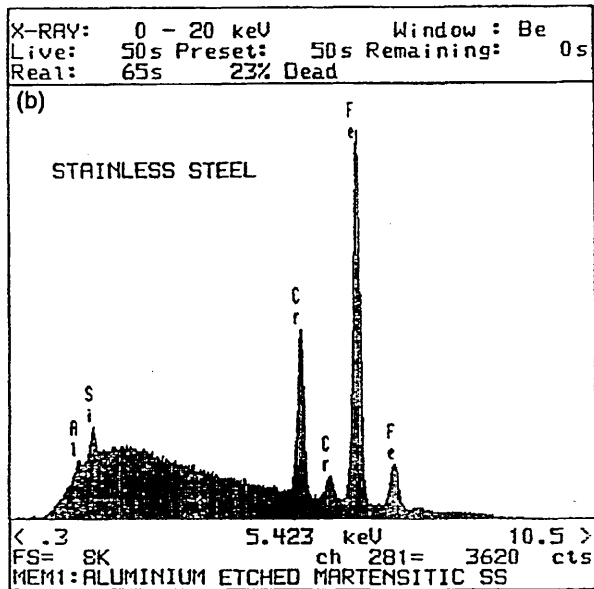
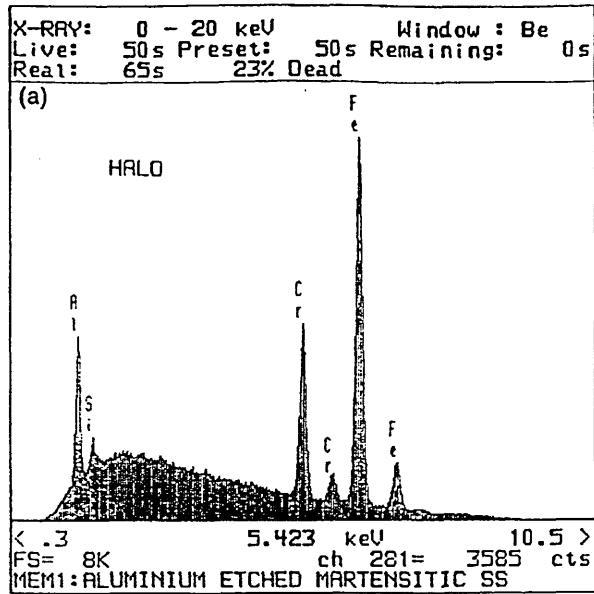


Figure 6. Energy Dispersive Analysis (EDX) of regions A (a) and B (b) in Figure 5(a).

Boxman *et al.*<sup>7</sup> suggest typical droplet temperatures of approximately 2000°C and typical transport velocities around 100 m s<sup>-1</sup>. While the typical target to substrate distance is 20–80 cm, the estimated flight time comes up to 2–8 ms. The free surface vapourisation rate of Al *in vacuo* at 1500°C is approximately  $2 \times 10^{-2} \text{ g cm}^{-2} \text{ s}^{-1}$ .<sup>21</sup> A 0.5  $\mu\text{m}$  diameter Al droplet should evaporate and therefore disappear during flight after approximately 1 ms. This conclusion is confirmed by earlier related findings attributed to the generation of TiAl droplets. There, small TiAl droplets suffer a loss of Al, obviously caused by fractionated evaporation of Al, (free surface vaporisation rate of Ti: at 1500°C:  $3 \times 10^{-5} \text{ g cm}^{-2} \text{ s}^{-1}$ ). Large droplets, however, with a higher overall Al content are maintained during flight and after arrival the

original target composition.<sup>17</sup> In the case of the higher melting materials the vast majority of droplets are strictly spherical in shape. It may be assumed consequently that all of them have already solidified under the actual geometrical conditions during flight.<sup>9,17</sup> Only very few non-spherical droplets were found for TiAl (Figure 3(c)) and one singular, rather large example for Zr (Figure 3(e)). In the case of Cr, surprisingly small droplets were observed. This result can be attributed to the fact, that liquid and solid Cr exhibits an extraordinary (up to several orders of magnitude higher) vapour pressure (Table 2)<sup>22</sup> than the neighbouring high melting materials Ti, Zr, Nb and Mo.<sup>21</sup> Therefore, even solidified Cr droplets may shrink due to sublimation either during flight or after arrival. The number of Cr droplets is twice as high as for example Zr (Table 2). Assuming that this result is not an inherent statistical error of the evaluation method used, one can argue that the chromium target might have picked up oxygen stemming from the residual gas, when molten under the influence of the cathodic arc. It has been reported that a Cr<sub>2</sub>O<sub>3</sub> content of only 1 mass per cent depresses the melting point to 1770°C,<sup>22</sup> thus the melting point drops into the range between Ti and Zr.

On the other hand Nb and Mo behave quite similarly. Both the maximum droplet size and the number of droplets are comparable. Although Ta and W have not been investigated explicitly here, no further reduction of defects should be expected with cathode melting temperatures beyond 2000°C.

In the case of Cu as a target material, the following conclusions may be drawn: the considerable lack of very small droplets may be explained with the same arguments applying for Al. Cu exhibits very similar vapour pressure properties to that of Al (Table 2). In addition one can argue, that Cu has very different thermal and electrical properties in comparison to the high melting materials investigated here. Table 2 gives a thermal conductivity of 394 W m<sup>-1</sup> K<sup>-1</sup> and a resistivity of 1.7 μΩ cm for Cu in comparison to 16–91.3 W m<sup>-1</sup> K<sup>-1</sup> and 5.7–54 μΩ cm for Ti, Zr, Cr, Nb and Mo.<sup>23</sup> If it is true that the average target temperature<sup>24</sup> and the target cooling efficiency play an important role in the suppression of droplets, then the extremely high thermal conductivity of Cu may serve as a reasonable explanation for reduced droplet production due to the reduced front-surface temperature of the target.<sup>7</sup> The thermal properties of Cu overrule the importance of the melting point in this case. However, the melting point seems to be high enough to allow the majority of droplets to solidify during flight preventing considerably the formulation of flat splashes on the substrate surface. The role of the resistivity may be interpreted in a similar manner. Superheating of the metal melt under the influence of high locally constricted arc current densities may be minimised by the extremely low resistivity of Cu. Indeed, Anders *et al.*<sup>5</sup> have found the thermally and electrically highly conductive materials Cu and Ag to behave more like W rather than as the similar melting point materials Ni and Pt do. Both latter materials are characterised by low thermal conductivity and high resistivity values (Table 2).

In the preceding sections results obtained on uncoated samples only have been discussed. Figures 7(a), (b) and (c) show the surface morphology of TiAl, Cr and Mo etched samples after the deposition of approximately 3 μm of TiAlN. These results show a similar number of droplets to the equivalent surfaces after etching (Figures 3(c), (f) and (h)). A quantitative comparison of visually evaluated droplet numbers from SEM micrographs shows that the number of defects does not change dramatically after the application of the TiAlN coatings. That proves in the

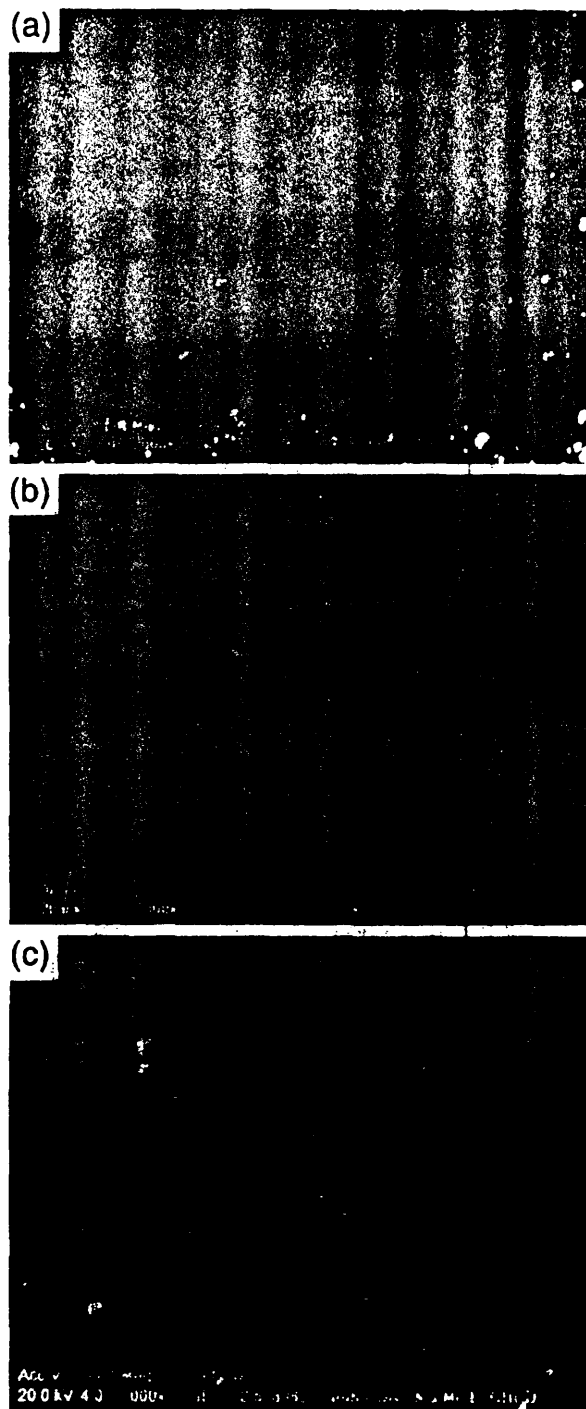


Figure 7. Scanning Electron Micrographs showing the surface topography after (a) titanium–aluminium, (b) chromium and (c) molybdenum ion etching, respectively, after the deposition of 3 μm of TiAlN.

first place the assumption that every droplet causes a detectable growth defect and that no droplets are being 'buried' during film growth. In the case of TiAl etched and TiAlN coated samples slightly more defects are counted, namely  $110 \times 10^3 \text{ mm}^{-2}$ , than those for the etched sample (Table 2). For Cr etched coatings the resulting number of defects was  $6 \times 10^3 \text{ mm}^{-2}$ , somewhat less

than in the etched case. On first assumption the deviation of these values from those of the etched samples may be due to a statistical error in the applied counting method. However, as no droplets are generated during UBM deposition, it must be concluded that droplets stemming from the etching phase, independent of their size, have generated growth defects reaching right through the complete coating to the surface. Only if the decrease in the defect number on Cr etched samples is indeed not a statistical effect and there are indications on SEM that some of the smaller Cr droplets might have been covered and buried by the subsequent TiAlN coating process. It is obvious that the 3  $\mu\text{m}$  thick TiAlN film cannot cover similar or larger size droplets completely. SEM micrographs of TiAl and Cr etched TiAlN coated surfaces taken at higher magnifications, (Figure 8(a) and (b)) show gaps around the very large size defects. These gaps may be correlated to shadowing effects due to the line of sight nature of the sputter process. However, smaller defects ( $d < 1 \mu\text{m}$ ) seem to be incorporated rather tightly into the coating matrix. The TEM cross-section included in Figure 9 show at 60K magnification a  $\approx 0.5 \mu\text{m}$  thick defect growing from a smaller droplet at the interface parallel to the growth direction towards the film surface. No gaps or voids are observed. The diameter of growth defect increases only during the initial growth stage and then stays constant. There is obviously a significant difference in droplet

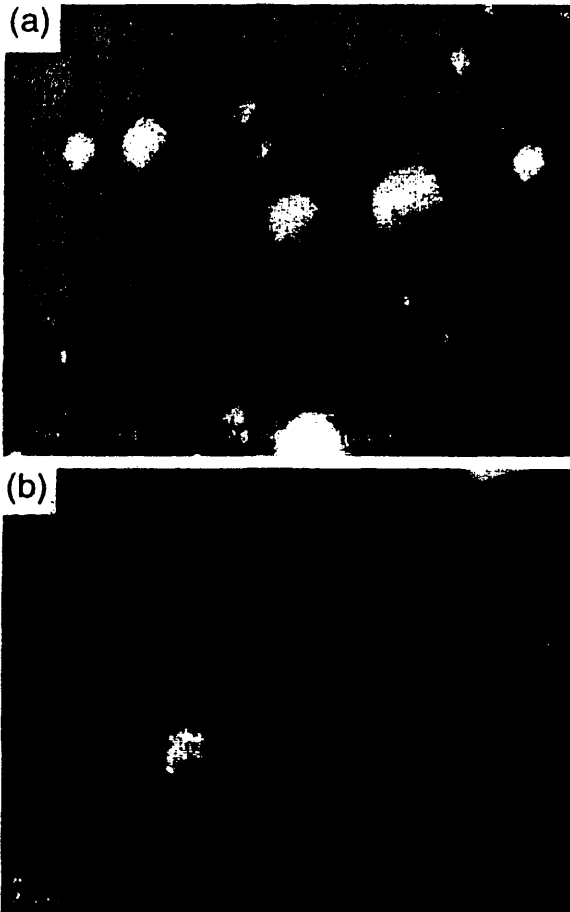


Figure 8. Scanning Electron Micrographs showing the surface topography, at a higher magnification after (a) titanium-aluminium and (b) chromium ion etching, respectively, after the deposition of 3  $\mu\text{m}$  of TiAlN.

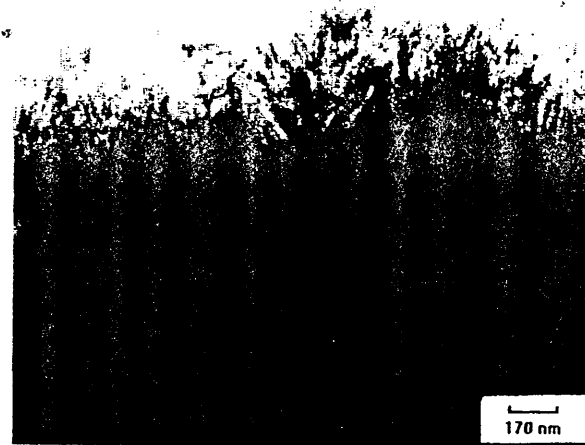


Figure 9. A cross section Transmission Electron Micrograph of a TiAlN coating.

cross sections found in arc deposited coatings. Small droplets incorporated into the coating during film deposition cause growth defects, which decrease in diameter during further film growth<sup>9</sup> and seem to be 'healed' after 3  $\mu\text{m}$  of further growth, as TEM cross sections of purely arc deposited TiN coatings show.

Finally the roughness of coated samples will be briefly discussed. Here we also found a significant improvement towards a smoother surface if one replaces the TiAl etching step with a Cr or Mo etch. A reduction in surface roughness by a factor of 3 has been reproducibly achieved. If one compares these results with published roughness values, in particular, with a purely arc TiAlN deposition process<sup>13,14</sup> the scale of process improvement becomes fully apparent Table 3.

Field tests of coated drills have shown that the results on dry cutting of cast iron at high cutting speeds directly benefit from an improved surface roughness. The lifetime of version (B) coated drills may be doubled in the case of version (C).<sup>18,25</sup> These large differences cannot be observed, when operating drills with lubricants.

**Conclusions**

The results gained from the present study may be summarised as follows:

- The melting point of the cathode target material clearly affects the number of droplets or growth defects incorporated into the growing TiAlN coating. The use of etching materials with high melting points reduces the droplet counted on the etched

Table 3

(A)	Pure arc process	$R_a$ : 0.3-0.5 $\mu\text{m}$
(B)	ABS process (TiAl etch)-	$R_a$ : 0.15 $\mu\text{m}$
(C)	ABS process (Cr etch)-	$R_a$ : 0.05 $\mu\text{m}$

samples as well as the number of growth defects in the UBM deposited hard coating.

- The number of defects in a 3  $\mu\text{m}$  coating is practically identical with the number of droplets counted directly after the metal ion etching steps. No significant burying phenomena of droplets have been observed (except for very small Cr droplets). Gaps and voids have only been found for defects considerably larger than 1  $\mu\text{m}$  in diameter.
- The proposed process steps to produce a smooth TiAlN coating, namely ion etching with either Cr or Mo and TiAlN deposition by UBM, leads to superior results either as compared with a wholly TiAl based ABS process or in particular to a purely cathodic arc deposition technique. Cr and Mo ion etched and TiAlN UBM coated samples show even fewer defects ( $6 \times 10^3 \text{mm}^{-2}$ ) than the much less droplet sensitive cathodic arc TiN deposition ( $100 \times 10^3 \text{mm}^{-2}$ )<sup>9,26</sup> with their above mentioned healing effects.<sup>9</sup>

Kang et al. have recently shown the affirmative power of SEM based semi-quantitative image analysis on the evaluation of droplet generation in various cathodic arc process modifications of TiN deposition. In particular with respect to droplet sizes in the range 0.1–1.0  $\mu\text{m}$ .<sup>26</sup> Although, in themselves, the observations gained in the present paper are conclusive, it would seem worthwhile to extend our investigations by using this powerful analytical method to produce even more precise results.

#### Acknowledgements

The work presented has been partially, supported by funds of the BRITE/EURAM project BE 4118 'COCO' and the national UK research programme LINK SURFACE ENGINEERING project no. GK/K76351. The authors want to express their thanks to G Gregory, from the MRI, at Sheffield Hallam University, who has prepared the TEM cross-section sample and micrograph.

#### References

1. Münz, W.-D., Hauzer, F.J.M. and Schulze, D., *Surf. Coat. Technol.*, 1992, 50, 169.

2. Håkansson, G., Hultman, L., Sundgren, J.-E., Greene, J.E. and Münz, W.-D., *Surf. Coat. Technol.*, 1991, 48, 51.
3. Petrov, I., Losbichler, K., Bergstrom, D., Greene, J.E., Münz, W.-D., Hurkmans, T. and Trinh, T., to be published in *Thin Solid Films*.
4. Weber, T., Verhoeven, J., Saris, F.W., Osipowicz, T. and Münz, W.-D., *Nuc. Instr. Meths. Phys. Res.*, 1995, B106, 159.
5. Münz, W.-D., Hurkmans, T., Keiren, G. and Trinh, T., *J. Vac. Sci. Technol.*, 1993, A11(5), 2583.
6. Sproul, W.D., Rudnik, P.J., Legg, K.O., Münz, W.-D., Petrov, I. and Greene, J.E., *Surf. Coat. Technol.*, 1993, 56, 179.
7. Boxman, R.L. and Goldsmith, S., *Surf. Coat. Technol.*, 1992, 48, 51.
8. Anders, S., Anders, A., Yu, K.M., Yao, X.Y. and Brown, I.E., *IEEE, Trans. Plasma Science*, 1993, 21(5), 440.
9. Ljungcrantz, H., Hultman, L., Sundgren, J.-E., Håkansson, G. and Karlsson, L., *Surf. Coat. Technol.*, 1994, 63, 123.
10. Ramalingam, S. and Qi, C.B., Kim, K., *US Pat*, 1987, 4673, 977.
11. Ertürk, E., Heuvel, H.J. and Dederichs, H.G., *Surf. Coat. Technol.*, 1989, 39/40, 455.
12. Akari, K., Tamagaki, H., Kumekiri, T., Tsuji, K., Koh, E.S. and Tai, C.N. *Surf. Coat. Technol.*, 43/44, 312 (1990).
13. Ertürk, E., Heuvel, H.J. and Dederich, H.G., *Plasma Surface Engineering*, DGM, eds E. Broszeit, W.-D. Münz, H. Oechsner, R.T. Rie and G.K. Wolf. Informationsgesellschaft Verlag, Oberursel, Germany, 1988, p. 553.
14. Coll, B.F., Fontana, R., Gates, A. and Sathrum, P., *Mat. Sci. Eng.*, 1991, A140, 816.
15. Coll, B.F., Sathrum, P., Fontana, R., Peyre, J.P., Duchateau, D. and Benmalek, M., *Surf. Coat. Technol.*, 1992, 62, 57.
16. Tanaka, Y., Gur, T.M., Kelly, M., Hagstrom, S.B., Ikeda, T., Wakihira, K. and Satoh, H., *J. Vac. Sci. Technol. A.*, 1992, 10, 1749.
17. Münz, W.-D., Lewis, D.B., Creasey, S., Hurkmans, T., Trinh, T. and v IJzendorf, W., *Vacuum*, 1995, 46(4), 323.
18. Smith, I.J., PhD thesis, Sheffield Hallam University, unpublished work, 1995.
19. Hauzer Techno Coating Europe BV, Venlo. The Netherlands, BRITE-EURAM project BE 4118 'COCO'.
20. Daalder, J.D., *J. Phys., D., Applied Physics*, 1976, 9, 2379.
21. ASTM Handbook, Vol. 51, Surface Engineering. ASTM International, Materials Park, OH, USA, 1994, p. 558.
22. Sully, A.H. and Brandes, E.A., *Metallurgy of Rare Metals: Chromium*. Butterworths and Co Ltd Publishers, London, 1967, p. 78.
23. *Smithells Metals Reference Book*, 7th Ed., eds E.A. Brandes and G.B. Brook. Butterworth-Heinemann Ltd, Oxford, UK, 1992.
24. Zenner, R.L.D., Multi-Arc Internal Report, 19 October, 1986, referenced by 7.
25. Münz, W.-D., Smith, I.J., Donahue, L.A. and Brooks, J.S., patent pending.
26. Kang, G.H., Uchida, H. and Koh, E.S., *Surf. Coat. Technol.*, 1994, 68/69, 141.

# SEM image analysis of droplet formation during metal ion etching by a steered arc discharge

S. Creasey, D.B. Lewis, I.J. Smith, W.-D. Münz \*

*Materials Research Institute, Sheffield Hallam University, City Campus, Pond Street, Sheffield, S1 1WB, UK*

## Abstract

During cathodic arc metal ion etching a pronounced influence of the melting point of the target material on droplet formation was found. Low melting point materials showed quite an enhanced tendency to generate droplets with respect to number and size. Under the process parameters used the TiAl alloy target showed the highest number of droplets generated ( $100 \times 10^3 \text{ mm}^{-2}$ ). Even using target materials with high melting points such as Zr (MP: 1850 °C), Cr (MP: 1870 °C) and Nb (MP: 2450 °C) severe differences were observed. Cr played a special role as 90% of its droplets were smaller than 0.5  $\mu\text{m}$ . For Zr with a melting point close to Cr the same percentage of droplets were less than 0.80  $\mu\text{m}$  in diameter, clearly indicating a larger average droplet diameter. On the other hand, among the high melting materials the number of Cr droplets was 5 times higher than that of Nb and twice as high as that of Zr. Metals with melting points greater than 2000 °C showed very similar effects of droplet generation, with mean droplet densities of  $3\text{--}5 \times 10^3 \text{ mm}^{-2}$ . A comparison between the as-etched and UBM coated samples indicates that the number of droplets deposited during the etching phase with TiAl and Mo formed an identical number of growth defects in the coating. In the case of Cr the number of defects on top of the coated surface was less than the number of droplets deposited during the etching phase. © 1997 Elsevier Science S.A.

**Keywords:** Droplet formation; Growth defects; Metal ion etching; SEM image analysis; Steered arc discharge

## 1. Introduction

Metal ion etching is an important step in cathodic arc evaporation and combined steered arc evaporation/unbalanced magnetron sputtering techniques to achieve and promote high and reliable adhesion values for PVD hard coatings on steel substrates [1,2]. However, it is very well known that during this process droplets are generated which adhere badly to the substrate surface and cause growth defects particularly in TiAlN coatings [3], which in special cases substantially reduce the performance of coated tools [4]. In a previous paper [5] it has been shown that the melting temperature of the cathodic target material influences the size and number of droplets generated during the metal ion etching step. In the present paper, image analysis techniques are applied to create a quantitative impression of the droplet problem. In the following Cu, TiAl (50:50 at.%), Ti, Zr, Cr, Nb and Mo are investigated as etching media. Additionally the droplet morphology of a 3  $\mu\text{m}$  thick TiAlN coating has been investigated with TiAl, Cr and Mo as metal etching

source and the unbalanced magnetron (UBM) as deposition source.

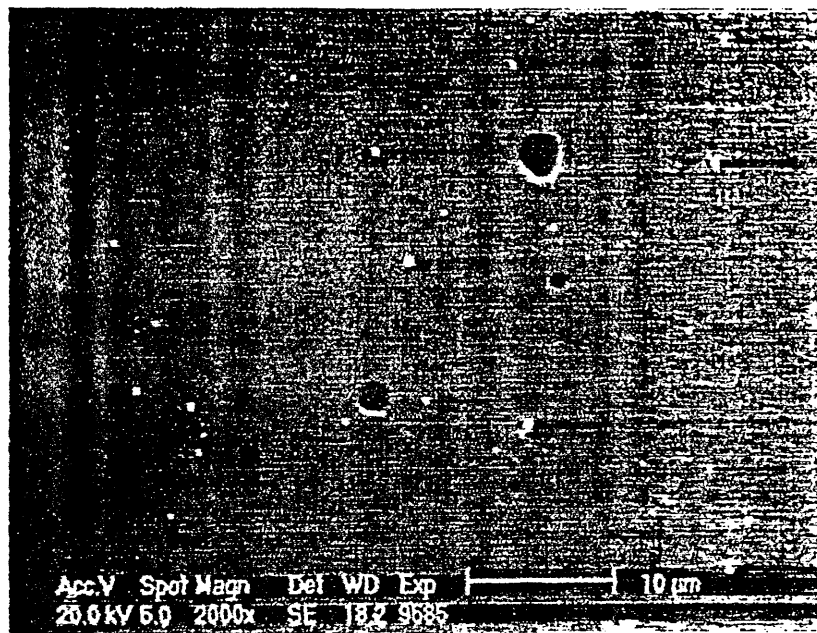
To avoid interpretation difficulties the following clarification will be made: In the following investigation, the macroparticles produced by the cathodic arc discharge and deposited on the substrate during etching phase are designated as “droplets”. On top of these “droplets”, “growth defects” are generated during the UBM sputtering phase, which extend through the growing film [5].

## 2. Experimental details

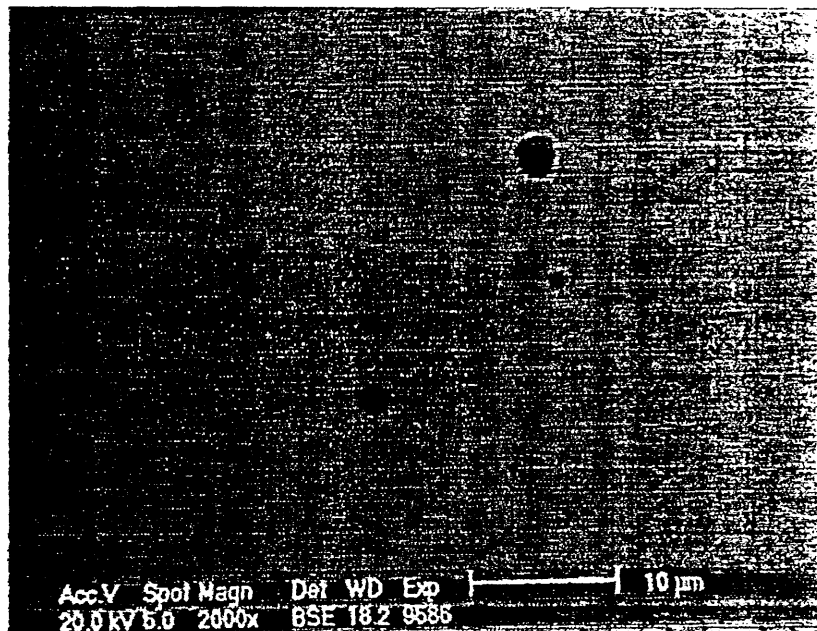
### 2.1. Etching and coating conditions

All coating experiments were performed in a commercially available industrially sized PVD coater HTC-1000 ABS produced by Hauzer Techno Coating Europe BV, Venlo, The Netherlands [2]. The following data describe the etching process briefly:  $U_{\text{Etch}} = -1200 \text{ V}$ ,  $I_{\text{Arc}} = 100 \text{ A}$ ,  $P_{\text{Ar}} = 2 \times 10^{-3} \text{ mbar}$ ,  $T_{\text{Etch}} \approx 450 \text{ °C}$ ,  $t_{\text{Etch}} = 10 \text{ min}$ ,  $H_{\text{II}} = 50 \text{ G}$  with a distance from target to substrate of  $\approx 30 \text{ cm}$ . All target materials were cast. Full

\*Corresponding author. Tel: 01142 533500; Fax: 01142 533501.



(a)



(b)

Fig. 1. Scanning electron micrographs showing secondary and backscattered electron images from identical regions of a substrate after cathodic arc etching with a Cr target.

details on the process parameters used in the current investigation are given in [5].

The substrate materials used were austenitic stainless steel (316). All the substrates were 30 mm in diameter, 5 mm thick and polished to a 1  $\mu\text{m}$  diamond finish.

## 2.2. Image analysis

The morphology of the metal ion etched and metal ion etched and coated samples was examined using a

Philips XL40 scanning electron microscope. The number, size, area, shape and distribution of droplets and growth defects was assessed using the image analysis software Featurescan<sup>®</sup> [6] in conjunction with the SEM. It has recently been shown that SEM based image analysis is a powerful technique for the evaluation of droplet generation, particularly with respect to droplets in the size range 0.1–1.0  $\mu\text{m}$  in various TiN cathodic arc process deposition modifications [7].

The major requirement for image analysis is that there

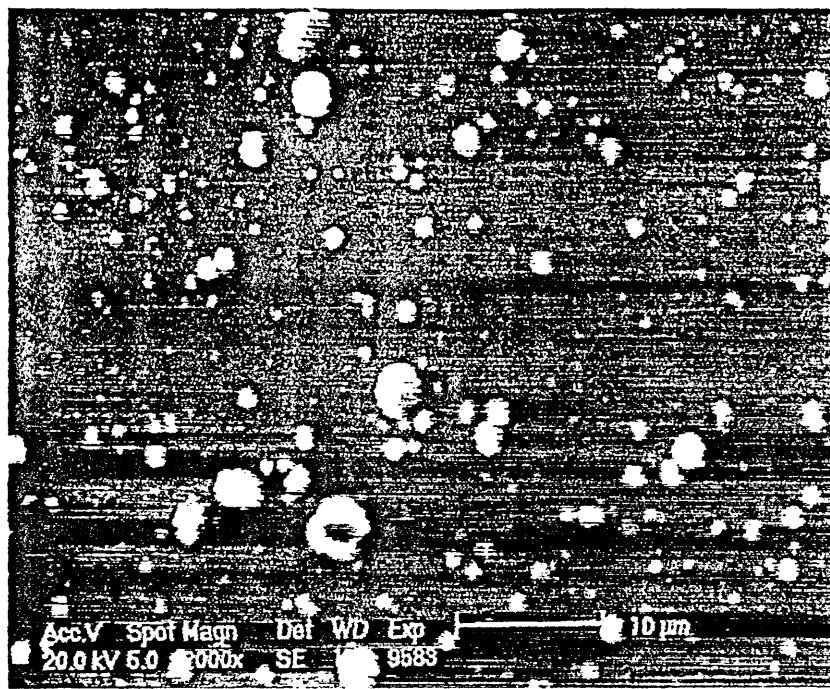


Fig. 2. A scanning electron micrograph from a TiAl etched substrate which had been coated with 3  $\mu\text{m}$  of TiAlN.

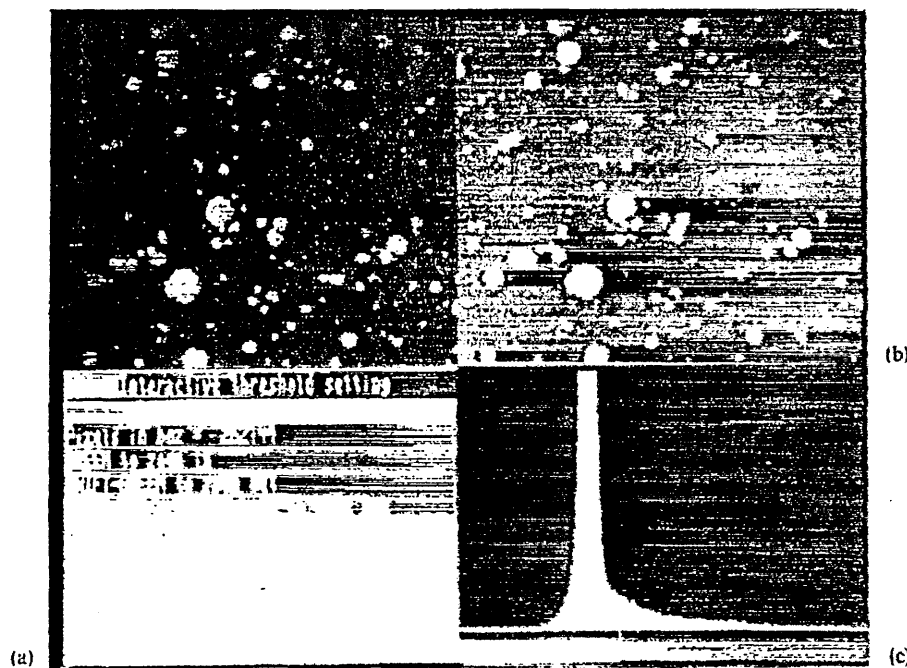


Fig. 3. Micrographs showing thresholding of the signal intensity of the SEM image shown in Fig. 2: (a) binary image; (b) digitised image; (c) histogram displaying the distribution of grey levels within the image.

There must be a significant contrast between the features of interest and the background. Secondary and backscattered electron images from identical regions of a substrate surface, after cathodic arc etching with Cr are included in Fig. 1a and b respectively. The secondary electron image (Fig. 1a) clearly shows a significant contrast between droplets and background, whereas in the

backscattered image (Fig. 1b) the droplets are almost indistinguishable from the background. Thus, the specimens for this paper were imaged using the secondary electron, rather than the backscattered electron imaging mode.

A secondary electron image from a TiAl etched substrate which had been coated with 3  $\mu\text{m}$  of TiAlN is

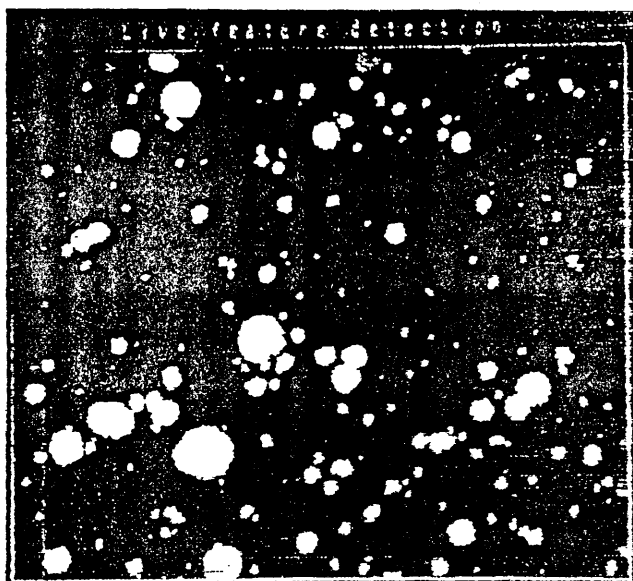


Fig. 4. An image showing the features detected in the image shown in Fig. 2.

shown in Fig. 2. The secondary electron image from the SEM was subsequently converted to a digital image with a range of grey levels from 0 to 255 (Fig. 3b). The primary basis of detection is to threshold ranges of signal intensities (Fig. 3a and c), which are subsequently used to detect features with different grey levels from the background intensity (Fig. 4). Measurements are made on the features detected. The set up, detection and measurements used for image analysis is shown in Table 1.

### 3. Results and discussion

#### 3.1. Cathodic arc etching process

The number, fraction of sample surface area covered by droplets,  $A_d$ , maximum diameter, mean diameter, circularity factors, size range at 90%-ile and size distribu-

tion of the droplets generated during cathodic arc etching for all target materials have been evaluated quantitatively by image analysis (M 4000). The estimated spatial resolution for small droplets is  $0.12 \mu\text{m}$  in diameter. Bar charts showing the size distribution of droplet formation are included (Fig. 5a-g). Tables 2 and 3 summarise the results in terms of number, fraction of sample surface area covered by droplets, maximum diameter, size range at 90%-ile, and mean diameter,  $d^*$ . Surface roughness values  $R_a$  and  $R_z$  [5] have also been included in Table 2 for comparison purposes. Quantitative analysis indicates the highest number of droplets for TiAl alloy is  $100 \times 10^3 \text{ mm}^{-2}$  whereas the number of droplets for the lower melting point Cu is less at  $60 \times 10^3 \text{ mm}^{-2}$ . Comparing the droplet size distributions for TiAl and Cu shows significant differences between the two target materials (Fig. 5a and b). In the size range up to  $1 \mu\text{m}$  the TiAl etched substrate had almost twice the number of droplets of that of Cu, whereas for the size range  $2-4 \mu\text{m}$  the number of droplets detected for the two materials was almost identical. In the size range  $4-8 \mu\text{m}$  however, more droplets were detected on substrates after cathodic arc etching with Cu. The importance of the melting temperature of cathodic arc target materials has been pointed out by [5]. Purely on the basis of melting temperature one would predict that the Cu target should generate, for all size ranges, many more droplets than the TiAl alloy target. However, in the case of Cu as a target material the lower incidence of droplets in the size range up to  $1 \mu\text{m}$  may be explained in terms of vapour pressure. Cu exhibits a much higher vapour pressure than TiAl. Hence, the small Cu droplets generated during cathodic arc etching evaporate and some disappear during flight from the target to the substrate. Droplet vaporisation has also been observed for Al [5] which has a similar vapour pressure to that of Cu. Larger droplets because of their lower surface area to volume ratio are speculated not to change significantly in size during flight from target to substrate.

The maximum droplet size detected was  $7.4 \mu\text{m}$  for

Table 1  
Image analysis set up detection, measurement and sizing

Image source-live, resolution $1024 \times 1024$ , noise reduction 20 samples
Features touching frame edges excluded, features smaller than 5 pixels excluded
Measurements from basic field area and feature data: field area, no of particles detected, area of features detected. From field area and area of features detected fraction of sample surface area covered by particles is determined
Morphological measurements: feret projections 60, perimeter measurements
Measurements derived from feret and perimeter: mean particle diameter, circularity, maximum particle diameter, particle diameter at 90%-ile
Magnification used $\times 4000$ , field width $46.944 \mu\text{m}$ and field height $46.2705 \mu\text{m}$
Resolution of $1024 \times 1024$ pixels hence minimum dia particle which can be measured is approx. $0.12 \mu\text{m}$
Area of each field $1961 \mu\text{m}^2$ ; total area of 60 fields $0.1176 \text{ mm}^2$

Mean feret is the average of 60 feret projections and is taken as the particle diameter. Circularity factors are calculated from  

$$\text{circularity factor} = \frac{\text{perimeter}}{2\sqrt{\text{area} \times \pi}}$$
 where the circularity factor for a circle is 1.

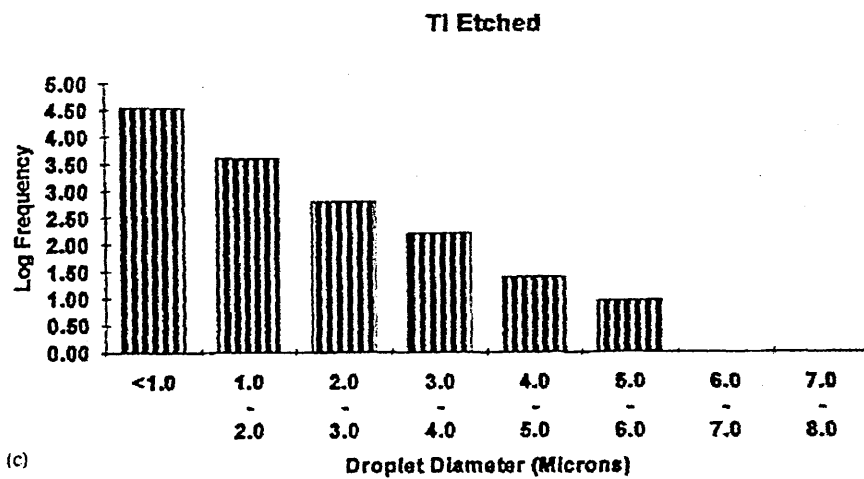
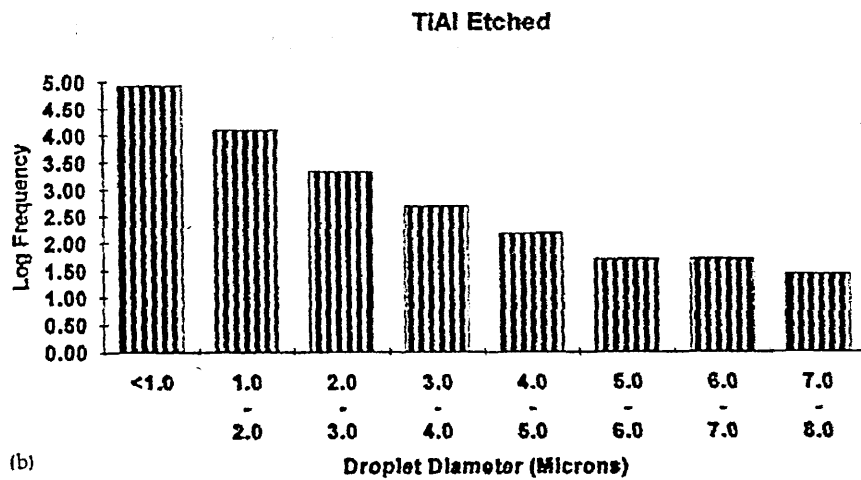
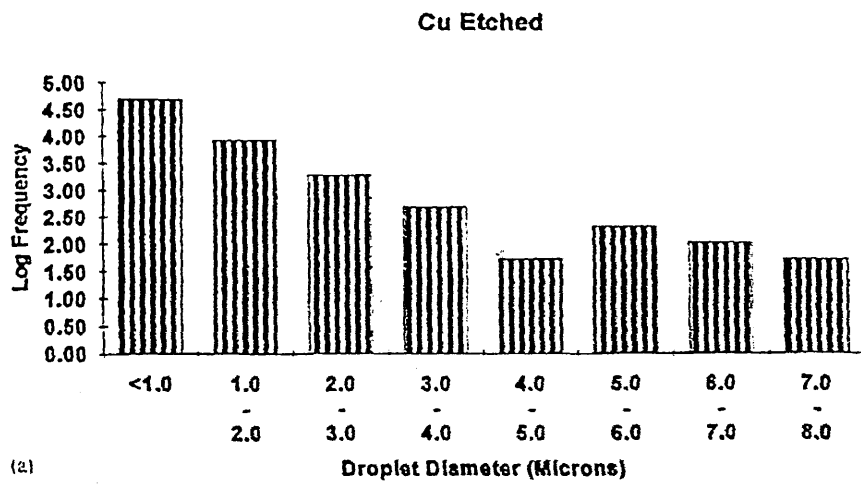


fig. 5. Bar charts showing the size distribution of droplets on metal ion etched surfaces: (a) copper alloy; (b) titanium-aluminium; (c) titanium; (d) zirconium; (e) chromium; (f) niobium; (g) molybdenum.

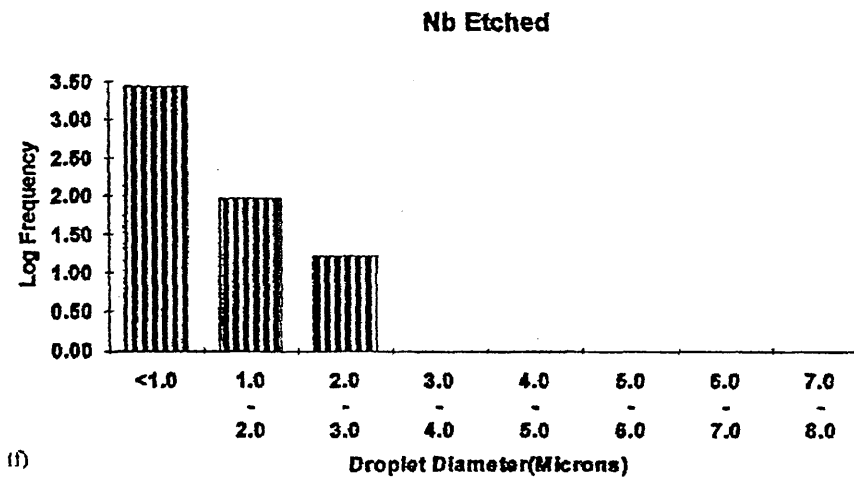
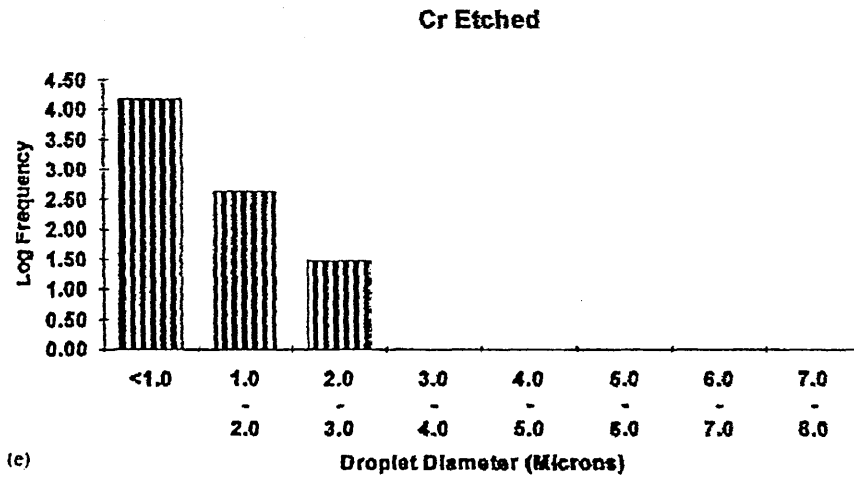
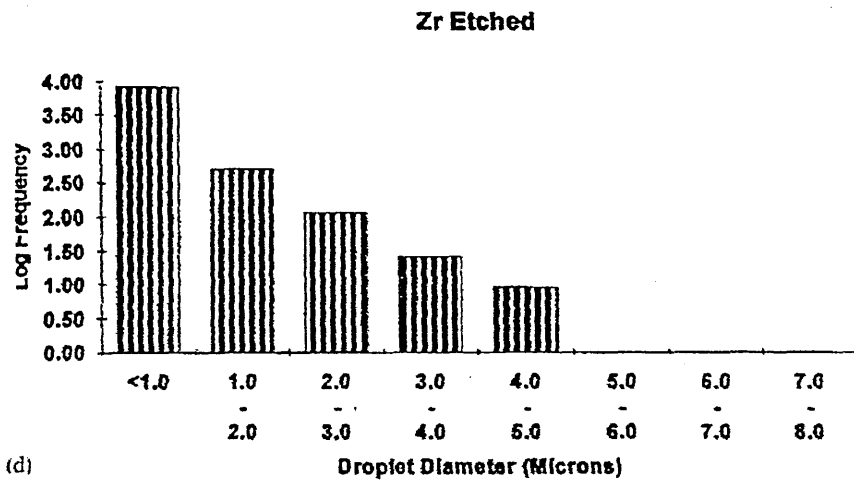


Fig. 5. (continued)

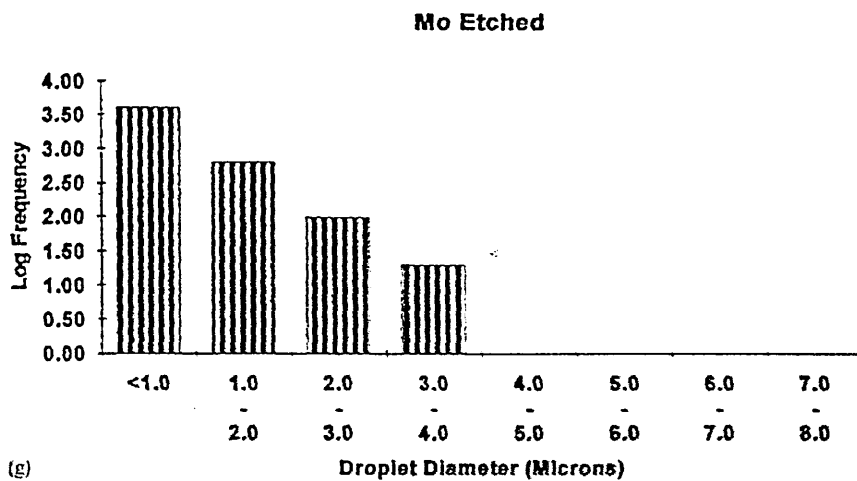


Fig. 5. (continued)

the TiAl alloy. The maximum droplet diameter decreases rapidly with increasing melting temperature as can be observed for Cu, TiAl, Ti and Zr cathode materials (Table 2). For materials with higher melting temperatures ( $>2000$  °C), both the maximum droplet size and the number of droplets generated seem to be independent of the melting temperature. In fact the maximum droplet diameter was larger for the higher melting point Mo compared with Cr and Nb.

The majority of the large Cr droplets were between  $\sim 2$   $\mu\text{m}$  in diameter, with a maximum particle diameter of  $2.4$   $\mu\text{m}$  which was smaller than those observed from the higher melting point materials Nb and Mo,  $2.9$   $\mu\text{m}$  and  $3.9$   $\mu\text{m}$  respectively. In the case of Cr surprisingly small droplets were observed compared with that of the similar melting point material Zr. The droplet size distribution

distributions for the Zr and Cr showed significant differences between the two target materials (Fig. 5d and e). Thus, the substrate etched with the Cr target had significantly fewer droplets with diameters greater than  $1$   $\mu\text{m}$  than that etched with Zr. In fact for Cr 90% of the droplets had diameters less than  $0.5$   $\mu\text{m}$ . For Zr the same percentage of droplets had diameters less than  $0.86$   $\mu\text{m}$ , which was reflected in its larger average droplet size,  $d^*$ . These results can be attributed to the fact, that like Cu in comparison to TiAl, liquid and solid Cr exhibits an extraordinarily, up to several orders of magnitude, higher vapour pressure (Table 2, [8]) than the neighbouring high melting materials Ti, Zr, Nb and Mo [9]. Therefore, even solidified Cr droplets may shrink due to sublimation either during flight or after arrival at the substrate [5].

Material	Melting point (MP) (°C)	Vapour pressure at 2000 °C (mbar)	Maximum droplet size ( $\mu\text{m}$ )	Number of droplets/area ( $\times 10^3$ $\text{mm}^{-2}$ )	$R_z$ ( $\mu\text{m}$ ) [5]	$R_c$ ( $\mu\text{m}$ ) [5]
Cu	1000	53	7.2	60	0.055	1.22
TiAl	1450	*	7.4	100	0.071	1.08
Ti	1660	$2.6 \times 10^{-1}$	5.3	40	0.017	0.78
Zr	1850	$20 \times 10^{-3}$	4.8	8	0.011	0.50
Nb	1870	13	2.4	15	0.009	0.14
Mo	2450	$2.6 \times 10^{-6}$	2.9	3	0.005	0.10
Mo	2650	$5.3 \times 10^{-5}$	3.9	5	0.009	0.14

Not available.

Table 3

Material	Mean droplet diameter $d^*$ ( $\mu\text{m}$ )	Circularity of droplets at 80%-ile	Fraction of sample area covered by droplets, $A_d$	Droplet diameter at 90%-ile ( $\mu\text{m}$ )
Cu alloy	0.63	1.5	0.034	1.3
TiAl	0.63	1.4	0.045	1.16
Ti	0.55	1.2	0.0073	1.01
Zr	0.5	1.15	0.0027	0.86
Nb	0.4	1.2	0.0021	0.56
Mo	0.4	1.15	0.0008	0.56
Mo	0.58	1.15	0.0018	1.16

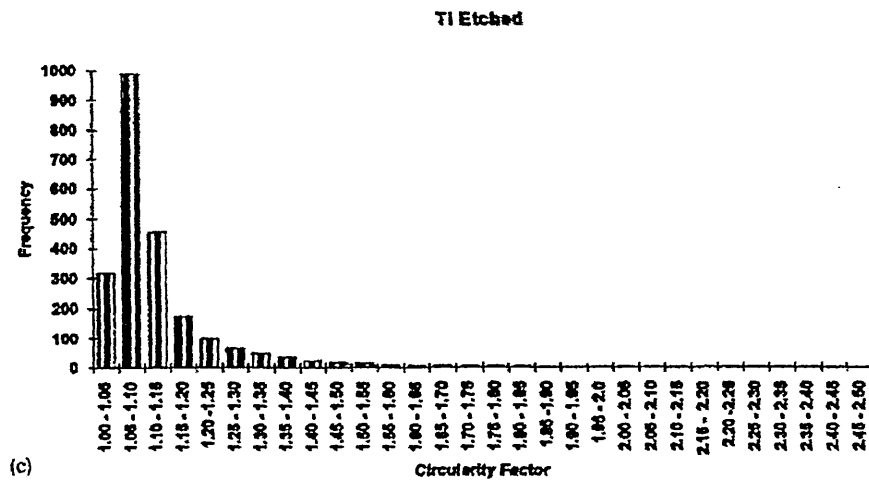
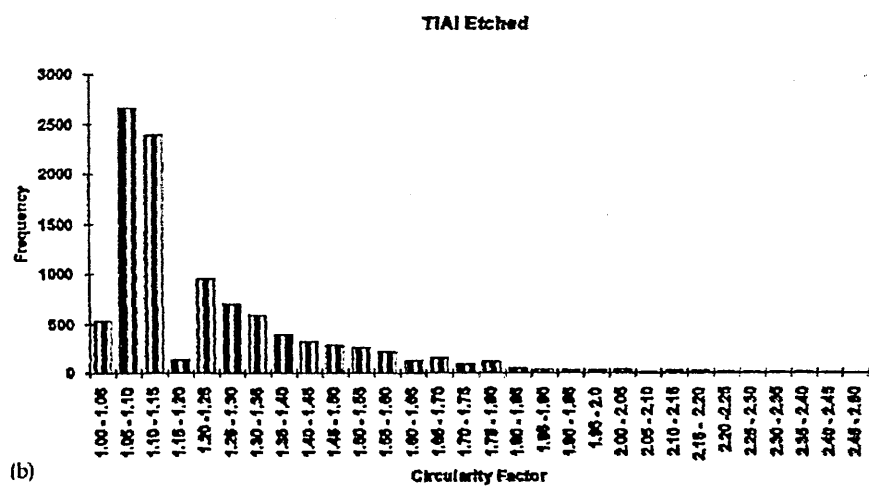
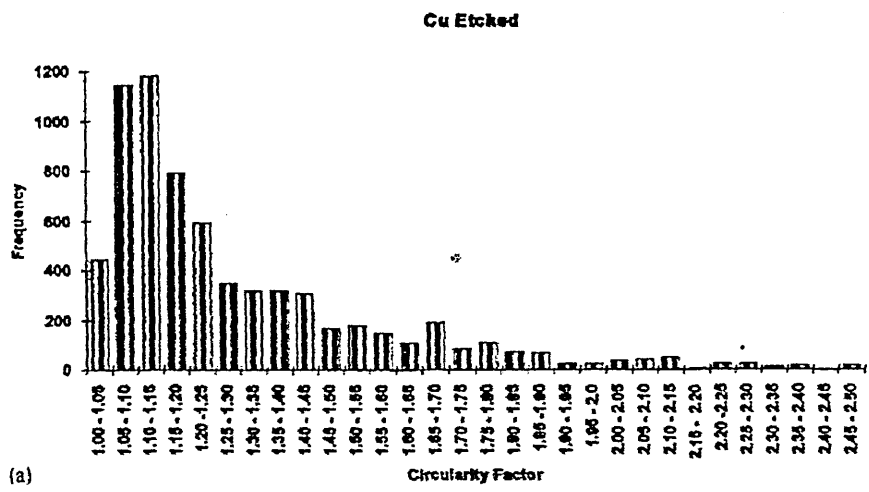


Fig. 6. Bar charts showing the circularity factors of droplets on metal ion etched surfaces: (a) copper alloy; (b) titanium-aluminum; (c) titanium; (d) zirconium; (e) chromium; (f) niobium; (g) molybdenum.

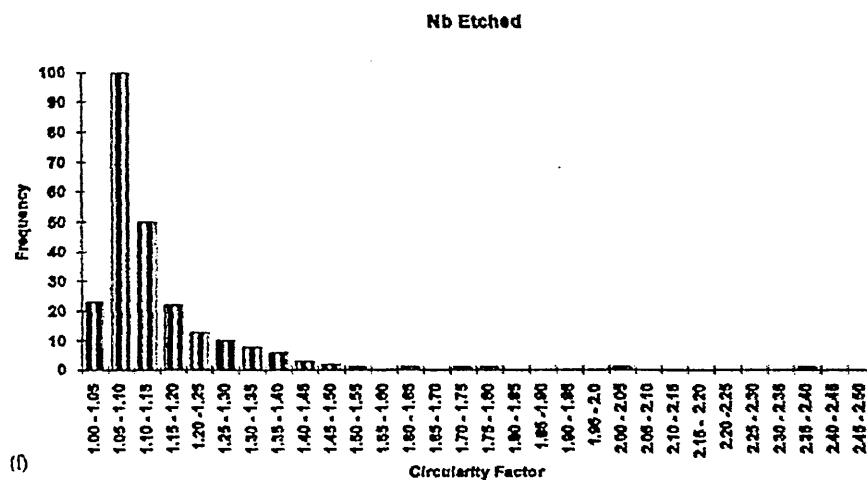
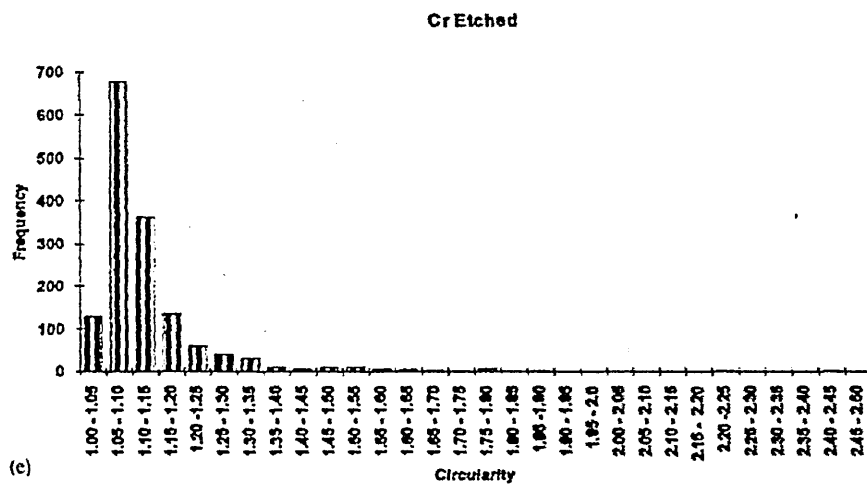
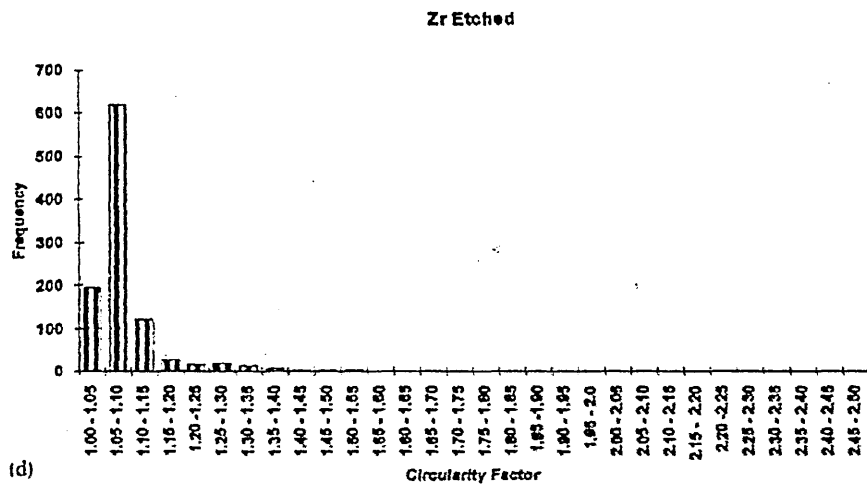


Fig. 6. (continued)

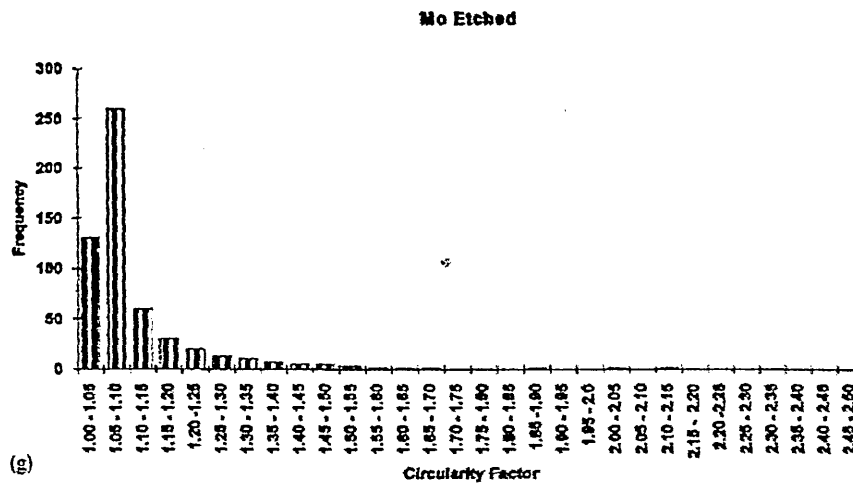


Fig. 6. (continued)

The number of droplets found for Cr and Zr show a surprisingly contradictory picture even though the melting points are rather similar. There are almost twice the number of droplets generated for Cr than for Zr namely  $15 \times 10^3 \text{ mm}^{-2}$  and  $8 \times 10^3 \text{ mm}^{-2}$  respectively. One possible explanation is that the Cr target may have absorbed oxygen from the residual gas, when molten, under the influence of the cathodic arc. It has been reported that a  $\text{Cr}_2\text{O}_3$  content of only 1 mass% depresses the melting point to  $1770^\circ\text{C}$  [10], thus lowering the melting point into the range between Ti and Zr.

Bar charts show frequency versus droplet circularity factor for all investigated target materials (Fig. 6a-g). In the case of the higher melting Ti, Zr, Cr, Nb and Mo the majority of the droplets had circularity factors close to 1 with 80% of the droplets having circularity values between 1.0 and 1.25 (Table 3). This indicates clearly that the vast majority of droplets detected are strictly spherical in shape. SEM examination of the Ti etched substrate showed that the majority of droplets on the surface were spherical (Fig. 7a). It may be assumed consequently that the majority of them have solidified under the actual geometrical conditions already during flight [3,5,11,12]. For the lower melting point materials, TiAl and Cu, the same percentage of droplets had circularity factors of up to 1.35 and 1.45 respectively (Table 3), thus indicating a number of non-spherical droplets detected on the substrate surface after

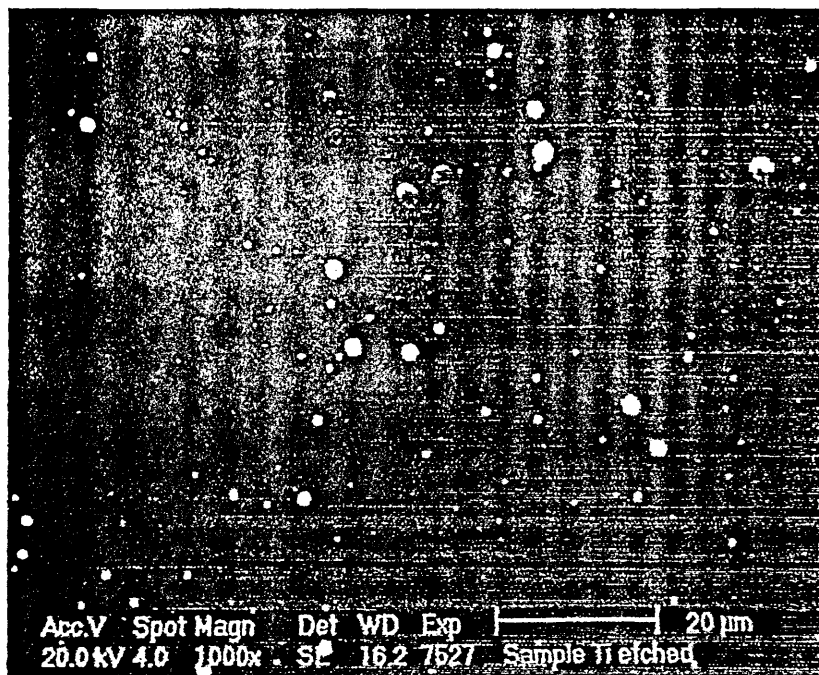
cathodic arc etching using these materials. SEM examination of the Cu etched substrate showed a number of non-spherical droplets on the surface (Fig. 7b). This would indicate that a number of droplets arrived molten at the substrate surface resulting in a non-spherical splash like morphology. This phenomenon is particularly significant when Al is used as the etching media [5].

### 3.2. Cathodic arc etching and UBM TiAlN coating process

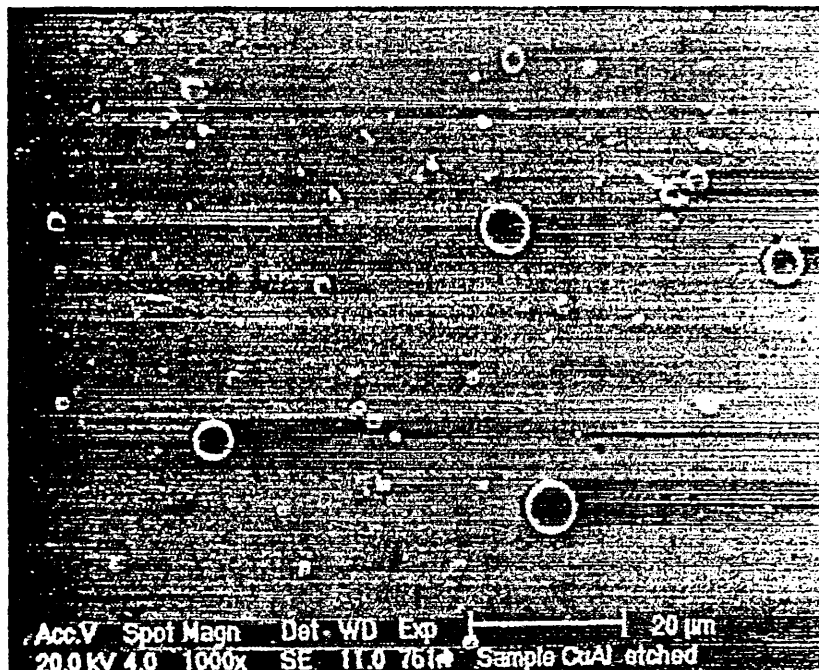
The surface morphology of TiAl, Cr and Mo etched substrates has been evaluated quantitatively (M 4000) by image analysis after the deposition of  $3 \mu\text{m}$  of TiAlN by the UBM. This was performed to compare the number of droplets generated during cathodic arc etching with the number of growth defects detectable on top of the coating surface after cathodic arc etching and UBM coating of a  $3 \mu\text{m}$  layer of TiAlN. The number, fraction of sample surface area covered by growth defects,  $A_d$ , maximum diameter, mean diameter, size range at 90%-ile and size distribution of the growth defects was evaluated. The quantitative evaluation of droplet numbers by image analysis shows, that the number of defects does not change dramatically after the application of the TiAlN coatings. That proves in the first place the assumption that every droplet causes a growth defect and that practically no droplets are "buried" during film growth. In the case of TiAl and

Table 4

Material	Maximum droplet diameter ( $\mu\text{m}$ )	Number of droplets/area ( $\times 10^3 \text{ mm}^{-2}$ )	Mean droplet diameter $\bar{d}^*$ ( $\mu\text{m}$ )	Fraction of sample area covered by droplets	Droplet diameter at 90%-ile ( $\mu\text{m}$ )
TiAl etched	7.4	100	0.63	0.045	1.16
TiAl etched and TiAlN coated	7.6	110	0.93	0.096	1.72
Cr etched	2.4	15	0.4	0.0021	0.56
Cr etched and TiAlN coated	3.8	8	0.76	0.005	1.46
Mo etched	3.9	5	0.58	0.0018	1.16
Mo etched and TiAlN coated	5.8	6	1.1	0.009	2.1



(a)



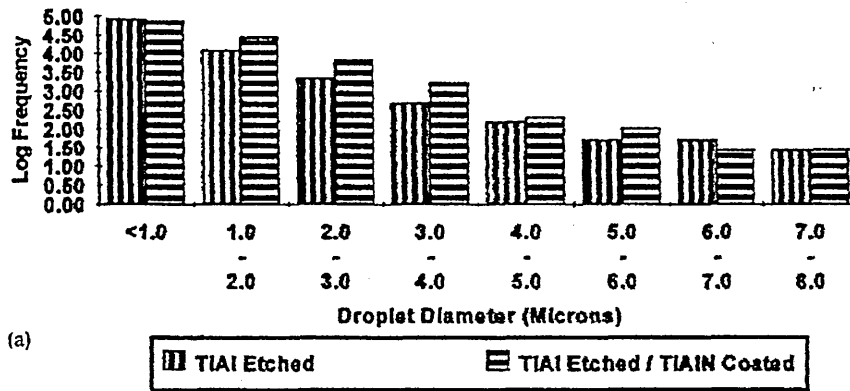
(b)

Fig. 7. Scanning electron micrographs of (a) a Ti etched substrate and (b) a Cu etched substrate.

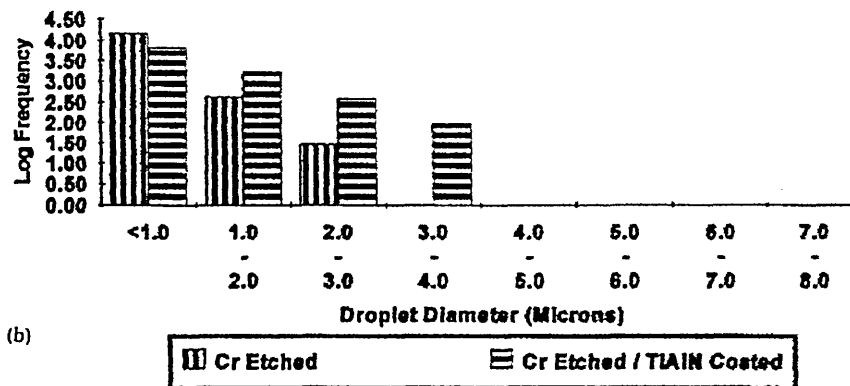
lo etched and TiAlN coated samples even slightly more defects being counted namely  $110 \times 10^3 \text{ mm}^{-2}$  and  $\times 10^3 \text{ mm}^{-2}$  than those for the etched sample (Table 4). However, for Cr etched coatings the resulting number of defects was  $8 \times 10^3 \text{ mm}^{-2}$ , therefore approximately half of that of the etched case. In the case of Cr etched samples there are obviously indications that some of the smaller Cr droplets might have been covered and

buried by the subsequent TiAlN coating process. Bar charts comparing the size distribution of droplets on metal ion etched surfaces with those after metal ion etching and coating with  $3 \mu\text{m}$  of TiAlN are shown in Fig. 8a–c. As would be expected size analysis indicated that the growth defects had a systematically larger diameter than the corresponding droplets from which they form. It has been shown that the size of growth

### Comparison of Droplet Size Distribution TiAl Etched and After TiAlN Coating



### Comparison of Droplet Size Distribution Cr Etched and After Coating with TiAlN



### Comparison of Droplet Size Distribution Mo Etched and after TiAlN Coating

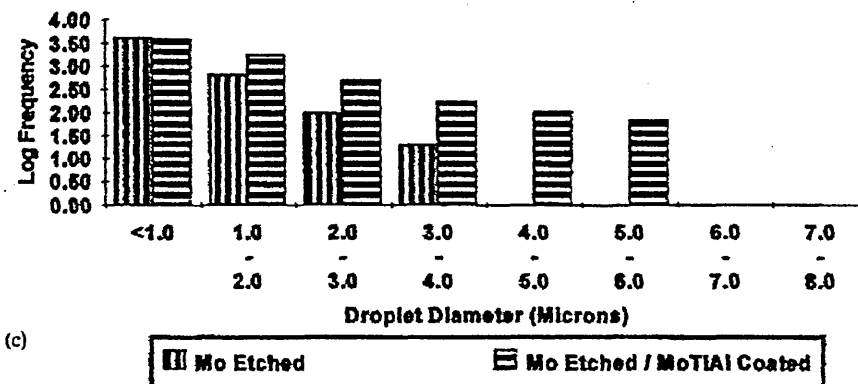


Fig. 8. Bar charts comparing the size distribution of droplets on metal ion etched surfaces with those after metal ion etching and coating with  $3 \mu\text{m}$  of TiAlN: (a) titanium-aluminium; (b) chromium; (c) molybdenum.

effects increases only during the initial growth stage and then remains constant [5,13]. The size of the growth defects represents the size attained during this initial growth stage. Thus, leading to the conclusion that above minimum thickness the defect size should be almost independent of coating thickness. Although Cr contained more growth defects than the higher melting Mo, size analysis showed Mo to have significantly more defects with diameters between 2 and 6  $\mu\text{m}$ . In fact for the Cr etched TiAlN coating no growth defects above 6  $\mu\text{m}$  were found, whilst for the Mo etched coating the resulting number of defects with diameters between 4 and 6  $\mu\text{m}$  was  $174 \text{ mm}^{-2}$ . The previous results are also affected by a larger average defect size and a greater percentage area of sample covered by defects for the Mo etched coating.

## Conclusions

The following conclusions may be drawn:

- 1) The melting point of the cathode target material clearly affects the number and size of droplets or growth defects incorporated into the growing TiAlN coating. The maximum droplet diameter and density decreases rapidly with increasing melting temperature of the cathode target material.
- 2) Circularity measurements showed the vast majority of droplets generated from the higher melting materials were spherical indicating full solidification of the droplets during flight. For the lower melting materials TiAl and Cu a relatively higher proportion of the droplets generated were non-spherical.
- 3) For the TiAl and Mo etched specimens the number of defects in a 3  $\mu\text{m}$  TiAlN coating is practically identical with the number of droplets counted directly after the metal ion etching steps. Burying phenomena of droplets have been only observed for the very small Cr droplets.

- (4) The use of metallic etching materials with high melting temperatures considerably reduces the size and number of growth defects in the UBM deposited 3  $\mu\text{m}$  thick TiAlN coatings.

## Acknowledgement

The work presented has been partially supported by funds of the national UK research programme LINK SURFACE ENGINEERING project no. GK/K76351 (Multi-Coat).

## References

- [1] G. Håkansson, L. Hultman, J.-E. Sundgren, J.E. Greene, W.-D. Münz, *Surf. Coat. Technol.* 48 (1991) 51.
- [2] W.-D. Münz, F.J.M. Hauzer, D. Schulze, *Surf. Coat. Technol.* 50 (1992) 169.
- [3] W.-D. Münz, D.B. Lewis, S. Creasey, T. Hurkmans, T. Trinh, W.v. Ijzendorf, *Vacuum* 46 (4) (1995) 323.
- [4] I.J. Smith, D. Gillibrand, J.S. Brooks, W.-D. Münz, S. Harvey, R. Goodwin, *Surf. Coat. Technol.* 90 (1997) 164.
- [5] W.-D. Münz, I.J. Smith, D.B. Lewis, S. Creasey, *Vacuum* 48 (5) (1997) 473.
- [6] Featurescan, Link Analytical High Wycombe, 1991.
- [7] G.H. Kang, H. Uchida, E.S. Koh, *Surf. Coat. Technol.* 68–69 (1994) 141.
- [8] ASTM Handbook, vol. 51, Surface Engineering, ASTM International, Materials Park, OH, 1994, p. 558.
- [9] E.A. Brandes, G.B. Brook (Eds.), *Smithells Metals Reference Book*, 7th Edn., Butterworth-Heinemann, Oxford, 1992.
- [10] A.H. Sully, E.A. Brandes, *Metallurgy of Rare Metals: Chromium*, Butterworths, London, 1967, p. 78.
- [11] H. Ljungcrantz, L. Hultman, J.-E. Sundgren, G. Håkansson, L. Karlsson, *Surf. Coat. Technol.* 63 (1994) 123.
- [12] B.F. Coll, R. Fontana, A. Gates, P. Sathrum, *Mater. Sci. Eng.* A140 (1991) 816.
- [13] I. Petrov, P. Losblicher, D. Bergstrom, J.E. Greene, W.-D. Münz, T. Hurkmans, T. Trinh, accepted for publication in *Thin Solid Films*.



## Oxidation behaviour of nanoscale TiAlN/VN multilayer coatings

Z. Zhou<sup>a</sup>, W.M. Rainforth<sup>a,\*</sup>, D.B. Lewis<sup>b</sup>, S. Creasy<sup>b</sup>, J.J. Forsyth<sup>b</sup>, F. Clegg<sup>b</sup>, A.P. Ehiasarian<sup>b</sup>, P.Eh. Hovespian<sup>b</sup>, W.-D. Münz<sup>b</sup>

<sup>a</sup>Department of Engineering Materials, University of Sheffield, Sheffield S1 3JD, UK

<sup>b</sup>Materials Research Institute, Sheffield Hallam University, Sheffield S1 1WB, UK

### Abstract

Nanoscale multilayer TiAlN/VN coatings were grown using combined cathodic arc/unbalanced magnetron deposition (arc bond sputtering, ABS) in an industrial-sized physical vapour deposition machine. The thermal behaviour of TiAlN/VN coatings in air was studied using thermo-gravimetric analysis, X-ray diffraction (XRD), scanning electron microscopy and transmission electron microscopy (TEM). Coatings were heat treated in air for 30 min at 550, 600, 638 and 672 °C. Surface oxidation occurred at  $\geq 550$  °C at the coating surface.  $V_2O_5$  was found to form at  $\geq 600$  °C by XRD.  $V_2O_5$ ,  $TiO_2$ ,  $AlVO_4$  were identified at 600 °C, with possible  $Al_2TiO_5$  and  $VO_2$  phases. TEM revealed a non-uniform oxide/coating interface, with preferential oxidation along columnar grain boundaries, presumably because these provide a fast track for diffusion. At 672 °C, the entire coating volume was oxidised, and the coating spalled.

© 2003 Elsevier B.V. All rights reserved.

**Keywords:** TiAlN/VN; Oxidation; Thermo-gravimetric analysis; X-ray diffraction; Transmission electron microscopy

### 1. Introduction

High speed machining without the use of environmental harmful lubrication requires milling tools capable of withstanding the applied stress at higher temperatures. Coatings with low friction coefficient and/or high oxidation resistance are, therefore, required. During the cutting operation, degradation of the coatings occurs by a mixture of wear, oxidation and diffusion (which results in a intermixing of layers) [1]. TiAlN/VN multilayers have been shown to have excellent sliding wear resistance ( $1.26 \times 10^{-17}$  m<sup>3</sup>/N m) and low friction coefficient ( $\mu = 0.4$ , pin-on-disc,  $Al_2O_3$  ball counterpart) in comparison to other wear protective coatings [2,3], e.g. TiAlN/CrN ( $\mu = 0.7$ – $0.9$ ). Laboratory sliding wear tests of TiAlN/VN coatings under dry sliding conditions of 5 N normal load,  $Al_2O_3$  ball counterpart and 10 cm/s speed, yielded wear debris containing the lubricious surface oxide of  $V_2O_5$  detected by Raman spectroscopy [4], indicating that oxidation was a key factor during the milling performance.

In the present work, the thermal behaviour of TiAlN/VN coatings was studied by thermo-gravimetric analysis (TGA), X-ray diffraction (XRD), Scanning electron microscope (SEM) and various Transmission electron microscopy (TEM) techniques to elucidate the phase constitution and oxidation kinetics as a function of temperature.

### 2. Experimental

TiAlN/VN superlattice coatings were grown on stainless steel substrates in an industrial scale physical vapour deposition coating machine (HTC-1000 ABS, manufactured by Hauzer Techno Coating BV, Venlo, The Netherlands). Details of deposition processing were given by Münz et al., e.g. [5]. The substrate rotation unit provided threefold rotation to achieve multilayer and facilitate homogenous deposition on 3-D shaped surfaces, such as cutting tools. Coatings were deposited with a substrate bias voltage of  $-75$  V.

A Cahn TG 131 microbalance was used for the thermo-gravimetry work. The specifications of this microbalance are a temperature drift stability of 10  $\mu$ g/°C, temperature repeatability of  $\pm 3$  °C and a mass sensitivity of 1  $\mu$ g. TGA allows the determination of

\*Corresponding author. Tel.: +44-114-222-2000; fax: +44-114-222-5943.

E-mail address: [m.rainforth@sheffield.ac.uk](mailto:m.rainforth@sheffield.ac.uk) (W.M. Rainforth).

onset point of oxidation and the extent of weight gain. All coatings were deposited on stainless steel 304 coupons ( $50 \times 15 \times 1 \text{ mm}^3$ ). The coupons were covered on both sides with coating material, including the hole drilled for fixing the sample in TG furnace, so that the oxidation would only occur in the coating, and the substrate would only become oxidised when the coating failed. Oxidation of TiAlN/VN was assessed dynamically by TGA in a linear-temperature-ramp ( $400\text{--}1000 \text{ }^\circ\text{C}$  at  $1 \text{ }^\circ\text{C}/\text{min}$ ) mode. Coatings were also heat-treated for 30 min at 550, 600, 638 and  $672 \text{ }^\circ\text{C}$ , respectively, in a conventional air atmosphere furnace in order to relate the TG traces with phase transformations on the coating surfaces, in particular, the formation of  $\text{V}_2\text{O}_5$ . These temperatures were selected based on the TG trace.

The oxidised surfaces were examined by XRD (Bragg–Brentano geometry) using a Philips MRD-Xpert, from  $10$  to  $90^\circ$  ( $2\theta$ ). Oxidised surfaces were subsequently characterised by SEM, (Philips, XL30) with resolution better than  $5 \text{ nm}$ , equipped with Link-Isis EDX analysis.

Cross-sections of the as-deposited coatings and oxidised surfaces were prepared for TEM observation, as detailed in Ref. [6]. The coating oxidised at  $600 \text{ }^\circ\text{C}$  was investigated in greatest detail. Samples were characterised by a 2010FEGTEM equipped with a scanning transmission unit and an energy dispersive X-ray (EDX) detector with Link-Isis interface.

### 3. Results and discussion

#### 3.1. Thermo-gravimetric analysis

Fig. 1 plots TGA oxidation rate measurement for the TiAlN/VN coating on stainless steel coupon, together with an un-coated stainless steel coupon, using the linear-temperature-ramp ( $400\text{--}1000 \text{ }^\circ\text{C}$  at  $1 \text{ }^\circ\text{C}/\text{min}$ ). The differential mass gains as a function of temperature are also plotted ( $dm/dt$ ). The TGA of the un-coated stainless steel coupon was acquired to exclude any mass gains resulting from the substrate to the coating TGA curve, especially at high temperature when the diffusion dominated and coating spallation occurred. A significant mass increase occurred with the coating at  $638 \text{ }^\circ\text{C}$  (onset for rapid oxidation), with detectable steady mass gains at  $\geq 550 \text{ }^\circ\text{C}$ , up to  $672 \text{ }^\circ\text{C}$ . A rough calculation, which assumes oxidation of TiAlN/VN to a simple distribution of oxides (as indicated by the XRD) and using the TG data for mass gain, indicated that 28% of the coating was oxidised at  $603 \text{ }^\circ\text{C}$ , but that all of the coating and some of the substrate had oxidised at  $672 \text{ }^\circ\text{C}$ . Severe surface spallation occurred at  $672 \text{ }^\circ\text{C}$ , which is below the melting point of  $\text{V}_2\text{O}_5$  ( $690 \text{ }^\circ\text{C}$  according to [7]), consistent with the calculation from the mass gain that all the coating was converted to oxides at this temperature.

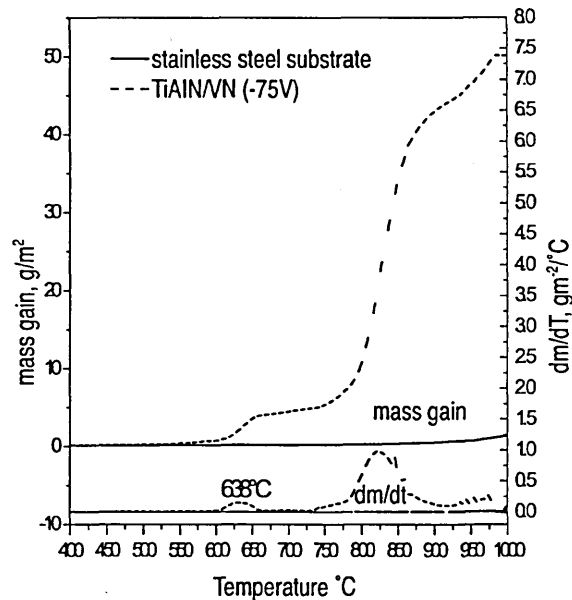


Fig. 1. Thermo-gravimetric oxidation rate measurement in air using a linear-temperature-ramp at  $1 \text{ }^\circ\text{C}/\text{min}$  from  $400$  to  $1000 \text{ }^\circ\text{C}$ .

#### 3.2. XRD of as-deposited coating and heat-treated coating

Coatings were heat-treated for 30 min at 550, 600, 638 and  $672 \text{ }^\circ\text{C}$ , respectively, with temperatures chosen on the basis of the TG trace. Fig. 2 gives XRD results of the as-deposited coating and coatings oxidised in air for 30 min at 550, 600 and  $638 \text{ }^\circ\text{C}$ , respectively. The as-deposited coating exhibited a single phase B1–NaCl structure, with strong (1 1 1) and (2 2 0) peaks. Thirty minutes heat treatment at  $550 \text{ }^\circ\text{C}$  made little difference according to XRD, but the (1 1 1) peak decreased, (2 0 0) and (2 2 0) peaks increased. Coatings oxidised at  $600 \text{ }^\circ\text{C}$  for 30 min were quite different, with phases identified as  $\text{V}_2\text{O}_5$ ,  $\text{TiO}_2$  (rutile) and  $\text{AlVO}_4$ . No  $\text{Al}_2\text{O}_3$  was detected. Peaks from the original coating disappeared at  $\geq 600 \text{ }^\circ\text{C}$ , either due to an oxide thickness that exceeded the X-ray penetration depth, or spallation of the coating. The latter was unlikely, since a strong substrate signal was not found. As the heat treatment temperature increased to  $638 \text{ }^\circ\text{C}$ , phase constituents on the surface remained the same, but a strong (0 0 1)  $\text{V}_2\text{O}_5$  peak was observed. The coating heat-treated at  $672 \text{ }^\circ\text{C}$  exhibited severe spallation, to the extent that the products of coating oxidation were lost from the oxidised surface, and therefore no XRD was conducted on this sample.

XRD results suggest that little  $\text{V}_2\text{O}_5$  formed at  $550 \text{ }^\circ\text{C}$ . A significant amount was obtained after 30 min at  $600 \text{ }^\circ\text{C}$ , in conjunction with oxidation products of  $\text{AlVO}_4$  and  $\text{TiO}_2$ . A significant amount of  $\text{V}_2\text{O}_5$

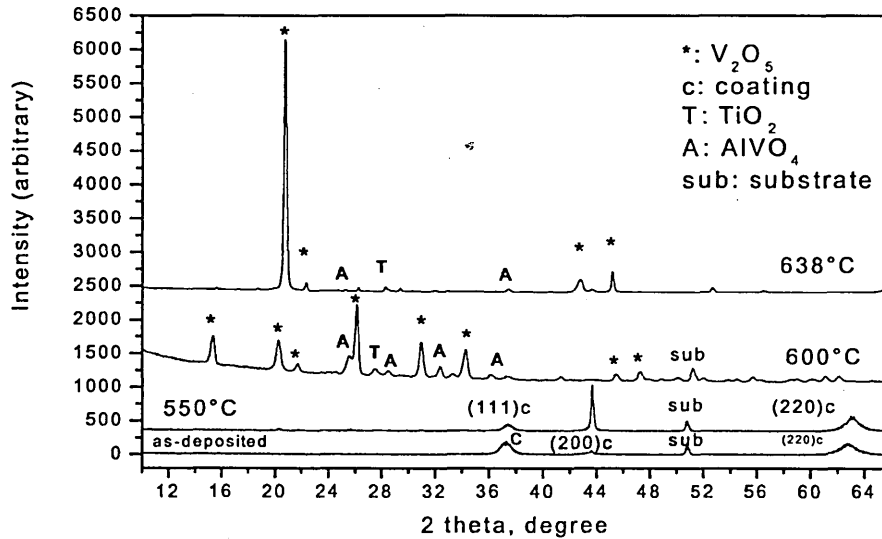


Fig. 2. XRD traces of the as-deposited TiAlN/VN coating and coatings oxidised at 550, 600 and 638 °C, respectively.

remained at 638 °C, and the phase exhibited strong preferred orientation of (0 0 1).

### 3.3. SEM of the oxidation surface

Fig. 3 shows the as-deposited coating, including growth defects resulting from incorporation of droplets during the cathodic arc pre-treatment step. Apart from growth defects, the coating surface had a smooth surface finish. Fig. 4 gives SEM images of the surface following 30 min at 550 °C in air. At this stage, XRD did not identify any oxidation, while TG suggested oxidation had taken place, as shown by a steady increase of mass gain, as confirmed by SEM images. Identification of the oxides at this temperature will, therefore, require cross-sectional TEM, which is currently underway.

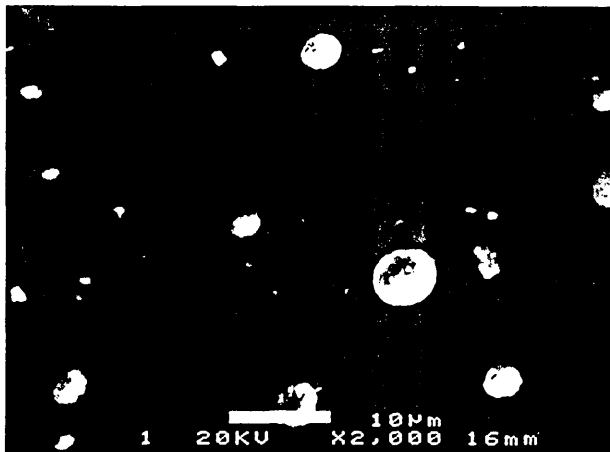


Fig. 3. SEM image of the surface morphology of as-deposited coating.

Fig. 5a shows a typical oxidised surface after 600 °C for 30 min. The surface was uniformly oxidised, with no apparent preferential oxidation at the surface defects. It has three main features: (a) surface plates, (b) surface needles and (c) fine particles below the outermost surface, as indicated on the micrograph. Fig. 5b gives typical EDX map groups of the region circled in Fig. 5a. Note the overlapping of Ti  $k_{\beta}$  (4.931 keV) and V  $k_{\alpha}$  (4.952 keV) in the EDX spectrum. Maps of this region demonstrated that the long and thin needles are Al- and Ti-deficient, but V-rich. Adjacent to these were the plates, which were Al- and Ti-rich, but V-depleted. The fine particles underneath are Al- and Ti-rich, but V-deficient with respect to the long and thin needles.

Fig. 6 gives an SEM image and an EDX/map group of the surface oxidised at 638 °C for 30 min. Apart

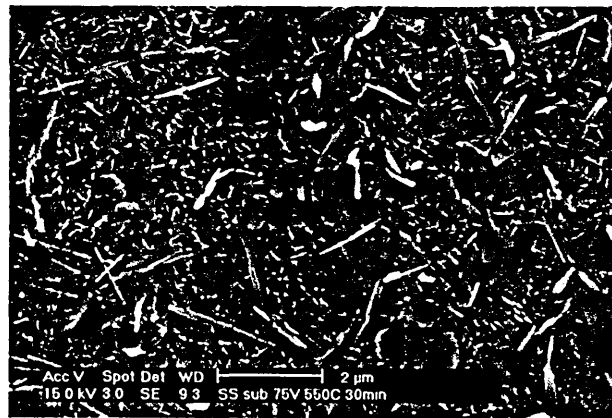


Fig. 4. SEM images of the surface morphology of coating heat-treated at 550 °C for 30 min.

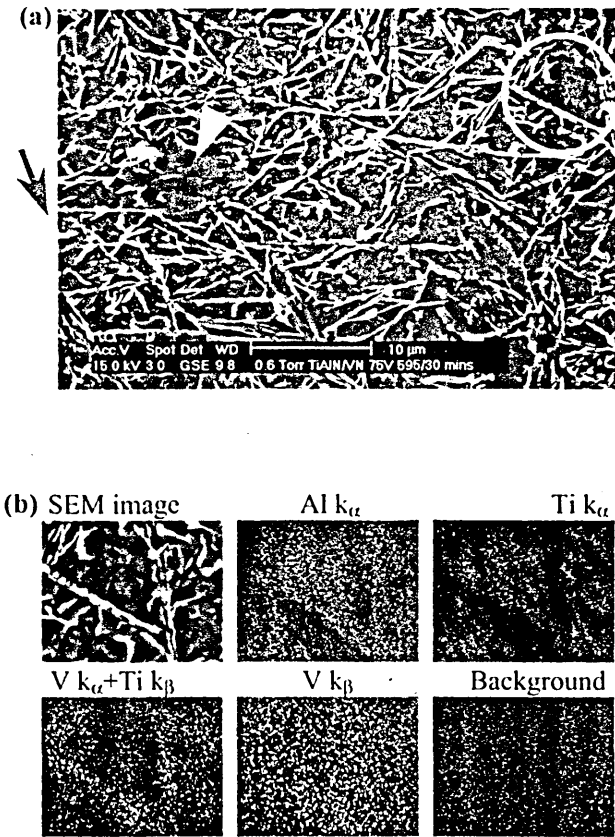


Fig. 5. (a) SEM images of the surface morphology of coating heat-treated at 600 °C for 30 min and (b) area EDX/mapping analysis of the region circled in Fig. 5a.

from the needle particles as seen in samples heat-treated at 600 °C, plates, approximately parallel to the surface plane were present, e.g. area circled. EDX maps show that V-rich regions expanded to cover a greater proportion of the surface at this temperature. This is consistent with the XRD traces, where strong (0 0 1) preferred  $V_2O_5$  was found at this temperature in contrast to the random signal found at 600 °C.

Fig. 7 gives an SEM image of the oxidised surface after 30 min at 672 °C. It shows extensive spallation of the coating. Therefore, no further EDX analysis has been done, as coating had probably all gone according to TGA.

### 3.4. TEM of the cross-sections at 600 °C

Fig. 8a gives a scanning TEM bright field image of the coating after 30 min exposure at 600 °C in air. It revealed that the oxide consisted of two sub-layers. The layer next to the non-oxidised coating was porous, containing nano-crystalline particles, confirmed by the ring diffraction pattern (inset). The outermost layer was composed of several different phases with particle and

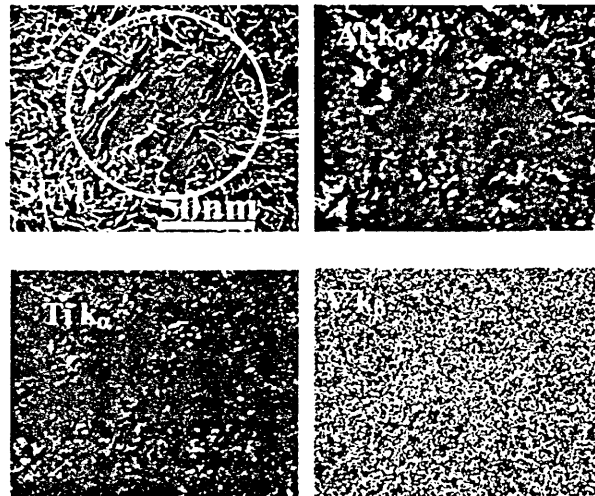


Fig. 6. SEM images of the surface morphology of coating heat-treated at 638 °C for 30 min, and area EDX/mapping analysis.

needle morphology. Fig. 8b gives EDX maps that show the distribution of Al, V and Ti. In the outermost oxide region, angular particles, rich in Al and V, were present, interspersed with Ti-rich particles, which were present to a greater depth than the Al/V-rich particles.

Electron diffraction studies of the angular particle arrowed in Fig. 8a, indicated that it was  $AlVO_4$ , which has a triclinic structure. This is consistent with the EDX data (Fig. 8b) and the XRD spectra (Fig. 2). These  $AlVO_4$  particles are believed to be those fine particles below the outermost oxidation surface observed by SEM in Fig. 5a (region circled). There are only two compounds in the  $Al_2O_3-V_2O_5$  system,  $AlVO_4$  (triclinic) [8] and  $AlV_2O_4$  (cubic, spinel) [9], but the current study has found no evidence for the presence of  $AlV_2O_4$ . The bright particle in the Ti EDX map in Fig. 8b, which

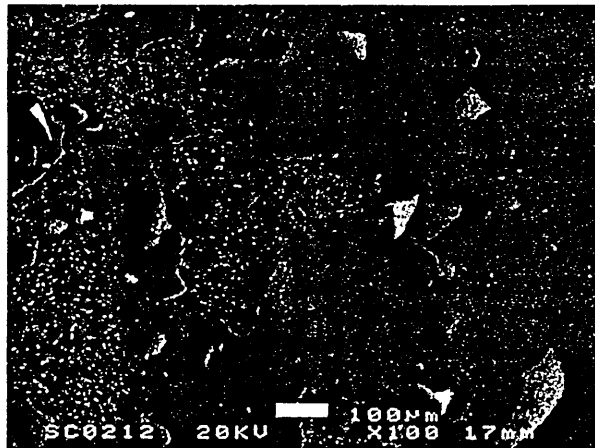


Fig. 7. SEM images of the surface morphology of coating heat-treated at 672 °C for 30 min.

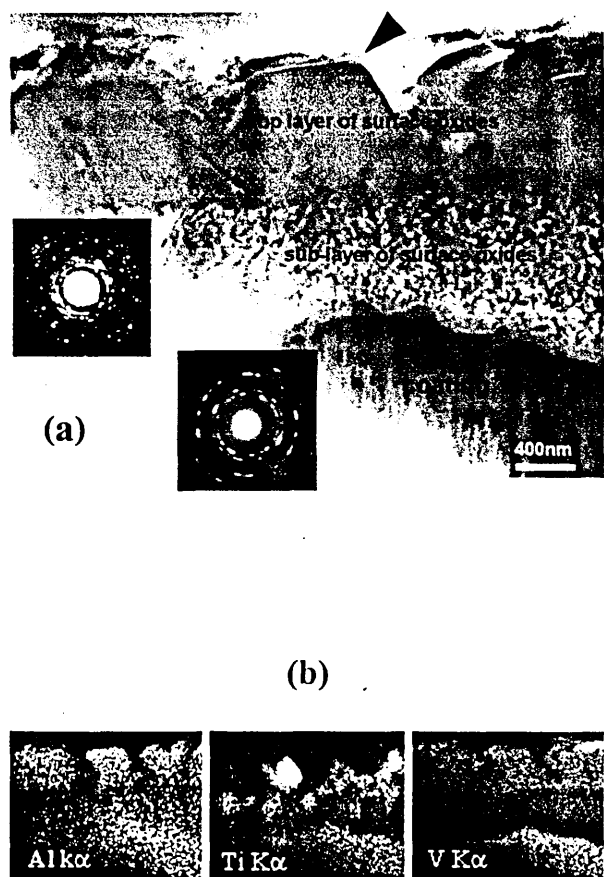


Fig. 8. (a) Bright field image of oxide sub-layers of the coating oxidised 30 min at 600 °C. Insets are selected area diffraction patterns of the bottom sub-layer and non-oxidised coating. (b) STEM/EDX map group showing elemental distributions.

was adjacent to the  $\text{AlVO}_4$  particle, noted above, was identified by selected area electron diffraction as  $\text{TiO}_2$  (rutile).

Cross-sectional TEM samples did not contain the large particles on the outermost surface, region (arrowed) of the SEM image in Fig. 5a. It is probable that these particles were lost during TEM sample preparation, suggesting they had poor adherence to the surface.

The phases of the bottom layer of the two sub-layers of surface oxides could not be uniquely identified. Rutile- $\text{TiO}_2$  particles and  $\text{V}_2\text{O}_5$  needles were positively identified. However, additional reflections were present within the selected area diffraction pattern in Fig. 8a that could not be attributed to  $\text{V}_2\text{O}_5$  or  $\text{TiO}_2$ . The diffraction pattern can be indexed according to the sum of the major diffraction planes of  $\text{V}_2\text{O}_5$  (2 0 0 and 1 0 0),  $\text{VO}_2$  (1 0 0 and 2 2 0) and  $\text{Al}_2\text{TiO}_5$  (2 3 0 and 0 0 6), but this does not represent a unique identification.

Fig. 8a also shows a non-uniform interface between coating and oxide. Preferential oxidation was observed along the columnar grain boundaries at the interface

between the coating and the oxide, presumably because these provide a fast track for diffusion.

Interpretation of the reaction sequences leading to the phases observed is made difficult by the absence of detailed thermodynamic data (experimental or calculated) for this complex multicomponent system. The first reaction products appeared to be  $\text{V}_2\text{O}_5$ ,  $\text{Al}_2\text{TiO}_5$ ,  $\text{TiO}_2$  and intermediate phases in the complex phase transformation series from  $\text{VO} \rightarrow \text{VO}_2 \rightarrow \text{V}_2\text{O}_5$ , i.e.  $\text{VO}_2$  in V–O system [10]. This is consistent with the work of Lugscheider et al. [11], who observed a stable polycrystalline mixture of  $\text{V}_2\text{O}_5$  and  $\text{VO}_2$  up to 605 °C in the vanadium oxides deposited by reactive MSIP–PVD process. In addition, Mayrhofer et al. [12] found  $\text{VO}_2$  in the wear debris after tribological test at 700 °C of similar coatings to those studied here. In any event, it appears probable that the VN oxidised directly to a variety of compounds within the V–O system, with  $\text{V}_2\text{O}_5$  as the dominant phase.

The fact that little  $\text{AlVO}_4$  was present in the inner oxide sub-layer suggests that it formed later in the reaction sequence, and was not a direct oxidation product from the coating.  $\text{AlVO}_4$  can be prepared by the solid-state reaction of  $\text{Al}_2\text{O}_3$  (through  $\gamma\text{-Al}_2\text{O}_3$  or bayerite  $\text{Al}(\text{OH})_3$ ) and  $\text{V}_2\text{O}_5$ , but this requires long reaction times at 600–650 °C [13]; however, no interaction was found between  $\text{V}_2\text{O}_5$  phase and  $\gamma\text{-Al}_2\text{O}_3$  in air for 5 h at 500 °C by XRD [14]. While it cannot be ruled out that  $\text{AlVO}_4$  was derived from such a reaction, the absence of any positive identification of an  $\text{Al}_2\text{O}_3$  polymorph strongly suggests that  $\text{AlVO}_4$  was formed by reaction of  $\text{Al}_2\text{TiO}_5$  and  $\text{V}_x\text{O}_y$ .

A number of questions remain for future work. The formation of  $\text{V}_2\text{O}_5$  is believed to be critical in the low friction behaviour of these coatings. The cross-sectional TEM of the sample oxidised at 600 °C (Fig. 8) does not show  $\text{V}_2\text{O}_5$  in the outer layer, presumably because the quantity of this phase was reduced by the production of  $\text{AlVO}_4$ . This is consistent with SEM images (Fig. 5), which suggest that while some  $\text{V}_2\text{O}_5$  needles may penetrate the oxide surface, they are present in a relatively small area fraction. It would appear that the temperature must reach 638 °C before substantial quantities of this phase are produced on the oxide surface (Fig. 6).

The second issue for further work is that clear experimental evidence is required of the location of Al in the reaction product of  $\text{TiAlN}$  and therefore the source of Al in the formation of  $\text{AlVO}_4$ . The most probable reaction sequence is that the  $\text{TiAlN}$  oxidises to  $\text{Al}_2\text{TiO}_5$  at 600 °C, and this phase subsequently reacts with the  $\text{V}_x\text{O}_y$  to give  $\text{AlVO}_4$  and  $\text{TiO}_2$ . Further work is ongoing to investigate the structure of this inner nanocrystalline layer and to determine the distribution of Al from the coating to the outer oxide layer using high-resolution electron energy loss spectroscopy (EELS),

which should allow better spatial resolution than the EDX used here.

#### 4. Conclusions

During continuous heating TG experiments (1 °C/min), surface oxidation occurred at  $\geq 550$  °C at the coating surface. At 672 °C, the entire coating volume was oxidised, and the coating spalled.

V<sub>2</sub>O<sub>5</sub> was found to form at  $\geq 600$  °C by XRD. A substantial quantity of V<sub>2</sub>O<sub>5</sub> was present on the outermost surface of coating at 638 °C with (0 0 1) preferred orientation.

The oxide after 30 min at 600 °C comprised a two-layer structure. The outer layer consisted of rutile-TiO<sub>2</sub> and AlVO<sub>4</sub>. The inner layer had a nano-crystalline structure, which could not be uniquely identified, but was believed to consist of V<sub>2</sub>O<sub>5</sub>, VO<sub>2</sub> and Al<sub>2</sub>TiO<sub>5</sub>.

#### Acknowledgments

Financial support from Engineering and Physical Science Research Council (EPSRC), UK, Grant No. GR/N23998/01 is acknowledged.

#### References

- [1] Q. Luo, W.M. Rainforth, W.-D. Münz, Surf. Coat. Technol. 146–147 (2001) 430.
- [2] W.-D. Münz, L.A. Donohue, P.Eh. Hovsepian, Surf. Coat. Technol. 125 (2000) 269.
- [3] P.Eh. Hovsepian, D.B. Lewis, W.-D. Münz, Surf. Coat. Technol. 133–134 (2000) 166.
- [4] C.P. Constable, J. Yarwood, P. Hovsepian, L.A. Donohue, D.B. Lewis, W.-D. Münz, J. Vac. Sci. Technol. A 18 (2000) 1681.
- [5] W.-D. Münz, D.B. Lewis, P.Eh. Hovsepian, C. Schönjahn, A. Ehiasarian, I.J. Smith, Surf. Eng. 17 (2001) 15.
- [6] Z. Zhou, I. Reaney, D. Hind, S.J. Milne, A.P. Brown, R. Brydson, J. Mater. Res. 17 (2002) 2066.
- [7] International Chemical Safety Cards, ICSC:0596.
- [8] JCPDF card: 39-376.
- [9] JCPDF card: 25-26.
- [10] J. Cui, D. Da, W. Jiang, Appl. Surf. Sci. 133 (1998) 225.
- [11] E. Lugscheider, O. Knotek, K. Bobzin, S. Barwulf, Surf. Coat. Technol. 133-134 (2000) 362.
- [12] P.H. Mayrhofer, M. Stoiber, C. Mitterer, P.Eh. Hovsepian, W.-D. Münz, ABS(Arc-Bond-Sputtering) days, 23-24 July, Sheffield, 2002.
- [13] O. Yamaguchi, T. Uegaki, Y. Miyata, K. Shimizu, J. Am. Ceram. Soc. 70 (8) (1987) C198.
- [14] G.A. El-Shobaky, K.A. El-Shobaky, F.H.A. Abdalla, Thermochim. Acta 96 (1985) 129.

## The effect of (Ti + Al):V ratio on the structure and oxidation behaviour of TiAlN/VN nano-scale multilayer coatings

D.B. Lewis<sup>a,\*</sup>, S. Creasey<sup>a</sup>, Z. Zhou<sup>b</sup>, J.J. Forsyth<sup>a</sup>, A.P. Ehiasarian<sup>a</sup>, P.Eh. Hovsepian<sup>a</sup>, Q. Luo<sup>a</sup>, W.M. Rainforth<sup>b</sup>, W.-D. Münz<sup>a</sup>

<sup>a</sup>Materials Research Institute, Sheffield Hallam University, Sheffield S1 1WB, UK

<sup>b</sup>Department of Engineering Materials, University of Sheffield, Sheffield S1 3JD, UK

### Abstract

Nano-scaled multilayered TiAlN/VN coatings have been grown on stainless steel and M2 high speed steel substrates at  $U_B = -85$  V in an industrial, four target, Hauzer HTC 1000 coater using combined cathodic steered arc etching/unbalanced magnetron sputtering. X-ray diffraction (XRD) has been used to investigate the effects of process parameters (Target Power) on texture evolution (using texture parameter  $T^*$ ), development of residual stress ( $\sin^2 \psi$  method) and nano-scale multilayer period. The composition of the coating was determined using energy dispersive X-ray analysis. The thermal behaviour of the coatings in air was studied using thermo-gravimetric analysis, XRD and scanning electron microscopy. The bi-layer period varied between 2.8 and 3.1 nm and in all cases a  $\{110\}$  texture developed with a maximum value  $T^* = 4.9$ . The residual stress varied between  $-5.2$  and  $-7.4$  GPa. The onset of rapid oxidation occurred between 628 and 645 °C depending on the (Ti + Al):V ratio. After oxidation in air at 550 °C  $\text{AlVO}_4$ ,  $\text{TiO}_2$  and  $\text{V}_2\text{O}_5$  phases were identified by XRD with the  $\text{AlVO}_4$ ,  $\text{TiO}_2$  being the major phases. The formation of  $\text{AlVO}_4$  appears to disrupt the formation of  $\text{Al}_2\text{O}_3$  which imparts oxidation resistance to TiAlN based coatings. Increasing the temperature to 600 and 640 °C led to a dramatic increase in the formation of  $\text{V}_2\text{O}_5$  which was highly oriented (0 0 1) with a plate-like morphology. At 640 °C there was no evidence of the coating on XRD. Increasing the temperature to 670 °C led to further formation of  $\text{AlVO}_4$  and a dramatic reduction in  $\text{V}_2\text{O}_5$ .

© 2003 Elsevier B.V. All rights reserved.

**Keywords:** Nano-scale multilayers; TiAlN/VN coatings; Oxidation; X-ray diffraction; Scanning electron microscopy

### 1. Introduction

TiAlN/CrN, TiAlN/VN and CrN/NbN nano-scaled multilayered coatings with typical periods  $\lambda$  between 3 and 4 nm have been successfully produced economically under production conditions in industrially sized coating equipment [1]. TiAlN/CrN [2,3] exhibits excellent high-temperature wear resistance and oxidation resistance, whereas CrN/NbN [4,5], has excellent anti-corrosion performance. Nano-scaled, multilayered TiAlN/VN coatings exhibit at room temperature, low coefficients of friction,  $\mu = 0.4$ – $0.5$  and low sliding wear coefficients of  $1.2 \times 10^{-17} \text{ m}^3 \text{ N}^{-1} \text{ m}^{-1}$  which is two orders of magnitude lower compared to TiAlN/CrN ( $\mu = 0.7$ ,  $K_c = 2.38 \times 10^{-16} \text{ m}^3 \text{ N}^{-1} \text{ m}^{-1}$ ) and CrN/NbN ( $\mu =$

$0.69$ ,  $K_c = 2.1 \times 10^{-15} \text{ m}^3 \text{ N}^{-1} \text{ m}^{-1}$ ) systems. The lowest value of the coefficient of friction is due to the formation of a vanadium oxide ( $\text{V}_2\text{O}_5$ ), which acts as a dry lubricant [1]. At temperatures above 640 °C the VN component in the multilayer is completely oxidised to  $\text{V}_2\text{O}_5$  and at temperatures above 670 °C, the  $\text{V}_2\text{O}_5$  starts to melt resulting in loss of coating integrity making them unsuitable in higher temperature applications. However, one important area where the low coefficient of friction can be utilised is in the coating of M2 HSS cutting tools which have a maximum operating temperature of typically approximately 550 °C. The lower coefficient of friction of these coatings may, therefore, be particularly beneficial in the high speed machining of softer materials, e.g. Al alloys, Inconel alloys, where friction between work piece material and tool is of particular importance. This paper summarises results on the effect of (Ti + Al):V ratio on the structure and

\*Corresponding author. Tel.: +44-114-225-4074; fax: +44-114-225-3501.

E-mail address: [b.d.lewis@shu.ac.uk](mailto:b.d.lewis@shu.ac.uk) (D.B. Lewis).

Table 1  
Target configuration, analysis and bi-layer thickness

Sample	Power to target (kW)				Al (at.%)	Ti (at.%)	V (at.%)	(Ti+Al):V	Bi-layer thickness (nm)
	Ti–Al	Ti–Al	V	V					
1	10	10	5.5	5.5	32.5	30.9	36.6	1.73	2.8
2	10	10	7	7	28.5	27.8	43.7	1.29	3.0
3	10	10	8	8	26.9	26.3	46.8	1.14	3.0
4	11.5	11.5	7	7	32.2	29.2	38.6	1.59	3.1

oxidation behaviour of TiAlN/VN nano-scale multilayer coatings.

## 2. Experimental details

TiAlN/VN coatings investigated were deposited by reactive unbalanced magnetron sputtering in a Hauzer Techno Coating HTC 1000-4 using the arc bond sputter process [6]. In all the processes  $2 \times V$  targets (99.9%) and  $2 \times \text{Ti–Al}$  (50:50) targets were used and the power applied to each target is given in Table 1. The coatings were deposited at bias voltages of  $U_B = -75$  V for 1.5 h and  $U_B = -85$  V for 1.5 h using the target powers shown in Table 1. All the coatings were deposited at a constant temperature of 450 °C on to stainless steel and M2 HSS substrates in a common Ar+N<sub>2</sub> atmosphere at a total pressure of  $4.5 \times 10^{-3}$  mbar. A more detailed description of the process parameters used is described elsewhere [1,7–10].

The textures present in the as-deposited coatings were determined by the Harris inverse pole figure method (Texture  $T^*$ ) [11]. The bi-layer period of the nano-scale multilayer,  $\Delta$ , was measured directly in the low angle region from the standard Bragg's equation [9]. Glancing angle parallel beam geometry was used to determine the state of residual stress present in the coatings [12]. The products which formed on the coatings surface after oxidation were identified by X-ray diffraction (XRD) using glancing angle ( $1^\circ$  incidence) and  $\theta/2\theta$  geometries.

The morphology of the oxidized surfaces was investigated using a FEI environmental scanning electron microscope. The atomic percentage of the metallic elements in each coating was determined using a ZAF 4 corrected energy dispersive X-ray (EDX) analysis.

A Cahn TG 121 microbalance was used for the thermo-gravimetry work.

The hardness was measured using a Knoop indenter,  $(HK)_{0.25}$ . Pin-on-disc measurements were made in dry sliding wear conditions using Al<sub>2</sub>O<sub>3</sub> balls, a 5 N load at a linear speed of 0.1 m s<sup>-1</sup>.

## 3. Results and discussion

### 3.1. Coating characterisation

#### 3.1.1. Composition

Elemental analyses of the metallic elements in the coatings under investigation are shown in Table 1. As can be predicted from the deposition parameters the (Ti+Al):V ratio decreases as the power to the pure V targets was increased, see Table 1.

#### 3.1.2. Structural analysis

Low angle XRD was used to determine the bi-layer periods,  $\Delta$  of the nano-scale multilayers, which were in the range of 2.8–3.1 nm, see Table 1. Texture measurements using the Harris inverse pole figure method for the four specimens under investigation are given in Table 2. In all cases the films developed with a pronounced  $\{110\}$  texture where the intensity of the texture increased with increasing vanadium content. Pronounced  $\{110\}$  textures have been observed when similar films were deposited at  $U_B = -75$  V [13]. In fact strong  $\{110\}$  textures are present in magnetron sputtered monolithically grown VN [14] films grown under similar bias voltage conditions indicating that under the deposition conditions used increasing the vanadium content favours the development of a  $\{110\}$  texture. This texture is in contrast to similar films which

Table 2  
Texture coefficient  $T^*$ , sliding wear, coefficient of friction,  $\mu$ , hardness, adhesion and residual stress

Sample	Texture coefficient, $T^*$			Sliding wear (m <sup>3</sup> N <sup>-11</sup> m <sup>-11</sup> )	$\mu$	Hardness Knoop (Hk) <sub>0.25</sub>	Adhesion critical load N ( $L_c$ )	Residual stress (GPa)
	(111)	(200)	(220)					
1	0.2	1.7	4.1	4.5E–17	0.59	3377	55	–5.2
2	0.3	1.1	4.3	2.8E–17	0.52	3378	42	–6.4
3	0.3	0.9	4.9	5.8E–17	0.64	3752	55	–7.4
4	0.3	0.9	4.5	1.76E–16	0.57	3451	49	–6.6

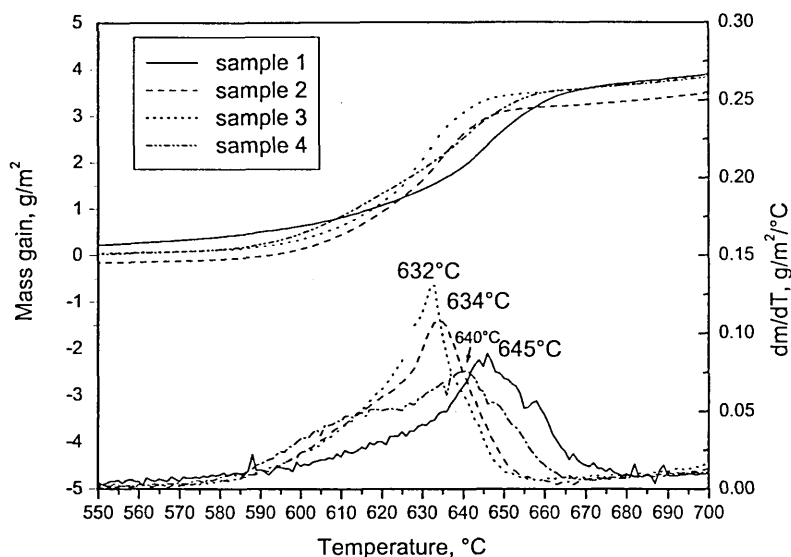


Fig. 1. Thermo-gravimetric oxidation measurement in air using a linear ramp of  $1\text{ }^{\circ}\text{C min}^{-1}$  from 400 to 1000  $^{\circ}\text{C}$  for samples 1–4.

developed a pronounced  $\{1\ 1\ 1\}$  texture when deposited under similar conditions of bias voltage (i.e.  $U_B = -85\text{ V}$ ), but at a lower total pressure,  $P_T$  of  $3.8 \times 10^{-3}$  mbar [13]. At the same bias voltage increasing the total gas pressure  $P_T$  decreases the energy of the bombarding ions and therefore, has a similar influence on texture formation as reducing the bias voltage. Therefore, the texture developed at  $U_B = -85\text{ V}$  using a total pressure  $P_T = 5 \times 10^{-3}$  mbar is similar to that developed at  $U_B = -75\text{ V}$  using a total pressure  $P_T = 3.8 \times 10^{-3}$  mbar that is a  $\{1\ 1\ 0\}$  texture in both cases.

### 3.1.3. Residual stress hardness, sliding wear, coefficient of friction ( $\mu$ ) and adhesion

Residual stress, hardness, sliding wear, coefficient of friction ( $\mu$ ) and adhesion values for the four coatings under investigation are shown in Table 2. All the coatings investigated exhibited residual compressive stress states. The stresses varied between  $-5.2\text{ GPa}$  for sample 1 and  $-7.4\text{ GPa}$  for sample 3. The hardness values mirror those of the residual stresses with minimum and maximum hardness values for samples 1 and 3, respectively. The sliding wear varied between  $1.76 \times 10^{-16}$  and  $2.8 \times 10^{-17}\text{ m}^3\text{ N}^{-1}\text{ m}^{-1}$ , whilst the  $\mu$  varied between 0.52 and 0.64 with no clear trend of (Ti+Al):V ratio

## 3.2. Oxidation studies

### 3.2.1. Thermal gravimetric analysis

Fig. 1 plots thermal gravimetric analysis (TGA) oxidation rate measurements for TiAlN/VN coatings (coupons from samples 1 to 4) deposited on stainless steel substrates. The measurements were dynamic TGA

using a linear temperature ramp (400–1000  $^{\circ}\text{C}$  at  $1\text{ }^{\circ}\text{C min}^{-1}$ ). The differentiated mass gains as a function of temperature are also displayed. Significant increases in mass gain (onset of rapid oxidation) occurred between 632 and 645  $^{\circ}\text{C}$  for all the coatings, which is in contrast to monolithic TiAlN coatings where the onset of rapid oxidation occurred above 800  $^{\circ}\text{C}$  [15]. The temperature at which the onset of rapid oxidation occurred was also dependent on the (Ti+Al):V ratio in the coating, see Table 1. The higher the (Ti+Al):V ratio the higher the temperature at which rapid oxidation occurred, for example for sample 3 ((Ti+Al):V ratio 1.14) the onset of rapid oxidation was 632  $^{\circ}\text{C}$  whereas for sample 1 ((Ti+Al):V ratio 1.73) the onset of rapid oxidation was 645  $^{\circ}\text{C}$ .

### 3.2.2. Scanning electron microscopy

Scanning electron micrographs (SEM) typical of the surfaces of samples 1–4 oxidised for 1 h in air at 550, 600, 640 and 670  $^{\circ}\text{C}$  are shown, respectively, in Figs. 2–8. After oxidation at 550  $^{\circ}\text{C}$  samples 1 and 4 exhibit an almost uniformly oxidised surface containing only a few needle-like particles, see Fig. 2. In contrast, samples 2 and 3 showed numerous needle-like particles at the surface, see Fig. 3. EDX analysis showed that the needle-like particles were rich in vanadium, i.e.  $\text{V}_2\text{O}_5$ . Increasing the heat treatment temperature to 600  $^{\circ}\text{C}$  resulted in the development of platelet type morphology at the surface in all four specimens. The volume fraction of the platelets at the surface was the greatest in sample 3 (compare Figs. 4 and 5), i.e. the coating containing the highest V content. EDX analysis showed the particles with platelet type morphology were richer in V than the surrounding regions thus leading one to the

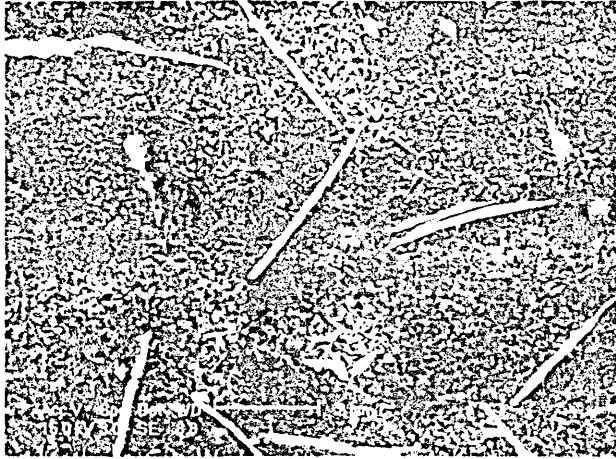


Fig. 2. A SEM of the surface of an oxidised TiAlN/VN coating sample 1, heat treated in air at 550 °C for 1 h.



Fig. 4. A SEM of the surface of an oxidised TiAlN/VN coating, sample 1, heat treated in air at 600 °C for 1 h.

conclusion that they are  $V_2O_5$ . With the exception of sample 3 increasing the heat treatment temperature to 640 °C resulted in more extensive development of the plate-like morphology of the  $V_2O_5$  phase, (compare Figs. 6 and 7). This supports the evidence from the XRD patterns which show increasing intensity of the (0 0 1) texture of  $V_2O_5$  for all coatings except sample 3 as the heat treatment temperature was increased to 640 °C. When the coatings were heat treated in air at 670 °C the plate like morphology completely disappeared to be replaced by regions with either blocky or needle like morphologies but there was no evidence of localised melting, see Fig. 8. EDX analysis showed the needle-like regions contained mainly Ti whilst the blocky regions contained both the elements Al and V.

### 3.2.3. X-ray diffraction

Glancing angle X-ray diffraction patterns (GAXRD) ( $1^\circ$  incidence) of samples 1–4 heated in air at 550 °C are shown in Fig. 9. The following phases could be identified,  $V_2O_5$  (41-1426),  $TiO_2$  (21-1276) and  $AlVO_4$  (31-0034), together with the {1 1 1} and {2 0 0} (not shown in figure) reflections from the coating. However, when one compares the intensity of the (0 0 1) reflection for  $V_2O_5$  in the GAXRD patterns it is clear that samples 1 and 4 contained relatively small amounts of  $V_2O_5$  when compared with samples 2 and 3, the latter containing the highest intensity for the (0 0 1) reflection. The presence of coating peaks in the GAXRD pattern at  $1^\circ$  incidence clearly indicates an extremely thin oxide layer at the surface. A total oxide layer thickness of  $\sim 0.08 \mu\text{m}$  was calculated based on attenuation measurements of the {1 1 1} reflection from the

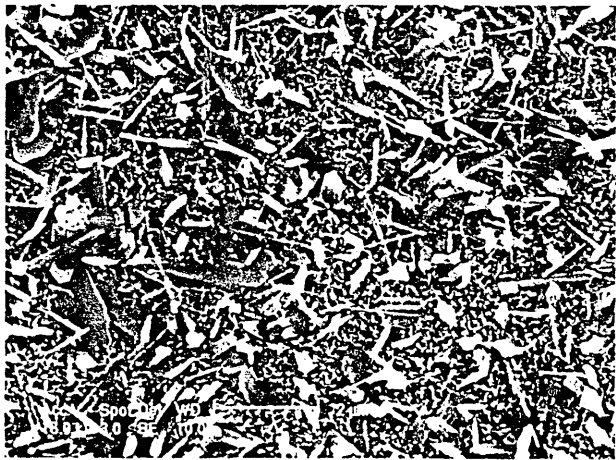


Fig. 3. A SEM of the surface of an oxidised TiAlN/VN coating sample 3, heat treated in air at 550 °C for 1 h.

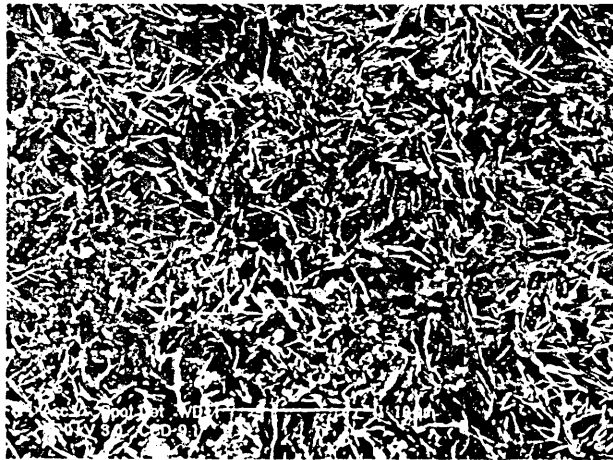


Fig. 5. A SEM of the surface of an oxidised TiAlN/VN coating, sample 3, heat treated in air at 600 °C for 1 h.

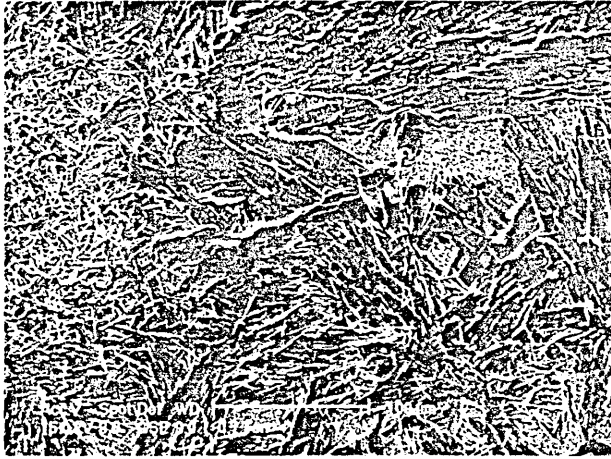


Fig. 6. A SEM of the surface of an oxidised TiAlN/VN coating, sample 1, heat treated in air at 640 °C for 1 h.

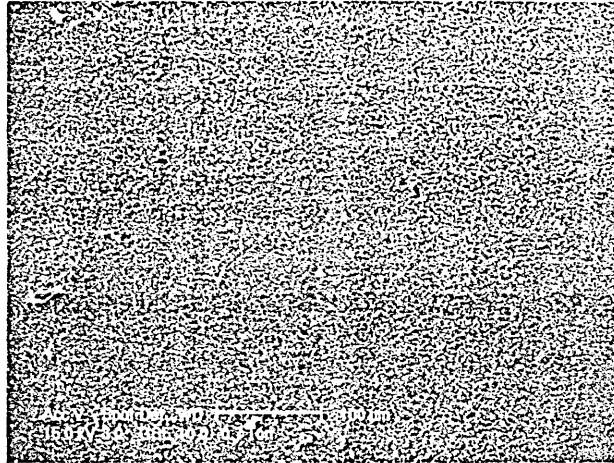
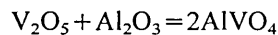


Fig. 7. A SEM of the surface of an oxidised TiAlN/VN coating, sample 3, heat treated in air at 640 °C for 1 h

coating. In samples 1 and 4 where the Al:V ratio was almost unity the majority of any  $V_2O_5$  formed was reduced to  $AlVO_4$ . In contrast, in samples 2 and 3 where the Al:V ratio was much less than unity, more free  $V_2O_5$  was present. XRD patterns ( $\theta/2\theta$ ) of coatings heated in air for 1 h at 600 °C are shown in Fig. 10. In all cases the patterns contained the same phases as were present at 550 °C, i.e.  $V_2O_5$ ,  $TiO_2$  and  $AlVO_4$ . However, there was a dramatic increase in  $V_2O_5$  relative to the other phases present. Furthermore, the  $V_2O_5$  phase which formed was highly oriented with the majority of grains having their (0 0 1) planes parallel to the coating surface. The highly oriented (0 0 1)  $V_2O_5$  phase identified in the  $\theta/2\theta$  XRD patterns is consistent with the plate like morphology observed in the SEM images. However, there was still evidence of reflections from the coating (not shown in figure) thus indicating that the coating was still intact. Increasing the heat treatment further to a temperature of 640 °C resulted, with the exception of sample 3, in further increases in the intensity of the (0 0 1) texture in the  $V_2O_5$ , Fig. 11 and is clearly consistent with the increased plate like morphology observed in the SEM images. Reflections from the coating have now disappeared indicating that the coating (not shown in figure) was almost completely oxidised. Further increases in temperature to 670 °C, Fig. 12 resulted in a dramatic decrease in the intensity of the  $V_2O_5$  and corresponding increase in the intensity of the  $AlVO_4$ . The strong (0 0 1) texture present in samples 1, 2 and 4 after heat treating in air at 640 °C had completely disappeared. Thus, the  $V_2O_5$  which had formed at the lower temperature was reduced by the formation of  $AlVO_4$ . This was clearly consistent with SEM observations which showed completely different surface morphologies after heating for 1 h in air at 670 °C. Thus, the oxides present were mainly  $TiO_2$  (rutile)

and  $AlVO_4$  and indeed SEM and EDX analysis showed two phases one Ti rich and one Al and V rich.

$AlVO_4$  phase forms from a solid state reaction between  $V_2O_5$  and  $Al_2O_3$  of the following type [16–18].



However, according to Refs. [16–18] the reaction between  $V_2O_5$  and  $Al_2O_3$  to form  $AlVO_4$  requires prolonged heating between 600 and 650 °C to go to completion. In the current work  $AlVO_4$  phase could be identified at temperatures as low as 550 °C, which is much lower than previously observed. One possible explanation is that at 550 °C the reaction is occurring mainly at the surface where diffusion rates are at least an order of magnitude faster than in the bulk. It is well

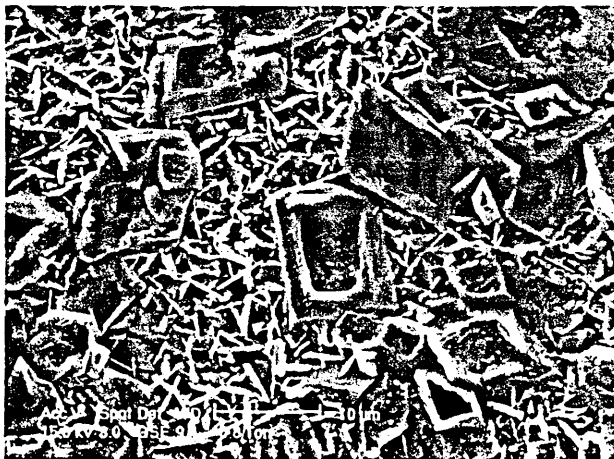


Fig. 8. A SEM of the surface of an oxidised TiAlN/VN coating, sample 1, heat treated in air at 670 °C for 1 h.

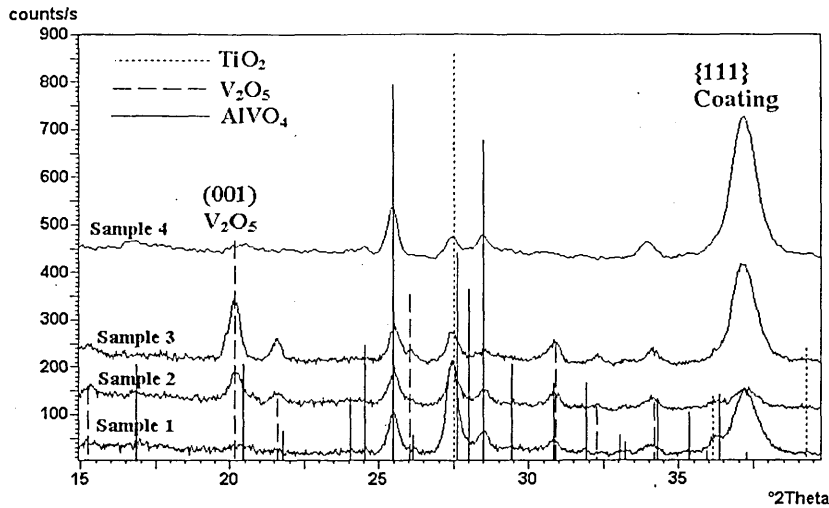


Fig. 9. GAXRD patterns of oxidised TiAlN/VN coating surfaces, heat treated in air at 550 °C for 1 h.

established that the onset of rapid oxidation of TiN to form rutile takes place at  $\sim 550$  °C [19,20]. In TiAlN coatings the onset of rapid oxidation takes place above  $\sim 800$  °C [15]. TiAlN oxidises to form a stable passive oxide double layer [19,20], the upper one Al rich and the lower one Ti rich which increases the oxidation resistance of TiAlN base coatings. Oxidation in TiAlN proceeds by the simultaneous diffusion of Al to the oxide/vapour interface and inward diffusion of O to the oxide/nitride interface. Thus, the oxidation resistance of TiAlN is conferred by the presence of a continuous  $\text{Al}_2\text{O}_3$  rich layer at the surface. In TiAlN/VN coatings

oxidised at 550 °C the presence of major reflections from the  $\text{AlVO}_4$  phase and only minor amounts of  $\text{V}_2\text{O}_5$  (particularly in samples 1 and 4) would suggest that any  $\text{Al}_2\text{O}_3$  which formed at the surface reacted with  $\text{V}_2\text{O}_5$  to form  $\text{AlVO}_4$ . Therefore, the reaction of  $\text{Al}_2\text{O}_3$  with  $\text{V}_2\text{O}_5$  disrupts the protective  $\text{Al}_2\text{O}_3$  layer from TiAlN/VN coatings. In the absence of a protective  $\text{Al}_2\text{O}_3$  layer increasing the oxidation temperature to 600 or 640 °C results in rapid oxidation of the TiAlN/VN coatings (Fig. 1) to produce  $\text{V}_2\text{O}_5$ ,  $\text{TiO}_2$  and possibly  $\text{Al}_2\text{O}_3$  although no crystalline phase of  $\text{Al}_2\text{O}_3$  has been identified. No further significant increases in  $\text{AlVO}_4$

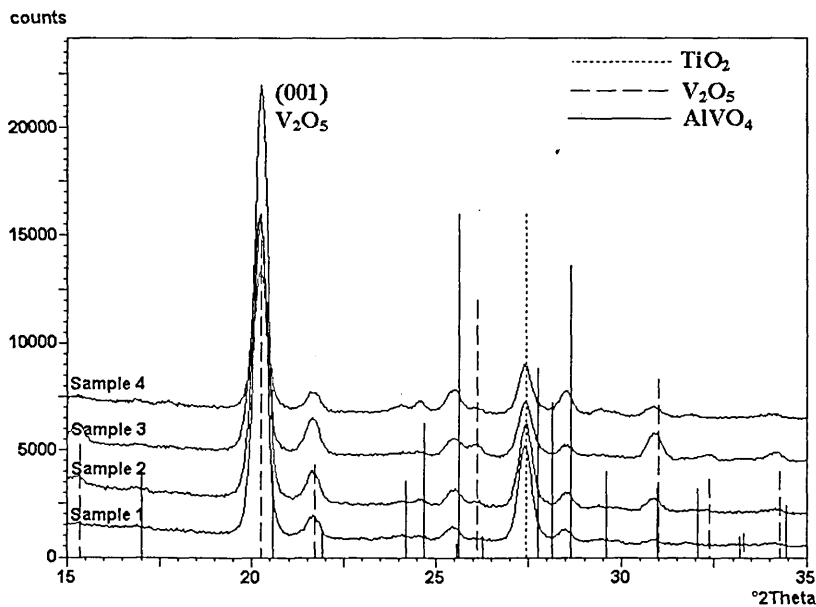


Fig. 10.  $\theta/2\theta$  XRD patterns of oxidised TiAlN/VN coating surfaces, heat treated in air at 600 °C for 1 h.

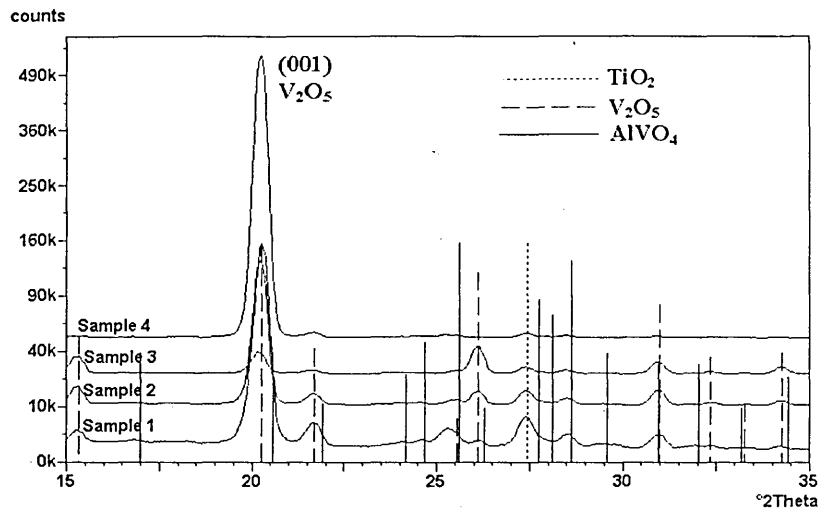


Fig. 11.  $\theta/2\theta$  XRD patterns of oxidised TiAlN/VN coating surfaces, heat treated in air at 640 °C for 1 h.

were observed indicating little or no further reaction between V<sub>2</sub>O<sub>5</sub> and Al<sub>2</sub>O<sub>3</sub> in the bulk at these temperatures. This is consistent with the SEM images which show penetration of the surface by platelets of V<sub>2</sub>O<sub>5</sub> at 600 and 640 °C, see Figs. 4–6. Increasing the temperature to 670 °C results in the formation of AlVO<sub>4</sub> that was clearly identified by both XRD and EDX analysis. Therefore, at 670 °C the temperature is sufficiently high for the reaction of V<sub>2</sub>O<sub>5</sub> with Al<sub>2</sub>O<sub>3</sub> to proceed in the bulk to form AlVO<sub>4</sub> [16–18].

The formation of V<sub>2</sub>O<sub>5</sub> is believed to be critical to the low friction behaviour of these coatings. At 550 °C the oxidation of V appears to be dominated by the

formation of AlVO<sub>4</sub>. Only at temperatures of 600 and 640 °C significant quantities of V<sub>2</sub>O<sub>5</sub> are formed leading one to the conclusion that these temperatures must be generated locally before low friction conditions prevail.

#### 4. Conclusions

- The onset of rapid oxidation in these coatings takes place at temperatures between 632 and 645 °C, which is ~150 °C lower than for monolithic TiAlN coatings. The higher the (TiAl):V ratio the higher the temperature of onset of rapid oxidation.

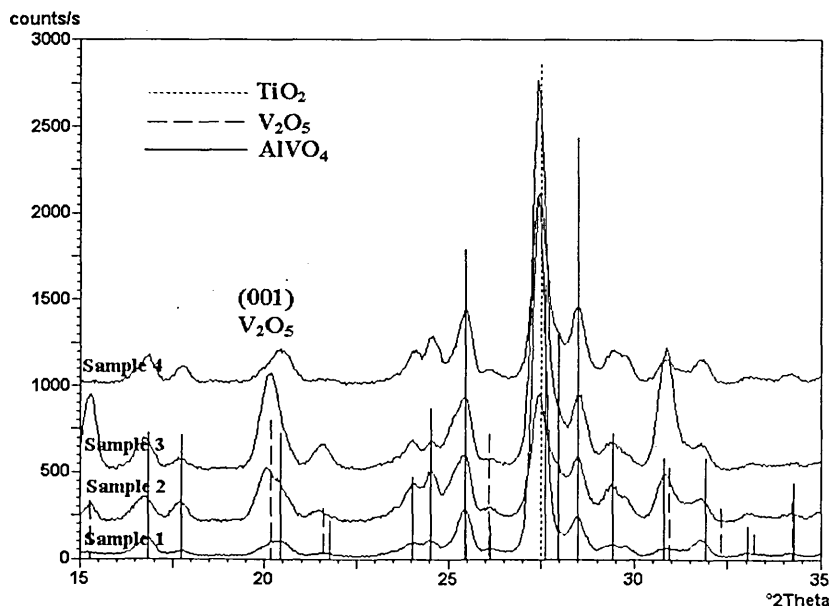


Fig. 12.  $\theta/2\theta$  XRD patterns of oxidised TiAlN/VN coating surfaces, heat treated in air at 670 °C for 1 h.

- A reaction which occurs between  $\text{Al}_2\text{O}_3$  and  $\text{V}_2\text{O}_5$  to form  $\text{AlVO}_4$  was responsible for disrupting the formation of  $\text{Al}_2\text{O}_3$  which imparts oxidation resistance on TiAlN based coatings. This reaction lowers the oxidation resistance of TiAlN/VN nano-scale multi-layer coatings when compared with monolithic TiAlN based coatings.
- The relative amounts of  $\text{V}_2\text{O}_5$  which formed was observed to depend on the (Ti+Al):V ratio.
- The  $\text{V}_2\text{O}_5$  phase with a plate like morphology was oriented with the (0 0 1) plane parallel to the coating surface.

### Acknowledgments

Financial support from Engineering and Physical Science Research Council (EPSRC), UK, Grant No GR/N23998/01 is acknowledged.

### References

- [1] W.-D. Münz, D.B. Lewis, P.Eh. Hovsepian, C. Schönjahn, A. Ehiasarian, I.J. Smith, *Surf. Eng.* 17 (2001) 15.
- [2] D.B. Lewis, I. Wadsworth, W.-D. Münz, R. Kuzel Jr., V. Valvoda, *Surf. Coat. Technol.* 116–119 (1999) 284.
- [3] I. Wadsworth, I.J. Smith, L.A. Donohue, W.-D. Münz, *Surf. Coat. Technol.* 94–5 (1997) 315.
- [4] P.Eh. Hovsepian, D.B. Lewis, W.-D. Münz, S.B. Lyon, M. Tomlinson, *Surf. Coat. Technol.* 120–121 (1999) 535.
- [5] P.Eh. Hovsepian, D.B. Lewis, W.-D. Münz, *Surf. Coat. Technol.* 133–134 (2000) 166.
- [6] W.-D. Münz, D. Schulze, F. Hauzer, *Surf. Coat. Technol.* 50 (1992) 169.
- [7] L.A. Donohue, W.-D. Münz, D.B. Lewis, et al., *Surf. Coat. Technol.* 93 (1997) 69.
- [8] P.Eh. Hovsepian, D.B. Lewis, W.-D. Münz, A. Rouzaud, P. Juliet, *Surf. Coat. Technol.* 116–119 (1999) 727.
- [9] D.B. Lewis, I.P. Wadsworth, W.-D. Münz, R. Kuzel Jr., V. Valvoda, *Surf. Coat. Technol.* 116–119 (1999) 284.
- [10] P.Eh. Hovsepian, D.B. Lewis, W.-D. Münz, *Surf. Coat. Technol.* 133–134 (2000) 166.
- [11] G.B. Harris, *Phil. Mag.* 43 (1952) 113.
- [12] D.E. Geist, A.J. Perry, J.R. Treglio, V. Valvoda, D. Rafaja, *Adv. X-ray Anal.* 38 (1995) 471.
- [13] D.B. Lewis, P. Eh. Hovsepian, W.-D. Münz, Seventh International Symposium on Trends and Applications of Thin Films, TAFT 2000 Nancy France, 28–30 March 2000, Société Française du Vide.
- [14] G. Farges, E. Beuprez, M.C. Staine-Catherine, *Surf. Coat. Technol.* 54–55 (1992) 115.
- [15] W.-D. Münz, *J. Vac. Sci. Technol. A* 4 (1986) 2717.
- [16] O. Yamaguchi, T. Uegaki, Y. Miyata, K. Shimizu, *J. Am. Ceram. Soc.* 70 (8) (1987) 198.
- [17] F.H.A. Abdalla, G.A. El-Shobaky, N.A. Hassan, *Bull. Soc. Chim. Belg.* 103 (11) (1994) 665.
- [18] 2000 JCPDS—International Centre for Diffraction Data.
- [19] D. McIntyre, J.E. Greene, G. Håkansson, J.-E. Sundgren, W.-D. Münz, *J. Appl. Phys.* 67 (1990) 1542.
- [20] L.A. Donohue, I.J. Smith, W.-D. Münz, I. Petrov, J.E. Greene, *Surf. Coat. Technol.* 94/95 (1997) 226.



# Effects of temperature on the chemistry and tribology of co-sputtered MoS<sub>x</sub>-Ti composite thin films

A. Savan<sup>a,\*</sup>, M.C. Simmonds<sup>b</sup>, Y. Huang<sup>b</sup>, C.P. Constable<sup>b</sup>,  
S. Creasey<sup>b</sup>, Y. Gerbig<sup>a</sup>, H. Haefke<sup>a</sup>, D.B. Lewis<sup>b</sup>

<sup>a</sup>CSEM Swiss Center for Electronics and Microtechnology Inc., rue Jaquet-Droz 1, CH-2007, Neuchâtel, Switzerland

<sup>b</sup>Materials Research Institute, Sheffield Hallam University, City Campus, Sheffield S1 1WB, United Kingdom

Received 20 August 2004; received in revised form 26 January 2005; accepted 21 April 2005

Available online 23 May 2005

## Abstract

Co-sputtered thin films of MoS<sub>x</sub> with Ti were deposited in order to investigate the film's tribological behaviour under various conditions. The mechanical properties of the composite films were investigated by pin-on-disk wear testing in air with 50% relative humidity, indicating improved performance compared to pure MoS<sub>x</sub> thin films. Additional pin-on-disk measurements on films tested at increasing temperature reveal a sharp drop-off in performance between 250 °C and 350 °C. High resolution X-ray photoelectron spectroscopy, field-emission gun scanning electron microscopy, Raman microscopy and X-ray diffraction measurements have been used to follow the oxidation behaviour of the films as a function of temperature and correlate it to film performance. Results indicate that whereas significant surface oxidation occurs at relatively low temperatures, significant degradation in tribological performance is observed only when bulk oxidation takes place.

© 2005 Elsevier B.V. All rights reserved.

PACS: 68.60.Dv; 62.20.Qp; 81.65.Mq

Keywords: Molybdenum; Sulphur; Tribology; Oxidation

## 1. Introduction

Sputter-deposited MoS<sub>x</sub> (where  $x \approx 1.6$ ) films are used for lubrication under vacuum and in space applications, where they can exhibit low friction coefficients and long lifetimes [1]. In humid air, the tribological performance of sputter-deposited MoS<sub>x</sub> films is greatly reduced [2–4], making pre-launch testing difficult and significantly restricting possible terrestrial applications. Co-sputter deposition with different elements or compounds, for example MoS<sub>x</sub>-Au, MoS<sub>x</sub>-Ni or MoS<sub>x</sub>-Sb<sub>2</sub>O<sub>3</sub> resulted in some improvement in tribological performance in air [5,6]. Likewise, MoS<sub>x</sub>-metal periodic multilayer films [7] show some improvement in tribological testing in humid air, compared

to pure MoS<sub>x</sub> films. More recently, Pb [8] and Ti [9] were shown to be effective additives for use in ambient air. Tribological results obtained in moist air using the MoS<sub>2</sub>-Ti composite system [10,11] show an order of magnitude improvement in wear endurance, compared to pure MoS<sub>2</sub> films. Simmonds et al. [12] found an improvement of nearly an order of magnitude in film lifetime for tribological tests in moist air with several composite systems including Ti. These results suggest an approach for making MoS<sub>x</sub> thin films with sufficiently improved solid lubricant performance to be usable in ambient air in a wider range of commercial and industrial applications.

The effects of oxygen and water vapour on the structure and properties of MoS<sub>x</sub> are complex. Oxygen is usually detected in MoS<sub>x</sub> thin films after sputter deposition, and has been characterized as substituting for sulphur as an MoS<sub>2-x</sub>O<sub>x</sub> phase [13]. A study using lateral force microscopy found only a slight dependence of MoS<sub>2</sub> friction coefficient on humidity [14]. In those measure-

\* Corresponding author. Current address: Forschungszentrum caesar, Ludwig-Erhard-Strasse 2, 53175 Bonn, Germany. Tel.: +49 228 96 56 318.  
E-mail address: [savan@caesar.de](mailto:savan@caesar.de) (A. Savan).

ments, wear did not occur except at high humidities (50% relative humidity), where it was attributed to damage at the edges of MoS<sub>2</sub> single layers. Examining the critical role of oxygen in MoS<sub>2</sub> films, Fleischauer and Lince [15,16] have reviewed the reports of structure, morphology and performance that were observed by different groups, and pointed out the difference between oxygen presence coming from oxygen substitution (for sulphur) occurring during sputter deposition, and oxidation (of molybdenum) coming about during use.

Incorporation of additives to MoS<sub>x</sub> has also been investigated in order to extend the temperature range where the films can be used. Pure MoS<sub>2</sub> has a very low oxidation rate below 400 °C, but increasingly significant oxidation is found at higher temperatures [17]. High speed machining operations such as turning, drilling and milling, especially when done dry, involve tool temperatures of 500–600 °C and more. Co-deposition with PbO was reported to increase the wear endurance in ambient air at room temperature, and to provide an “adaptive” route to improved performance at higher temperatures [18], through the formation of lubricious oxides such as MoO<sub>3</sub> and PbMoO<sub>4</sub>. MoS<sub>2</sub>-Ti has been reported both to begin oxidising at temperatures above 400 °C in air [19], and to be promising for machining operations.

For these new composite lubricants, an ability to perform well in a variety of environmental conditions is crucial if they are to become widely used in practical applications. While the presence of an additive (dopant) to MoS<sub>x</sub> frequently results in improved performance in air, better understanding of how the additives affect the structure and chemistry of the composite coating may help in choosing the additive element(s), and defining their limitations. In this study, we have characterized the tribological and mechanical behaviour of MoS<sub>2</sub> co-sputtered with Ti under varying conditions of humidity and temperature. The mechanism of film failure at elevated temperatures has also been investigated. We report on a clear correlation between tribological behaviour and oxidation of the MoS<sub>x</sub> composite thin films.

## 2. Experimental details

Composite films were grown by radio-frequency (RF) magnetron co-sputtering from one pure MoS<sub>2</sub> target (diameter 5 cm, 99.5% pure) and a pure titanium target (diameter 5 cm, 99.95% pure). The MoS<sub>2</sub> target was operated at 300 W and the volume fraction of dopant was varied over the range 0–20% by changing the Ti target power (typically over the range of 0–100 W). Growth rates for pure films were determined using stylus profilometry and these data were used to calculate the target power required for a specific dopant concentration. The actual film composition was then measured using wavelength dispersive X-ray (WDX) analysis rather than energy dispersive X-ray (EDX) analysis, because for WDX the Mo and S peaks

do not overlap. A sample of natural molybdenite was used as a standard for stoichiometric MoS<sub>2</sub>, and used as the basis for normalizing and calculating the ratios of Mo/S in the thin film samples. The analysis revealed that the value for  $x$  in MoS<sub>x</sub> was fairly constant at approximately 1.6. Film thickness was kept constant at 1.0 μm. Base pressure prior to deposition was less than  $1 \times 10^{-5}$  Pa. A working pressure of argon of  $\sim 5 \times 10^{-1}$  Pa was used during sputtering. Depositions were performed at room temperature with the substrate temperature remaining below 325 K during deposition. Thin films were grown onto glass (roughness,  $R_a \sim 1$  nm), polished cemented carbide (Sandvik P30, WC-Co) and polished AISI 440C steel ( $R_a < 0.01$  μm) substrates. In all cases a chromium adhesion layer was included between the substrate and the composite film.

High resolution scanning electron microscope (HRSEM) images were taken with a Philips XL30 ESEM-FEG using a field emission gun and an accelerating voltage of around 30 kV in high vacuum mode. The structure of the as-deposited and oxidised coatings was investigated by X-ray diffraction (Cu  $K\alpha$ ) using glancing angle (GAXRD) at 1° incidence and  $\theta/2\theta$  geometries. Unlike the other characterisation techniques such as Raman spectroscopy or scanning electron microscopy, GAXRD has very limited spatial resolution. Therefore the X-ray diffraction results presented here are representative of the sample as a whole and not any localised region.

X-ray photoelectron spectroscopy (XPS) analysis was performed on a Kratos Axis 165 XPS spectrometer using monochromatic Al  $K\alpha$  (1486.6 eV) radiation and a magnetic snorkel lens. The analyses were undertaken in a vacuum of around  $5 \times 10^{-7}$  Pa. Survey scans were performed at a pass energy of 80 eV. High resolution scans of peaks of interest were performed at a pass energy of 20 eV. In this configuration the FWHM peak width of the Ag 3d<sub>5/2</sub> peak is around 0.6 eV. The energy analyser was calibrated using the Ag 3d and Auger lines prior to use. Peak deconvolution was done by constraining the areas of the Mo 3d<sub>5/2</sub> and Mo 3d<sub>3/2</sub> peaks to a ratio of 3:2 corresponding to the peak areas expected from electron degeneracy rules.

Standard pin-on-disk tribotesting was performed on films grown onto 440C steel substrates. The tests were done using a velocity  $10 \text{ cm s}^{-1}$ , air atmosphere with 50% relative humidity (RH), using 6 mm diameter AISI 52100 steel balls and a load of 5 N, resulting in a mean Hertzian contact pressure of approximately 1 GPa. Each data point represents the average obtained from four samples grown during two different depositions. Measured lifetimes were generally repeatable within about 20% and measured friction coefficients within about 5%. The results quoted here are for the mean friction coefficients over the duration of the test. We have chosen to report the mean friction coefficient rather than either the minimum or steady state friction coefficient, as the most appropriate friction coefficient in this study. For the pure MoS<sub>x</sub> thin films, the friction coefficient was erratic over the film lifetime with no

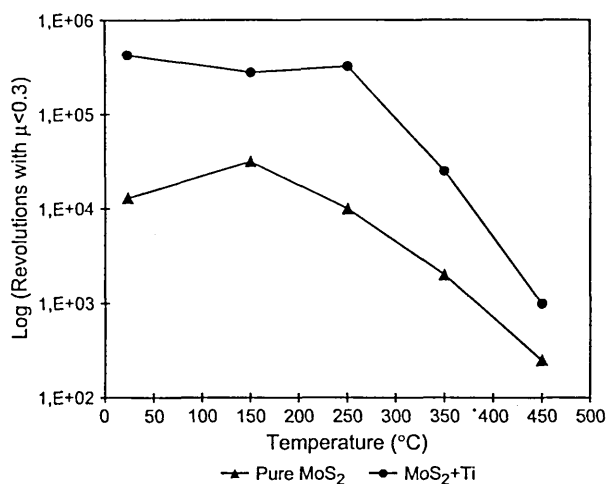


Fig. 1. MoS<sub>x</sub>-Ti thin film endurance (lifetime) determined from pin-on-disk tribometer tests versus temperature. Test conditions: Ø6 mm WC ball, coated HSS disk, load of 5 N, friction radius of 5 mm, sliding speed of 10 cm/s, test stopped when friction coefficient  $\mu > 0.3$  (variation between repeated samples and tests typically less than or equal to  $\pm 20\%$ ). The lines shown between points are only as guides.

pronounced run-in period. In this case, it was not possible to quote a steady state value, and the minimum friction coefficient has no statistical relevance. Whilst not entirely accurate perhaps, the mean friction coefficient gives some measure of film performance and allows comparison with the composite films. For these films, the run-in period was short (a few hundred revolutions) and was followed by a long, stable, steady-state regime and finally by abrupt failure. The mean and steady state friction coefficients were, to a first approximation, the same.

Analyses of the films after temperature-controlled tribometer testing were performed using a Renishaw Raman System 2000 spectrometer. This system comprised of an integral Raman microscope, a stigmatic single spectrograph, and a Peltier-cooled CCD detector (400 × 600 pixels). The microscope attachment was an Olympus BH2 system. The holographic notch filters allowed a lower spectral limit of  $\sim 150 \text{ cm}^{-1}$ . The excitation wavelength used was 632.8 nm (25 mW laser) from a HeNe laser. A maximum illumination of 4–5 mW was possible at the sample in a 1–2  $\mu\text{m}$  spot, through a standard 50× microscope objective. The penetration depth of the laser beam, i.e. the sampling depth, is a difficult parameter to calculate for Raman microscopy primarily because visible light is the excitation source, which is subject to more external factors than other probing methods. The main factors controlling this are: reflectivity of the surface, density, colouration, and topography. The penetration depth into these metallic-like PVD coatings is low, approximately 100–200 nm. However, even with this low penetration depth, the spectra obtained still arise from a spatial range corresponding to many lattice unit cells.

Samples for transmission electron microscope (TEM) analysis were prepared by cutting cross-sections of

approximately  $2 \times 3 \text{ mm}^2$  in size, using a cooled, high-speed SiC disc saw. Two such blocks were glued on a glass plate with the coated side face-to-face for metallographic grinding and polishing, which reduced them to a thickness of  $\sim 50 \mu\text{m}$ . These samples were then glued on a copper grid having a slot hole for ion-beam milling. The Ar ion-beam milling (Gatan Precision Ion Polishing System, USA) was done at 5 keV,  $\pm 5\text{--}10^\circ$ , to reach electron transparency in the cross-section of the coating region. The samples were examined using an analytical Philips CM-20 TEM operating at 200 kV.

### 3. Results

#### 3.1. Tribological performance

Fig. 1 shows film endurance versus temperature of the MoS<sub>x</sub>-Ti composites. For comparison, typical results obtained for pure MoS<sub>x</sub> films are also shown. At room temperature, the composite films exhibit lifetimes of around 500,000 revolutions, which compare favourably to conventional MoS<sub>x</sub> thin films which have lifetimes of about 10,000 revolutions (Fig. 2), similar to that reported previously [20]. Using samples coated at the same time and then stored in ambient air, film lifetime tested at various intervals over a twelve month period showed no statistically significant change in wear characteristics [21].

Excellent film endurance was maintained as the temperature increased, with no statistically significant loss in performance up to a temperature of  $\sim 250^\circ\text{C}$ . For the films tested at a temperature of  $350^\circ\text{C}$ , there was a significant reduction of about an order of magnitude in lifetime, although the films still endured for about 25,000 revolutions. At  $450^\circ\text{C}$ , a further reduction to around 1000 revolutions was observed. The relationship between endurance and temperature showed a very similar trend to that observed for conventional MoS<sub>x</sub> thin films, but with consistently higher comparative values.

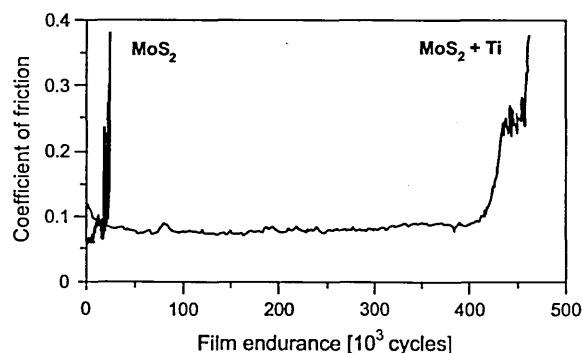


Fig. 2. Typical pin-on-disk tribometer data showing friction coefficient versus film endurance (number of revolutions) in comparative testing of pure MoS<sub>2</sub> and MoS<sub>2</sub>-Ti thin films in room temperature air with a relative humidity of 50%.

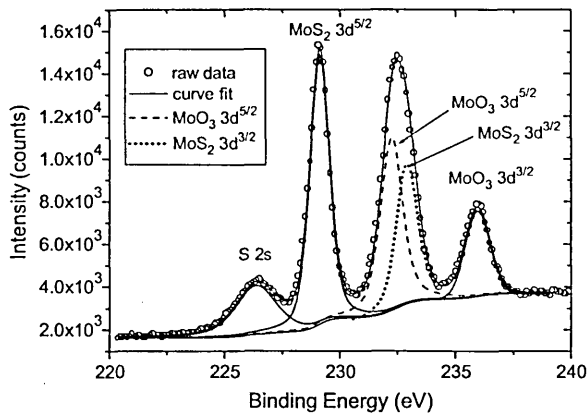


Fig. 3. High resolution XPS scans of the Mo 3d (and S 2s) region for the as-grown film showing a typical peak deconvolution.

### 3.2. XPS analyses

Fig. 3 shows high resolution XPS measurements, taken on the MoS<sub>x</sub>-Ti composite film tested at room temperature, in the energy region for Mo 3d binding. The data is well-fitted by postulating a mixture of two phases, MoS<sub>2</sub> and MoO<sub>3</sub>, being present. The Mo 3d<sub>5/2</sub> peak for the MoS<sub>2</sub> phase has a peak position of 228.7 eV, while the peak position for the MoO<sub>3</sub> phase at 233.0 eV shows good agreement with values in the literature [22]. The appearance of MoO<sub>3</sub> is not unusual and can be accounted for by post-deposition oxidation of the MoS<sub>2</sub> surface.

Fig. 4 shows the effect of temperature on the surface chemistry. For the as-deposited films, the spectrum has well-defined peaks corresponding to a mixed MoS<sub>2</sub> and MoO<sub>3</sub> layer; the predominant phase being MoS<sub>2</sub>. When the films are exposed to a relatively modest increase in temperature up to 150 °C there is a significant change in the Mo 3d spectrum. The peaks ascribable to the MoS<sub>2</sub> phase virtually disappear, and the MoO<sub>3</sub> phase dominates the spectra. By

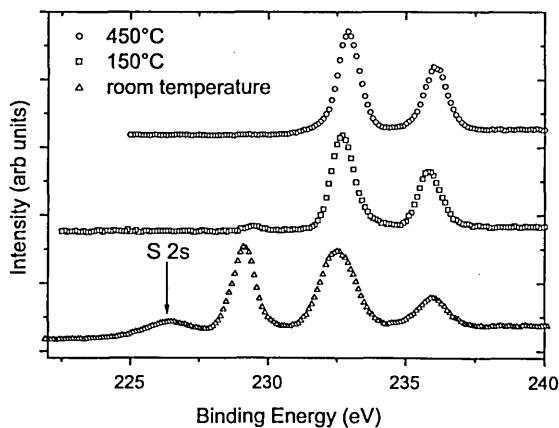


Fig. 4. High resolution XPS scan of the Mo 3d (and S 2s) peaks versus exposure temperature. The peaks ascribed to MoS<sub>2</sub> virtually disappear after heating at 150 °C, and only peaks associated with MoO<sub>3</sub> are seen at 450 °C.

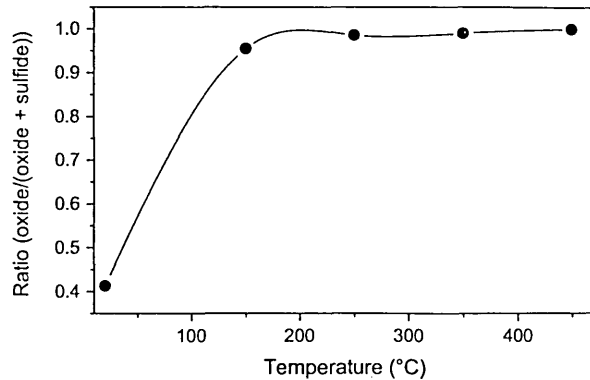


Fig. 5. Proportion of oxidized Mo out of the total of Mo-O and Mo-S bonding measured by XPS, versus temperature to which the samples were exposed.

the time temperature reaches 450 °C, only the MoO<sub>3</sub> phase is observed. This transition from a mixed film of MoS<sub>2</sub> and MoO<sub>3</sub> to predominantly single phase MoO<sub>3</sub> is quantified in Fig. 5. At room temperature, approximately 60% of the detected Mo atoms were present as MoS<sub>2</sub> while 40% were present as MoO<sub>3</sub>. Raising the temperature to 150 °C resulted in 95% of Mo atoms being present as MoO<sub>3</sub>, and at 250 °C, 98% were present as MoO<sub>3</sub>.

### 3.3. Raman spectroscopy

Figs. 6 and 7 show the Raman spectra of the MoS<sub>x</sub>-Ti thin films exposed to different temperatures, as well as the Raman spectra obtained from standards of interest. For the as-grown films, there is good agreement between the observed spectra and the spectra obtained from the MoS<sub>2</sub> standard. Similar spectra are obtained up to a temperature of 250 °C. For the sample exposed to 350 °C, a significant transition is observed, with a large peak at ~820 cm<sup>-1</sup>, which corresponds well to the dominant band of the MoO<sub>3</sub> standard. Another band at ~300 cm<sup>-1</sup> becomes more

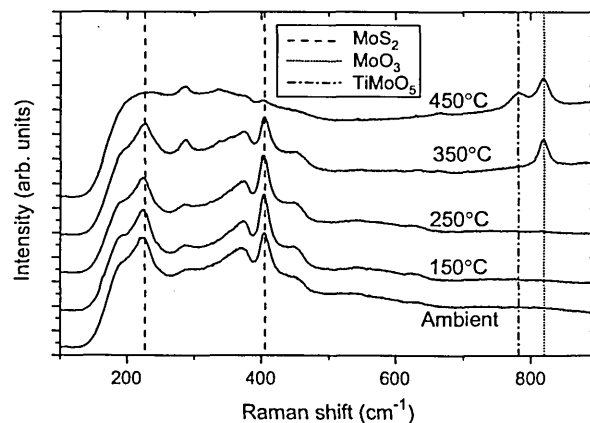


Fig. 6. Stacked plot of Raman spectra of MoS<sub>x</sub>-Ti films after exposure to various temperatures.

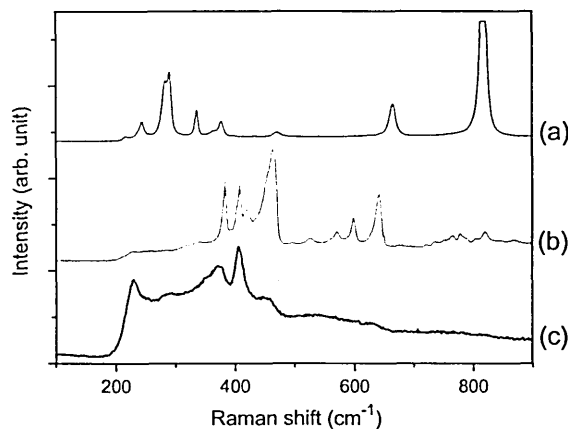


Fig. 7. Stacked plot of Raman spectra of (a) MoO<sub>3</sub> standard (b) MoO<sub>2</sub> standard and (c) MoS<sub>2</sub> standard.

prominent, which corresponds to the second most intense band of the MoO<sub>3</sub> standard. However, at 350 °C the dominant MoS<sub>2</sub> bands are still apparent, indicating the presence of both phases in these films. As the temperature rises to 450 °C the MoS<sub>2</sub> bands virtually disappear and the bands ascribable to MoO<sub>3</sub> dominate the spectrum. In none of the spectra is there evidence of other molybdenum oxide phases formation, e.g. MoO<sub>2</sub>. The spectrum at 450 °C also has an unidentified peak at around 780 cm<sup>-1</sup>. There are no bands from MoS<sub>2</sub>, MoO<sub>2</sub>, MoO<sub>3</sub> or TiO<sub>2</sub> (spectra not shown here) that could be associated with this peak. One possible identification could be TiMoO<sub>5</sub>. Unfortunately, attempts to synthesize this as a standard proved unsuccessful.

In Fig. 8, the integrated peak intensity of the dominant MoO<sub>3</sub> band at 820 cm<sup>-1</sup> has been plotted versus exposure temperature. At room temperature and at 150 °C, there is no evidence of any band at 820 cm<sup>-1</sup>. At 250 °C there is evidence of a very weak band at 820 cm<sup>-1</sup> although it is close to the instrument detection limit. An increase in

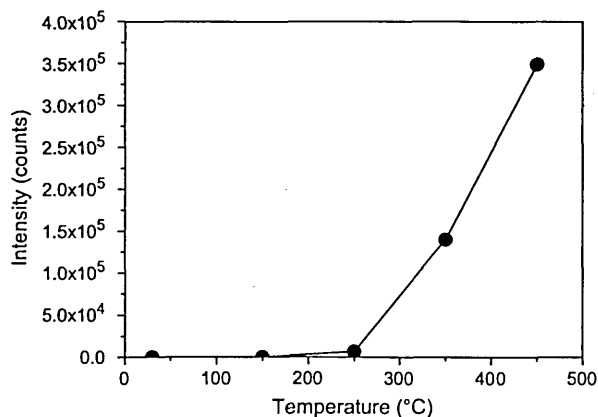


Fig. 8. Integrated peak intensity versus sample exposure temperature of the MoO<sub>3</sub> band at 820 cm<sup>-1</sup>.

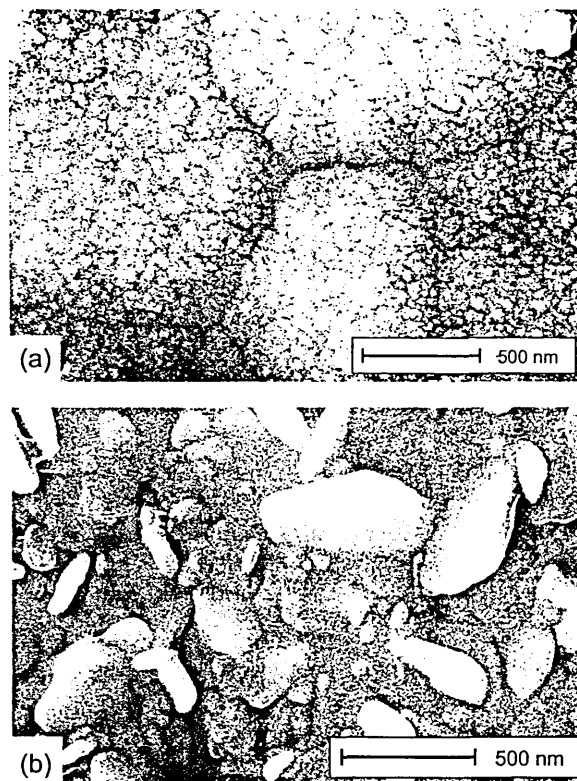


Fig. 9. FEG-SEM micrographs of the surface of the (a) as-received sample, (b) after exposure to a temperature of 350 °C.

temperature from 250 to 350 °C led to a large increase (approximately 20×) in the peak intensity, and the intensity continued to increase rapidly as the temperature rose to 450 °C.

### 3.4. High Resolution SEM

Fig. 9 shows high resolution micrographs of the MoS<sub>x</sub>-Ti composites after exposure to different temperatures. The as-grown film is seen in Fig. 9(a), having a very fine structure with surface features in the 50–100 nm range. The surface topography remains essentially unchanged up to a temperature of 250 °C. At a temperature of 350 °C there was a dramatic change in surface topography with the observation of platelets of 200–1000 nm in length and approximately 100 nm in thickness (Fig. 9b).

### 3.5. X-ray diffraction

Fig. 10(a) shows a  $\theta/2\theta$  X-ray diffraction pattern of the as-deposited film. The pattern is characterised by a broad peak at  $2\theta = 12.7^\circ$  corresponding to the (002) basal plane of the MoS<sub>x</sub> phase ( $d$ ' spacing 0.69 nm) and a diffuse peak at  $2\theta \sim 40^\circ$  resulting from overlapping broad peaks from the MoS<sub>x</sub> phase. The  $d$ ' spacing for the (002) plane of bulk MoS<sub>2</sub> is 0.615 nm. Peaks with  $d$ ' spacing larger than those of bulk values are often measured in sputter deposited films

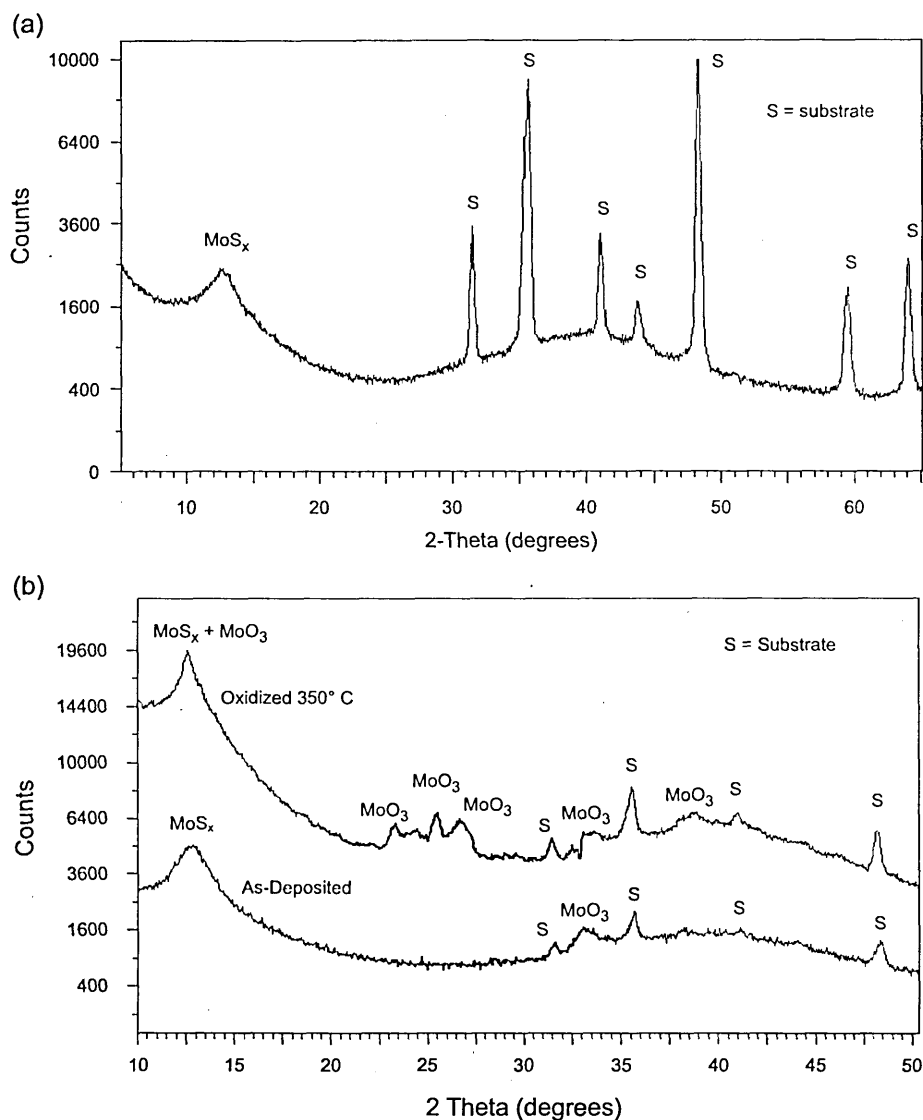


Fig. 10. (a)  $\theta/2\theta$  X-ray diffraction pattern of the as-deposited sample. (b) Glancing angle X-ray diffraction patterns of the as-deposited sample and sample exposed to 350 °C (spectra offset for clarity).

[22,23]. The sharp peaks in the pattern correspond to those from the cemented carbide substrate. Glancing angle X-ray diffraction (GAXRD) patterns of as-deposited and oxidised (350 °C) films are shown in Fig. 10(b). In the pattern from the as-deposited film, peaks from the  $\text{MoS}_x$  coating and the cemented carbide substrate are present as in the corresponding  $\theta/2\theta$  scan, but with less substrate contribution. Furthermore, the presence of peaks at  $2\theta \sim 33^\circ$  indicate some evidence of  $\text{MoO}_3$  in the as-deposited film, thus supporting the evidence observed in XPS spectra. In the film oxidised at 350 °C the GAXRD pattern shows weak reflections corresponding to  $\text{MoO}_3$  in addition to those from the coating and cemented carbide substrate. After oxidation at 350 °C, the major peak at  $2\theta \approx 12.7^\circ$  can be interpreted as a composite peak from the (002)  $\text{MoS}_2$  basal plane and the (020) plane of  $\text{MoO}_3$ .

### 3.6. Transmission electron microscopy

Fig. 11 shows a TEM cross-section of an  $\text{MoS}_x$ -Ti thin film after exposure to 350 °C. A dense, uniform  $\text{MoS}_x$ -Ti film is apparent. The diffraction pattern (not shown) indicates this layer to be amorphous. The thickness of this layer is over 1  $\mu\text{m}$ , which is nearly as thick as the as-grown film. It is interesting to note the appearance of a crack between the Cr adhesion layer and the  $\text{MoS}_x$ -Ti film. While it is possible that this is an artifact of TEM sample preparation, no cracks were observed in coatings exposed to lower temperatures. An oxide layer on the  $\text{MoS}_x$ -Ti thin film was also noted, although because of the low contrast it is difficult to see. Fig. 12 shows a higher magnification image of this layer. The platelet type oxide structure, similar to that in the HRSEM image of Fig. 9(b), can also be seen.

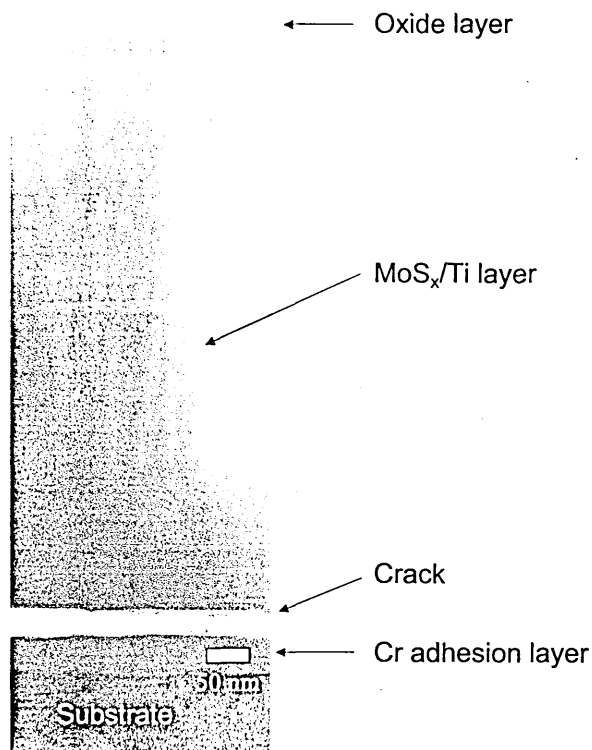


Fig. 11. TEM of the MoS<sub>x</sub>-Ti after exposure to 350 °C.

In this image the oxide layer is approximately 100–200 nm thick, although because of the large variation in platelet sizes the thickness of this layer does vary from region to region. The diffraction pattern in Fig. 12 corresponds to that expected for MoO<sub>3</sub>.

#### 4. Discussion

If we compare the XPS results (in particular Fig. 5) with the tribological results (Fig. 1) there appears to be little correlation between them. Specifically, the onset of the drop of in tribological performance is at around 350 °C while the oxidation of MoS<sub>2</sub> observed by XPS analysis starts at room temperature and is virtually complete by 150 °C. The reason for this poor correlation is probably associated with the surface sensitivity of XPS analysis. The electrons from the Mo 3d region have a kinetic energy of around 1255 eV. We can estimate the mean free path ( $\lambda$ ) of these photoelectrons from the following equation:

$$\lambda = 0.41 \left[ \frac{A(\text{g mol}^{-1})10^{24}}{\rho(\text{kg m}^{-3}) \cdot N(\text{mol}^{-1})} E_k(\text{eV}) \right]. \quad (1)$$

Where  $A$  is the atomic mass of the element,  $\rho$  is the material bulk density,  $N$  is the Avogadro number and  $E_k$  is the photoelectron kinetic energy. This gives a value for  $\lambda$  of 1.6 nm. The majority (~95%) of electrons that contribute to

the observed peaks originate within  $3\lambda$  of the surface (i.e. around 5 nm). The XPS analysis shows that there is significant oxidation of the surface layer to a depth of at least 5 nm even at room temperature, and that this oxidation is virtually complete at temperatures as low as 150 °C. When we compare the XPS data with the tribological results, it can be seen that this surface oxide growth has little observable effect on film performance in pin-on-disk tribometer tests. Nevertheless, these results may have implications on the lifetime of such films in practical applications. The data as a whole indicates that MoO<sub>3</sub> has poor lubricating properties. In start-stop applications at modest temperature levels, significant oxidation may occur and film lifetimes could be significantly reduced from what would be expected from the continuous rotation of pin-on-disk tribometer tests.

If we compare the results from the Raman spectroscopy (in particular Fig. 8) with the tribology results (Fig. 1) then a much better correlation is observed between the onset of oxidation from MoS<sub>2</sub> to MoO<sub>3</sub> and the tribological performance. The sampling depth of Raman is around 100–200 nm and so this is a much less surface-sensitive technique than XPS analysis. For samples up to 250 °C, little or no evidence of oxidation is observed, while for samples at 350 °C and 450 °C a strong band associated with the formation of MoO<sub>3</sub> is seen. At 350 °C the bands associated with MoS<sub>2</sub> and MoO<sub>3</sub> are of similar intensity, suggesting that the oxide layer is around the same thickness as the sampling depth (i.e. around 100–200 nm). At 450 °C, the bands associated with the MoS<sub>2</sub> have virtually disappeared, suggesting that the oxide layer is thicker than the sampling depth. The intensity of the oxide signal shows good correlation with the tribological results and strongly

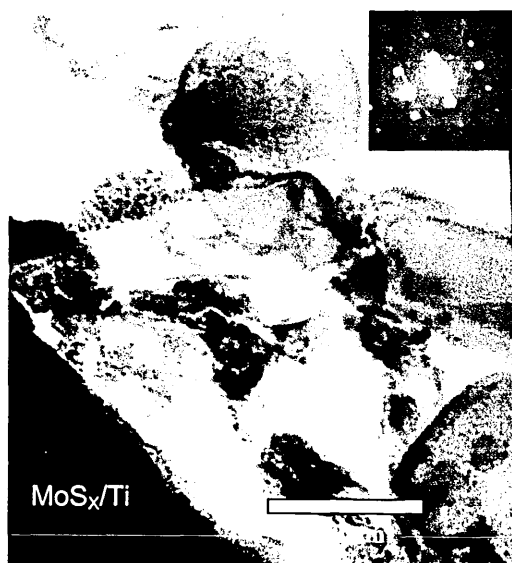


Fig. 12. TEM of the interface between the oxidised layer formed after exposure to 350 °C, and the unoxidised MoS<sub>x</sub>-Ti thin film below. The inset diffraction pattern, taken from the oxidised layer, corresponds to MoO<sub>3</sub>.

indicates that the transition from surface to internal oxidation results in the drop-off in performance.

The HRSEM images tend to support this hypothesis. Fig. 9(a) shows the as-grown films to have a very fine structure with surface features in the 50–100 nm range. At a temperature of 350 °C there is a dramatic change in surface topography with the observation of platelets of 200–1000 nm in length and 100 nm or less in thickness. This change in topography correlates well with the change in tribological performance. From the Raman results, it would seem likely that these are MoO<sub>3</sub> crystals. The MoO<sub>3</sub> structure is hexagonal, which is similar to the observed platelet structure.

The TEM data shows similar results to the HRSEM, with a platelet-type surface oxide layer. It also suggests that a thick, coherent layer of MoS<sub>x</sub>-Ti layer remains even after the film have failed in tribological testing. We can suggest two possible reasons for the tribological failure. The first is that the TEM clearly shows cracking at the MoS<sub>x</sub>-Ti interface. This film delamination could contribute to failure. Another possible explanation is that the contact pressure during the high-load, accelerated tribo-testing could lead to localised heating and hence more oxide growth, and resulting high friction and failure.

## 5. Conclusions

MoS<sub>x</sub>-Ti composites have been shown to have good lubrication properties up to temperatures of 350 °C and not to deteriorate with storage over a twelve month period. At 350 °C there is a transition from surface oxidation to internal oxidation of the films, with the MoS<sub>2</sub> being oxidised to MoO<sub>3</sub> with a platelet type structure. These films show poor lubricating properties.

## References

- [1] M.R. Hilton, P.D. Fleischauer, *Surf. Coat. Technol.* 54/55 (1992) 435.
- [2] M. Suzuki, *Lubr. Eng.* 57 (2001) 23.
- [3] I.L. Singer, S. Fayeulle, P.D. Ehni, *Wear* 195 (1996) 7.
- [4] K.J. Wahl, M. Belin, I.L. Singer, *Wear* 214 (1998) 212.
- [5] B.C. Stupp, *Thin Solid Films* 84 (1981) 257.
- [6] T. Spalvins, *Thin Solid Films* 118 (1984) 375.
- [7] M.R. Hilton, R. Bauer, S.V. Didziulis, M.T. Dugger, J.M. Keen, J. Scholhamer, *Surf. Coat. Technol.* 53 (1992) 13.
- [8] K.J. Wahl, D.N. Dunn, I.L. Singer, *Wear* 230 (1999) 175.
- [9] V. Bellido-Gonzalez, A.H.S. Jones, J. Hampshire, T.J. Allen, J. Witts, D.G. Teer, K.J. Ma, D. Upton, *Surf. Coat. Technol.* 97 (1997) 687.
- [10] V.C. Fox, N. Renevier, D.G. Teer, J. Hampshire, V. Rigato, *Surf. Coat. Technol.* 117–119 (1999) 492.
- [11] N.M. Renevier, V.C. Fox, D.G. Teer, J. Hampshire, *Surf. Coat. Technol.* 127 (2000) 687.
- [12] M.C. Simmonds, A. Savan, E. Pflüger, H. Van Swygenhoven, *Surf. Coat. Technol.* 126 (2000) 15.
- [13] J.R. Lince, M.R. Hilton, A.S. Bommannavar, *Thin Solid Films* 264 (1995) 120.
- [14] A. Schumacher, N. Kruse, R. Prins, E. Meyer, R. Lüthi, L. Howard, H.-J. Güntherodt, L. Scandella, *J. Vac. Sci. Technol. B* 14 (2) (1996) 1264.
- [15] J.R. Lince, M.R. Hilton, A.S. Bommannavar, *Surf. Coat. Technol.* 43/44 (1990) 640.
- [16] P.D. Fleischauer, J.R. Lince, *Tribol. Int.* 32 (1999) 627.
- [17] A.R. Lansdown, *Molybdenum Disulphide Lubrication*, Elsevier Science, Amsterdam, The Netherlands, 1999, p. 40.
- [18] J.S. Zabinski, M.S. Donley, V.J. Dyhouse, N.T. McDevitt, *Thin Solid Films* 214 (1992) 156.
- [19] N.M. Renevier, H. Oosterling, U. König, H. Dautzenberg, B.J. Kim, L. Geppert, F.G.M. Koopmans, J. Leopold, *Surf. Coat. Technol.* 172 (2003) 13.
- [20] M.C. Simmonds, A. Savan, E. Pflüger, H. Van Swygenhoven, *J. Vac. Sci. Technol., A, Vac. Surf. Films* 19 (2001) 609.
- [21] A. Savan, Y. Gerbig, E. Jeanpetit, H. Haefke, *Proceedings of the International Tribology Conference, Nagasaki, Japan, October 29–November 2, 2000*, p. 1115.
- [22] P.D. Fleischauer, *Thin Solid Films* 154 (1987) 309.
- [23] V. Buck, *Thin Solid Films* 198 (1991) 157.

# The role of the growth defects on the corrosion resistance of CrN/NbN superlattice coatings deposited at low temperatures

D.B. Lewis<sup>a,\*</sup>, S.J. Creasey<sup>a</sup>, C. Wüstefeld<sup>b</sup>, A.P. Ehiasarian<sup>a</sup>, P.Eh. Hovsepien<sup>a</sup>

<sup>a</sup> Materials Research Institute, Sheffield Hallam University, Howard Street, Sheffield S1 1WB, U.K.

<sup>b</sup> Freiberg University of Mining and Technology, Institut für Metallkunde, Gustav-Zeuner-Straße 5, D-09599 Freiberg, Germany

Received 16 June 2005; received in revised form 25 August 2005; accepted 29 August 2005

Available online 17 October 2005

## Abstract

CrN/NbN nano-scale multilayered coatings have been successfully deposited at a temperature of 250 °C on 304 stainless steel substrates by the combined cathodic arc/unbalanced magnetron technique (Arc Bond Sputter) with a thickness typically 3.0 μm at bias voltages  $U_B$  of –75 and –95 V. The microstructure and surface morphology of the coatings were examined in the as-deposited and corroded condition using an environmental scanning electron microscope (ESEM) in the gaseous secondary electron mode. The corrosion resistance of the coatings was determined by a potentiodynamic polarisation measurement in a 3% NaCl solution open to air at room temperature. In the ESEM images defects could be observed on the surface of the coatings and the number of these defects decreased with increasing bias voltage. ESEM images of the as-deposited coatings showed that microstructure adjacent to growth defects is under dense. These defects have been shown to be sites for preferential corrosive attack. However, even with these drawbacks the corrosion resistance as-measured by potentiodynamic polarisation was shown to be superior to that of the uncoated 304 stainless steel substrate, whilst the corrosion resistance of the CrN/NbN nano-scale multilayered coatings increased with increasing bias voltage. In all cases the corrosion resistance was inferior to similar CrN/NbN nano-scale multilayered coatings deposited at higher temperatures of 450 °C.

© 2005 Published by Elsevier B.V.

**Keywords:** CrN/NbN nano-scale multilayer coatings; Growth defects; Corrosion behaviour

## 1. Introduction

Increasingly chromium nitride coatings are being used as a replacement for electroplated hard chromium in various applications [1] because physical vapour deposition (PVD) processes are more environmentally friendly. These coatings have been considered because they have the required tribological and electrochemical properties together with good adhesion when deposited at low temperatures [1,2]. This makes them highly suitable for deposition on temperature sensitive materials such as plain carbon or low alloy steels. The microstructure of these monolithically grown coatings evolves as a rather open columnar structure, which can lead to rapid corrosion failure. However, the use of nano-scale compositionally modulated structures can offer a combination of

properties such as a high hardness, and wear resistance [3,4] coupled with reasonable corrosion resistance. In this context CrN/NbN nano-scale multilayered coatings [5–8] have performed particularly well in corrosion resistant applications because of the use of chemically stable metals Nb and Cr with a nano-scale multilayer architecture. These coatings were deposited by the unbalanced magnetron sputtering technique [arc bond sputter (ABS)] [9], in and industrial size PVD coater. The ABS coating technique uses a metal ion etching step using steered cathodic arc evaporation with a substrate bias voltage of  $U_B = -1200$  V prior to deposition, which results in enhanced coating/substrate adhesion as measured by critical load in a scratch adhesion test. However, in parallel to the favourable effect of improved adhesion, it is well known that typical arc droplets will be deposited on the substrate surface resulting in the formation of substantial growth defects [10–13]. These defects are deleterious due to local loss of adhesion [10], surface roughening [12], and the formation of surface shrinkage due to self-propulsion [13], which are unfavourable

\* Corresponding author.

E-mail address: [drbrianlewis@aol.com](mailto:drbrianlewis@aol.com) (D.B. Lewis).

conditions for tribological applications. Furthermore, atomic shadowing in the region adjacent to the particle results in the formation of a voided under dense region between the defect and the unperturbed area of the coating [14]. This results in solution pathways between the coating surface and the substrate thus leading to galvanic corrosion between the anodic substrate and cathodic coating [15]. Previous work was based on coatings deposited at temperatures of 400 °C [5,7,8,15], which is unsuitable for temperature sensitive materials such as plain carbon or low alloy steels. The basis of this work was to investigate the corrosion behaviour effect of CrN/NbN coatings deposited at a lower temperature of 250 °C.

## 2. Experimental details

### 2.1. Coating deposition

The CrN/NbN nano-scale multilayer coatings were deposited in a HTC 1000-4 four target (two Cr and two Nb) system manufactured by Hauzer Techno Coatings Europe BV [16]. Prior to coating the substrate surfaces were subjected to a metal ion etch from a cathodic arc discharge at a bias voltage,  $U_B = -1100$  V. In the second stage a stress reducing 0.25  $\mu\text{m}$  thick CrN base layer was deposited to increase adhesion between coating and substrate. Finally a CrN/NbN superlattice nano-scale multilayer coatings was deposited at bias voltages of  $U_B = -75$  V and  $U_B = -95$  V. The coatings were deposited at a constant temperature of 250 °C in a common Ar+N<sub>2</sub> atmosphere without shielding and the power to the Nb and Cr targets was 2  $\times$  6 and 2  $\times$  3 kW, respectively. M2 high steel speed steel and 304 austenitic stainless polished to a surface finish of  $R_a = 0.01$   $\mu\text{m}$  were used as substrate materials. A more detailed deposition of the deposition processes used for the low temperature (250 °C) nano-scale multilayer coatings is shown elsewhere [17].

### 2.2. Mechanical tests

A TAYLOR-HOBSON Talysurf\_120L with a 2  $\mu\text{m}$  radius diamond stylus with a resolution of 0.005  $\mu\text{m}$  was also used to measure the surface roughness. Plastic hardness was determined with the Fisherscope, normal load, 50 mN.

### 2.3. Structure and microstructure

X-ray diffraction was performed in both  $\theta/2\theta$  and glancing angle geometries using monochromatic Cu K $\alpha$  radiation. Textures present in the as-deposited coatings were determined both by the Harris inverse pole figure method (Texture  $T^*$ ) [18]

Bi-layer periods of the nano-scale multilayer,  $\Delta$ , were measured directly in the low angle region from the standard Bragg equation [19]. Glancing angle parallel beam geometry was used to determine the state of residual stress present in the coatings [20]. The coating surfaces were examined using an environmental scanning electron microscope (ESEM) and images obtained in the gaseous secondary electron (GSE) mode. The GSE mode was used in order to eliminate charging effects on the corroded surfaces.

### 2.4. Electrochemical corrosion tests

The corrosion resistance of the CrN/NbN nano-scale multilayer coatings was determined by a potentiodynamic polarisation measurement in a 3% NaCl solution open to air at room temperature. A coated sample was placed in a glass filled with the 3% NaCl solution and polarised as the working electrode. Fixing a wire around the sample made an electrical contact. Initially the solution was aerated with oxygen for 55 min. During this period the sample and the electrodes were already in the solution. Samples were then cathodically cleaned at a potential of  $-1.5$  V for 100 s, which was followed by a 40 min period to allow stabilisation of the free corrosion potential. Potentiodynamic measurements were made between polarising potentials from  $-1$  to  $+1$  V at a scan rate of 0.5 mV/s. Values of potential were referred to a standard calomel electrode, using potentiostat EG and G Model 273.

## 3. Experimental results and discussion

### 3.1. As-deposited coatings

Results of the measurements of the bi-layer period are included in Table 1. The bi-layer periods for the coatings deposited at  $U_B = -75$  V and  $U_B = -95$  V were similar at 2.27 and 2.25 nm, respectively. All the coatings were single phase and developed with a pronounced  $\{111\}$  texture, which increased with increasing bias voltage, Table 1. In parallel the residual stress increased from 4.4 GPa at  $U_B = -75$  V to 5.2 GPa at  $U_B = -95$  V, Table 1.

Environmental images (ESEM) of the sample surfaces, as shown in Fig. 1, which were taken at the same magnification and show fewer growth defects in the coating deposited at higher bias voltage. A combination of higher residual stresses and increases ad-atom mobility result in fewer growth defects with increasing bias voltage [7]. Indeed cessation of growth of coating growth defects has been observed with increasing bias voltage. A reduction in the number of growth defects is further supported by the observed decreases in surface roughness with

Table 1  
Results of coating thickness, bi-layer period, plastic hardness and surface roughness

Coating	Coating thickness [ $\mu\text{m}$ ]	Bi-layer period [nm]	Plastic hardness [GPa]	Residual stress GPa	Surface roughness [ $R_a$ $\mu\text{m}$ ]	Texture parameter $T^*$		
$-75$ V bias	3.5	2.27	51	4.4	0.079	$\{111\}$ 3.51	$\{100\}$ 0.24	$\{110\}$ 0.73
$-95$ V bias	3.25	2.25	69	5.2	0.051	4.55	0.17	0.16

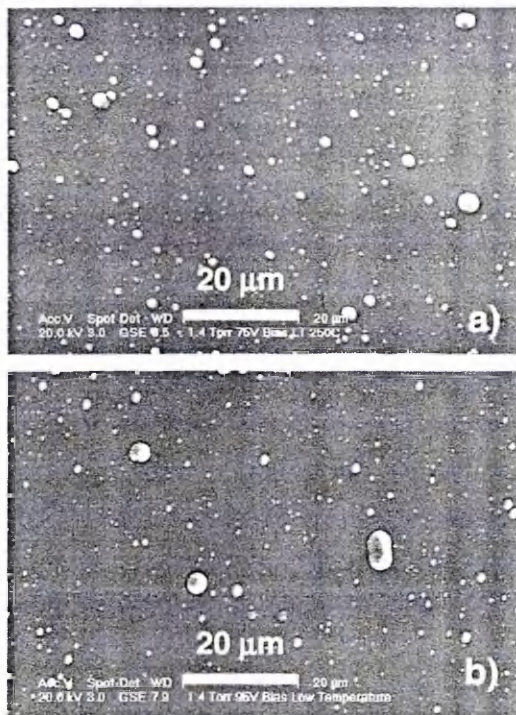


Fig. 1. Environmental Scanning Electron Microscope (ESEM) images of the samples' surfaces (a)  $U_B = -75$  V; (b)  $U_B = -95$  V trial.

increasing bias voltage, see Table 1. This decrease in coating roughness results from an increased smoothing of the coating surface with increasing bias voltage [6] and a reduction in the number of growth defects [7]. A particular feature of CrN/NbN coatings is the shape of the growth defects. In contrast to other coatings deposited by the ABS technique, e.g. TiAlN/VN [7] and TiAlN/CrN [10] coatings, many of the growth defects are not spherical but oval and indeed the long axis of the defects are aligned along a common axis in the specimen, see Fig. 2. One possible explanation is that the principal residual stresses  $\sigma_1$  and  $\sigma_2$  are not equal resulting in asymmetrical growth of the growth defect. Higher magnification images of the coating surfaces deposited at  $U_B = -75$  V and  $U_B = -95$  V are shown in Fig. 3(a) and (b). The micrographs record a plan view of the surface showing the tops of the individual columns. Coatings

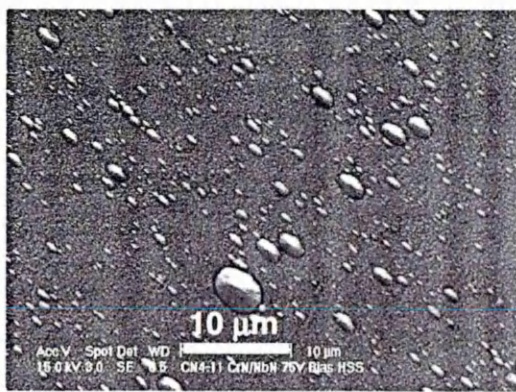


Fig. 2. Environmental Scanning Electron Microscope (ESEM) images of the sample surface showing asymmetry of growth defects.

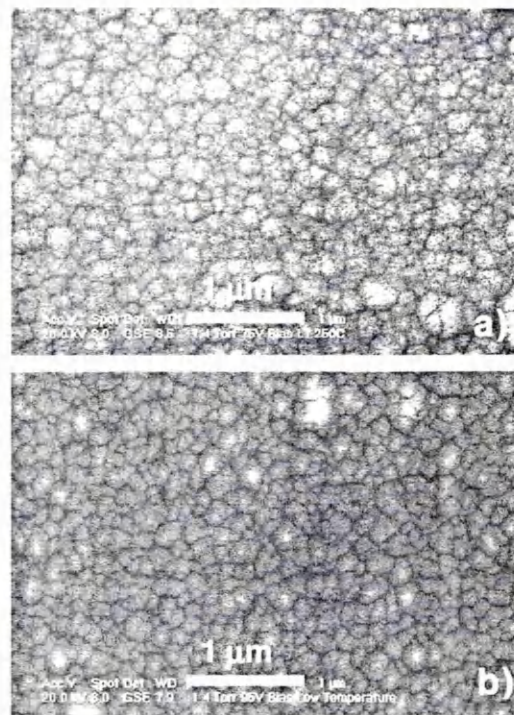


Fig. 3. Environmental Scanning Electron Microscope (ESEM) images of the samples' surfaces showing plan view of grain structure at the surface (a)  $U_B = -75$  V; (b)  $U_B = -95$  V trial.

are characterised by a relatively fine dense columnar grain structure. In contrast the coating microstructure adjacent to growth defects is under dense see Fig. 4(a) to (d). Micrograph in Fig. 4(a) shows a fractured growth defect thus exposing the coating's microstructure under the growth defect. The microstructure in the lower region of the growth defect is rough and severely under dense while the microstructure of the growth defect is composed of dense columnar grains extending in feather like pattern growing from a central core. It is well established that growth defects are formed from droplets produced during the cathodic arc metal ion etching stage [13,21,22]. These dramatic differences in microstructure are due to the fact that the upper and lower edges of the droplet are exposed to different amounts of ion bombardment [14]. The top of the defect grows in a regime of intense ion bombardment whilst in the lower region is in shadow from the droplet resulting in a less intense ion bombardment and therefore a porous under dense microstructure.

### 3.2. Coatings after potentiodynamic corrosion tests

Fig. 5(a), (b), (c) and d show the coating surface after exposure to the potentiodynamic polarisation measurement in a 3% NaCl solution. There is clear evidence of selective corrosion at growth defects. The defects have been expelled thus exposing the under dense region to the corrosive media (3% NaCl). In Fig. 5(a), (c) and (d) there is clear evidence that the pits formed in the under dense regions extend from the surface to the substrate. This is further supported by energy-

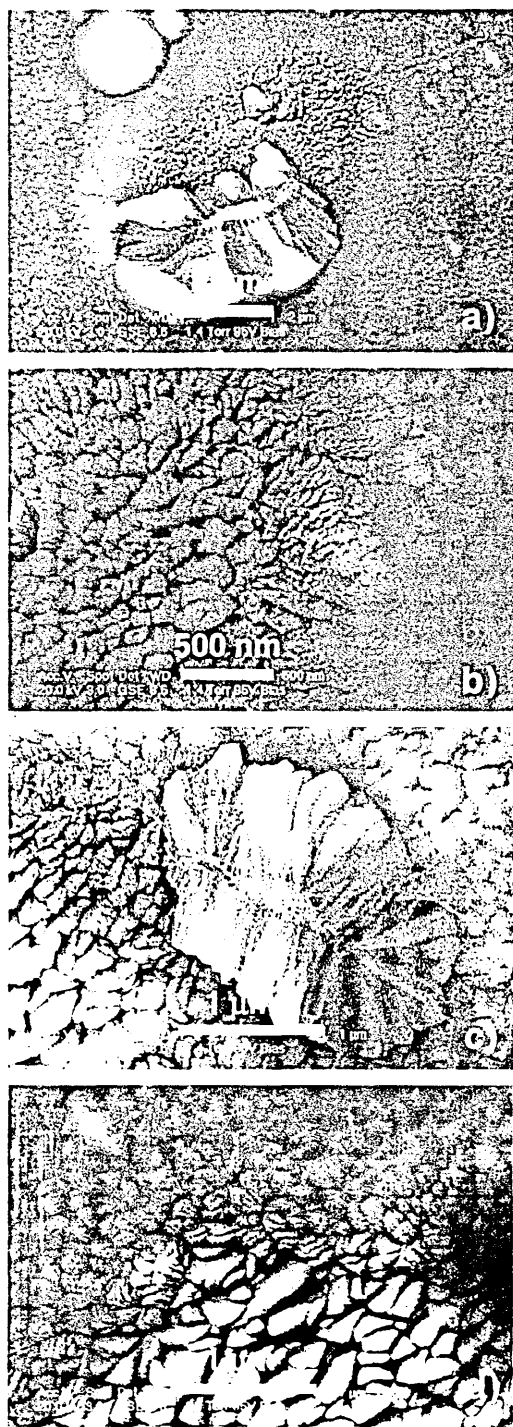


Fig. 4. Environmental Scanning Electron Microscope (ESEM) images of  $U_H = -75$  V sample: (a) a broken growth defect: (b) open grain structure in the hole containing another growth defect:  $U_H = -95$  V trial sample (c) a broken growth defect showing the columnar grains and (d) interface coating/growth defect.

dispersive X-ray (EDX) analysis at the edge of the under dense region which shows the presence of iron from the corrosion product, see Fig. 6(a) and (b), which show an X-ray distribution map and associated electron image of a pit formed in region containing a growth defect. In the image the crystals

of cubic morphology on the corroded metal surfaces are sodium chloride crystals from the 3% salt solution. In general transition metal nitrides are relatively noble and therefore inert to chemical attack. However, the majority of PVD coatings do not behave to their full potential based on their theoretical

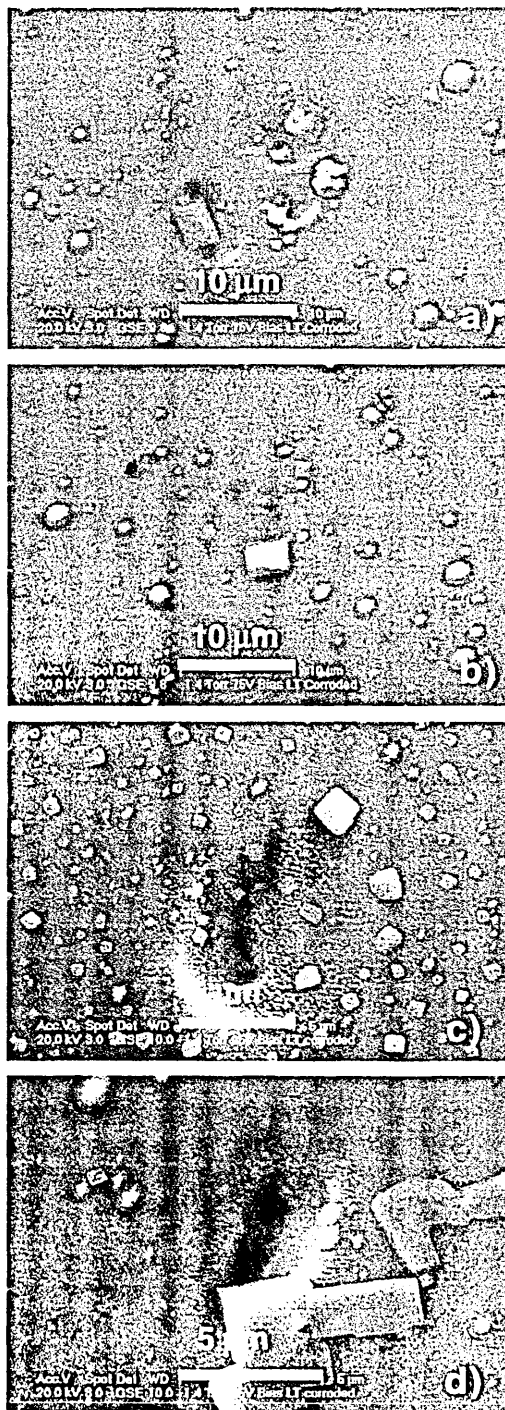


Fig. 5. (a) Corrosion at growth defects in the CrN/NbN coating deposited at  $U_H = -75$  V; (b) Corrosion at growth defects in the CrN/NbN coating deposited at  $U_H = -75$  V; (c) Corrosion at growth defects in the CrN/NbN coating deposited at  $U_H = -95$  V; (d) Corrosion at growth defects in the CrN/NbN coating deposited at  $U_H = -95$  V.

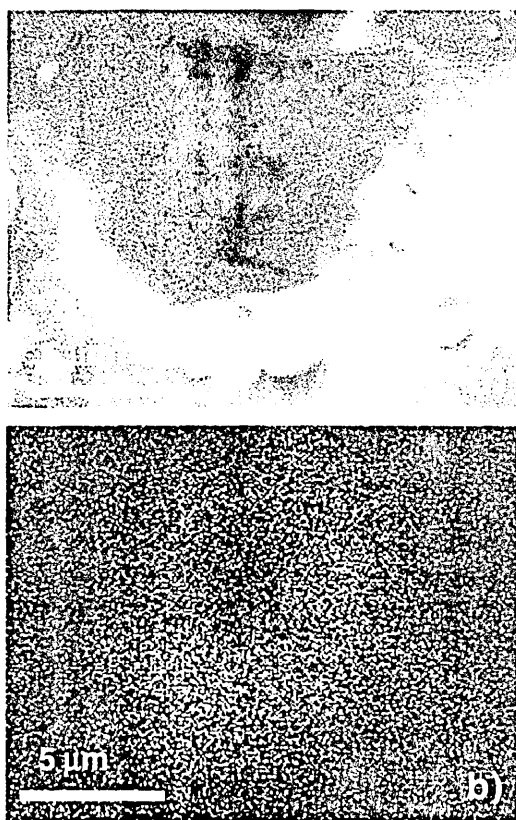


Fig. 6. Energy Dispersive X-ray analysis (EDX) of a corrosion site of the  $U_B = -75$  V sample: (a) secondary electron image, (b) X-ray distribution map Fe  $K\alpha$ .

corrosion resistance. This is due to presence of defects that present a solution path to the corrosive media resulting in galvanic corrosion and crevice corrosion between substrate (anode) and coating (cathode). All coatings contain some small degree of microporosity and are therefore susceptible to corrosion. However, ABS coatings also contain growth defects in addition to micro-porosity. The microstructure in the lower region of the growth defect is severely under dense and is therefore a further solution-pathway to the substrate surface and hence a potential region of pitting corrosion. The situation with the growth defects themselves becomes even more complicated however [15]. At the base of the growth defect is a droplet, which is compositionally metal rich and nitrogen deficient and therefore anodic with respect to the both the surrounding coating and growth defect. This results in corrosion of the droplet at the coating/substrate interface thus leaving a crater in the coating's surface, resulting in direct contact with the metal surface and hence localised galvanic corrosion at the substrate surface.

Fig. 7 shows potentiodynamic polarisation curves for the 304 stainless steel substrate and CrN/NbN nano-scale multilayer coatings deposited at bias voltages  $U_B = -75$  V and  $U_B = -95$  V. In both cases the corrosion current density is lower and the pitting potential higher in the CrN/NbN coatings. However, for the coated specimens increases in the bias voltage from  $U_B = -75$  V to  $U_B = -95$  V results in a lower corrosion

current density and higher pitting potential. Increases in bias voltage results in denser coatings with fewer voids and pores [23]. Denser coatings are conducive to better corrosion protection because there are fewer pathways for the corrosive media to penetrate the coating to the substrate surface. Furthermore, increases in bias voltage results in a reduction in the number of growth defects [7]. All growth defects are potential sites for localised pitting corrosion [5,15]. Therefore the increase corrosion resistance at higher bias voltage is predictable on the basis of increased densification and reduction in the number of growth defects. However, the corrosion resistance of coatings deposited at the lower temperature is lower than similar coatings deposited at higher temperatures. Typical corrosion current densities  $3$  to  $5 \times 10^{-7}$   $A\ cm^{-2}$  and  $1.0 \times 10^{-8}$   $A\ cm^{-2}$  with pitting potentials of 370 and 800 mV at bias voltages of  $-75$  and  $-120$  V, respectively, have been reported elsewhere [7]. Higher deposition temperature results in denser coatings with fewer voids and pores because of increased ad-atom mobility and therefore better corrosion resistance. In both low and high temperature cases higher bias voltages with fewer pores and growth defects exhibit better corrosion resistance despite the higher residual stresses present in the coatings. In the work of Ref. [5] it is suggested that in coatings with higher residual stresses areas adjacent to growth defects are prone to cracking once corrosion has commenced. Such behaviour is typical of internally stressed coatings where corrosion can initiate microcracks or pits, which can then grow as microcracks or pits. It would appear however, that the beneficial effects of increases in bias voltage in terms of denser coatings and fewer growth defects more than offsets the deleterious effects of increases in residual stresses resulting from increases in bias voltage. However, even with the drawbacks of low degrees of porosity and growth defects CrN/NbN nano-scale multilayer coatings even deposited at low temperatures of  $250$  °C are able to enhance corrosion resistance of the coatings, as determined by a potentiodynamic polarisation measurement in a 3% NaCl solution open to air at room temperature, when deposited on 304 stainless steel substrates.

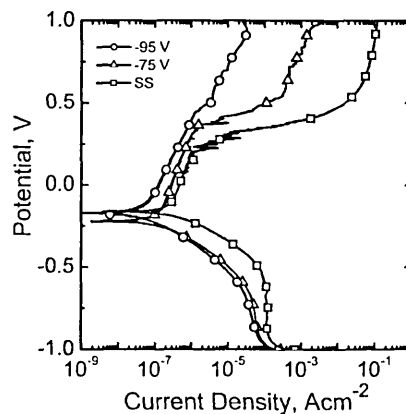


Fig. 7. Potentiodynamic polarisation curves of CrN/NbN coatings and a polished SS substrate.

#### 4. Conclusions

It has been shown that microstructure in the lower region of the growth defect is rough and severely under dense, whilst the growth defect microstructure is composed of dense columnar grains extending in feather like pattern growing from a central core.

Growth defects have been shown to be deleterious as the under dense region in the lower region is a solution-pathway to the substrate surface and hence a potential region of pitting corrosion. The droplet from which the growth defect forms is anodic with respect to the coating resulting in localised galvanic attack at the coating substrate interface.

In all cases the corrosion resistance of CrN/NbN nano-scale multilayer coatings deposited at low temperature (250 °C) are superior to that of the 304 substrate material in that they exhibit low corrosion current densities and higher pitting potentials than does the 304 material.

The corrosion resistance of the nano-scale multilayer coatings deposited at low temperature increases with increasing bias voltage but in all cases is inferior to similar coatings deposited at high temperature (450 °C).

#### References

- [1] T. Hurkmans, D.B. Lewis, J.S. Brooks, W.-D. Münz, Surf. Coat. Technol. 86/87 (1996) 192.
- [2] B. Navinsek, P. Panjan, I. Milosev, Surf. Coat. Technol. 97 (1997) 182.
- [3] T. Hurkmans, T. Trinh, D.B. Lewis, J.S. Brooks, W.-D. Münz, Surf. Coat. Technol. 76/77 (1995) 159.
- [4] L.A. Donohue, W.-D. Münz, D.B. Lewis, J. Cawley, T. Hurkmans, T. Trinh, I. Petrov, J. Greene, Surf. Coat. Technol. 93 (1997) 69.
- [5] P. Hovsepian, D.B. Lewis, W.-D. Münz, S.B. Lyon, M. Tomlinson, Surf. Coat. Technol. 120–121 (1999) 535.
- [6] W.-D. Münz, D.B. Lewis, P.Eh. Hovsepian, C. Schönjahn, A. Ehtasarian, I.J. Smith, Surf. Eng. 17 (2001) 15.
- [7] P.Eh. Hovsepian, D.B. Lewis, W.-D. Münz, Surf. Coat. Technol. 133/134 (2000) 166.
- [8] M. Tomlinson, S.B. Lyon, P.Eh. Hovsepian, W.-D. Münz, Vacuum 53 (1999) 117.
- [9] W.-D. Münz, D. Schulze, F. Hauzer, Surf. Coat. Technol. 50 (1992) 169.
- [10] W.-D. Münz, T. Hurkmans, G. Kieren, T. Trinh, J. Vac. Sci. Technol. A11 (5) (1993) 2583.
- [11] R.L. Boxman, S. Goldsmith, Surf. Coat. Technol. 48 (1992) 51.
- [12] H. Ljungcrantz, L. Hultman, J.-E. Sundgren, G. Håkansson, L. Karlsson, Surf. Coat. Technol. 63 (1994) 123.
- [13] W.-D. Münz, D.B. Lewis, S. Creasey, T. Hurkmans, T. Trinh, W. Vijzendorf, Vacuum 46 (1995) 323.
- [14] I. Petrov, P. Losbichler, D.B. Bergstrom, J.E. Greene, W.-D. Münz, T. Hurkmans, T. Trinh, Thin Solid Films 302 (1997) 179.
- [15] H. Wang, M.M. Stack, S.B. Lyon, P.Eh. Hovsepian, W.-D. Münz, Surf. Coat. Technol. 126 (2000) 279.
- [16] W.-D. Münz, D. Schulze, F. Hauzer, Surf. Coat. Technol. 50 (1992) 169.
- [17] P.Eh. Hovsepian, W.-D. Münz, A. Medlock, G. Gregory, Surf. Coat. Technol. 133/134 (2000) 508.
- [18] G.B. Harris, Phila. Mag. 43 (1952) 113.
- [19] D.B. Lewis, I.P. Wadsworth, W.-D. Münz, R. Kuzel Jr., V. Valvoda, Surf. Coat. Technol. 116/119 (1999) 284.
- [20] D.E. Geist, A.J. Perry, J.R. Treglio, V. Valvoda, D. Rafaja, Adv. X-ray Anal. 38 (1995) 471.
- [21] S. Creasey, D.B. Lewis, I.J. Smith, W.-D. Münz, Surf. Coat. Technol. 97 (1997) 163.
- [22] W.-D. Münz, I.J. Smith, D.B. Lewis, S. Creasey, Vacuum 48 (5) (1997) 473.
- [23] D.B. Lewis, D. Reitz, C. Wstefeld, R. Ohser-Wiedemann, H. Oettel, A.P. Ehtasarian, P.Eh. Hovsepian, in press.